Kinetic Insights into Dioxygen Activation by Biomimetic Thiolate-Ligated Iron Complexes

Maria B. Greiner

A dissertation

submitted in partial fulfillment of the

requirements for the degree of

Doctor of Philosophy

University of Washington

2023

Reading Committee

Julie A. Kovacs, Chair

Brandi Cossairt

Champak Chatterjee

Program Authorized to Offer Degree:

Chemistry

University of Washington

Abstract

Kinetic Insights into Dioxygen Activation by Biomimetic

Thiolate-Ligated Iron Complexes

Maria B. Greiner

Chair of Supervisory Committee:

Julie A. Kovacs

Department of Chemistry

Non-heme thiolate-ligated metalloenzymes such as isopenicillin N synthase (IPNS) and cysteine dioxygenase (CDO) dioxygen to produce catalytic oxidative intermediates including metal -superoxos, -hydroperoxos, and high-valent oxos. Thiolate-ligated metalloenzymes have been shown to form highly covalent metal ligand bonds and in return lower the activation energy barrier to dioxygen binding. Kinetic investigations of dioxygen binding to metalloenzymes provide insights into the mechanism of the enzyme and whether geometric rearrangements, spin-state changes, or solvent interactions affect dioxygen binding. This dissertation investigates the barrier

to dioxygen activation of the non-heme alkyl thiolate-ligated iron complex ($[Fe^{II}(S^{Me2}N_4(tren))]^+$) with variable low temperature stopped-flow kinetics. The reaction of $[Fe^{II}(S^{Me2}N_4(tren))]^+$ with dioxygen under pseudo first order conditions with excess dioxygen is shown to be first order with respect to dioxygen, and second order with respect to iron. These reaction orders are consistent with the formation of the peroxo-bridged diferric species $[(S^{Me2}N_4(tren))Fe^{III}]_2(\mu\text{-}O_2)]$. However, when the conditions are switched, under excess Fe, the first dioxygen derived intermediate Fe^{III}-superoxo is observed, $[Fe^{III}(S^{Me2}N_4(tren))(O_2)]^+$. The global fitting of experimental kinetic data determined that the rate determining step was the Fe^{III}-superoxo reacting with another Fe^{II} molecule to form the peroxo-bridge species, $[(S^{Me2}N_4(tren))Fe^{III}]_2(\mu\text{-}O_2)]$.

Low-temperature stopped-flow kinetic studies investigated the reversibility and mechanism of a well-characterized dioxygen derived Fe^{III}-superoxo, $[Fe^{III}(S_2{}^{Me2}N_2N^H(Pr,Pr))(O_2)]$, in aprotic and protic solvents (THF and MeOH). The different environments provided insights into ligand constraints and H-bond donors which have been shown to influence dioxygen binding kinetics and reversibility. The reaction is faster in aprotic THF versus protic MeOH, as well as irreversible in THF and reversible in MeOH. Hydrogen bonding in MeOH to the thiolate sulfur destabilization of the transition state, and an increase in the activation energy of dioxygen binding to Fe^{II}. The reaction between potassium superoxide and oxidized $[Fe^{III}(S_2{}^{Me2}N_2N^H(Pr,Pr))]^+$ was also investigated and the resulting kinetics support the dioxygen binding mechanism to $[Fe^{II}(S_2{}^{Me2}N_2N^H(Pr,Pr))]^+$ to involve inner-sphere, as opposed to outer-sphere, electron transfer.

The well characterized Fe^{III}-superoxo $[Fe^{III}(S_2{}^{Me2}N_2N^H(Pr,Pr))(O_2)]$ was shown to abstract external hydrogens with a BDFE of 93 kcal/mol with a KIE of 4.8 comparable to the strength of theβ-hydrogen Fe^{III}-superoxo in IPNS performs. In order to investigate a closer biomimetic model to IPNS, the *gem*-dimethyl groups adjacent to the thiolate sulfurs were removed to incorporate β-

hydrogens to the sulfur to form the complex, [$Fe^{II}(S_2{}^{\beta\text{-}H2}N_2N^H(Pr,Pr))$]. The structure of [$Fe^{II}(S_2{}^{\beta\text{-}H2}N_2N^H(Pr,Pr))$] more closely mimics the internal hydrogen abstraction mechanism proposed in the native enzyme. The change in the electronics affected the longevity of the Fe^{III}-superoxo intermediate and the addition of external hydrogen donors resulted in the observation of Fe intermediates. To further explore and isolate the Fe^{III}-superoxo the *β*-hydrogens were exchanged for deuteriums in order to investigate whether an internal or external hydrogen atom abstraction occurs causing the shorter lived [$Fe^{II}(S_2{}^{\beta\text{-}H2}N_2N^H(Pr,Pr))(O_2)$. The synthesis of the *β*-deuterium ligand will be discussed as well as preliminary characterizations of the complex and it's reactivity.

The [Fe^{II}(Cyclam-PrS)]$^+$ complex was shown to react with potassium superoxide in protic conditions to form a high-spin Fe^{III}-hydroperoxo. The hydroperoxo is proposed to be *trans* to the thiolate and is rare for small molecules as the electron density donated to the metal center from the sulfur tend to push ligands away. Furthermore, when [Fe^{II}(Cyclam-PrS)]$^+$ is reacted with nitric oxide, a mimic to dioxygen, a crystal structure of [Fe^{III}(Cyclam-PrS(NO))]$^+$ with the NO ligand bound *cis* to the thiolate. DFT is used to confirm if the Fe^{III}-hydroperoxo is *trans* or *cis* to the thiolate. Further investigation of the Fe^{III}-hydroperoxo utilizes dioxygen in protic solvent and alkylperoxos to observe if [Fe^{III}(Cyclam-PrS(OOH))]$^+$ can be synthesized with the shunt pathway.

Dedication

For my family

Paul, Becky, Gretchen, Heidi, Stesha

Acknowledgements

First and foremost, I give my deepest appreciation to my research advisor, Professor Julie Kovacs, for her passion of chemistry, invaluable and expansive knowledge of transition metal thiolate chemistry, and her value of determination in understanding science: do not be satisfied until every stone is turned over and examined. This process continues to resonate with me and has developed my critical thinking skills to greater heights, which ultimately allows great satisfaction for the results I produce. Julie also had the patience to, “be my bumpers,” so to speak, when I would hyper focus and not seen the broad

impacts of my research. Not only has Julie been a pillar in my scientific development, but she also created a space to experience all of the joy and grief that comes in life.. We have spent a many of conversations talking about those who are no longer with the living and honoring who they are through ourselves and work.

I would also like to thank the senior group members, Dr. Ben Leipzig, Dr. Maike Blakely, Dr. Maksym Dedushko, Dr. Penny Poon, and Dr. Alexandra Downing, whom elevated me through extensive scientific conversations, bringing other ideas to the forefront to develop me in my research. I would especially like to thank Dr. Penny Poon and Dr. Alexandra Downing, for their friendship, incredible support, and great adventures throughout my time at UW. Even through a pandemic, connecting through Mario Kart and being together made my time throughout graduate school enjoyable. Not to mention the rest of the current and former Kovacs group members: Dylan Rogers, Julian Smith-Jones, Paige Gannon, Bennet Karel, Douglas Baumgardner, and Chris Lowe, all extraordinary individuals whom have been a constant support system, through fun comradery as well as sharing in new scientific discoveries and getting dirty with replacing lab equipment.

Furthermore, the Department of Chemistry at the University of Washington instills a value of the individual while contributing to all who pursue knowledge and understanding. I greatly appreciate the professors and instructors I've met during my time at UW as a teaching assistant, in which I was given opportunities to share my love of chemistry with many students so that they too can learn and expand their minds. The friendships and encouragement from students to continue teaching while doing research, was refreshing so that others could gain from the experiences I could share and help them develop themselves into future scientists. I give my gratitude to the Inorganic Division, where I could share my new findings and deepen my understanding of my research through their queries. I would like to acknowledge my committee members throughout my graduate studies, Professors Brandi Cossairt, Alexandra Velian, Forrest Michael, Champak Chatterjee, and Jerry Seidler whose discussions and contributions to my exams improved the quality of my research and zeroed in my focus to finish projects instead of spreading myself too thin.

I express my gratitude to previous professors and my undergraduate advisor, Dr. Christine Saber, and the Gannon University Chemistry Department. I have known my talent in academia, and still have always strived towards more applications, and even considered medical school at one point on my journey simply to apply what I've learned. Soon, I discovered I would be best suited for applying my knowledge in the areas of research and pivoted my life to apply to the University of Washington – albeit 2 months before the application deadline. The professors at Gannon University are a community, and I was reminded how much love is in that community when my sister passed away. I am ever grateful for the support my past professors have for me to continue on the path I've set out for myself. I continue so that I may pay their love and support forward to, such that they can achieve what I have achieved and more.

Additionally, I show my appreciation for my parents, sisters, and created family who came along this scientific journey of mine, whether they wanted to or not. I've missed many holidays and vacations to pursue my goals, and for that they graciously understood and supported me. They've also had their fair share of restoring my patience and keeping my goals in mind, even when it took time away from their own passions. Thank you for being curious about my research and giving me a great foundation and work ethic to persevere through challenging experiences.

Finally, I want to give gratitude to the family I've created with Stesha, my wife. Your overwhelming and ongoing support throughout this process makes me excited to create the rest of our lives together. Our created family, whom I've experienced many firsts, and your tremendous support every day and the friendships that have been built remind me to be kind and always be there for those in need. I want to show some love to my late emotional companion animal, who had been with me since I'd moved to a strange new place, including multiple apartments, Thor. Throughout my time at UW, he was a constant friend, listening to many presentations so I could pretend I wasn't just talking to myself. Even though he is gone, still what grounds me and drives me to work hard is buying a house with a porch and a backyard for him to enjoy.

TABLE OF CONTENTS

Contents

Glossary

Å	Ångström
ACV	l-valine, l-cysteine, and l-α-aminoadipic acid
$^{Asp}O^-$	aspartic acid
ATR	attenuated total reflection.
BDFE	bond dissociation free energy
CDO	cysteine dioxygenase
CT	charge transfer
CV	cyclic voltammetry
$^{Cys}S^-$	cysteine
CYP450	cytochrome P450
DCM	dichloromethane
DFT	density functional theory
BS-DFT	broken symmetry DFT
EAS	electron absorbance spectroscopy
EPR	electron paramagnetic resonance
ENDOR	electron nuclear double resonance
ESI-MS	electrospray-ionization mass spectroscopy
Et_2O	diethyl ether
EtOH	ethanol
EXAFS	extended X-ray absorption fine structure
E°	standard electrode potential

ε	extinction coefficient
FT	Fourier transform
H_2O_2	hydrogen peroxide
HAT	hydrogen atom transfer
^{His}N	histidine
HOMO	highest occupied molecular orbital
HS	high-spin
Hz	Hertz
IBX-ester	iodoxybenzoate
IPNS	isopenicillin-N-synthase
J	coupling constant
KO_2	potassium superoxide
LS	low-spin
LUMO	lowest occupied molecular orbital
*m*CPBA	meta-chloroperoxybenzoic acid
MeCN	acetonitrile
MeOH	methanol
Me-THF	2-Methyltetrahydrofuran
MnLO	managanese lipoxygenase
MnSOD	superoxide dismutase
N_3^-	azide anion
NHase	nitrile hydratase
NMR	nuclear magnetic resonance

NTO	natural transition orbital
NO	Nitric oxide
$O^{\bullet}$	oxyl radical
$O_2^{\bullet-}$	superoxide anion
OH^-	hydroxide
OAD	oxo-atom donor
ORTEP	Oak Ridge Thermal-Ellipsoid Program
PDB	protein data bank
PFIB	pentafluoroiodosylbenzene
PhI	iodobenzene
PhIO	iodosylbenzene
$PhIO_2$	iodoxybenzene
PNO	pyridine-N-oxide
ppm	parts per million
QM/MM	quantum mechanics/molecular modeling
ROS	reactive oxygen species
rRaman	resonance Raman
SCE	saturated calomel electrode
SCO	spin crossover
$t_{1/2}$	half-life
TD-DFT	time-dependent density functional theory
TEA	triethylamine
TEMPOH	1-hydroxy-2,2,6,6-tetramethyl-piperidine

THF	tetrahydrofuran
TMC	1,4,8,11-tetramethyl-1,4, -8,11-tetraaza cyclotetradecane
TMCS	1-mercaptoethyl-4,8,11-trimethyl-1,4,8,11-tetraaza cyclotetradecane
tren	tris(2-aminoethyl) amine
UV-Vis	UV-visible
XAS	X-ray absorption spectroscopy
$\Delta H^{\ddagger}$	enthalpy of activation
$\Delta S^{\ddagger}$	entropy of activation
ΔG	Gibbs free energy
μ_{eff}	magnetic moment
σ^2_{oct}	variance in the octahedral angles
τ	five-coordinate geometry index
$\chi_{(T)}$	magnetic susceptibility

List of Numbered Complexes

Numbered Complexes for Chapter 2

1 $[Fe^{II}(S^{Me2}N_4(tren))]^+$

2 $[Fe^{III}(S^{Me2}N_4(tren))(O_2)]^+$

3 $[(Fe^{III}(S^{Me2}N_4(tren)))_2(\mu\text{-}O_2)]^{2+}$

4 $[Fe^{III}(S^{Me2}N_4(tren))(THF)]^{2+}$

Numbered Complexes for Chapter 3

1 $[Fe^{II}(S_2{}^{Me2}N_2N^H(Pr,Pr))]$

1•••HOMe $[Fe^{II}(S_2{}^{Me2}N_2N^H(Pr,Pr)]$•••H-OMe

2 $[Fe^{III}(S_2{}^{Me2}N_2N^H(Pr,Pr))(O_2)]$

3 $[Fe^{III}(S_2{}^{Me2}N_2N^H(Pr,Pr))]BF_4$

4 $[Fe^{III}(\eta^2\text{-}S^{Me2}O)(S^{Me2})N_2N^H(Pr,Pr)]^+$

5 $[Fe^{II}(S^{Me2}N_4(tren))]^+$

6 $[Fe^{III}(S^{Me2}N_4(tren))(O_2)]^+$

Numbered Complexes for Chapter 4

1 $[Fe^{II}(S_2{}^{Me2}N_2N^H(Pr,Pr))]$

2 $[Fe^{III}(S_2{}^{Me2}N_2N^H(Pr,Pr))]PF_6$

3 $[Fe^{III}(S_2{}^{Me2}N_2N^H(Pr,Pr))\text{-}O_2]$

4 $[Fe^{II}(S_2{}^{\beta\text{-}H2}N_2N^H(Pr,Pr))]$

4ox $[Fe^{III}(S_2{}^{\beta\text{-}H2}N_2N^H(Pr,Pr))]$

4-OMe $[Fe^{III}(S_2{}^{\beta\text{-}H2}N_2N^{H}(Pr,Pr))(OMe)]$

4-OH $[Fe^{III}(S_2{}^{\beta\text{-}H2}N_2N^{H}(Pr,Pr))(OH)]$

5 $[Fe^{III}(S_2{}^{\beta\text{-}H2}N_2N^{H}(Pr,Pr))\text{-}O_2]$

6 $[Fe^{III}(\eta^2\text{-}S^{Me2}O)(S^{Me2)}N_2N^{H}(Pr,Pr)]^+$

7 $[Fe^{III}S_2{}^{Me2}N_2N^{H}(Pr,Pr)(N_3)]$

8 $[Fe^{II}S_2{}^{D\text{-}\beta2}N_2N^{H}(Pr,Pr)]$

9 $[Fe^{III}(S_2{}^{\beta\text{-}H2}N_2N^{Me}(Pr,Pr))]$

Numbered Complexes for Chapter 5.

1 $[Fe^{II}CyclamPr,S]^+$

2 $[Fe^{III}CyclamPr,S(OOH)]^+$

3 $[Fe^{III}CyclamPr,S(NO)]$

List of Figures

Chapter 1 Figures

Chapter 2 Figures

Appendix A Figures

Chapter 3 Figures

Chapter 4 Figures

Chapter 5 Figures

List of Schemes

Chapter 4 Schema

List of Tables

Chapter 1 Tables

Chapter 2 Tables

Chapter 3 Tables

Chapter 4 Tables

Chapter 5 Tables

Chapter 1: Dioxygen Activation by Metalloenzymes and Thiolate-Ligated Biomimetic Models Complexes

1.1 Transition Metals in Bioinorganic Chemistry

Enzymes are formed from hundreds or thousands of amino acid chains that are folded in specific conformations, such as alpha helices and beta sheets. The specific conformations of the enzymes create specific landmarks for substrates to selectively bind and undergo their unique chemical processes to yield specific products.[1,2] Some enzymes evolved over time to incorporate earth abundant (in percentage) first-row transition metals, like manganese (2.33%), iron (5.63%), cobalt (0.0025%), and copper (0.006%) to perform reactions essential to sustain life.[3-6] The incorporation of transition metal ions facilitates the stabilization of the protein structure, the activation and transportation of dioxygen, the establishment of a reservoir for electrons for electron transport chains, the promotion of thermodynamically challenging catalytic reactivity such as C-H bond activation, and greener catalysis compared to the use of rare metals.[7-10] Transition metals can access different oxidation states to allow for different coordination numbers, change spin state, and therefore different steric geometries that affect ligand affinities. These slight changes in the coordination environment of the transition metal can alter the reactivity of the enzyme.

Bioinorganic chemistry is a multifaceted discipline that includes enzymology, biochemistry, inorganic coordination chemistry, and many spectroscopy techniques, with the goal of investigating the functions and mechanisms of metalloenzymes.[11] Studying the function of iron in metalloenzymes focuses on investigating the environment of the metal ion via the primary coordination sphere, and the substrates that bind at the active site.[12] While high-resolution crystal structures of native enzymes provide insight to the structure of the active sight, there are many

limitations of studying large metalloenzymes for their mechanism, such as being temperature sensitive and limited solubility non-aqueous solvents.[13-15] One approach to studying enzymes is by forming biomimetic transition metal complexes. The structural information obtained through crystallography allow for synthesis of structurally competent biomimetic models to incorporate similar coordination environments around the metal ion. Investigating the reactivity of biomimetic models tend to be simpler to monitor and their mechanism can be translated back to the metalloenzyme. The advantage of using biomimetic models is further discussed in section **1.4**

1.2 Dioxygen Activation in Metalloenzymes

Many heme and non-heme iron enzymes activate dioxygen to generate oxidative reactants that are important for the functionality of enzymes as shown in **Scheme 1.1**.[16] Activated dioxygen contributes to a vast number of reactions, some specific examples are carbon-carbon bond cleavage, oxygen-oxygen bond cleavage, hydroxylation, oxygen atom insertion, and hydrogen atom abstraction.[17-21] In terms of transition metals, dioxygen in the ground state is a paramagnetic diradical, or in a triplet state with two unpaired electrons in the anti-bonding π orbitals. The first excited state is roughly 95 kJ/mol higher in energy than the non-reactive triplet state and is more

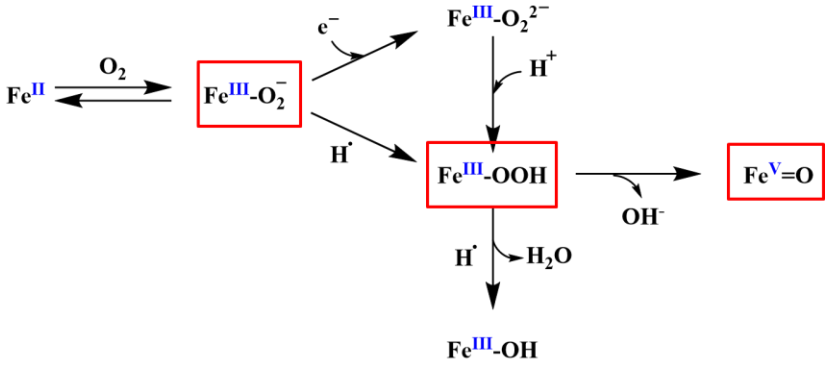

Scheme 1. 1 General scheme for dioxygen activation by mononuclear Fe^{II}, and the following oxidative species, Fe^{III}-superoxo, Fe^{III}-hydroperoxo, high valent $Fe^{IV/V}$-oxo, and Fe^{III}-hydroxide.

reactive.[22] The use of metals lowers the energy required to access the first excited state by donating an electron to the dioxygen to form a metal-superoxo radical.

The first reactive oxidant species to form is an Fe^{III}-superoxo (Fe^{III}-$O_2^{\bullet-}$), when Fe^{II} reduces dioxygen by one electron. As stated above, the transition from the triplet state of dioxygen is spin

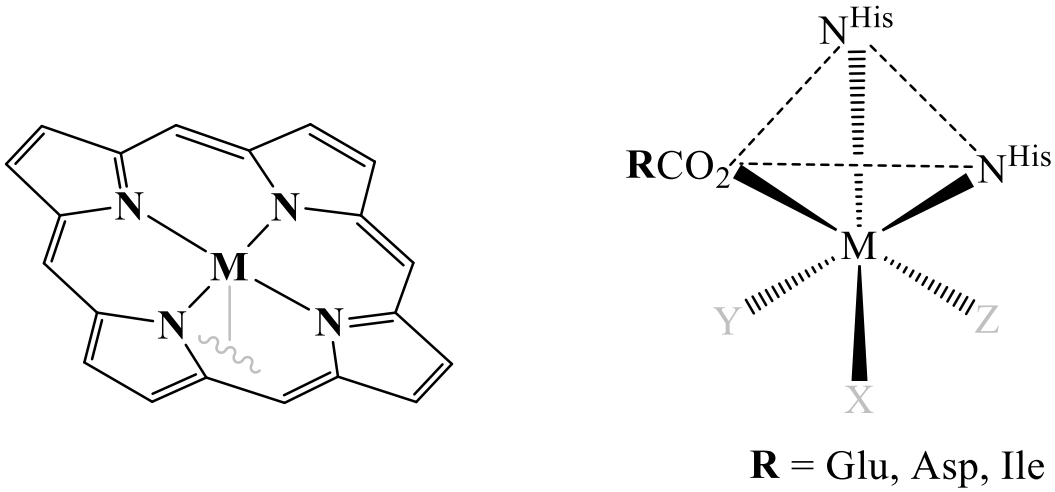

Scheme 1. 2 Left: ChemDraw of a heme porphyrin structure. **Right**: ChemDraw of the 2-His-1-carboylate facial triad of non-heme structure.[53]

forbidden and needs the metal cofactor to undergo this process. In a heme system (**Scheme 1.2, left**), where electron equivalents are stored in the ligand system or in an electron transport chain, the Fe^{III}-superoxo is reduced again to form an Fe^{III}-peroxo and proceeds on to form an Fe^{III}-hydroperoxo when hydrogen atoms are available in the protein environment. The non-heme pathway has more flexibility due to the more "open-faced" (**Scheme 1.2, right**) environment and has the second sphere environment tune the reactivity by having hydrogen-bonding donors, acid/base pairs, and non-bonded substrates providing a supply of electrons.[23] The Fe^{III}-superoxo is able to undergo hydrogen atom abstraction from a substrate to form the Fe^{III}-hydroperoxo. Formation of the hydroperoxo weakens the single O-O bond and the O-O bond can either undergo homo- or hetero-lytic cleavage to form a high-valent Fe^{IV}- or Fe^{V}-oxo. The investigation of the

mechanism of dioxygen activation remains a research focus in order to develop efficient catalysts utilizing inexpensive and environmentally friendly metals.[24,33]

The dioxygen active oxidants are important for the catalytic function of cysteine dioxygenase (CDO), which converts excess cysteine into cysteine sulfinic acid.[24] In isopenicillin N-synthase (IPNS), the Fe^{III}-O_2^- undergoes hydrogen atom abstraction (HAT) to form a Fe^{III}-hydroperoxo (Fe^{III}-OOH). An Fe^{III}-OOH intermediate is also believed to be responsible for the activity of the anticancer drug bleomycin.[25] Upon heterolytic O-O bond cleavage Fe^{III}-OOH compounds have been shown to covert to an Fe^{V}-oxo, which is considered to be the active oxidant of Cytochrome P450 (CYP450). The proposed mechanisms will be discussed more in the following sections, **1.1.2.1**, **1.2.2.1**, and **1.2.2.2**.

1.3 Effects of Thiolates on Metalloenzymes

The primary coordination spheres of metalloenzymes are usually made up of nitrogen and oxygen atoms, however, some metalloenzymes have thiolates from cysteinate residues bound to the metal center.[7,12] Thiolate ligated metal ions experience unique properties due to the delocalization of electrons. Cysteinates form highly covalent metal-sulfur bonds and experience the nephelauxetic effect. The nephelauxetic effect or “cloud expanding” effect, is the delocalization of electron density onto the sulfur’s orbitals and lowering the metal ion’s reduction potential.[26,27] The delocalization of electron density off of the metal center impacts the spin state and favors lower spin states.[28,29] With regards to dioxygen activation, computational studies have shown that incorporating thiolates lowers the energy needed by 26 kcal/mol when dioxygen is bound to the metal, in comparison to nitrogen.[30] Metal complexes with bound thiolates also have intense colored electron absorption transitions, which provide a convenient spectroscopic handle to observe their reactivity as they are sensitive to the changes in their ligand environment.[31,32]

1.3.1 Iron Heme-Metalloenzyme Cytochrome P450

A heme-metalloenzyme is a type of enzyme that is composed of a porphyrin ring, a planar structure made up of four pyrrole units connected by methine bridges, with a metal ion in the center, typically first row transition metals.[34] Cytochrome P450 (CYP450) are the first group of metalloenzymes to be classified as a "superfamily" as there are more than 21,000 members to date across numerous organisms.[35] Cytochrome P450 consists of a heme iron bound by four nitrogens in an equatorial plane and is proximally coordinated by a cysteine residue as a thiolate. These proteins were discovered by their Fe^{II}-carbon monoxide difference spectrum that had an absorbance at 450 nm, thus the spectral shift provides a basis for naming of the various enzymes and oxidation states of the iron center for the superfamily. CYP450 has been considered the chemical blow torch of enzymes as the enzyme family is key in biodegradation of pharmaceuticals, and other oxidation chemistry that is chemically challenging.[36] The area of industrial catalysis has utilized these naturally occurring enzymes for their highly selective and catalytic efficient oxidation on a broad range of substrates.[37] One example of enzymes performing challenging catalytic reactions not seen in nature is from the Arnold group's investigation of a cytochrome P411 that utilizes dioxygen to perform carbene and nitrene transfers.[38] Enzyme dioxygen activation catalysis is a greener form of chemistry than the use of trace earth metals and hazardous chemical environments and more sustainable and beneficial to the production of consumer products.[39,40]

The mechanism of CYP450, **Figure 1.1** has been established through use of X-ray crystallography, EPR/ENDOR (electron-nuclear double resonance), resonance Raman spectroscopy, and reaction rate measurements for hydrogen and deuterium substituted substrates[41-43] to identify the oxidation state of iron and oxygen active intermediates and mechanism. The resting state of the active site of the enzyme consist of a low-spin Fe^{III} that then the electronic structure of which is transformed by the binding of hydrocarbon substrate. The binding of the substrate converts the iron to high spin by changing the geometry.[44] The majority of cytochrome P450s require NAD(P)H driven redox partners to supply electrons to reduce metal species. The first reduction happens after binding of the substrate to reduce the Fe^{III} hydrocarbon bound to Fe^{II}, which allows dioxygen to bind and form an Fe^{III}-superoxo. The next reduction occurs to transform the Fe^{III}-superoxo to generate a reactive Fe^{III}-peroxo. A series of protonations occur to form a Fe^{III}-hydroperoxo known as Compound 0. Evidence for Compound 0 includes electron paramagnetic

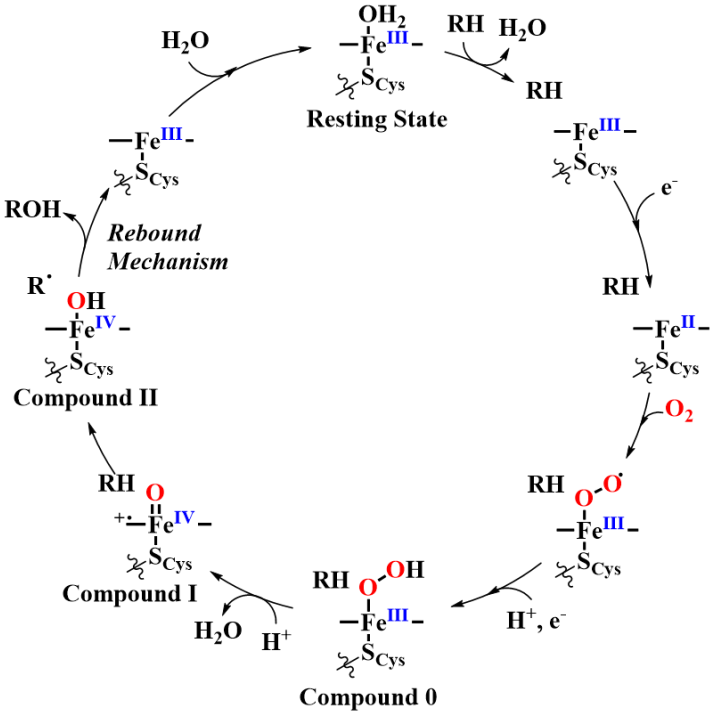

Figure 1. 1 Catalytic cycle of dioxygen activation by cytochrome P450. Oxidation and dioxygen derived species are highlighted.[36]

resonance (EPR) that revealed a low-spin iron species, and resonance Raman (rRaman) showed two vibrational stretches consistent with a bound peroxo species, ν_{O-O} = 799 cm^{-1} and ν_{Fe-O} = 559 cm^{-1}.[44] The weak O-O stretch provides evidence for a "push and pull" effect from the axial thiolate donating electron density back into the iron center. Compound 0 then undergoes heterolytic cleavage of the O-O bond by protonating the distal oxygen and forming a high valent formal Fe^{IV}-oxo heme radical,[45] meaning that the electron density is delocalized on the thiolate and porphyrin ring. The oxo is labeled as Compound 1 and has been observed via cryogenic electronic absorption, cryogenic EPR/ENDOR spectroscopy, and extended X-ray absorption fine structure (EXAFS) where the Fe-O bond was 1.65 Å.[46,47] The Fe^{IV}-oxo is considered the chemical blowtorch of oxygen insertion as it can activate inert C-H bonds of upwards to 100 kcal/mol.[48] The ability to activate such strong C-H bonds is attributed to the thiolate donating electrons back into the metal making the Fe^{IV}-oxo more basic than average metal-oxos.[49] Through hydrogen atom abstraction, an Fe^{IV}-hydroxide, Compound 2, is formed along with a carbon based radical on the hydrocarbon substrate. Evidence for the formation of Compound 2 was shown by EXAFS which found the Fe-O bond to be 1.82 Å.[47] Compound 2 has been shown to have to competing pathways to reach the resting state, either through the more commonly known radical rebound mechanism or through an alkene producing pathway.[50,51] The rebound mechanism has been difficult to study in the native enzyme, and the mechanism is not fully understood. Recently, a suitable coordination environment of a Fe^{III}-hydroxide (Fe^{III}-OH), which was synthetically challenging to create, yet Goldberg and coworkers were able to support an Fe^{III}-OH in a porphyrinoid complex and reacted with various carbon radicals to understand that the rebound mechanism proceeds through either a concerted or stepwise pathway of electron transfer and cation transfer, much like the mechanism of hydrogen atom transfer can be concerted or through a stepwise electron- , proton- transfer.[52]

1.3.2 Non-Heme Metalloenzymes

Non-heme metalloenzymes share many characteristics of heme metalloenzymes, the key difference is that the metal ion is not held in a typical porphyrin ring, but other coordination environments such as the 2-histidine-1-carboxylate facial triad.[53] The structural difference allows for non-heme enzymes to have their substrates or cofactors, such as dioxygen, to interact in a *cis* fashion with the reactive oxygen species. There are also non-heme enzymes that incorporate cysteines and utilize dioxygen to perform their chemistry such as isopenicillin N synthase and cysteine dioxygenase. The biomimetic models discussed in this dissertation are applicable to these thiolates-ligated enzymes.

1.3.2.1 Isopenicillin N Synthase

Isopenicillin N-synthase (IPNS), a non-heme iron enzyme that contains a metal center bound

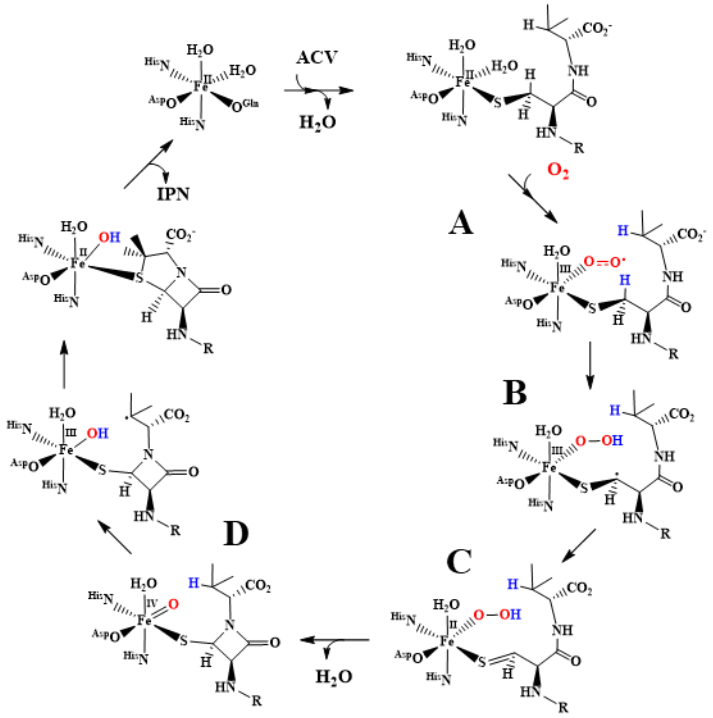

Figure 1. 2 Proposed mechanism of IPNS with key intermediates labeled: **A**) FeIII-superoxo, **B**) Fe^{III}-OOH, **C**) Fe^{II}-OOH-thioaldhyde, **D**) Fe^{IV}-oxo.[58]

in a 2-histidine-1-carboxylate facial triad with a glutamine, Gln330 side chain, all within a hydrophobic environment created by the distorted double-stranded beta helix.[54] Once the substrate, *δ*(L-α-aminoadipoyl) -L-cysteinyl-D-valine (ACV) is bound IPNS contains a cysteine in the first coordination sphere.[55] IPNS is responsible for synthesizing *β*-lactams as a precursor to penicillin.[56] Currently, bacteria are becoming resistant to penicillin due to a *β*-lactamase that targets and breaks down the 5-membered *β*-lactam ring that binds to the cell wall of the bacteria and allows other macromolecules to penetrate the cell.[57] The development of derivatives of thiazolidine-containing β-lactam antibiotics, to which bacteria are less resistant, would be aided by establishing biomimetic

models of the key reactants proposed in the IPNS mechanism to develop a better understanding of their reactivity.

The proposed mechanism of IPNS has been examined through kinetic, spectroscopic, and crystallographic studies of the native Fe enzyme as well as Mn^{II}-substituted IPNS.[59] Binding of the substrate ACV to the Fe results in Cys-SH deprotonation to form an Fe-S^{Cys} thiolate bond. When exposed to dioxygen, the iron reduces dioxygen to form a reactive Fe^{III}-superoxo (**Figure 1.2**, **A**). The enzyme positions the substrate so that the Fe^{III}-superoxo is poised to abstract a hydrogen from the cysteinyl β-carbon (BDFE = 93 kcal/mol).[60,61] In order to provide evidence that the Fe^{III}-superoxo abstracts the β-hydrogen, the ACV substrate was deuterated in order to accumulate the transient superoxo intermediate. Once accumulated, the species was spectroscopically observed using rapid freeze-quench Mössbauer spectroscopy, and transient electric absorption spectroscopy using a stopped-flow instrument at 515 nm.[62,63] Vibrational data of the putative superoxo species have yet to be reported.[62,63] After abstraction of the β-hydrogen, an Fe^{III}-hydroperoxo (**Figure 1.2**, **B**) is proposed to form, which is then reduced by the resulting thioalkyl radical, to form a reduced Fe^{II}-hydroperoxo (**Figure 1.2, C**) along with a carbon sulfur double bond (RC=S). Upon heterolytic cleavage of the putative peroxo O-O bond, water and a high valent Fe^{IV}-oxo (**Figure 1.2**, **D**) form. This second reactive oxidant (Fe^{IV}-oxo) then abstracts a hydrogen atom from the valinyl iPr group (BDFE = 96 kcal/mol) to form an Fe^{III}-hydroxide species, and a valinyl radical, which then attacks the alkyl thiolate to form the final thiazolidine ring and the resting state Fe^{II}-center.[58]

Fe^{III}-superoxos are less well- known to be strong oxidants, especially one that is powerful enough to cleave a C-H bond with BDFE = 93 kcal/mol.[58] It was previously thought that superoxos

were not capable of performing such strong hydrogen atom abstraction. The Kovacs group recently published an alkyl thiolate iron complex, [$Fe^{II}(S_2{}^{Me2}N_2N^H(Pr,Pr)$], that can support a Fe^{III}-superoxo capable of extracting hydrogens from tetrahydrofuran (THF) that has a BDFE = 92 kcal/mol.[64] In **Chapter 4** structural modification of the [$Fe^{II}(S_2{}^{Me2}N_2Pr,Pr)$] complex will be discussed and shown to also support a Fe^{III}-superoxo that has implications of modeling the IPNS mechanism.

1.3.2.2 Cysteine Dioxygenase

Another non-heme Fe enzyme surrounded by three histidine residues with a thiolate in the first coordination sphere, cysteine dioxygenase (CDO), utilizes dioxygen to oxidize cysteinate (RS^-) to cysteine sulfinic acid (RSO_2^-).[65] High levels of cysteine is implicated into the neurological disorders of Parkinson's and Alzheimer's[66-68], which demonstrate the importance of properly functioning cysteine dioxygenase. Another recent study has shown that cysteine is linked to

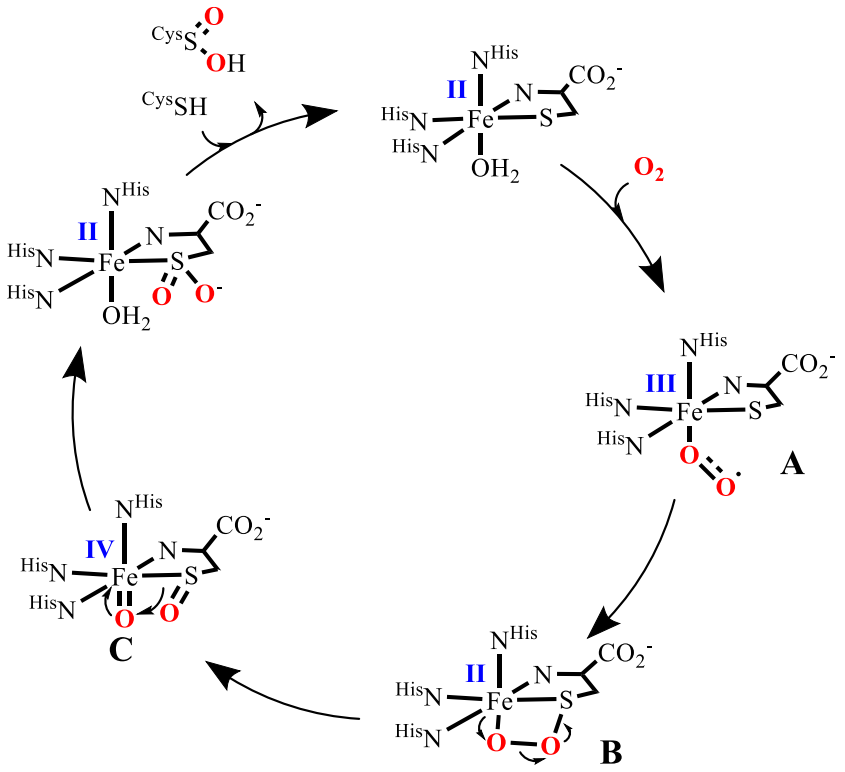

Figure 1. 3 Proposed mechanism for cysteine dioxygenase with dioxygen derived species, **A**) Fe^{III}-superoxo, **B**) Fe^{II}-peroxythiolate, and **C**) Fe^{IV}-oxo.[72]

disabling tumor suppression, in that inactive or methylated CDO does not regulate cysteine.[69-71] Tumors use the abundance of cysteine to create a "net" of cysteine to protect themselves from chemo or radiation allowing the tumor to metastasize.

The mechanism by which CDO oxygenates the sulfur of cysteine is not fully understood. One proposed mechanism based on theoretical calculations[72] is shown below, **Figure 1.3**. The resting state of Fe^{II} is such that the substrate cysteine binds to the iron active site via its sulfur atom, which lowers the activation energy for oxygen to bind *cis* to the cysteine's sulfur to form an Fe^{III} superoxo intermediate (**Figure 1.3**, **A**). The superoxo is then thought to couple to the sulfur and form a bicyclic sulfur iron peroxo intermediate, Fe^{II}-peroxythiolate (**Figure 1.3**, **B**), which has not been seen experimentally, but computationally is a possibility.[73] This peroxo can then undergo heterolytic cleavage and form a high valent Fe^{V}=O and a singly oxygenated sulfur (**Figure 1.3, C**). After the formation of the high valent iron oxo, the oxygen can then *cis* migrate to the sulfur to afford the cysteine sulfinate. A transient absorbance spectrum was collected for CDO yielding an intermediate with absorption bands at 500 nm and 650 nm, proposed to be either the Fe^{III}-superoxo or the peroxy thiolate.[74] There have only been a few Fe^{III}-superoxo model complexes reported, and only one with an alkyl thiolate.[64,75-78] The proposed intermediates **B** and **C** have yet to be spectroscopically observed in the enzyme.

1.4 Benefits of Biomimetic Modeling

Studying the active site of enzymes poses several challenges such as the enzyme-substrate interactions, the number of different ligands coordinated to the metal ion and observing the intermediates along the catalytic pathway. Some techniques used to investigate the native enzyme are quantum mechanics and molecular modeling (QM/MM) and experimental manipulations such as freeze quenching the enzyme along the catalytic pathway and utilizing spectroscopic techniques

such as Extended X-ray Absorption Fine Structure (EXAFS) and electron paramagnetic resonance (EPR) helps to characterize the active site.[79-81]

The use of small model molecules is used to study metalloenzymes because the models can mimic the coordination environment of the metal ion, through the synthesis of specific ligand architectures to provide insight into the electronic and structural properties of the metal ion within the enzyme. Transition metal model complexes allow for more stoichiometric control in organic solvents, substrate interactions, pH changes, and lower temperatures. Small model molecules can be used to probe the mechanism of the enzyme by mimicking the enzyme-substrate complex, via kinetics. Being able to stoichiometrically add dioxygen to a small model molecule and monitor the reactivity allows one to observe intermediates that are unobservable in the native enzyme. Overall biomimetic models permit for better signal to noise or resolution of spectroscopic techniques for characterization compared to their biological enzyme.[82] Biomimetic models are used to elucidate the mechanism of the native enzyme, and the use of kinetics also provides knowledge to elucidate reaction steps of the reaction pathway.

1.5 Kinetic Rates for Dioxygen Binding in Heme, Non-heme, Nitrogen, and Thiolate-Ligated Models

Some kinetic techniques to observe dioxygen binding to native enzymes or biomimetic models are flash photolysis,[83] rapid freeze-quenching,[84] and cryogenic stopped-flow.[85] Stopped-flow combined with electronic absorption spectroscopy provides “real-time” spectroscopic evidence of rapid accumulation and decay of intermediates involved in oxygen activation.[86] Stopped-flow experiments with $[Fe^{II}(S^{Me2}N_4(tren))]^+$ and $[Fe^{II}(S_2{}^{Me2}N_2N^H(Pr,Pr)]$ will be the focus in **Chapter 2** and **3** of this dissertation. The stopped-flow method is generally preferred for solution-phase reactions, which include dissolved metal complexes or solubilized gases such as dioxygen. The

stopped-flow instrument is equipped with two or more syringes, that are driven by automatic pistons, which rapidly inject the reactants into a mixing chamber (**Figure 1.4**). After mixing, the reactants are now at half the concentration of the starting reactants and the solution passes into the observation cell. The stainless-steel observation cell is immersed in an ethanol cooling bath and is

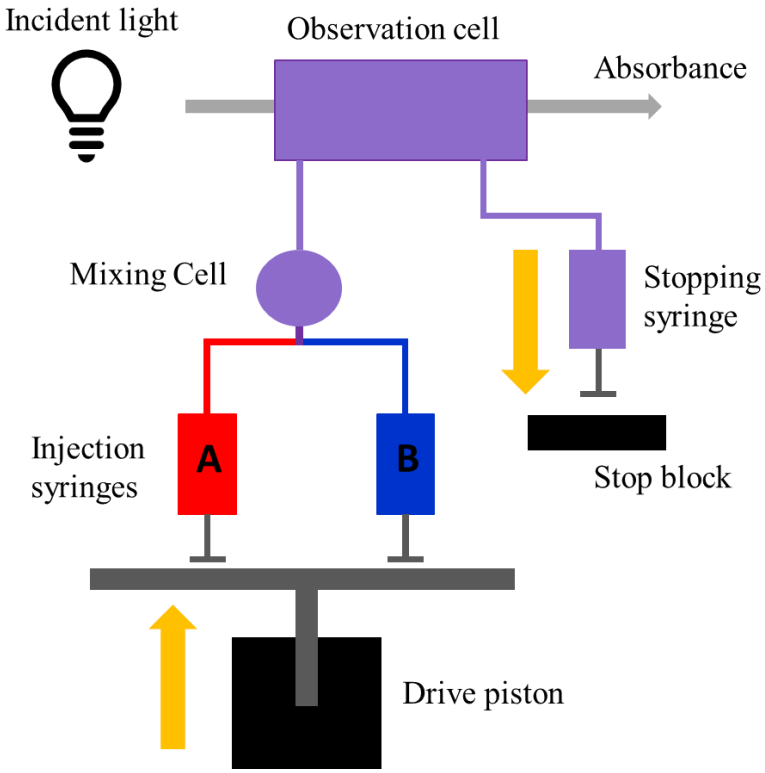

Figure 1. 4 General schematic of the stopped-flow system.

capable of reaching temperatures of -80 °C. As the solution is driven through the observation cell, it flows to the stopping syringe, that when filled strikes the stop block, and stops the flow. Once the solution is stopped, the recording of the absorption starts, and the change is monitored for a length of time. The stopped-flow instrument is equipped with two different collection modes, the charge coupled device (CCD) which collects the full spectrum, and the photomultiplier which monitors the change in absorption at a single wavelength; mostly used for millisecond timescale

reactions. The observed rates can then be compared to the concentration of reactants to determine rate constants. In the case of dioxygen, rate constants can be determined for reversible and irreversible reactions with non-heme iron complexes like [$Fe^{II}(S_2{}^{Me2}N_2N^H(Pr,Pr)$], **Chapter 3**. The use of stopped-flow provides kinetic and mechanistic insights applicable to the rational design of selective oxidative catalysts. Below is a summary of mononuclear model complexes for which dioxygen binding rates and activation parameters have been reported and a brief analysis of some of the factors that dictate the reactivity and how they are related to enzymes.

The contribution of ligand constraints and H-bond donors on the reactivity of biomimetic models reported in **Table 1.1**, are reminiscent of the influence of protein constraints and H-bond donors on metalloenzymes for dioxygen binding. Protein constraints have been shown to have a dramatic effect on electronic structure and reactivity of enzymes.[87-91] For example, the reduction

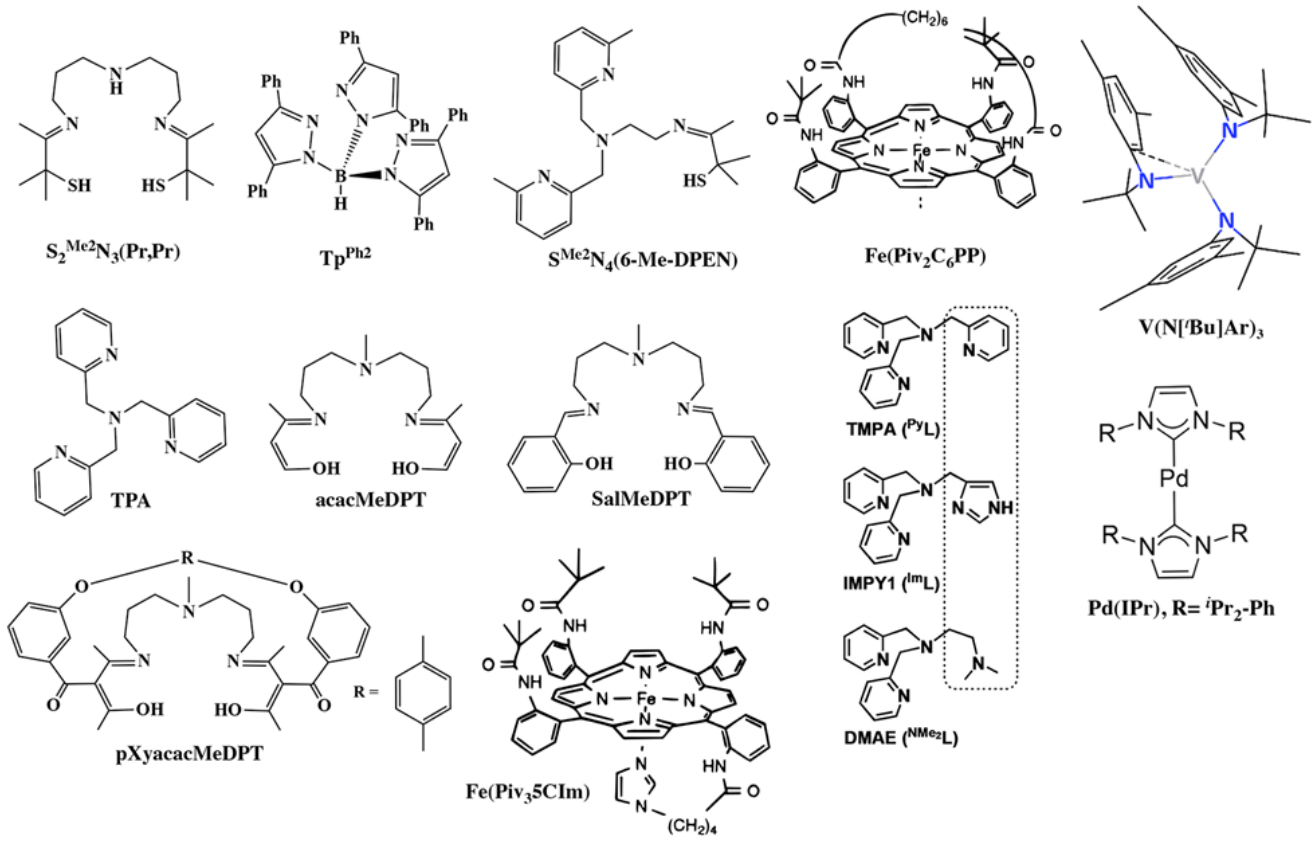

Scheme 1. 3 Chemdraw depiction of the ligands in **Table 1.1**.[87, 105-108, 113-116]

potential and electron transfer kinetics of blue copper proteins are controlled by protein structural constraints.[92] Hydrogen-bond donors can also influence the stability of metastable enzyme intermediates and influence reaction pathways.[93-96]

Comparison of the activation barriers (E_A) and rate constants (*k*) associated with dioxygen binding to the porphyrin-like systems such as salen (N,N′-Ethylenebis(salicylimine)), porphyrins, or acac (acetylacetone)(**Scheme 1.3**),[97,98] are faster than the non-heme systems.[105] The energy of activation is also lower for both synthetic and biological systems.[99-103] Some non-heme complexes containing more flexible ligands with independent arms, such as TPA, TMPA (Tris(2-pyridylmethyl)amine), tren (Tris(2-aminoethyl)amine), and Tp (Trispyrazolylborate) (**Scheme 1.3**), bind dioxygen more readily on par with heme systems. Non-heme iron models that possess a rigid backbone like [$Fe^{II}(S_2{}^{Me2}N_2N^H(Pr,Pr)$] have shown to have slower dioxygen binding.[105] The difference in activation barriers and rate constants can be attributed to the smaller rearrangement required for ligands to bind to the more readily accessible open face of a porphyrin-like metal ion. This property is important to consider in regards to facilitating O_2 release in O_2 transport proteins. Irreversible O_2 binding is important if the enzyme function involves the metal-superoxo species, as is the case with IPNS and CDO.

Table 1.1 Comparison of Kinetic Parameters for Dioxygen Binding to Mononuclear Fe^{II}, Mn^{II}, Co^{II}, and Cu^{I} Model complexes* and Biological Active Sites.

	Solvent (T)	k_{on}, $M^{-1}\ s^{-1}$	$\Delta H^{\ddagger}$, $kJ \cdot mol^{-1}$	$\Delta S^{\ddagger}$, $J \cdot mol^{-1}K^{-1}$	ref
3-, 4-, and 5-Coordinate Complexes					
$[Fe^{II}(S_2{}^{Me2}N_2N^{H}(Pr,Pr)]$ (**3.1**)	THF (-40 ˚C)	5.02(5) x 10^1	19.3(8)	-127(4)	105
	THF (0 ˚C)	2.66(28) x 10^2			
	MeOH (-30 ˚C)	0.79(6)	30(2)	-123(7)	
	MeOH (0 ˚C)	4.4(5)			
$[Fe^{II}(S^{Me2}N_4(tren))]^+$ (**2.1**)	MeOH (-40 ˚C)	5.82(3) x 10^7	34(15)	55(68)	104
$[Mn^{II}(S^{Me2}(6\text{-}MeDPEN)]^+$	MeCN (-40 ˚C)	7.17(45) x 10^2	26(2)	-76(7)	106,107
$[Cu^{I}(TPA)(THF)]^+$	THF (25 ˚C)	1.3 x 10^9	7.62	-45.1	108
$[\ ^{NMe2}LCu^{I}\ ]$ [a]	THF (-80 ˚C)	6.90(2) x 10^7	32.1	80.1	109
$^{Im}LCu^{I}(MeCN)$ [b]	THF (-80 ˚C)	1.80(3) x 10^8	23.4	35.1	109
$L^1Cu^{I}(MeCN)$ [c]	THF (-50 ˚C) [d]	1.56(2) x 10^3	18(2)	-100(10)	110
$(Me_6tren)Cu^{I}(EtCN)$	EtCN (-50 ˚C)	8.7(4) x 10^5	17.1(6)	-52(3)	111
$(TMPA)Cu^{I}(EtCN)$	EtCN (-50 ˚C)	5.0(3) x 10^5	31.6(5)	10(3)	112
Co^{II}(acacMeDPT)	acetone (-50 ˚C)	1.0(1) x 10^6	5.0	-109	113
Co^{II}(SalMeDPT)	acetone (-50 ˚C)	2.10(4) x 10^5	12.6	-80	113,115
Co^{II}(pXyacacMeDPT)	acetone (-50 ˚C)	1.74(5) x 10^6	28	-13	113
$V(N[^tBu]Ar)_3$	toluene (-53 ˚C)	40(3) x 10^3	13.8(8)	-92(4)	114
$[Pd(IPr)_2]$ [e]	toluene (-80 ˚C)	6.1(1) x 10^3	18(3)	-54(4)	116
$[Pd(IPr)(P(p\text{-}tolyl)_3)]$ [e]	THF (-80 ˚C)	1.2 x 10^3	9.2	-117	117
Five Coordinate Porphyrin Complexes					
[Fe($Piv_3$5CIm)]	Toluene (25 ˚C)	4.3 x 10^8	0.75(33)	-117(3)	97
$[Fe^{II}(Piv_2C_9)(RS)]^{1-}$	Toluene (20 ˚C)	3.5 x 10^6			98
Biological Systems					
Cyt bo_3 Ubiquinol Oxidase	H_2O (25 ˚C)	3.8 x 10^7			100
H-NOX [f]	H_2O (25 ˚C)	2.5(3) x 10^7			101
Hemoglobin (α-human)	H_2O (25 ˚C)	2.8 x 10^7			102
Fe-Mb (horse)	H_2O (22 ˚C)	9.8 x 10^7	23	-30	103

[a] ^{NMe2}L = DMAE of Scheme 1.3, [b] ^{Im}L = impy1 of Scheme 1.3, [c] L^1 = β-diketiminate (R= Me) [d]These values were obtained using flash photolysis methods. [e]IPr = 1,3-bis(diisopropyl)phenylimidazol-2-ylidene which is an N-heterocyclic carbene, [f]H-NOX = Heme Nitric oxide/Oxygen binding

**Scheme 1.3 for drawings of the ligands.*

1.6 Chapter 1 References

(1) Ushimaru, R. and Abe, I. Unusual Dioxygen-Dependent Reactions Catalyzed by Nonheme Iron Enzymes in Natural Product Biosynthesis. *ACS Catal.* **2023**, 13, 2, 1045-1076 DOI: 10.1021/acscatal.2c05247

(2) Salgado, E. N.; Radford, R. J.; Tezcan, F. A. Moetal-Directed Protein Self-Assembly. *Acc. Chem. Res.* **2010**, 43, 5, 661-672 DOI: 10.1021/ar900273t

(3) Maret W. The Metals in Biological Periodic System of the Elements: Concepts and Conjectures. *Int. J. Mol. Sci.* **2016**, 17, 66, 1-8, DOI: 10.3390/ijms17010066

(4) Suga, M.; Akita, F.; Hirata, K.; Ueno, G.; Murakami, H.; Nakajima, Y.; Shimizu, T.; Yamashita, K.; Yamamoto, M.; Ago, H.; Shen, J. R. Native Structure of Photosystem II at 1.95A° Resolution Viewed by Femtosecond X-Ray Pulses. *Nature.* **2015**, 517, 99–103, DOI: 10.1038/nature13991

(5) Young, I. D.; Ibrahim, M.; Chatterjee, R.; Gul, S.; Fuller, F. D.; Koroidov, S.; Brewster, A. S.; Tran, R.; Alonso-Mori, R.; Kroll, T.; Michels-Clark, T.; Laksmono, H.; Sierra, R. G.; Stan, C. A.; Hussein, R.; Zhang, M.; Douthit, L.; Kubin, M.; De Lichtenberg, C.; Vo Pham, L.; Nilsson, H.; Cheah, M. H.; Shevela, D.; Saracini, C.; Bean, M. A.; Seuffert, I.; Sokaras, D.; Weng, T. C.; Pastor, E.; Weninger, C.; Fransson, T.; Lassalle, L.; Bräuer, P.; Aller, P.; Docker, P. T.; Andi, B.; Orville, A. M.; Glownia, J. M.; Nelson, S.; Sikorski, M.; Zhu, D.; Hunter, M. S.; Lane, T. J.; Aquila, A.; Koglin, J. E.; Robinson, J.; Liang, M.; Boutet, S.; Lyubimov, A. Y.; Uervirojnangkoorn, M.; Moriarty, N. W.; Liebschner, D.; Afonine, P. V.; Waterman, D. G.; Evans, G.; Wernet, P.; Dobbek, H.; Weis, W. I.; Brunger, A. T.; Zwart, P. H.; Adams, P. D.; Zouni, A.; Messinger, J.; Bergmann, U.;

Sauter, N. K.; Kern, J.; Yachandra, V. K.; Yano, J. Structure of Photosystem II and Substrate Binding at Room Temperature. *Nature.* **2016**, 540, 453–457, DOI: 10.1038/nature20161

(6) Abundance of elements in the earth's crust and in the sea, CRC Handbook of Chemistry and Physics, 97th edition (**2016–2017**), p. 14-17

(7) Holm, R. H.; Kennepohl, P.; Solomon, E. I. Structural and Functional Aspects of Metal Sites in Biology. *Chem. Rev.* **1996**, 96, 7, 2239–2314, DOI: 10.1021/cr9500390

(8) Jasniewski, A. J.; Que, L. Dioxygen Activation by Nonheme Diiron Enzymes: Diverse Dioxygen Adducts, High-Valent Intermediates, and Related Model Complexes. Chem. Rev. 2018, 118 (5), 2554–2592.

(9) Ray, K.; Lee, Y. M.; Nam, W. Dioxygen Activation Chemistry by Synthetic Mononuclear Nonheme Iron, Copper and Chromium Complexes. Coord. *Chem. Rev.* **2017**, 334, 25–42, DOI: 10.1016/j.ccr.2016.07.006

(10) Lewis, J. C.; Coelho, P. S.; Arnold, F. H. Enzymatic Functionalization of Carbon–Hydrogen Bonds. *Chem. Soc. Rev*. **2011**, 40 (4), 2003–2021, DOI: 10.1039/C0CS00067A

(11) Kaim, W.; Schwederski, B.; Klein, A. *Bioinorganic Chemistry: Inorganic Elements in the Chemistry of Life An Introduction and Guide*. Wiley, **2013**, 2nd edition

(12) Lippard, S. J.; Berg, J. M. *Principles of Bioinorganic Chemistry*. University Science Books: Mill Valley, CA, **1994**; P 411

(13) Sallmann, M. and Limberg, C. Utilizing the Trispyrazolyl Borate Ligand for the Mimicking of O_2-Activating Mononuclear Nonheme Iron Enzymes. *Acc. Chem. Res.* **2015**, 48, 10, 2734-2743. DOI: 10.1021/acs.accounts.5b00148

(14) Poreba, M.; Szalek, A.; Kasperkiewicz, P.; Rut, W.; Salvesen, G. S.; Drag, M. Small Molecule Active Site Directed Tools for Studying Human Caspases. *Chem. Rev.* **2015**, 115, 22, 12546-12629 DOI: 10.1021/acs.chemrev.5b00434

(15) Segall, Y. Biomimetic Chemistry as a Useful Tool for Studying Reactive Metabolites of Pesticides. *J. Agric. Food. Chem.* **2011**, 59, 7, 2845-2856 DOI: 10.1021/jf102262p

(16) Solomon, E. I.; Goudarzi, S.; Sutherlin, K. D.; O_2 Activation by Non-Heme Iron Enzymes. *Biochemistry*. **2016**, *55*, 6363-6374, DOI: 10.1021/acs.biochem.6b00635

(17) Nam, W. Synthetic Mononuclear Nonheme Iron-Oxygen Intermediates. *Acc. Chem. Res.* **2015**, 48, 8, 2415-2423 DOI: 10.1021/acs.accounts.5b00218

(18) Guo, M.; Lee, Y.; Gupta, R.; Seo, M. S.; Ohta, T.; Wang, H.; Liu, H.; Dhuri, S. N.; Sarangi, R.; Fukuzumi, S.; Nam, W. Dioxygen Activation and O-O Bond Formation Reactions by Manganese Corroles. *J. Am. Chem. Soc.* **2017**, 139, 44, 15858-15867 DOI: 10.1021/jacs.7b08678

(19) Wu, P.; Fan, F.; Song, J.; Peng, W.; Liu, J.; Li, C.; Cao, Z.; Wang, B. Theory Demonstrated a "Coupled" Mechanism for O_2 Activation and Substrate Hydroxylation by Binuclear Copper Monooxygenases. *J. Am. Chem. Soc.* **2019**, 141, 50, 19776-19789 DOI: 10.1021/jacs.9b09172

(20) Ray, K.; Pfaff, F. F.; Wang, B.; Nam, W. Status of Reactive Non-Heme Metal-Oxygen Intermediates in Chemical and Enzymatic Reactions. *J. Am. Chem. Soc.* **2014**, 136, 40, 13942-13958 DOI: 10.1021.ja507807v

(21) Gordon, J. B.; Vilbert, A. C.; DiMucci, I. M.; ManMillan, S. N.; Lancaster, K. M.; Moenne-Loccoz, P.; Goldberg, D. P. Activation of Dioxygen by a Mononuclear Nonheme Iron Complex: Sequential Peroxo, Oxo, and Hydroxo Intermediates. *J. Am. Chem. Soc.* **2019**, 141, 44, 17533-17547 DOI: 10.1021/jacs.9b05274

(22) Kroneck, P. M. H. and Torres, M. E. S. *Sustaining Life on Planet Earth: Metalloenzymes Mastering Dioxygen and Other Chewy Gases*. Vol 15, Springer, New York **2015** 1-12

(23) Kovaleva, E. G.; Lipscomb, J. D. Versatility of Biological Non-Heme Fe(II) Centers in Oxygen Activation Reactions. Nat. Chem. Biol. **2008**, 4 (3), 186–193.

(24) Blakely, M. N.; Dedushko, M. A.; Poon, P. C. Y.; Villar-Acevedo, G.; Kovacs, J. A. Formation of a Reactive Alkyl Thiolate-Ligated Fe^{III}-Superoxo Intermediate Derived from Dioxygen. *J. Am. Chem. Soc.* **2019**, *141*, 1867-1870, DOI: 10.1021/jacs.8b12670

(25) Wonwoo, N. Synthetic Mononuclear Nonheme Iron-Oxygen Intermediates. *Acc. Chem. Res.* **2015**, *48*¸2415-2423, DOI: 10.1021/acs.accounts.5b00218

(26) Villar-Acevedo, G.; Nam, E.; Fitch, S.; Benedict, J.; Freudenthal, J.; Kaminsky, W.; Kovacs, J. A. Influence of Thiolate Ligands on Reductive N-O Bond Activation. Probing the O2- Binding Site of a Biomimetic Superoxide Reductase Analogue and Examining the Proton-Dependent Reduction of Nitrite. *J. Am. Chem. Soc.* **2011**, 133 (5), 1419–1427 DOI: 10.1021/ja107551u

(27) Shearer, J.; Scarrow, R. C.; Kovacs, J. A. Synthetic Models for the Cysteinate-Ligated Non-Heme Iron Enzyme Superoxide Reductase: Observation and Structural Characterization by XAS of an Fe III −OOH Intermediate. *J. Am. Chem. Soc*. **2002**, 124 (39), 11709–11717. DOI: 10.1021/ja012722b

(28) Green, M. T. Role of the Axial Ligand in Determining the Spin State of Resting Cytochrome P450. J. Am. Chem. Soc. 1998, 120, 10772-10773, DOI: 10.1021/JA980994H

(29) Kennepohl, P.; Neese, F.; Schweitzer, D.; Jackson, H. L.; Kovacs, J. A.; Solomon, E. I. Spectroscopy of Non-Heme Iron Thiolate Complexes: Insight into the Electronic Structure of the Low-Spin Active Site of Nitrile Hydratase. Inorg. Chem. 2005, 44, 1826-1836, DOI: 10.1021/ic0487068

(30) Goudarzi, Serra; Babicz, Jeffrey. T., Jr; Kabil, Omer; Banerjee, Ruma; Solomon, Edward. I. Spectroscopic and Electronic Structure Study of ETHE1: Elucidating the Factors Influencing Sulfur Oxidation and Oxygenation in Mononuclear Nonheme Iron Enzymes. *J. Am. Chem. Soc.* **2018,** *140*, 14887-14902, DOI: 10.1021/jacs.8b09022.

(31) Coggins, M. K. and Kovas, J. A. Structural and Spectroscopic Characterization of Metastable Thiolate-Ligated Manganese(III)-Alkylperoxo Species. *J. Am. Chem. Soc*. **2011**, 133, 12470-12473, DOI: 10.1021/ja205520u

(32) Kovacs, J. A. Synthetic Analogues of Cysteinate-Ligated Non-Heme Iron and Non-Corrinoid Cobalt Enzymes. *Chem. Rev*. **2004**, 104, 825-848, DOI: 10.1021/cr020619e

(33) Barry, S. M. and Challis, G. L. Mechanism and Catalytic Diversity of Rieske Non-Heme Iron Dependent Oxygenases. *ACS Catalysis.* **2013**, *3*, 1-29, DOI: 10.1021/cs400087p

(34) Gujarathi, P. B. Review on synthetic advances in porphyrins and metalloporphyrins. *Int. J. Chem. Studies* **2020**, 8, 3, 23-32 DOI: 10.22271/chemi.2020.v8.i3a.9459

(35) Danielson, P. B. The cytochrome p450 superfamily: biochemistry, evolution and drug metabolism in humans. *Curr Drug Metab* **2002**, 3, 6, 561-597 DOI: 10.2174/1389200023337054

(36) Rittle, J.; Green, M. T. Cytochrome P450 compound I: capture, characterization, and C-H bond activation kinetics. *Science*. **2010**, *330*, 933- 937, DOI: 10.1126/science.1193478

(37) Trindade, A. F.; Gois, P. M. P.; Afonso, C. A. M. Recyclable Stereoselective Catalysts. Chem. Rev. 2009, 109, 418-514, DOI: 10.1021/cr800200t

(38) Renata, H.; Lewis, R. D.; Sweredoski, M. J.; Moradian, A.; Hess, S.; Wang, Z. J.; Arnold, F. H. Identification of Mechanism-Based Inactivation in P450-Catalyzed Cyclopropanation Facilitates Engineering of Improved Enzymes. *J. Am. Chem. Soc.*, **2016**, *138*, 12527-12533, DOI: 10.1021/jacs.6b06823

(39) Tarczykowska, A.; Kochanski, B.; Kaluzny, K.; Zukow, W. Enzymes – important players in green chemistr. *J. Education, Health and Sport* **2017**, 7, 9, 217-223 DOI: 10.5281/zenodo.893337

(40) Hollmann, F.; Arends, I. W. C. E.; Buehler, K.; Schallmey, A.; Buhler, B. Enzyme-mediated oxidations for the chemist. *Green Chemistry* **2011**, 13, 226-265 DOI: 10.1039/c0gc00595a

(41) Unterweger, B.; Drinkwater, N.; Johanesen, P.; Lyras, D.; Dumsday, G. J.; McGowan, S. X-ray crystal structure of cytochrome P450 monooxygenase CYP101J2 from

Sphingobium yanoikuyae strain B2. *Proteins* **2017** 85, 5, 945-950 DOI: 10.1002/prot.25227

(42) Mak, P. J. and Denisov, I. G. Spectroscopic studies of the cytochrome P450 reaction mechanism. *Biochim Biophys Acta Proteins Proteom.* **2018**, 1866, 1, 178-204 DOI: 10.1016/j.bbapap.2017.06.021

(43) Guengerich, F. P. Chapter Nine -Kinetic Deuterium Isotope Effects in Cytochrome P450 Reaction. *Methods in Enzymology* **2017**, 596, 217-238 DOI: 10.1016/bs.mie.2017.06.036

(44) Shaik, S.; Cohen, S.; Wang, Y.; Chen, H.; Kumar, D.; Thiel, W. P450 enzymes: their structure, reactivity, and selectivity-modeled by QM/MM calculations. *Chem. Rev*. **2010**, 110, 949–1017, DOI: 10.1021/cr900121s

(45) Green, M. T. Evidence for Sulfur-Based Radicals in Thiolate Compound I Intermediates. *J. Am. Chem. Soc.* **1999**, 121, 34, 7939-7940, DOI: 10.1021/ja991541v

(46) Jeffreys, L. N.; Girvan, H. M.; McLean, K. J.; Munro, A. W. Characterization of Cytochrome P450 Enzymes and Their Applications in Synthetic Biology. *Methods Enzymol.* **2018**, 608, 189-261 DOI: 10.1016/bs.mie.2018.06.013

(47) Zhang, Y.; Biggs, J. D.; Mukamel, S. Characterizing the Intermediates Compound I and II in the Cytochrome P450 Catalytic Cycle with Nonlinear X-ray Spectroscopy: A Simulation Study. *Chem. Phys. Chem.* **2015**, 16, 9, 2006-2014 DOI: 10.1002/cphc.201500064

(48) Liu, J. G.; Shimizu, Y.; Ohta, T.; Naruta, Y. *J. Am. Chem. Soc*. **2010**, 132 (11), 3672–3673. DOI:

(49) Green, M. T.; Dawson, J. H.; Gray, H. B. Oxoiron(IV) in Chloroperoxidase Compound II Is Basic: Implications for P450 Chemistry. *Science*, **2004**, 304, 5677, 1653-1656, DOI: 10.1126/science.1096897

(50) He, X and Ortiz de Montellano, P. R. Radical rebound mechanism in cytochrome P-450-catayzed hydroxylation of the multifaceted radical clocks apha- and beta-thujone. *J. Biol. Chem.* **2004**, 279, 38, 39479-39484 DOI: 10.1074/jbc.M406838200

(51) Grant, J. L.; Hsieh, C. H.; Makris, T. M. Decarboxylation of fatty acids to terminal alkenes by cytochrome P450 compound I. *J. Am. Chem. Soc.* **2015**, 137, 15, 4990-4943 DOI: 10.1021/jacs.5b01965

(52) Zaragoza, J.P.T; Yosca, T. H.; Siegler, M. A.; Moenne-Loccoz, P.; Green, M. T; Goldberg, D. P. Direct Observation of Oxygen Rebound with an Iron-Hydroxide Complex. *J. Am. Chem. Soc.* **2017**, 139,39, 13640-13643, DOI: 10.1021/jacs.7b07979

(53) Hegg, E. L.; Jr, L. Q. The 2-His-1-Carboxylate Facial Triad - An Emerging Structural Motif in Mononuclear Non-Heme Iron(II) Enzymes. *Eur. J. Biochem.* **1997**, 250, 3, 625–629, DOI: 10.1111/j.1432-1033.1997.t01-1-00625.x

(54) Elkins, J. M.; Rutledge, P.J.; Burzlaff, N. I.; Clifton, I. J.; Adlington, R. M.; Roach, R. L.; Baldwin, J. E. Isopenicillin N Synthase From Aspergillus Nidulans (Anaerobic AC-Vinylglycine Fe Complex) PDB, **2003**. DOI: 10.2210/pdb1ODN/pdb

(55) Burziaff, N. I.; Rutledge, P. J.; Clifton, I. J.; Hensgens, C. M. H.; Pickford, M.; Adlington, R. M.; Roach, P. L.; Baldwin, J. E. The Reaction Cycle of Isopenicillin N Synthase Observed by X-Ray Diffraction. *Nature* **1999**, 401 (6754), 721–724. DOI: 10.1038/44400.

(56) Arnstein, H. R. V.; Clubb, M. E. The Biosynthesis of Penicillin. V. Comparison of valine and hydroxyvaline as penicillin presursors. *Biochem. J.* **1957**, 65, 4, 618-627, DOI: 10.1042/BJ0650618

(57) Smalla, K.; Cook, K.; Djordjevic, S. P.; Klümper, U.; Gillings, M. Environmental Dimensions of Antibiotic Resistance: Assessment of Basic Science Gaps. *FEMS Microbiol. Ecol*. **2018**, 94 (12), 195. DOI: 10.1093/femsec/fiy195

(58) Roach, P. L.; Clifton, I. J.; Hensgens, C. M.; Shibata, N.; Schofield, C. J. Hajdu, J.; Baldwin J. E. Structure of Isopenicillin N Synthase Complexed with Substrate and the Mechanism of Penicillin Formation. *Nature*. **1997**, *137* (6635), 827-830, DOI: 10.1038/42990.

(59) Roach, P. L.; Clifton, I. J.; Fillipt, V.; Harlost, K.; Bartont, G. J.l Hajdut, J.; Anderssontt, I.; Schofield, C. J.; Baldwin, J. E. Crystal structure of isopenicillin N synthase is the first from a new structural family of enzymes. *Nature*. **1995**, *375*, 6533 700-704, DOI: 10.1038/375700a0.

(60) McNeill, L. A.; Brown, T. J. N.; Sami, M.; Clifton, I. J.; Burzlaff, N. I.; Claridge, T. D. W.; Adlington, R. M.; Baldwin, J. E.; Rutledge, P. J.; Schofield, C. J. Terminally Truncated Isopenicillin N Synthase Generates a Dithioester Product: Evidence for a Thioaldehyde Intermediate during Catalysis and a New Mode of Reaction for Non-Heme Iron Oxidases. *Chem. – A Eur. J*. **2017**, 23 (52), 12815-12824, DOI: 10.1002/chem.201701592

(61) Rauk, A.; Yu, D.; Armstrong, D. A. Oxidative Damage to and by Cyestine in Proteins: An Ab Initio Study of the Radical Structures, C-H, S-H, and C-C Bond Dissociation

Energies, and Transition Structures for H Abstraction by Thiyl Radicals. J. Am. Chem. Soc. 1998, 120 (34), 8848-8855, DOI: 10.1021/JA9807789

(62) Tamanaha, E.; Zhang, B.; Guo, Y.; Chang, W.; Barr, E. W.; Xing, G.; St. Clair, J.; Ye, S.; Neese, F.; Bollinger, J. M.; et al. Spectroscopic Evidence for the Two C-H-Cleaving Intermediates of Aspergillus Nidulans Isopenicillin N Synthase. J. Am. Chem. Soc. 2016. 138 (28), 8862-8874, DOI: 10.1021/jacs.6b04065

(63) Blakely, M.N. Insights into Dioxygen Activation by Biomimetic Alkyl Thiolate-Ligated Iron Complexes. Ph. D. Dissertation, University of Washington, Seattle, WA, 2019

(64) Ellison, J. J.; Nienstedt, A.; Shoner, S. C.; Barnhart, D.; Cowen, J. A., Kovacs, J. A., Reactivity of Five-Coordinate Models for the Thiolate-Ligated Fe Site of Nitrile Hydratase. *J. Am. Chem. Soc.* **1998**, 120 (23), 5691-5700. DOI: 10.1021/ja973129q

(45) Parales, R. E.; Resnick, S. M. Applications of Aromatic Hydrocarbon Dioxygenases in Biocatalysis in the Pharmaceutical and Biotechnology Industries. Patel, RN., editor. CRC Press; Boca Raton, Fl.: **2006**.

(65) Yamanaka, Y.; Kato, Y.; Hashimoto, K.; Iida, K.; Nagasawa, K.; Nakayama, H.; Dohmae, N.; Noguchi, K.; Noguchi, T.; Yohda, M.; et al. Time-Resolved Crystallography of the Reaction Intermediate of Nitrile Hydratase: Revealing a Role for the Cysteinesulfenic Acid Ligand as a Catalytic Nucleophile. *Angew. Chemie Int. Ed*. **2015**, 54 (37), 10763–10767. DOI: 10.1002/anie.201502731

(66) Sen, A.; Hongpaisan, J. Hippocampal Microvasculature Changes in Association with Oxidative Stress in Alzheimer's Disease. Free Radic. *Biol. Med.* **2018**, 120, 192–203 DOI: 10.1016/j.freeradbiomed.2018.03.034

(67) Heafield, M. T.; Fearn, S.; Steventon, G. B.; Waring, R. H.; Williams, A. C.; Sturman, S. G. Plasma cysteine and sulphate levels in patients with motor neurone, Parkinson's and Alzheimer's disease. *Neurosci. Lett*. **1990**, 110, 216−220 DOI: 10.1016/0304-3940(90)90814-P

(69) Jeschke, J.; O'Hagan, H. M.; Zhang, W.; Vatapalli, R.; Calmon, M. F.; Danilova, L.; Nelkenbrecher, C.; Van Neste, L.; Bijsmans, I. T. G. W.; Van Engeland, M.; et al. Frequent Inactivation of Cysteine Dioxygenase Type 1 Contributes to Survival of Breast Cancer Cells and Resistance to Anthracyclines. *Clin. Cancer Res.* **2013**, 19 (12), 3201-3211. DOI: 10.1158/1078-0432.CCR-12-3751

(70) Yamashita, K.; Waraya, M.; Kim, M. S.; Sidransky, D.; Katada, N.; Sato, T.; Nakamura, T.; Watanabe, M. Detection of methylated CDO1 in plasma of colorectal cancer; a PCR study. *PLoS One* **2014**, 9, 12, DOI: 10.1371/journal.pone.0113546

(71) Chen, M.; Zhu, J.; Mu, W.; Guo, L. Cysteine dioxygenase type 1 (CDO1): Its functional role in physiological and pathophysiological processes. *Genes & Diseases* **2022**, DOI: 10.1016/j.gendis.2021.12.023

(72) Swathi, A.; Visser, S. P. de. The Mechanism of Cysteine Oxygenation by Cysteine Dioxygenase Enzymes. *J. Am. Chem. Soc* **2007**, 129 (48), 14846–14847, DOI: 10.1021/ja0758178

(73) Tchesnokov, E. P.; Faponle, A. S.; Davies, C. G.; Quesne, M. G.; Turner, R.; Fellner, M.; Souness, R. J.; Wilbanks, S. M.; De Visser, S. P.; Jameson, G. N. L. An Iron–Oxygen Intermediate Formed during the Catalytic Cycle of Cysteine Dioxygenase. *Chem. Commun.* **2016**, 52, 8814–8817. DOI: 10.1039/C6CC03904A

(74) Tchesnokov, E. P.; Faponle, A. S.; Davies, C. G.; Quesne, M. G.; Turner, R.; Fellner, M.; Souness, R. J.; Wilbanks, S. M.; De Visser, S. P.; Jameson, G. N. L. An Iron–Oxygen Intermediate Formed during the Catalytic Cycle of Cysteine Dioxygenase. *Chem. Commun*. **2016**, 52, 8814–8817, DOI: 10.1039/C6CC03904A

(75) Fischer, A. A.; Lindeman, S. V.; Fiedler, A. T., A synthetic model of the nonheme iron–superoxo intermediate of cysteine dioxygenase. *Chem. Comm*. **2018**, 54, 11344-11347. DOI: 10.1039/c8cc06247a

(76) Hong, S.; Sutherlin, K. D.; Park, J.; Kwon, E.; Siegler, M. A.; Solomon, E. I.; Nam, W., Crystallographic and spectroscopic characterization and reactivities of a mononuclear non-haem iron(III)-superoxo complex. *Nature Comm*. **2014**, 5, 5440-5446. DOI: 10.1038/ncomms6440

(77) Chiang, C. -W.; Kleepsies, S. T.; Stout, H. D.; Meier, K. K.; Li, P. -Y.; Bominaar, E. L.; Que, L., Jr.; Munck, E.; Lee, W. -Z., Characterization of a Paramagnetic Mononuclear Nonheme Iron- Superoxo Complex. *J. Am. Chem. Soc.* **2014**, 136, 10846-10849. DOI: 10.1021/ja504410s

(78) Winslow, C.; Lee, H. B.; Field, M. J.; Teat, S. J.; Rittle, J., Structure and Reactivity of a High-Spin, Nonheme Iron(III)- Superoxo Complex Supported by Phosphinimide Ligands. *J. Am. Chem. Soc*. **2021**, 143, 13686-13693. DOI: 10.1021/JACS.1C05276

(79) Jeschke, G. EPR Techniques for Studying Radical Enzymes. *Biochim. Biophys. Acta - Bioenerg.* **2005**, 1707 (1), 91–102, DOI: 10.1016/J.BBABIO.2004.02.012

(80) Šrajer, V.; Schmidt, M. Watching Proteins Function with Time-Resolved X-Ray Crystallography. *J. Phys. D. Appl. Phys.* **2017**, 50 (37), DOI: 10.1088/1361-6463/aa7d32

(81) Tzeliou, C. E.; Mermigki, M. A.; Tzeli, D. Review on the QM/MM Methodologies and Their Application to Metalloproteins. *Molecules* **2022**, 27, 2660 1-28 DOI: 10.3390/molecules27092660

(82) Kovacs, J. A. and Brines L. M. Understanding How the Thiolate Sulfur Contributes to the Function of the Non-Heme Iron Enzyme Superoxide Reductase. *Acc. Chem. Res.* **2007**, *40* 501-509, DOI: 10.1021/ar600059h.

(83) Worrall, D. R. and Williams, S. L. Chemical Applications of Lasers - Diffuse-Reflectance Laser Flash Photolysis. *Encyclopedia of Modern Optics* **2005**, 31-38 DOI: 10.1016/B0-12-369395-0/00940-4

(84) Tavares, P. and Pereira, A. S. Fast Kinetics – Stopped-Flow and Rapid Freeze-Quench. *Radiation in Bioanalysis* **2019** vol 8. Springer, Cham DOI: 10.1007/978-3-030-28247-9_13

(85) Kryatov, Sergey V. and Rybak-Akimova, Elena V. Kinetics and Mechanisms of Formation and Reactivity of Non-heme Iron Oxygen Intermediates. *Chem. Rev*. **2005**, 105, 2175-2226, DOI: 10.1021/cr030709z

(86) Korendovych, I. V.; Kryatov, S. V.; Rybak-Akimova, E. V. Dioxygen Activation at Non-Heme Iron: Insights from Rapid Kinetic Studies. *Acc. Chem. Res.* **2007**, 40, 510-521 DOI: 10.1021/ar600041x

(87) Guo, Cunlan; Yu, Jingxian; Horsley, John R.; Sheves, Mordechai; Cahen, David; Abell, Andrew D., Backbone-Constrained Peptides: Temperature and Secondary Structure Affect Solid-State Electron Transport. *The Journal of Physical Chemistry B* **2019,** *123* (51), 10951-10958, DOI: 10.1021/acs.jpcb.9b07753

(88) Kavanaugh, J. S.; Rogers, P. H.; Arnone, A., Crystallographic Evidence for a New Ensemble of Ligand-Induced Allosteric Transitions in Hemoglobin: The T-to-THigh Quaternary Transitions. *Biochemistry* **2005,** *44*, 6101-6121, DOI: 10.1021/bi047813a.

(89) Clark, K. M.; Yu, Y.; Marshall, N. M.; Sieracki, N. A.; Nilges, M. J.; Blackburn, N. J.; van der Donk, W. A.; Lu, Y., Transforming a Blue Copper into a Red Copper Protein: Engineering Cysteine and Homocysteine into the Axial Position of Azurin Using Site-Directed Mutagenesis and Expressed Protein Ligation. *J. Am. Chem. Soc.* **2010,** *132*, 10093-10101, DOI: 10.1021/ja102632p

(90) Hegg, E. L.; Mortimore, S. H.; Cheung, C. L.; Huyett, J. E.; Powell, D. R.; Burstyn, J. N., Structure-Reactivity Studies in Copper(II)-Catalyzed Phosphodiester Hydrolysis. *Inorg. Chem.* **1999,** *38*, 2961-2968, DOI: 10.1021/ic981087g.

(91) Plegaria, J. S.; Duca, M.; Tard, C.; Friedlander, T. J.; Deb, A.; Penner-Hahn, J. E.; Pecoraro, V. L., De Novo Design and Characterization of Copper Metallopeptides Inspired by Native Cupredoxins. *Inorg. Chem.* **2015,** *54*, 9470-9482, DOI: 10.1021/acs.inorgchem.5b01330

(92) Colman, P. M.; Freeman, H. C.; Guss, J. M.; Murata, M.; Norris, V. A.; Ramshaw, J. A. M.; Venkatappa, M. P., Blue Copper structure & entatic state. *Nature* **1978,** *272*, 319, DOI:

(93) Mann, S. I.; Heinisch, T.; Ward, T. R.; Borovik, A. S., Peroxide Activation Regulated by Hydrogen Bonds within Artificial Cu Proteins. *J . Am. Chem. Soc.* **2017,** *139*, 17289-17292, DOI: 10.1021/jacs.7b10452.

(94) Borovik, A. S., Bioinspired Hydrogen Bond Motifs in Ligand Design: The Role of Noncovalent Interactions in Metal Ion Mediated Activation of Dioxygen. *Acc. Chem. Res.* **2005,** *38*, 54-61, DOI: 10.1021/ar030160q

(95) Cook, S. A.; Borovik, A. S., Molecular Designs for Controlling the Local Environments around Metal Ions. *Acc. Chem. Res.* **2015,** *48*, 2407-2414, DOI: 10.1021/acs.accounts.5b00212

(96) Cook, S. A.; Hill, E. A.; Borovik, A. S., Lessons from Nature: A Bio-Inspired Approach to Molecular Design. *Biochemistry* **2015,** *54*, 4167-4180, DOI: 10.1021/acs.biochem.5b00249

(97) Collman, J. P. ; Brauman, J. I.; Iverson, B. L. ; Sessler, J. L. ; Morris, R. M. ; Gibson, Q. H, Dioxygen and Carbonyl Binding to Iron(II) Porphyrins: A Comparison of the "Picket Fence" and "Pocket" Porphyrins. *J. Am. Chem. Soc.* **1983,** *105*, 3052-3064, DOI: 10.1021/JA00348A019

(98) Momenteau, M.; Reed, C.A., Synthetic heme dioxygen complexes. *Chem. Rev.* **1994,** *94*, 659-698, DOI: 10.1002/CHIN.199439305

(99) Purdy, M. M.; Koo, L. S.; Ortiz de Montellano, P. R.; Klinman, J. P., Mechanism of O2 Activation by Cytochrome P450cam Studied by Isotope Effects and Transient State Kinetics. *Biochemistry* **2006,** *45*, 15793-15806.

(100) Szundi, I.; Kittredge, C.; Choi, S. K.; McDonald, W.; Ray, J.; Gennis, R. B.; Einarsdottir, O., Kinetics and Intermediates of the Reaction of Fully Reduced Escherichia coli bo3 Ubiquinol Oxidase with O2. *Biochemistry* **2014,** *53*, 5393-5404, DOI: 10.1021/bi500567m

(101) Weinert, E. E.; Phillips-Piro, C. M.; Tran, R.; Mathies, R. A.; Marletta, M. A., Controlling Conformational Flexibility of an O2-Binding H-NOX Domain. *Biochemistry* **2011,** *50*, 6832-6840, DOI: 10.1021/bi200788x

(102) Springer, B. A.; Sligar, S. G.; Olson, J. S.; Phillips, G. N., Jr., Mechanisms of Ligand Recognition in Myoglobin. *Chem. Rev.* **1994,** *94*, 699-714, DOI: 10.1021/cr00027a007

(103) Antonini, E. ; Brunori, M, Hemoglobin and Myoglobin in Their Reactions with Ligands. *North-Holland: Amsterdam*, **1971**, 178, 4058, 296, DOI: 10.1126/science.178.4058.296

(104) Dedushko, M. A.; Greiner, M. B.; Downing, A. N.; Coggins, M. K.; Kovacs, J. A., Electronic Structure and Reactivity of Dioxygen-Derived Thiolate-Ligated Fe-Peroxo and Fe(IV) Oxo Compounds. *J. Am. Chem. Soc.* **2022,** *144* (19), 8515-8528, DOI: 10.1021/jacs.1c07656

(105) Greiner, Maria; Downing, Alexandra, N.; Blakely, Maike N.; Piquette, Marc C.; Kovacs, Julia A. Cryogenic Stopped-Flow Kinetic Studies Involving the Formation of a Thiolate-Ligated FeIII-Superoxo *Manuscript Submitted*

(106) Coggins, M. K.; Sun, X.; Kwak, Y.; Solomon, E. I.; Rybak-Akimova, E.; Kovacs, J. A. , Characterization of Metastable Intermediates Formed in the Reaction Between a Mn(II) Complex and Dioxygen, Including a Crystallographic Structure of a Binuclear Mn(III)-Peroxo Species. *J. Am. Chem. Soc.* **2013,** *135*, 5631-5640, DOI: 10.1021/ja311166u

(107) Poon, P. C. Y.; Dedushko, M. A.; Sun, X.; Yang, G.; Toledo, S.; Hayes, E. C.; Johansen, A.; Piquette, M. C.; Rees, J. A.; Stoll, S.; Rybek-Akimova, E.; Kovacs, J. A., How Metal Ion Lewis Acidity and Steric Properties Influence the Barrier to Dioxygen Binding, Peroxo O-O Bond Cleavage, and Reactivity. *J. Am. Chem. Soc.* **2019,** *141* (38), 15046-15057, DOI: 10.1021/jacs.9b04729

(108) Fry, H.C.; Scaltrito, D.V.; Karlin, K.D.; Meyer, G.J. The rate of O2 and CO binding to a copper complex, determined by a "flash-and-trap" technique, exceeds that for hemes. *J. Am. Chem. Soc.* **2003,** *125*, 4657-4663, DOI: 10.1021/ja034911v

(109) Lucas, H.R.; Meyer, G.J.; Karlin, K.D., CO and O2 binding to pseudo-tetradentate ligand-copper(I) complexes with a variable N-donor moiety: kinetic/thermodynamic investigation reveals ligand-induced changes in reaction mechanism. *J. Am. Chem. Soc.* **2010,** *132*, 12927 – 12940, DOI: 10.1021/ja104107q

(110) Aboelella, N. W.; Kryatov, S. V.; Gherman, B. F.; Brennessel, W. W.; Young, V. G.; Sarangi, R. ; Rybak-Akimova, E. V.; Hodgson, K. O.; Hedman, B.; Solomon, E. I.; Cramer, C. J.; Tolman, W. B., Dioxygen Activation at a Single Copper Site: Structure, Bonding, and Mechanism of Formation of 1:1 Cu-O2 Adducts. *J. Am. Chem. Soc.* **2004,** *126*, 16896-16911, DOI: 10.1021/ja045678j.

(111) Weitzer, M.; Schindler, S.; Brehm, G.; Hörmann, E.; Jung, B.; Kaderli, S.; Zuberbühler, A., *Inorg. Chem.* **2003,** *42*, 1800-1806.

(112) Zhang, C. X; Kaderli, S.; Costas, M.; Kim, E.; Neuhold, Y.-M.; Karlin, K. D.; Zuberbuhler, A. D., Copper(I)-Dioxygen Reactivity of [(L)CuI]+ (L) Tris(2-pyridylmethyl)amine): Kinetic/Thermodynamic and Spectroscopic Studies Concerning the Formation of Cu-O2 and Cu2-O2 Adducts as a Function of Solvent Medium and 4-Pyridyl Ligand Substituent Variations. *Inorg. Chem.* **2003,** *42*, 1807-1824, DOI: 10.1021/ic0205684

(113) Rybak-Akimova, E. V.; Otto, W.; Deardorf, P.; Roesner, R.; Busch, D. H., Kinetics and Equilibrium of Dioxygen Binding to a Vacant Site in Cobalt(II) Complexes with Pentadentate Ligands. *Inorg. Chem.* **1997,** *36*, 2746-2753, DOI: 10.1021/ic961371c

(114) Cozzolino, A. F.; Tofan, D.; Cummins, C. C.; Temprado, M.; Palluccio, T. D.; Rybak-Akimova, E. V.; Majumdar, S.; Cai, X.; Captain, B.; Hoff, C. D., Two-Step Binding of O2 to a Vanadium(III) Trisanilide Complex To Form a Non-Vanadyl Vanadium(V) Peroxo Complex. *J. Am. Chem. Soc.* **2012,** *134*, 18249-18252, DOI: 10.1021/ja309621h

(115) Cini, R.; Orioli, P., Co(II)O2N3(Pr,Pr) with phenoxide similar to ours. *Inorg. Chim. Acta.* **1982,** *63*, 243.

(116) Palluccio, T. D.; Cai, X.; Majumdar, S.; Sarafim, L. F.; Tomson, N. C.; Wieghardt, K.; Cazin, C. S. J.; Nolan, S. P.; Cozzolino, A. F.; Rybak-Akimova, E. V.; Fernandez-Gonzalez, M. A.; Temprado, M.; Captain, B.; Hoff, C. D., Ligand-Directed Reactivity in Dioxygen and Water Binding to cis-[Pd(NHC)2(η2-O2)]. *J. Am. Chem. Soc.* **2018,** *140*, 264-276, DOI: g/10.1021/jacs.7b09905

(117) Cai, X.; Majumdar, S.; Fortman, G. C.; Cazin, C. S. J.; Slawin, A. M. Z.; Lhermitte, C.; Prabhakar, R.; Germain, M. E.; Palluccio, T. D.; Nolan, S. P.; Rybak-Akimova, E. V.; Temprado, M.; Captain, B.; Hoff, C. D., Oxygen Binding to [Pd(L)(L0)] (L= NHC, L0 = NHC or PR3, NHC = N-Heterocyclic Carbene). Synthesis and Structure of a Paramagnetic trans-[Pd(NHC)2(η1-O2)2] Complex. *J. Am. Chem. Soc.* **2011,** *133*, 1290-1293, DOI: 10.1021/ja1103348

Chapter 2: Investigation of Rapid Dioxygen Binding by a Non-Heme Single Thiolate-Ligated Fe^{II} Complex

Portions of this chapter have been republished or adapted with permission of the Journal of American Chemical Society from, "Electronic Structure and Reactivity of Dioxygen-Derived Aliphatic Thiolate-Ligated Fe-Peroxo and Fe(IV) Oxo Compounds" Dedushko, Maksym A.; Greiner, Maria B.; Downing, Alexandra N.; Coggins, Michael K.; Kovacs, Julie A. *J. Am. Chem. Soc.* **2022**, 144, 19, 8515-8528. DOI: 10.1021/jacs.1c07656

As well as from, "Superoxide Oxidation by a Thiolate-Ligated Iron Complex and Anion Inhibition." Dedushko, Maksym A.; Pikul, Jessica H.; Kovacs Julie A. *Inorg. Chem*. **2021**, 60, 10, 7250-7261 DOI: 10.1021/acs.inorgchem.1c00336

2.1 Introduction

Heme and non-heme enzymes utilize dioxygen to carry out biological and environmental functions required to sustain life.[1-5] Binding of dioxygen in heme enzymes is significantly faster than in their non-heme counterparts and characterizing or observing each one electron reduction of activated dioxygen is substantially more difficult. Much of our understanding of the properties of heme and non-heme iron enzyme dioxygen intermediates such as Fe^{III}-superoxos (Fe^{III}-$O_2^{\bullet-}$), Fe^{III}-peroxos (Fe^{III}-O_2^{-}), and high-valent iron oxos, ($Fe^{IV/V}$=O) comes from small molecule chemistry. [6-13] However, only superoxos and binuclear peroxos can be derived from dioxygen, or in some cases inorganic superoxides (KO_2). As discussed in the introductory chapter, only a small number of non-heme iron enzymes incorporate thiolates in the first coordination sphere, and their influence on a non-heme iron model will be further discussed here.

Previously, the Kovacs group has shown that the solvent bound $[Fe^{III}(S^{Me2}N_4(tren))(THF)]^{2+}$ (**4**) was able to oxidize superoxide (O_2^-) to afford quantitatively dioxygen (O_2) via a transient Fe^{III}-superoxo intermediate that is only observable via electronic absorption spectroscopy (EAS) at temperatures below -125 °C.[14] The proposed short-lived Fe^{III}-superoxo, $[Fe^{III}(S^{Me2}N_4(tren))(O_2)]^+$ (**2**), is also observed in the reaction between $[Fe^{II}(S^{Me2}N_4(tren))]^+$ (**1**) and dioxygen at -130 °C in MeOH/EtOH (1:1) **Figure 2.1**, with a characteristic band at λ_{max} = 690 nm. Even under these extreme conditions a substantial amount of the peroxo-bridged dinuclear species, $[(Fe^{III}(S^{Me2}N_4(tren)))_2(\mu\text{-}O_2)]^{2+}$ (**3**), at λ_{max} = 465 nm is observed along with the 690 nm band. Note that the 465 nm band is asymmetrically broadened at -130 °C due to the addition of two peaks

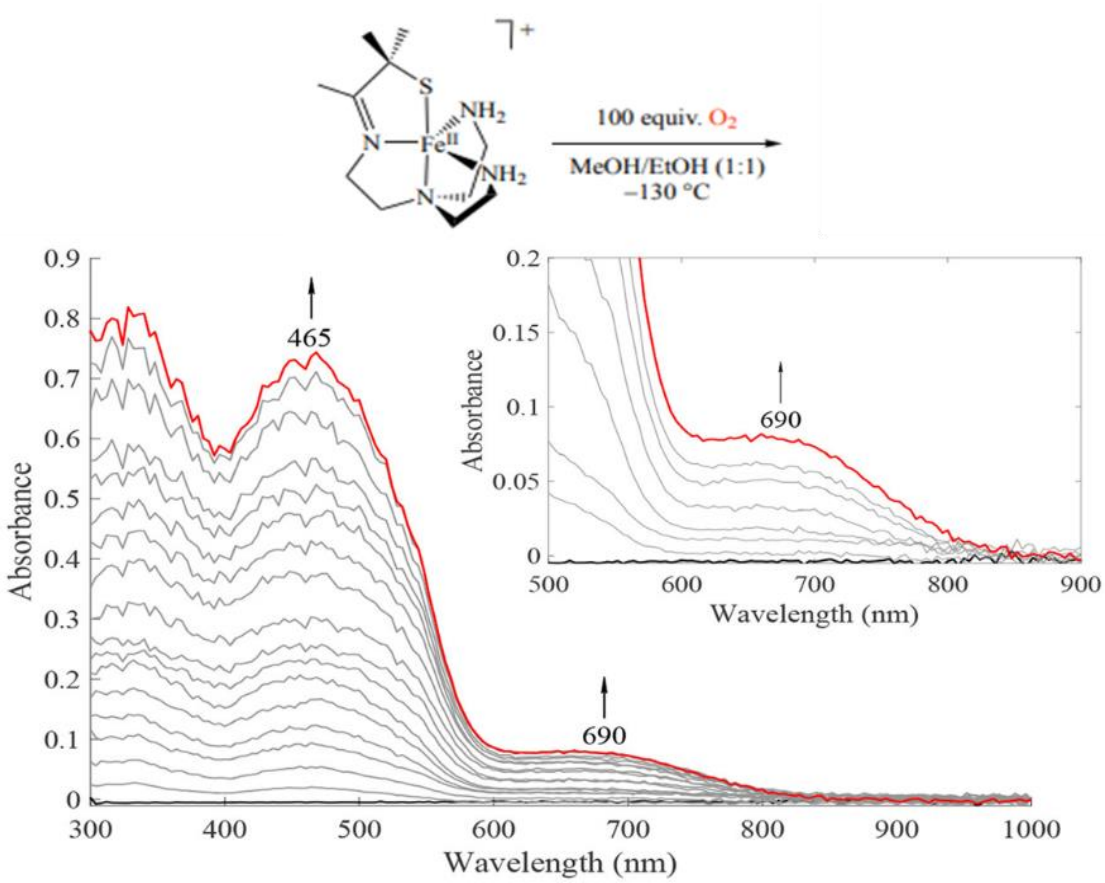

Figure 2.1 EAS of $[Fe^{II}(S^{Me2}N_4(tren))]^+$ **1** (0.1 mM) to saturated O_2 (~ 3.6 mM) solution of MeOH/EtOH (1:1) at -130 °C observed growth of mixture of intermediates. Insert of 500 - 900 nm region for clarity.

centered around 400 and 530 nm. Gaussian fits[15] were employed to the EAS spectrum in **Figure 2.1** and are consistent with two species: the proposed Fe^{III}-superoxo **2** that has three bands are λ_{max} = 401, 530, and 690 nm, and the binuclear peroxo **3** at 465 nm, **Figure 2.2**. Slight warming to -115 °C causes the electronic absorption broad 465 nm band to sharpen and the 690 nm associated with **2** to disappear and convert to a second metastable species rapidly and irreversibly, **3** with a λ_{max} of 465 nm. Time-dependent density functional theory calculations, specifically broken symmetry density functional theory, were performed to elucidate the characteristic peaks that would be associated with the proposed species **2**, **Figure 2.3**. Analysis of the natural transition orbitals (NTOs) responsible for the observed calculated bands resulted the higher energy bands to

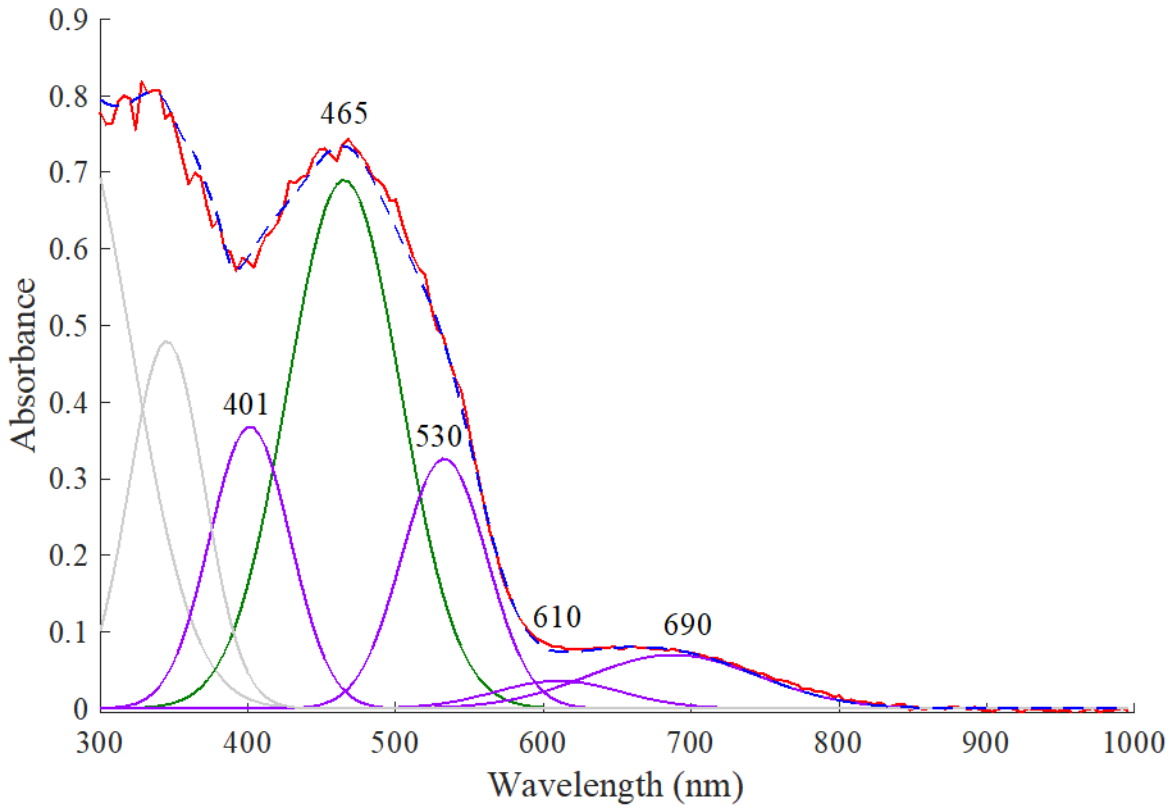

Figure 2.2 Gaussian fits (using Fityk[15]) to EAS of **1** (0.1 mM) and saturated O_2 (~ 3.6 mM) in 1:1 MeOH/EtOH. Experimental data in red, sum of the Gaussian fits to simulated experimental data in blue, Gaussian fits to proposed **2** at λmax = 401, 530, 610 and 690 nm in purple, Gaussian fit to **3** at λ_{max} = 465 nm in green, and higher energy bands depicted in grey.

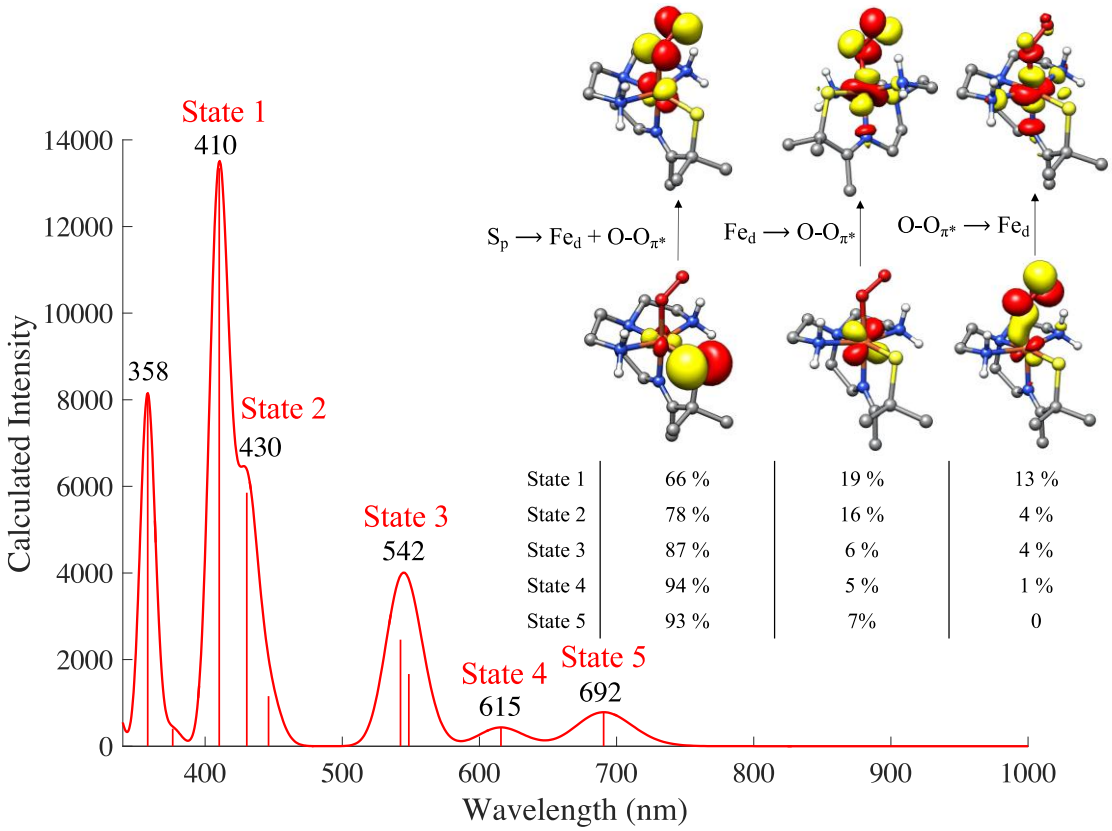

Figure 2.3 TD-DFT calculate electronic absorption spectrum of $[(Fe^{III}(S^{Me2}N_4(tren)))_2(\mu\text{-}O_2)]^{2+}$ (**3**), including percentages of natural transition orbitals (NTO) describing the charge transfer (CT) transitions.

be superoxo π*(O-O) → $d_{x^2-y^2}$(Fe), and d_{xy}(Fe) → π*(O-O) charge transfers at λ_{max}^{calc} = 410, 430, and 542 nm, supporting the broad nature of the 465 nm band, and the lower energy bands were primarily thiolate to metal superoxo (RS^- → $Fe\text{-}O_2^{\bullet-}$) charge transfer bands λ_{max}^{calc} = 692 nm At temperatures ranging from -40 to -115 °C, the **3** is the only species observed to form in reactions between **1** and dioxygen under standard EAS where the concentration of O_2 is variable and in excess. Once **3** is formed, solutions of **3** are stable for weeks in a -80 °C freezer.[16] Given the relative stability of this intermediate, **3** has been characterized by EAS to have a λ_{max} of 465 nm with an extinction coefficient of ~3000 $M^{-1}cm^{-1}$ in MeOH and is EPR silent in both parallel and perpendicular mode. The release of dioxygen was quantitatively determined and consists with a

Fe:O_2 2:1 ratio. Hydrogen peroxide (H_2O_2) detection upon acidification of **3** *in situ* provides additional support for an antiferromagnetically coupled peroxo-bridged dimer formation for **3**. The focus of **Chapter 2** will be on kinetic experiments to elucidate the dioxygen activation mechanism of **1** to form the putative Fe^{III}-superoxo **2** and its conversion to **3** and provide more evidence for the putative **2**.

2.2 Results and Discussion

2.2.1 Mechanism of Dioxygen Activation

The general kinetic scheme is shown in **Scheme 2.1**, the first intermediate for dioxygen activation is a Fe^{III}-superoxo and assumed to be reversible as previous evidence of dioxygen evolution as described previously. Once **2** is formed it goes on to react with another molecule of **1** to form the final species of interest, **3**. Formation of **3** is assumed to be irreversible upon the evidence that **3** is stable via monitoring EAS under an argon stream or under vacuum on for an hour. However, there is another pathway possible where **2** is not observed in which **1** reacts with dioxygen directly to form **3** at moderately low temperatures respectively.

The overall rate expression that describes the formation of **3** is represented by **Eq 2.1** and can be derived using the steady-state approximation with respect to the concentration of Fe^{III}-superoxo

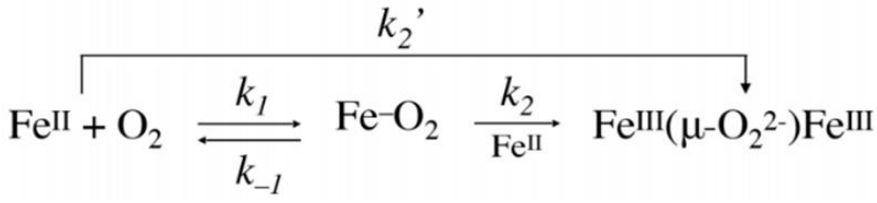

Scheme 2.1 Reaction scheme for the two pathways for the formation of peroxo-bridged dimer **3** in the reaction between **1** and O_2 and the corresponding rate constants.

2, [FeO_2].Terms are defined as k_1 is the formation of **2**, k_{-1} is the dissociation of dioxygen from **2**,

and k_2 for the conversion of the Fe^{III}-superoxo **2** to dinuclear peroxo **3** with another molecule of

$$\text{rate} = k_1[Fe^{II}]_0[O_2] - k_{-1}[FeO_2] + k_2[FeO_2][Fe^{II}]_t \qquad \text{Eq. 2.1}$$

$$k_1[Fe^{II}]_0[O_2] = [FeO_2](k_{-1} + k_2[Fe^{II}]_t) \qquad \text{Eq. 2.2}$$

$$[FeO_2] = \frac{k_1[Fe^{II}]_0[O_2]}{(k_{-1} + k_2[Fe^{II}]_t)} \qquad \text{Eq. 2.3}$$

$$\text{rate} = k_1[Fe^{II}]_0[O_2] - \frac{k_{-1}k_1[Fe^{II}]_0[O_2]}{(k_{-1} + k_2[Fe^{II}]_t)} + \frac{k_2k_1[Fe^{II}]_0[O_2][Fe^{II}]_t}{(k_{-1} + k_2[Fe^{II}]_t)} \qquad \text{Eq. 2.4}$$

Fe^{II} at a given time, $[Fe^{II}]_t$, and k_2' is the rate of which **3** is formed without observing the putative **2**. Solving for the Fe^{III}-superoxo concentration, $[FeO_2]$, in **Eq 2.3** and substituting back into **Eq 2.1**, affords the rate expression of **Eq 2.4**.

Three scenarios result depending on the relative magnitude of the two terms in the denominator of **Eq 2.4**, k_{-1} and $k_2[Fe^{II}]_t$ respectively. The scenarios are as followed: (**1**) $k_{-1} >> k_2[Fe^{II}]_t$, (**2**) $k_2[Fe^{II}]_t >> k_{-1}$, or (**3**) $k_{-1} = k_2[Fe^{II}]_t$. Each case will be described below in detail and discussed in terms of kinetic data collected to provide insight into the mechanism of activation of dioxygen by **1** in the formation of **3**.

*2.2.1.1 Scenario (**1**): $k_{-1} >> k_2[Fe^{II}]_t$*

$$\text{rate} = k_1[Fe^{II}]_0[O_2] - \frac{k_{-1}k_1[Fe^{II}]_0[O_2]}{k_{-1}} + \frac{k_2k_1[Fe^{II}]_0[O_2][Fe^{II}]_t}{k_{-1}} \qquad \text{Eq. 2.5}$$

$$\text{rate} = \frac{k_2k_1[Fe^{II}]_0[O_2][Fe^{II}]_t}{k_{-1}} \qquad \text{Eq. 2.6}$$

$$\text{rate} = k_{obs}[Fe^{II}]^2_{0/t} \qquad \text{Eq. 2.7}$$

$$k_{obs} = \frac{k_2k_1[O_2]}{k_{-1}} \qquad \text{Eq. 2.8}$$

$$\text{rate} = k_{obs}[O_2] \qquad \text{Eq. 2.9}$$

$$k_{obs} = \frac{k_2k_1[Fe^{II}]^2_{0/t}}{k_{-1}} \qquad \text{Eq. 2.10}$$

In the first scenario, the assumption that the rate at which O_2 dissociates from Fe^{III}-superoxo (k_{-1}) is significantly faster than the rate at which Fe^{II} **1** traps Fe^{III}-superoxo **2** ($k_2[Fe^{II}]_t$), then **Eq 2.5** simplifies to **Eq 2.6**. This would be equivalent to a rapid pre-equilibrium step involving the formation of **2**, followed by a rate-determining step involving the formation of **3**. The rate of formation of **3** under pseudo-first order conditions with excess dioxygen, the rate expression simplifies to **Eq 2.7**, where the observed rate constant, k_{obs}, defined as **Eq 2.8**, is dependent on the concentration of O_2, and the slope of a k_{obs} vs $[O_2]$ plot would equate to k_1k_2/k_{-1}. Scenario 1 closely examined the kinetic experiments discussed later, and will show that k_2 is rate determining and is reflected by the slope of k_{obs} vs $[O_2]$ plot **Figure 2.6**, This provided a foothold to calculate the rate constant k_1 through global analysis. Under conditions of excess Fe^{II} **1**, the rate expression is represented by **Eq 2.9** and k_{obs} defined as **Eq 2.10** and a plot of k_{obs} vs $[Fe^{II}]^2$ would yield a slope

also equal to k_1k_2/k_{-1}. In conditions of excess dioxygen, the assumption that $k_{-1} >> k_2[Fe^{II}]_t$ is valid as the Fe^{III}-superoxo **2** is unobservable on the timescale of the stopped-flow instrument as will be discussed below in, and the amount of $[Fe^{II}]_t$ is very low. Conditions of excess Fe^{II} **1**, will be discussed in scenario 2 and 3, where the $k_2[Fe^{II}]_t$ term are not assumed to be negligible.

2.2.1.2 Scenario (2): $\boldsymbol{k_2[Fe^{II}]_t >> k_{-1}}$

In scenario (2) where the rate at which Fe^{II} **1** reacts with Fe^{III}-superoxo **2** ($k_2[Fe^{II}]_t$) is significantly faster than dioxygen dissociation (k_{-1}) and **1** is in excess, then the rate expression **Eq 2.11** simplifies to **Eq 2.12**. This assumption would be consistent of dioxygen association, k_1, being rate determining. The two-term rate expression under pseudo-first order conditions of excess **1**,

$$\text{rate} = k_1[Fe^{II}]_0[O_2] - \frac{k_{-1}k_1[Fe^{II}]_0[O_2]}{k_2[Fe^{II}]_t} + \frac{k_2k_1[Fe^{II}]_0[O_2][Fe^{II}]_t}{k_2[Fe^{II}]_t} \quad \text{Eq. 2.11}$$

$$\text{rate} = 2k_1[Fe^{II}]_0[O_2] - \frac{k_{-1}k_1[Fe^{II}]_0[O_2]}{k_2[Fe^{II}]_t} \quad \text{Eq. 2.12}$$

$$\text{rate} = k_{1obs}[O_2] + k_{2obs}[O_2] \quad \text{Eq. 2.13}$$

$$k_{1obs} = 2k_1[Fe^{II}]_0 \quad \text{Eq. 2.14}$$

$$k_{2obs} = -\frac{k_1k_{-1}[Fe^{II}]_0}{k_2[Fe^{II}]_t} \quad \text{Eq. 2.15}$$

Eq 2.13, where a linear plot of k_{1obs} vs $[Fe^{II}]$ (**Eq 2.14**), would have a slope equal to $2k_1$, while k_{2obs} (**Eq 2.15**) would still contain a conglomerate of rate constants, not easy to tease out with a plot of k_{2obs} vs $[Fe^{II}]$. This scenario is ruled out since the second term is negative, and rate constants are not negative.

*2.2.1.3 Scenario (**3**): $k_{-1} = k_2[Fe^{II}]_t$*

$\mathbf{k_{-1}} = k_2[Fe^{II}]_t$

$$\text{rate} = k_1[Fe^{II}]_0[O_2] - \frac{k_{-1}k_1[Fe^{II}]_0[O_2]}{(k_{-1} + k_2[Fe^{II}]_t)} + \frac{k_2k_1[Fe^{II}]_0[O_2][Fe^{II}]_t}{(k_{-1} + k_2[Fe^{II}]_t)}$$

$$\text{rate} = k_1[Fe^{II}]_0[O_2] - \frac{k_{-1}k_1[Fe^{II}]_0[O_2]}{2k_{-1}} + \frac{k_2k_1[Fe^{II}]_0[O_2][Fe^{II}]_t}{2k_{-1}}$$

$$\text{rate} = k_1[Fe^{II}]_0[O_2] - \frac{k_1[Fe^{II}]_0[O_2]}{k_{-1}} + \frac{k_2k_1[Fe^{II}]_0[O_2][Fe^{II}]_t}{2k_{-1}}$$

$k_{-1} = \mathbf{k_2[Fe^{II}]_t}$

$$\text{rate} = k_1[Fe^{II}]_0[O_2] - \frac{k_{-1}k_1[Fe^{II}]_0[O_2]}{(k_{-1} + k_2[Fe^{II}]_t)} + \frac{k_2k_1[Fe^{II}]_0[O_2][Fe^{II}]_t}{(k_{-1} + k_2[Fe^{II}]_t)}$$

$$\text{rate} = k_1[Fe^{II}]_0[O_2] - \frac{k_{-1}k_1[Fe^{II}]_0[O_2]}{2k_2[Fe^{II}]_t} + \frac{k_2k_1[Fe^{II}]_0[O_2][Fe^{II}]_t}{2k_2[Fe^{II}]_t}$$

$$\text{rate} = k_1[Fe^{II}]_0[O_2] - \frac{k_{-1}k_1[Fe^{II}]_0[O_2]}{2k_2[Fe^{II}]_t} + \frac{k_1[Fe^{II}]_0[O_2]}{k_2[Fe^{II}]_t}$$

Scheme 2.2 Scenario 3 where the denominators k_{-1} and k_2[Fe] are equal. The left is simplified in terms of k_{-1} while the right is simplified in terms of k_2[Fe]. Both cases do not simplify into a kinetic express that can be determined using traditional pseudo-first order kinetic experiments.

The last scenario, albeit more difficult than the last that needs to be considered, is if O_2 dissociation (k_{-1}) is relatively equal to that of superoxo **2** reacting with another molecule of **1**, ($k_2[Fe^{II}]_t$). This scenario would be more difficult to prove as the rate terms are convoluted as well, and kinetic experiments to determine the individual rate constants are not straightforward. Thus is the challenged of two-step reaction with a reversible step, **Scheme 2.2**.

2.2.2 Stopped Flow Kinetic Experiments

The rate of formation of the peroxo-bridged **3** was monitored at a range of low temperatures in two different pseudo-first order conditions, i.e., excess O_2 or **1**, on a cryogenic TgK Scientific stopped-flow instrument equipment with EAS in single mixing mode. All concentrations of reagents are reported in “after-mix” concentrations. The use of the stopped-flow allowed for precise kinetic data to be obtained of short-lived intermediates by either a monitoring at a single wavelength, photomultiplier mode, or a full spectrum to be obtained, CCD. As well as have known

concentration of O_2 solutions as the instrument is devoid of head space, unlike electronic absorption spectroscopy performed with dip probes in the Kovacs Lab that the dioxygen can be dissipate into the headspace.

2.2.2.1 Pseudo-first order with respect to dioxygen

The formation of **3** is complete in ~14 milliseconds at -40 °C and is too fast to be monitored

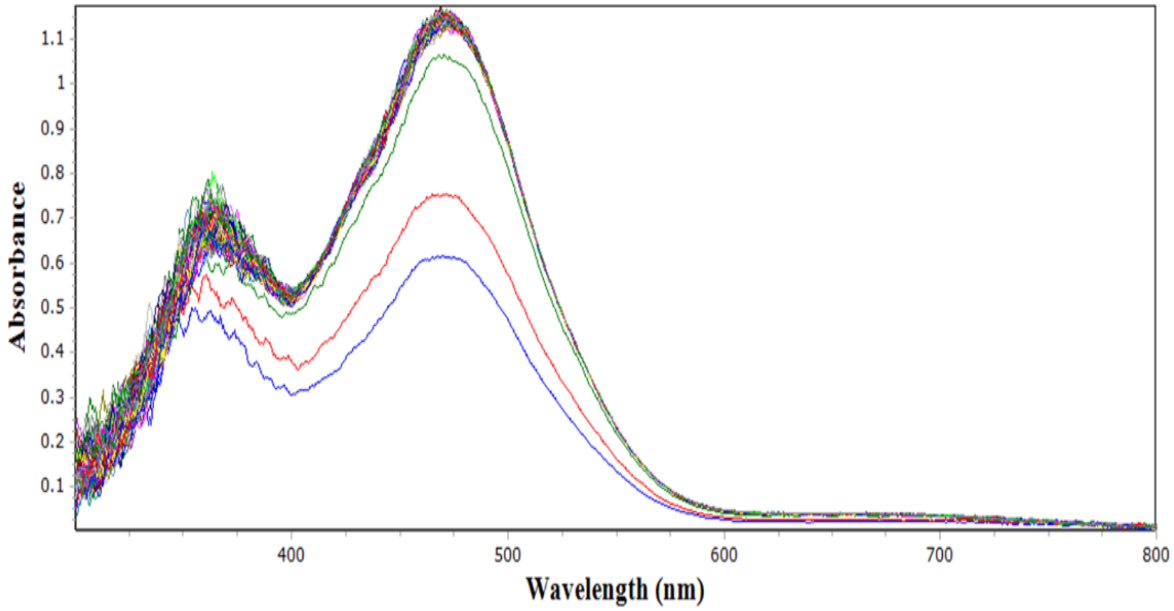

Figure 2.4 Formation of **3** on CCD mode with **1** (0.3 mM) and O_2 (4.3 mM) in MeOH at -45°C.

by the conventional full spectrum mode, CCD, **Figure 2.4**. Even on the fastest time scale for the CCD, the instrument is only able to obtain one scan before the formation of the **3** is over. Thus, for excess dioxygen, all kinetic data was obtained as kinetic traces at 465 nm on the photomultiplier **Figure 2.5**. Workup of the kinetic traces via methods of modified absorption versus time to obtain linear plots were not used as there are no effective time points to accurately determine the order of the rate constant.

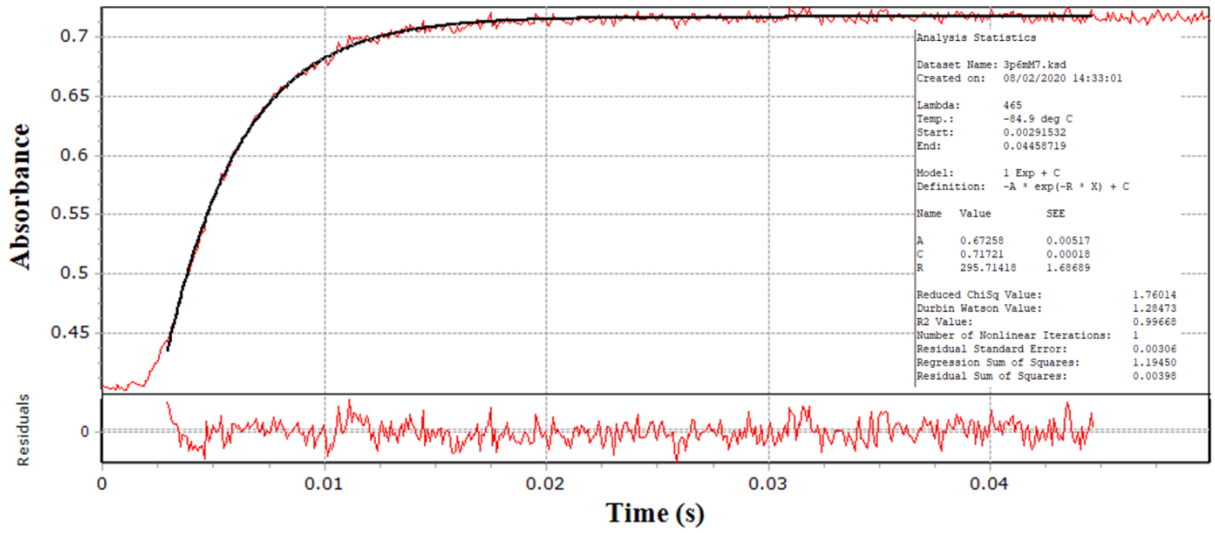

Figure 2.6 Kinetic trace at 465 nm obtained with photomultiplier detector of **1** (0.3 mM) and O_2 (4.3 mM) at -45 °C in MeOH.

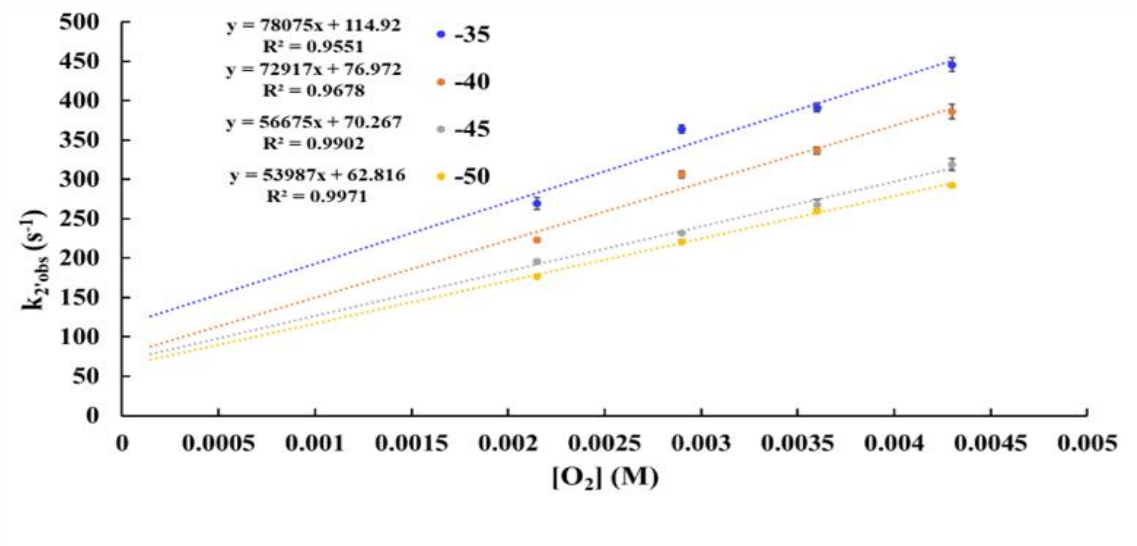

Figure 2.5 Dependence of the observed rate constant, $k_{2'obs}$ (s^{-1}), for the formation of **3** with the changing [O_2] (M) over the temperature range of -50 to -35 °C at constant [**1**] = 0.3 mM in MeOH

The kinetic trace was fitted using Kinetic Studio to the single exponential of **Eq 2.16**: with very small residual sum of squares, ssq = 0.00398, to obtain the pseudo-first-order rate constants, **Table**

2.1. Residuals weren't improved significantly when fit to a double exponential, or two-step process under excess dioxygen conditions as no intermediates are detected prior to formation of **3**.

The peroxo-bridged dinuclear species **3** was monitored by the growth of the absorption band at 465 nm under pseudo-first/second-order conditions with excess O_2 over the temperature range -50 to -35 °C **Figure 2.6**, with no intermediates detected throughout. Consistent with the reaction pathway of 2Fe + O_2 to **3**, k_2', **Scheme 2.1**. Reaction runs were taken in quintuplicate and analyzed using Grubb's test[17] providing a 95% confidence level on the pseudo-first-order rate constant, $k_2'_{obs}$.

Observed rate constants, $k_2'_{obs}$, were found to increase linearly with increasing dioxygen concentrations, indicating that the formation of peroxo-bridged **3** is first order with respect to dioxygen. Taking a log of observed rate and log of concentration also gives the order of the

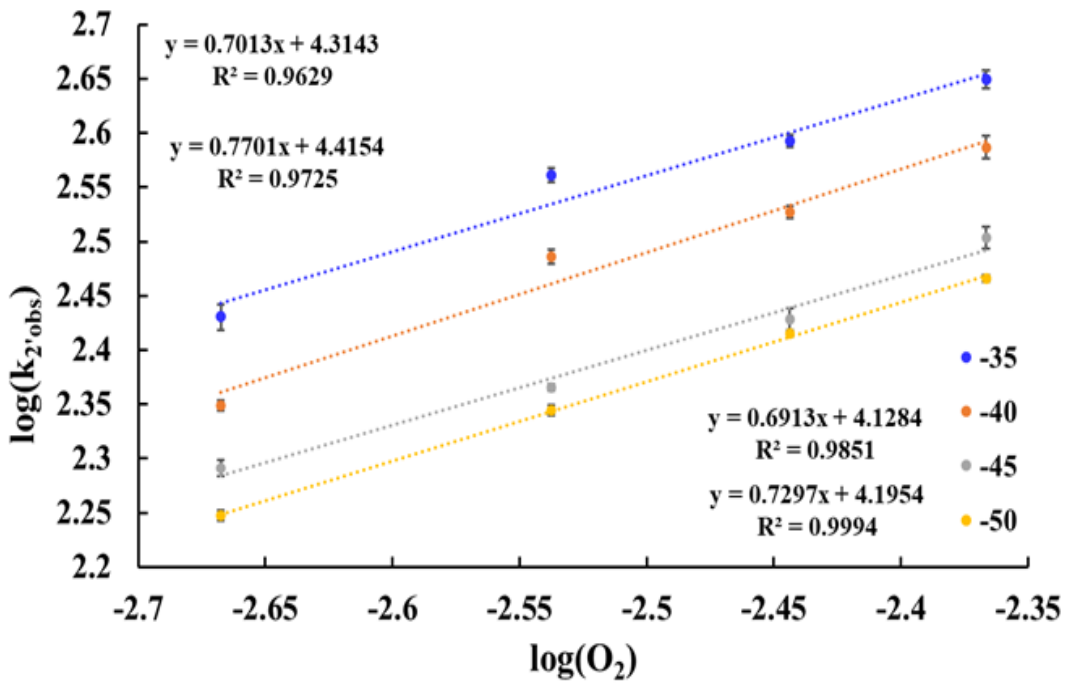

Figure 2.7 Log($k_{2'obs}$) vs log([O_2]) plot showing that the reaction is 1st order overall with respects to O_2. Conditions [**1**] = 0.2 mM and [O_2] = 4.3 mM in MeOH over a temperature range of -50 to -35 °C. Slope = 0.7.

reagent.[18] The log($k_{2}'_{obs}$) vs log([O_2]) plot yielded a slope of 0.77, **Figure 2.7**, consistent with the mechanism shown in **Scheme 2.1**, Fe:O_2 2:1. The temperature-dependent second-order rate constants, $k_{2}'_{expt}$, were obtained from the slopes of the $k_{2}'_{obs}$ versus [O_2] plot **Figure 2.6**.

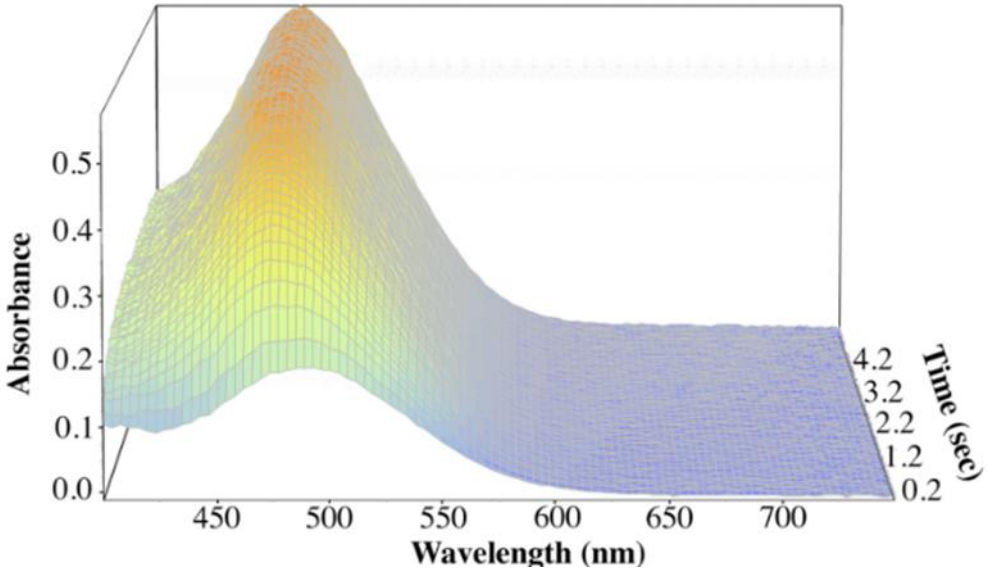

Figure 2.8 The formation of the **3** under pseudo-first order conditions with excess **1** (0.125 mM) and limiting [O_2] (0.0015 mM) at -40 °C, shows an intermediate, **2**, with λ_{max} = 490 nm forms prior to **3**.

The temperature-dependent non-zero intercept from **Figure 2.6** ($k_{2}'_{obs}$ vs O_2) indicates that a reversible step which is independent of dioxygen is involved in the formation of **3**, k_{-1expt}, consistent with the mechanism above being dioxygen dissociation of the superoxo.

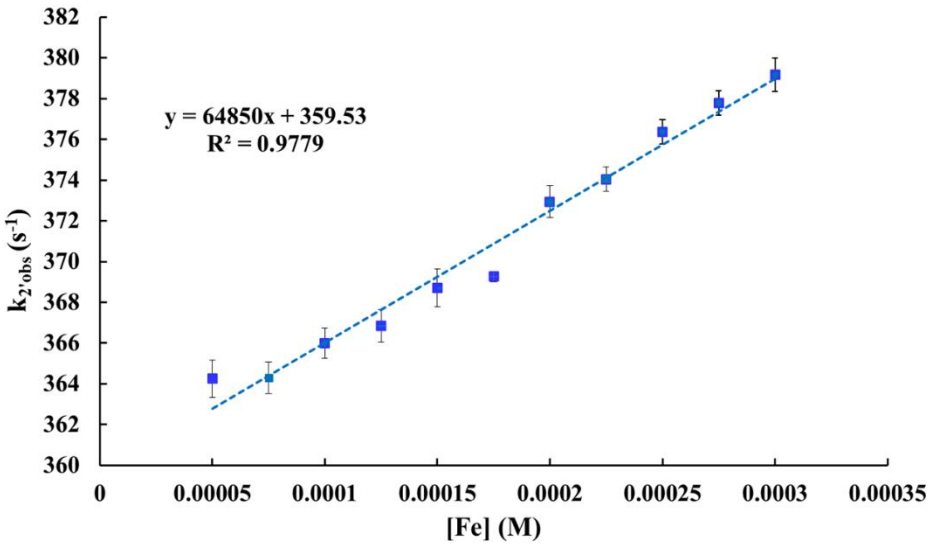

Figure 2.10 Dependence of **1** (0.3 mM) in excess [O_2] (4.3 mM) in MeOH at -40 °C, shows second order dependence of **1** on the formation of **3**.

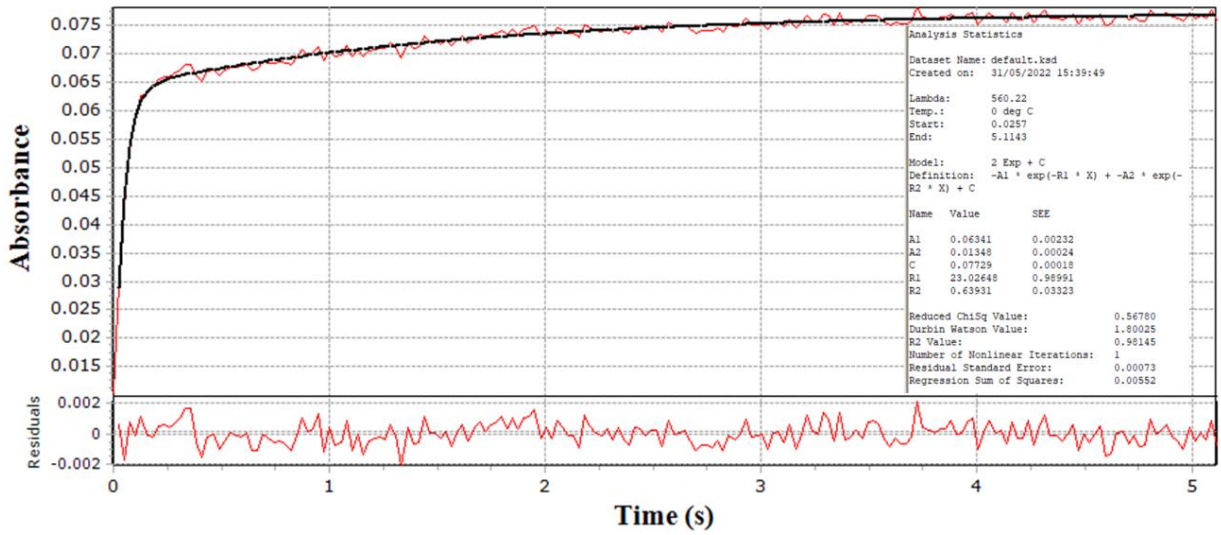

Figure 2.9 Kinetic trace at 560 nm for excess **1** (0.3 mM) and [O_2] (0.015 mM) in MeOH at -40 °C fit to a double exponential.

*2.2.2.2 Pseudo-first-order with respect to **1***

Under pseudo-first-order conditions with respect to **1** (0.10 – 0.25 mM) and limiting O_2 (0.015 mM), using a CCD detector, over the temperature range -55 to – 40 °C a new intermediate is observed at 490 nm, that within 1-2 scans rapidly converts to **3** at 465 nm, **Figure 2.8**. The

intermediate at 490 nm would most be consistent with that of the superoxo **2**, as previous evidence suggested and the superoxo would be the precursor to a peroxo-bridged **3**. Since **2** is observable under conditions of excess **1**, before the formation of **3**, k_2 is consistent with being the rate-determining step. Under conditions of excess **1**, the kinetic trace was scanned at multiple wavelengths and showed that at lower energy (525 nm to 560 nm), there was growth of two distinct species. One that grew in rapidly, **2**, then a more gradual growth to where it leveled off, or reach equilibrium, **3**, **Figure 2.10**. The pseudo-first-order rate constants were collected at λ_{max} of 560 nm because there is less overlap between the two intermediates. (**2**, 490 nm and **3** 465 nm) the kinetic traces fit best to a two-exponential term, instead of the single exponential as shown above in the excess dioxygen condition.

A double exponential fit would best describe a system that involves two molecules of **1** in the mechanism, which is consistent from above, and is confirmed by the log(k_{obs}) vs log([Fe^{II}]) plot

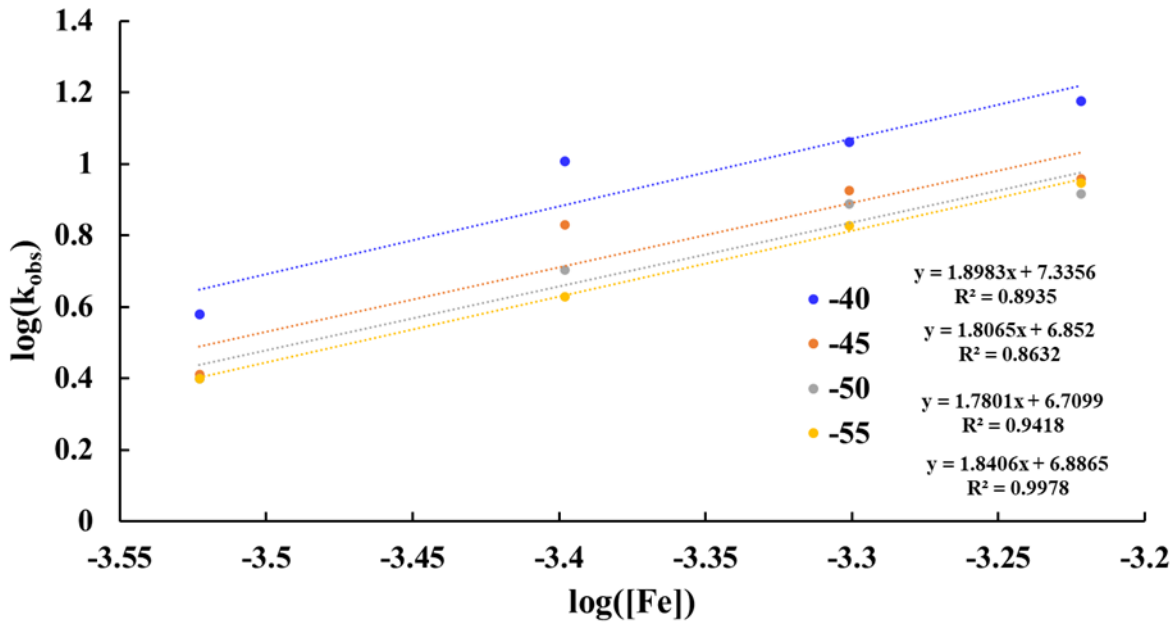

Figure 2.11 Log(k_{obs}) vs log([Fe]) plot for the formation of **3** under pseudo-first order conditions with excess **1** and limiting O_2 show 2nd order dependence on **1**. Conditions [**1**] = 0.3 mM and ([O_2] = 0.015 mM in MeOH over the temperature range of -50 to -35 °C.

that displays a slope of 1.9, giving that the overall formation of the peroxo is second order with respect to **1**. The observed pseudo-first-order rate constants increase linearly with the increase of $[Fe^{II}]^2$, which is consistent with Fe^{II} being first order in the pseudo-first order conditions, **Figure 2.11**. The large non-zero intercept is also consistent with a reversible step as seen above with the excess dioxygen study. The slope is equal to k_1k_2/k_{-1} and individual rate constants cannot be determined experimentally except k_{-1expt}, which is still an estimate.

2.2.3 Global Fitting to Determine Rate Constants

Experimentally the rate constants k_1 and k_2 are difficult to obtain, thus more rigorous mathematical methods were employed. Determining the rate constants k_{1calc} and k_{2calc} via global fits uses numerical methods of fitting the experimentally obtained data and consider the conditions

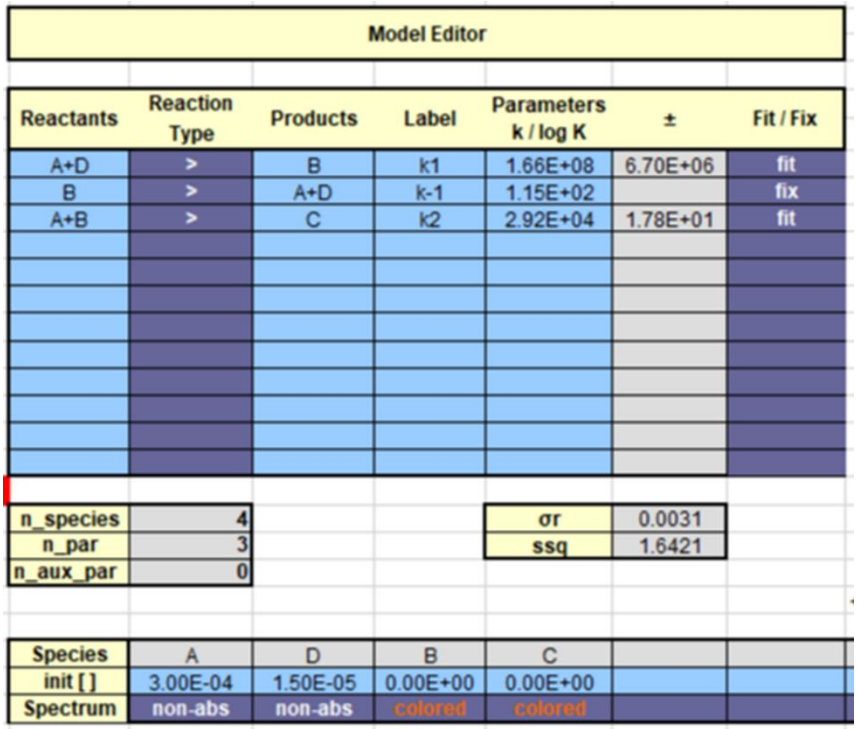

Model Editor

Reactants	Reaction Type	Products	Label	Parameters k / log K	±	Fit / Fix
A+D	>	B	k1	1.66E+08	6.70E+06	fit
B	>	A+D	k-1	1.15E+02		fix
A+B	>	C	k2	2.92E+04	1.78E+01	fit

n_species	4
n_par	3
n_aux_par	0

σr	0.0031
ssq	1.6421

Species	A	D	B	C
init [ ]	3.00E-04	1.50E-05	0.00E+00	0.00E+00
Spectrum	non-abs	non-abs	colored	colored

Figure 2.12 ReactLab Model Editor that contains the step-wise model in simply terms, A, B, C etc. while labeled with the respected rate that each step represents. Each step is selected to be fitted or fixed with initial guesses or experimentally determined values. Each species in the step-wise model is determined to contribute to the calculated spectrum via “non-abs” or “colored” Initial concentrations that represent the spectrum being fitted are also inputted.

of reagents and a sequential model to determine the rate constants. Fitting to the full spectrum provided more detail regarding the intermediates involved, than did the single kinetic trace at 465 nm to obtain a full picture of the mechanism. Spectra collected with the conditions of excess dioxygen (2.3 – 4.3 mM) and limiting Fe^{II} **1** (0.3 mM) in MeOH did not provide evidence to describe k_1, since the first scan of these conditions is 0.4 Abs of **3** and the reaction is essentially 40% complete, **Figure 2.4**. The spectrum obtained from the excess **1** with limiting dioxygen were utilized since a precursor was observed before the final formation of the **3** and would give the most accurate fit of k_1 scenario, **Figure 2.8**. Initial conditions of [**1**] = 0.3 mM and [O_2] = 0.015 mM, which were both non-absorbing species, as they wouldn't contribute to the calculated spectra. **1** is colorless and does not absorb in the region of 400-600 nm. Initial concentrations of the superoxo **2** and peroxo **3** were set to 0 mM and selected to be colored as the two intermediates are experimentally observed to absorb in the region from 450 – 500 nm. The initial guesses for k_{1calc} and k_{2calc} were set to $1x10^4$, which were of the same magnitude as the observed rate constants,

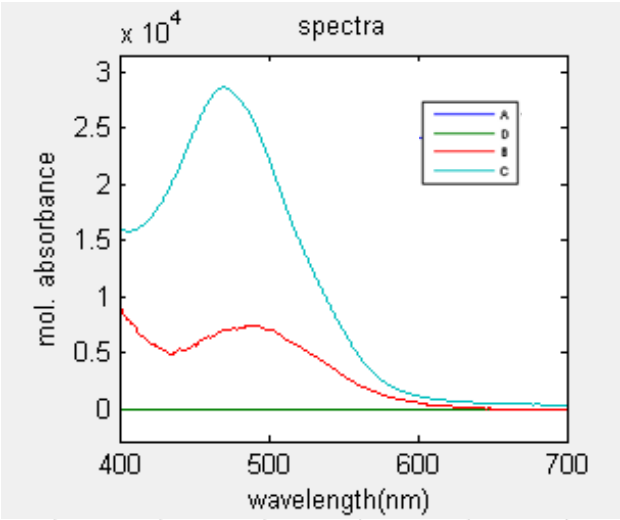

Reactants	Reaction Type	Products	Label	Parameters k / log K	±	Fit / Fix
A+D	>	B	k1	5.82E+07	2.56E+05	fit
B	>	A+D	k-1	7.70E+01		fix
A+B	>	C	k2	3.21E+04	3.24E+01	fit

Figure 2.13 Fitted spectrum of the step-wise model where k_1 initially was 1×10^5 and k_2 initially at 1×10^4. Resulted in a fitted spectrum that well reproduces the experimental spectrum under excess **1** conditions.

$k_{2}{}'_{expt}$ ($k_{2}{}'_{obs}$ vs O_2). No assumptions of which rate constant was smaller, and selected to be fitted, while k_{-1} was set to the experimentally determine k_{-1expt} values at each temperature (**Figure 2.12**). The step-wise model, shown in **Scheme 2.3**, used to fit the data is as follows: where A is **1**, D is dioxygen, B is superoxo **2**, and C is peroxo **3**. The rate constant associated with A + D → B is k_1, B → A + D is k_{-1}, and A + B → C is k_2.

Under these conditions, one iteration of the proposed model resulted in the scenario of k_{2calc} (10^{7}) being much larger than k_{1calc} (10^{4}), and the calculated absorption spectrum being the opposite

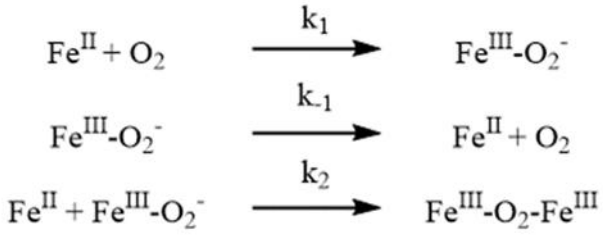

Scheme 2.3 Three step mechanism model employed for global fitting of time resolved spectra from reactions with **1** and O_2.

of what was observed experimentally, where the **3** species is the low absorbing band at 490 nm, and **2** is the strongly absorbing band at 465 nm. Revision of the initial guesses of k_{1calc} and k_{2calc} were made to 1 x 10^5 and 1 x 10^4, respectively. This scenario resulted in k_{1calc} ($10^{7\text{-}8}$) being much larger than k_{2calc} ($10^{3\text{-}4}$) and reproduced the experimentally observed spectrum (**Figure 2.13**) with **3** the species at 465 nm, and the **2** at 490 nm. The described process was repeated at each temperature. Rates obtained from global fits are in good agreement with k_2 being the rate determining step as $k_{2}{}'_{obs/expt}$ is of the same magnitude as k_{2calc}.

As shown in the inset of **Figure 2.14**, **2** at 490 nm forms during the first 40 ms of the reaction and then quickly converts to **3** over the next 350 ms under excess **1** and limiting dioxygen

conditions. Data points are collected every 25.7 ms when a CCD detector is used and the full spectrum is monitored, causing global fits to look linear during the initial part of the reaction. The

concentration of **1**, which is present in excess under pseudo-first-order conditions remains approximately constant.

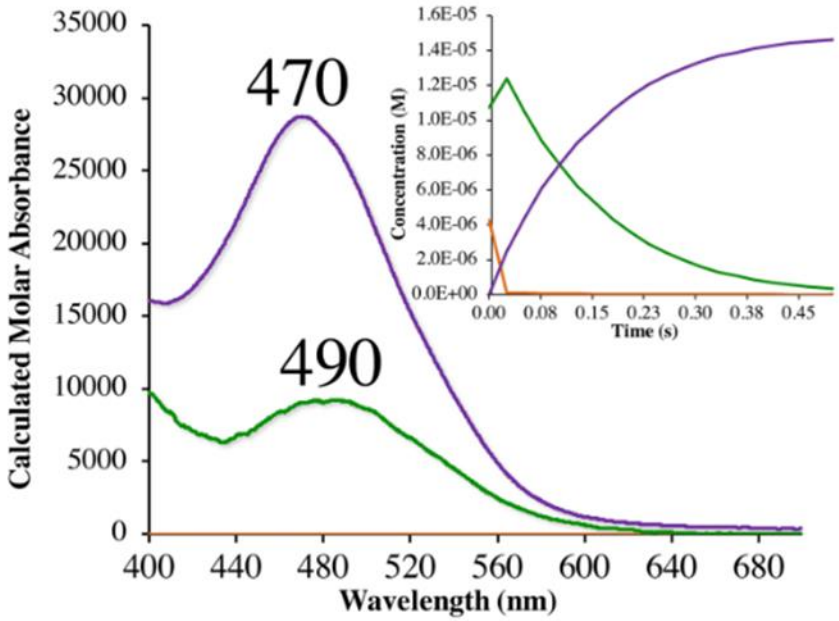

Figure 2.14 Calculated spectra obtained from global fits for the formation of **3** preceded by **2** at -40 °C with [Fe] = 0.3 mM and [O_2] = 0.015 mM and k_{-1calc} fixed to k_{-1expt}. Concentration profiles are shown in the inset where [O_2] = orange, [**2**] = green, and [**3**] = purple.

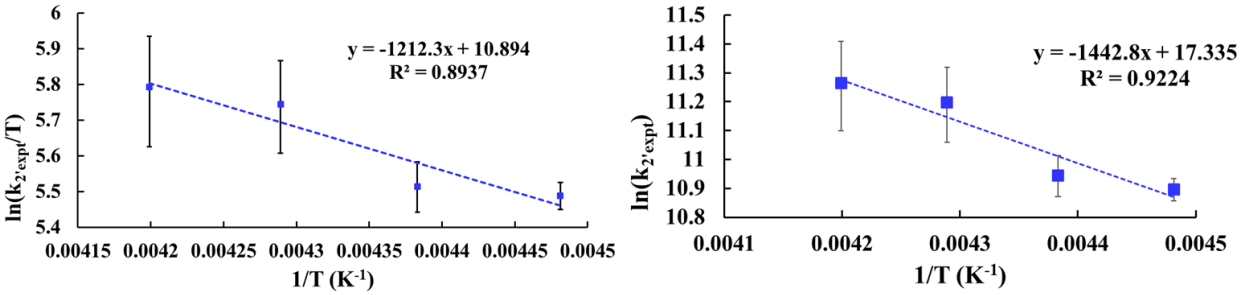

Figure 2. 15 Left: Eyring plot for formation of **3** via the reaction between **1** and O_2 in MeOH, from which the activation parameters $\Delta H_{2'expt}^{\ddagger}$ = 10(2) kJ•mol^{-1} and $\Delta S_{2'expt}^{\ddagger}$ = -100(10) J•mol^{-1}K^{-1} were obtained. **Right:** Arrhenius plot for the formation of **3** via the reaction between O_2 and **1** in MeOH, from which the activation parameter, $E_{a2'expt}$ = 12(3) kJ•mol^{-1} was obtained. Rate constants, $k_{2'expt}$, were obtained from the slope of $k_{2'obs}$ vs [O_2] plot.

2.2.4 Determination of Activation Parameters with Eyring and Arrhenius Analysis

The activation parameters for each rate constant, were obtained by Eyring and Arrhenius plots (**Figure 2.15, 2.16 ,2.17**) via experimentally determined second order rate constants, k_{-1expt} and $k_{2'expt}$, or calculated rate constants from global fitting, k_{1calc} and k_{2calc}, respectively, over the temperature range of -35 °C to -50 °C. The activation barrier of dioxygen binding ($\Delta H^{\ddagger}_{1calc}$ = 34(15) kJ•mol^{-1}; $\Delta S^{\ddagger}_{1calc}$ = +55(68) J•mol^{-1}K^{-1}; E_{a1calc} = 36(2) kJ•mol^{-1}) is significantly lower, specifically the activation enthalpy, than the barrier of **2** conversion to **3** ($\Delta H^{\ddagger}_{2calc}$ = 44(18) kJ•mol^{-1}; $\Delta S^{\ddagger}_{2calc}$ = +30(77) J•mol^{-1}K^{-1}; E_{a2calc} = 46(2) kJ•mol^{-1}), consistent with k_{2calc} being rate determining. The error associated with the entropy of activation ($\Delta S^{\ddagger}$) is too large to allow a meaningful conclusion regarding the associative versus dissociation nature of the system regarding k_{1calc} and k_{2calc}. The kinetic barrier of dioxygen release from **2**, k_{-1expt}, ($\Delta H^{\ddagger}_{-1expt}$ = 15(5) kJ•mol^{-1}; $\Delta S^{\ddagger}_{-1expt}$ = -140(20) J•mol^{-1}K^{-1}; E_{a1calc} = 16.7(6) kJ•mol^{-1}), is consistent with a rapid pre-equilibrium involving the formation of **2** from **1**. The activation parameters obtained from the direct formation of **3** from **1** and dioxygen, $k_{2'expt}$, is artificially low and does not have physical meaning because the rate is a conglomeration of rate constants, k_1, k_{-1}, and k_2, and would just supply insight to the overall system to be that of a small activation barrier of dioxygen binding

Table 2.1 Temperature-Dependent Kinetics Data for Reversible O_2 binding to **1** and Conversion of Fe^{III}-superoxo **2** to Dinuclear Peroxo **3** in MeOH with Activation Parameters

Temperature (K)	k_{1calc} **(M^{-1}s^{-1})**	k_{-1expt} **(s^{-1})**	$k_{2'expt}$ **(M^{-1}s^{-1})**	k_{2calc} **(M^{-1}s^{-1})**
238.15	1.66(7) x 10^{8}	1.2(4) x10^{2}	7.808(2) x 10^{4}	2.920(2) x 10^{4}
233.15	5.82(3) x 10^{7}	8(3) x10^{1}	7.292(3) x 10^{4}	3.210(3) x 10^{4}
228.15	4.50(2) x 10^{7}	7(1) x10^{1}	5.668(4) x 10^{4}	8.090(4) x 10^{3}
223.15	4.59(2) x 10^{7}	6.3(7) x 10^{1}	5.400(4) x 10^{4}	8.100(4) x 10^{3}
218.15	5.58(2) x 10^{7}*	4.8 x 10^{1}*	4.5 x10^{4}*	8.100(4) x 10^{3}*
$\Delta H^{\ddagger}$ (kJ•mol^{-1})	34(15)	15(5)	10(2)	44(18)
$\Delta S^{\ddagger}$ (J•mol^{-1}K^{-1})	55(68)	-140(2)	-100(100)	30(77)
E_a (kJ•mol^{-1})	36(2)	16.7(6)	12(3)	46(2)

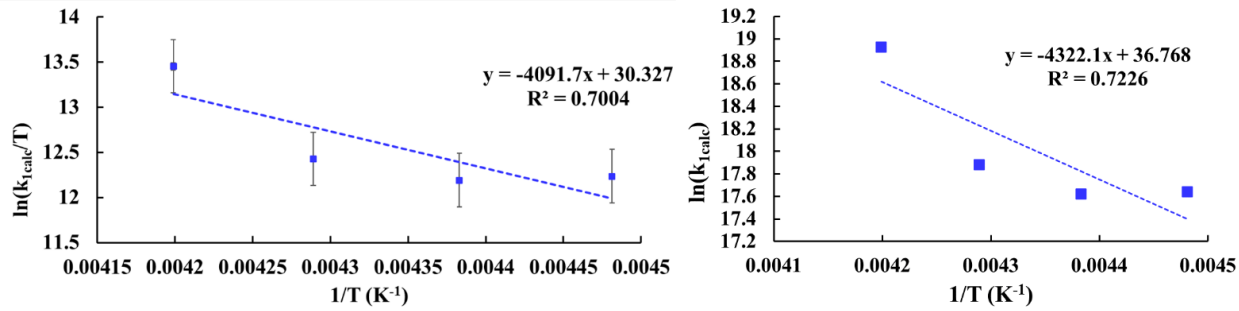

Figure 2. 17 Left: Calculated Eyring plot for O_2 associated of **1** and O_2 in MeOH for the formation of **2**, from which the activation parameters $\Delta H_{1calc}^{\ddagger}$ = 34(15) kJ•mol^{-1} and $\Delta S_{1calc}^{\ddagger}$ = +55(68) J•mol^{-1}K^{-1} were obtained. **Right:** Calculated Arrhenius plot for O_2 associated of **1** and O_2 in MeOH for the formation of **2,** from which the activation parameter, E_{a1calc} = 36(2) kJ•mol^{-1} was obtained. Calculated rate constants, k_{1calc}, were obtained from global fits at each temperature respectively.

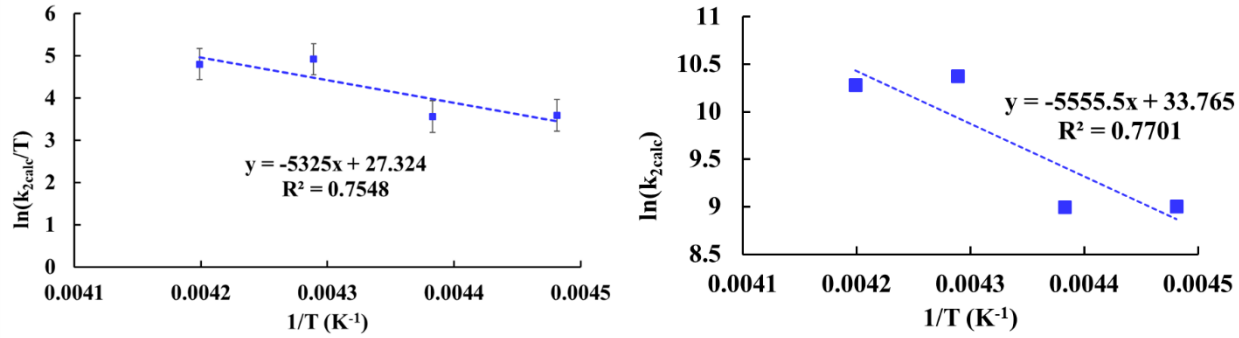

Figure 2. 16 Left: Calculated Eyring plot for formation of **3** of putative **2** and **1** in MeOH, from which the activation parameters $\Delta H_{2calc}^{\ddagger}$ = 44(18) kJ•mol^{-1} and $\Delta S_{2calc}^{\ddagger}$ = +30(77) J•mol^{-1}K^{-1} were obtained. **Right:** Calculated Arrhenius plot for formation of **3** of putative **2** and **1** in MeOH, from which the activation parameter, E_{a2calc} = 46(2) kJ•mol^{-1} was obtained. Calculated rate constants, k_{2calc}, were obtained from global fits at each temperature respectively.

through an associative process ($\Delta H^{\ddagger}_{2'expt}$ = 10(2) kJ•mol^{-1}; $\Delta S^{\ddagger}_{2'expt}$ = -100(100) J•mol^{-1}K^{-1}; $E_{a2'expt}$ = 12(3) kJ•mol^{-1}). Rate constants and activation parameters at each temperature are summarized in **Table 2.1**.

Based on the calculated activation parameters determined from global fitting, the Gibb's free energy of activation, **Figure 2.19** was calculated and revealed that the net reaction is -23.4 kJ•mol^{-}

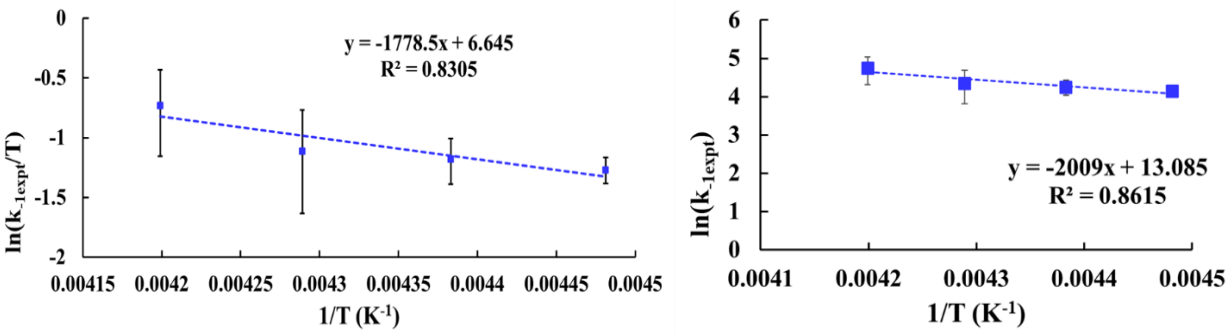

Figure 2. 18 Left: Eyring plot for formation of **3** via the reaction between **1** and O_2 in MeOH, from which the activation parameters $\Delta H_{-1expt}^{\ddagger}$ = 15(5) kJ•mol^{-1} and $\Delta S_{-1expt}^{\ddagger}$ = -140(20) J•mol^{-1}K^{-1} were obtained. **Right:** Arrhenius plot for the formation of **3** via the reaction between O_2 and **1** in MeOH, from which the activation parameter, $E_{a\text{-}1expt}$ = 16.7(6) kJ•mol^{-1} was obtained. Rate constants, k_{-1expt}, were obtained from the y intercept of $k_2{}'_{obs}$ vs [O_2] plot.

[1], and that the formation of the superoxo **2** (21.0 kJ•mol^{-1}) requires less energy than the transition state of the peroxo-bridged **3** (**Figure 2.19**; 35.6 -37.2 kJ•mol^{-1}), consistent with the **2** being short-lived and unobservable in certain conditions, while the peroxo-bridge **3** is relatively more stable.

2.3 Conclusions

The first step of dioxygen activation for both heme and non-heme iron enzymes is the formation of Fe^{III}-superoxo (Fe-$O_2^{\bullet-}$). Dioxygen binding is lower when thiolates are in the first coordination sphere, herein kinetic experiments were shown to be consistent with a mechanism involving reversible dioxygen binding to **1** and a rapid pre-equilibrium between superoxo **2** and **1** followed by rate-determining conversion of **2** to **3**. In excess dioxygen, a log(k_{obs}) vs log([Fe^{II}]) plot resulted in that the formation of **3** is second order with respect to **1**. The intense absorption band at λ_{max} = 465 nm associated with **3** was assigned to a peroxo π^*(O-O) to Fe(d_z^2) charge-transfer transition. An intermediate was detected (λ_{max}) = 490 nm) en route to peroxo **3** when kinetics data was collected under pseudo-first-order conditions with excess **1** and limiting O_2 at low temperatures on the millisecond time scale using a cryogenic stopped-flow instruments. The barrier to dioxygen binding was shown to be low (ΔH and E_a values), as had been theoretically

predicted for thiolate-ligated non heme enzymes such as IPNS. The barrier to the conversion of Fe^{III}-superoxo **2** to **3** (ΔH and E_a values) was shown to be significantly higher, consistent with this step being rate determining.

2.4 Experimental Details

2.4.1 General Methods

Reagents purchased from commercial vendors were of the highest purity available and used without further purification. $[Fe^{II}(S^{Me2}N_4(tren))(PF_6/BF_4)]$ **1** was synthesized as previously described.[19] Methanol (MeOH) was distilled over magnesium turnings and iodine and degassed prior to use. All manipulations were performed using Schlenk line techniques or under an N_2 atmosphere in a glovebox.

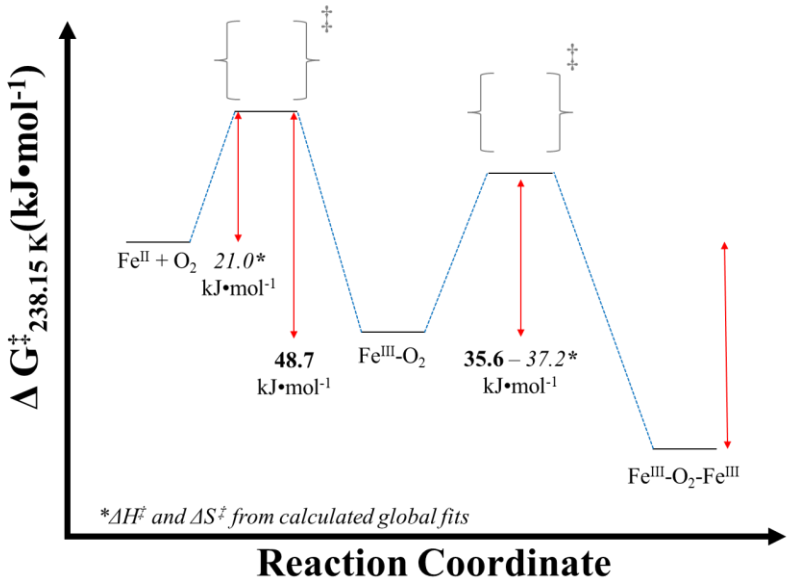

Figure 2. 19 Reaction Coordinate diagram of Gibb's Free Energy of activation for the spontaneous reaction of **1** with O_2 to reversibly bind to form superoxo **2** then going on to form peroxo-bridged **3**. The energy required to reach the transition state for **2** (21.0 kJ•mol^{-1}) is less than the energy required to form the transition state of the peroxo-bridged **3** (35.6-37.2 kJ•mol^{-1}). Gibb's Free Energy of Activation were determined via calculated activation parameters from global fits.

2.4.2 Kinetic Measurements

Solutions were prepared in a N_2-filled anaerobic glovebox ([O_2] < 0.5 ppm) and placed in Hamilton gastight (copyright) syringes equipped with nylon three-way values. Time-resolved spectra (400 – 700 nm) were acquired at low temperatures using a TgK Scientific (U.K.) CSF-61DX2 Multi-Mixing CryoStopped-Flow Instrument equipped with a tungsten visible light source. The stopped-flow instrument is equipped with PEEK tubing fitted inside stainless-steel plumbing, a 1.00 cm^3 quartz mixing cell, and an anaerobic kit purged with an inert gas. The temperature in the mixing cell was maintained to +/- 0.1 °C, and the mixing time was 2 – 3 ms. All flow lines of the instrument were extensively washed with degassed MeOH before charging the driving syringes with solutions containing the reactants. Between experiments the flow lines were purged with 7 mL of the next experiments solutions. The reactions were studied by rapid scanning spectrophotometry under pseudo-first order conditions with excess oxygen or iron complex. The O_2 concentrations was assumed not to change upon cooling, given that the system is closed, and the solutions were not in contact with the gas phase (small variations in the solvent density were not considered). Dilutions of the O_2-saturated solvent were performed anaerobically to obtain the desired [O_2]. All concentrations reported in stopped-flow experiments refer to "after mixing" conditions. Experiments were performed in single-mixing mode, with a 1:1 (v/v) mixing ratio. A series of three to six measurements were taken with outliers removed by Grubb's test 95% confidence interval prior to averaging.[17] Data analysis was performed with Kinetic Studio software from TgK Scientific.[20] Data was fit at a single wavelength (465 nm) **Eq 2.20** or a double exponential at 560 nm using the following equation **Eq 2.21**:

$$A_t = A_\infty - (A_\infty - A_0)e^{-k_{obs}t}$$

2.4.3 Preparation of Saturated Dioxygen Solution

Degassed solvent (THF or MeOH) was added to a round bottom flask fitted with a septum cap under a nitrogen atmosphere in the glovebox. Dry O_2 (from a gas cylinder) was bubbled through

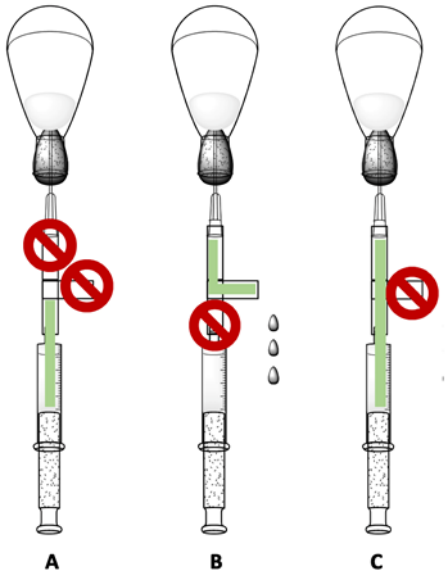

the solvent at 1 atm for 15 min. The solution was then allowed to equilibrate over 15 minutes at 25 °C in a temperature-controlled water bath. To load the syringe, the flask containing O_2 saturated THF or MeOH was inverted, and a gastight syringe equipped with a 3-way valve and needle was inserted through the septum (**Position A** in the Figure to the right). The valve was then turned to allow the saturated solution to flow through the open arm of the 3-way valve, leaving no headspace in the needle (**Position B**). The valve was then closed, and the dioxygen solution drawn into the syringe (**Position C**). The concentration of O_2 was taken as 8.5 mM in MeOH, and 7.9 mM in THF both at 25 °C.[21] Dilutions of the O_2-saturated solvent were performed anaerobically as described above with a prefilled syringe of solvent to obtain the desired [O_2].

2.4.4 Preparation of Dilution of Minimal Dioxygen Solution

Dilutions of the O_2-saturated solvent were performed anaerobically by attaching a second syringe filled with an excess of an appropriate

quantity of deoxygenated solvent to the open arm of the 3-way valve (**Position D** in Figure below). Air bubbles trapped in the valve by this process were purged by flowing the excess solvent through the needle down to the quantity of solvent necessary for the desired O_2 concentration (**Position E**). The valve was then turned to allow the two needles to communicate, and the saturated O_2 solution was drawn into the deoxygenated solvent until the desired O_2 concentration is met (**Position F**). The dilute O_2 solution was then allowed to equilibrate for 30 min after which time it was ready for

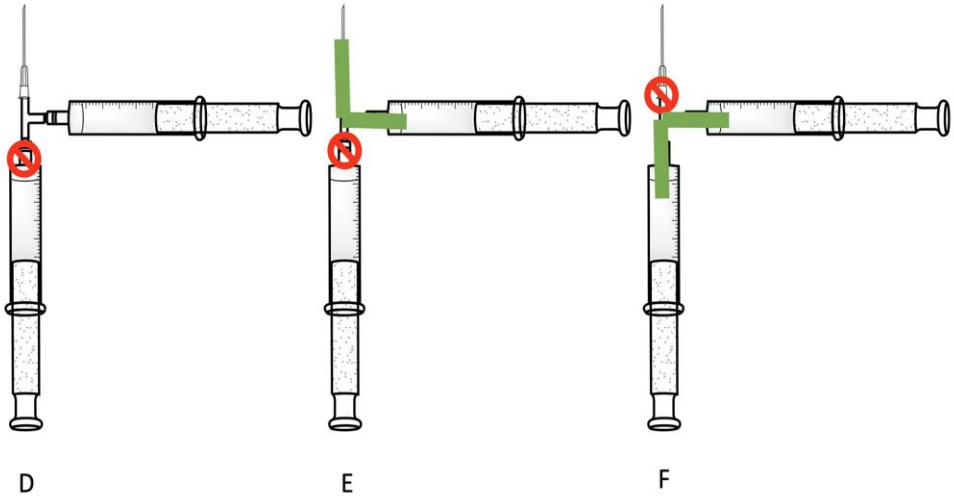

use. This dilution process can be repeated in the same manner if it is not practical to attain the desired O_2 concentration via one dilution.

2.4.5 ReactLab Kinetics for Global Analysis

TgK stopped-flow instrument came equipped with Jplus consulting ReactLab™ KINETICS version 1.1 ReactLab™ provides global analysis for fitting chemical reaction schemes and specified parameters to multi-variable EAS data. ReactLab™ software also offers reaction modeling and data simulation capabilities. The program, including all algorithms and the GUI frontend has been developed in Matlab® and compiled to produce the final deployable application. All raw data, model entry and results output are organized in Excel Workbooks, which are launched from, and dynamically linked to the ReactLab™ application. ReactLab™ requires Excel

analysis workbooks to retain a strict format, as is provided in the examples and templates. The use of Excel provides a familiar spreadsheet format for all experimental and analysis data and results and allows the independent application of Excel tools and features for further processing and graphical presentation. The Excel workbook saves all the information related to the reaction model and all fit related parameters and numerical analysis and can be reviewed independently without the ReactLab™ interface. Detailed explanation of setup and execution of ReactLab™ KINETICS for global analysis is discussed in Appendix A.

2.5 Chapter 2 References

(1) Goudarzi, Serra; Babicz, Jeffrey. T., Jr; Kabil, Omer; Banerjee, Ruma; Solomon, Edward. I. Spectroscopic and Electronic Structure Study of ETHE1: Elucidating the Factors Influencing Sulfur Oxidation and Oxygenation in Mononuclear Nonheme Iron Enzymes. *J. Am. Chem. Soc.* **2018,** *140*, 14887-14902, DOI: 10.1021/jacs.8b09022.

(2) Poulos, Thomas. L. Heme enzyme structure and function. *Chem. Rev*. **2014**, 114 (7), 3919–3962, DOI: 10.1021/cr400415k

(3) Fleischhacker, Angela. S. and Kiley, Patricia. J. Iron-containing transcription factors and their roles as sensors. *Curr. Opin. Chem. Biol*. **2011,** 15, 335−341, DOI: 10.1016/j.cbpa.2011.01.006

(4) Berlett, B. S., and Stadtman, E. R. Protein oxidation in aging, disease, and oxidative stress. *J. Biol. Chem*. **1997**, 272, 20313−20316, DOI: 10.1074/jbc.272.33.20313

(5) Kovaleva, Elena G. and Lipscomb, John D. Versatility of biological non-heme Fe(II) centers in oxygen activation reactions. *Nat. Chem. Biol.* **2008**, 4, 3 186-193, DOI: 10.1038/nchembio.71

(6) Blakely, M. N.; Dedushko, M. A.; Poon, P. C. Y.; Villar-Acevedo, G.; Kovacs, J. A. Formation of a Reactive, Alkyl Thiolate-Ligated FeIII-Superoxo Intermediate Derived from Dioxygen. *J. Am. Chem. Soc.* **2019**, *141*, 1867– 1870, DOI: 10.1021/jacs.8b12670

(7) Li, F.; Meier, K. K.; Cranswick, M. A.; Chakrabarti, M.; Van Heuvelen, K. M.; Munck, E.; Que, L., Jr. Characterization of a High-Spin Non-Heme FeIII OOH Intermediate and Its Quantitative Conversion to an FeIV=O Complex. *J. Am. Chem. Soc.* **2011**, *133*, 7256– 7259, DOI: 10.1021/ja111742z

(8) Que, L., Jr. The Road to Non-Heme OxoFerryls and Beyond. *Acc. Chem. Res.* **2007**, *40*, 493– 500, DOI: 10.1021/ar700024g

(9) Kovacs, J. A. How Iron Activates O2. *Science* 2003, *299*, 1024– 1025, DOI: 10.1126/science.1081792

(10) Borovik, A. S. Bioinspired Hydrogen Bond Motifs in Ligand Design: The Role of Noncovalent Interactions in Metal Ion Mediated Activation of Dioxygen. *Acc. Chem. Res.* 2005, *38*, 54– 61, DOI: 10.1021/ar030160q

(11) Costas, M.; Mehn, M. P.; Jensen, M. P.; Que, L. J. Dioxygen Activation at Mononuclear Nonheme Iron Active Sites: Enzymes, Models, and Intermediates. *Chem. Rev.* 2004, *104*, 939– 986, DOI: 10.1021/cr020628n

(12) Cho, J.; Jeon, S.; Wilson, S. A.; Liu, L. V.; Kang, E. A.; Braymer, J. J.; Lim, M. H.; Hedman, B.; Hodgson, K. O.; Valentine, J. S.; Solomon, E. I.; Nam, W. Structure and reactivity of a mononuclear non-haem iron(III)–peroxo complex. *Nat. Chem.* 2011, *478*, 502– 505, DOI: 10.1038/nature10535

(13) Lacy, D. C.; Gupta, R.; Stone, K. L.; Greaves, J.; Ziller, J. W.; Hendrich, M. P.; Borovik, A. S. Formation, Structure, and EPR Detection of a High Spin FeIV-Oxo Species Derived from Either an FeIII-Oxo or FeIII-OH Complex. *J. Am. Chem. Soc.* 2010, *132*, 12188– 12190, DOI: 10.1021/ja1047818

(14) Dedushko, M. A.; Pikul, J. H.; Kovacs, J. A. Superoxide Oxidation by a Thiolate-Ligated Iron complex and Anion Inhibition. *Inorg. Chem.* **2021**, 60, 10, 7250-7261, DOI: 10.1021/acs.inorgchem.1c00336

(15) Wojdyr, M. Fityk: A General-Purpose Peak Fitting Program. *J. Appl. Crystallogr.* **2010**, 43 (5), 1126–1128, DOI: 10.1107/S0021889810030499

(16) Dedushko, Maksym A.; Insights into Dioxygen Bond Activation and Formation by Small Biomimetic Complexes. Ph. D Dissertation, University of Washington, Seattle, WA, **2020**

(17) Grubbs, Frank E., Procedures for Detecting Outlying Observations in Samples. *Technometrics* **1969,** *11* (1), 1-21, DOI: 10.1080/00401706.1969.10490657

(18) Espenson, J. H. *Chemical Kinetics and Reaction Mechanisms*; McGraw-Hill Book Company: New York, **1981**.

(19) Shearer, Jason, Nehring, Jennifer, Lovell, Scott, Kaminsky, Werner, Kovacs, Julie A. Modeling the Reactivtiy of Superoxide Reducing Metalloenzymes with a Nitrogen and Sulfur Coordinated Iron Complex. *Inorg. Chem.* **2001**, 40, 22, 5483-5484, DOI: 10.1021/ic010221l

(20) ReactLab^{TM} Kinetics – Global Analysis and Reaction Modeling for Kinetic Processes. Jplus Consulting Pty Ltd, United Kingdom, **2023**.

(21) Kryatov, Sergey V. and Rybak-Akimova, Elena V. Kinetics and Mechanisms of Formation and Reactivity of Non-heme Iron Oxygen Intermediates. *Chem. Rev*. **2005**, 105, 2175-2226, DOI: 10.1021/cr030709z

Appendix to Chapter 2: Global Fitting

A. Notes on Global Fits, Numerical Methods, and Analyzing Results

This appendix contains instructions for software setup, descriptions, and examples of the input for performing the Global Fit Numerical Methods via Jplus Consulting ReactLab™ KINETICS software developed by Dr Peter King, Professor Marcel Maeder, and Dr. Sarah Cliffor at Jplus Consulting in Australia. This appendix is by no means a substitute for the ReactLab™ KINETICS manual, which contains detailed explanations of all the material, and more applications of the simulation feature that ReactLab™ KINETICS has to offer. The manual is available via: *https://jplusconsulting.com/products/reactlab-kinetics/*

A.1.1 Pre-populating Excel workbook

Note: All buttons selected will be italicized.

The process of global fitting electronic absorption spectra starts with collecting EAS data via CCD mode on the TgK stopped-flow instrument and exporting the data to a .CSV that can be opened in Excel. To obtain the .CSV file click the on the drop-down tab *File* and select the option to *Export*

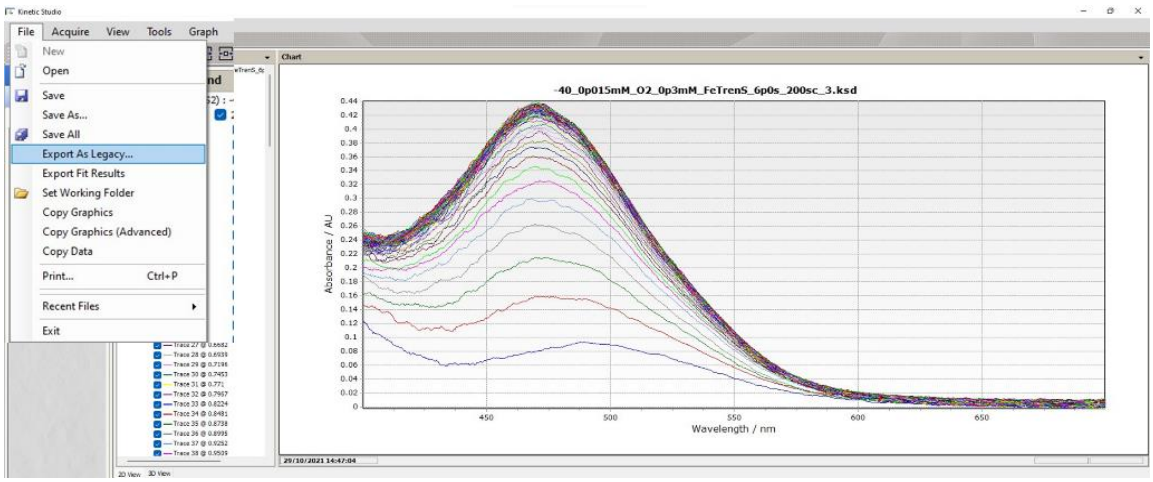

Figure A.1 Exporting EAS spectrum from Kinetic Studio software on the stopped-flow instrument to a .CSV to be opened by excel.

As Legacy… **Figure A.1**. This will bring up a window to save the file as the same name as the kinetic studio file (.ksd), and the type will be changed to a (*.csv). Once saved as a .csv, open the corresponding "Microsoft excel comma separated values" file. The file will contain the "File Info:" of the title of the file in the cell 1A. Column A are the wavelengths in nanometers scanned, and Row 2 are the scan time points in seconds. The format of this file needs to be corrected in order to copy and paste the Data into the Excel workbook that ReactLab™ will operate with. To do so, highlight all the data excluding the cell 1A, open a new sheet and transpose the data so that the wavelengths are now in Row 2 and the Time points are in Column A.

(**Tip:** To highlight large amounts of cells hold *Crtl+Shift* and use the arrow keys to highlight the columns and rows needed. To copy press *Crtl+C*. To transpose rows and columns, right click and choose the *Paste option: Transpose*)

Next, open a template workbook, located in the ReactLab KINETICS file under Excel Kinetics Examples. An Excel Workbook will open with various section. Locate the Data tab, this is where the EAS data that was transposed will be copied into. Copy the EAS data and right click on the yellow box to paste the data in. The "n_times" and "n_lam" will populate with the time points and number of wavelengths. Another way to do this process, is to select the original data, and transpose the data directly into the workbook as shown in **Figure A.2**. Once complete, save and rename the workbook to a location and name that corresponds to the experiment.

Tip: I add "(working)" to the end of the file to designate where I'm messing around with the data and initially guessing the models and data.

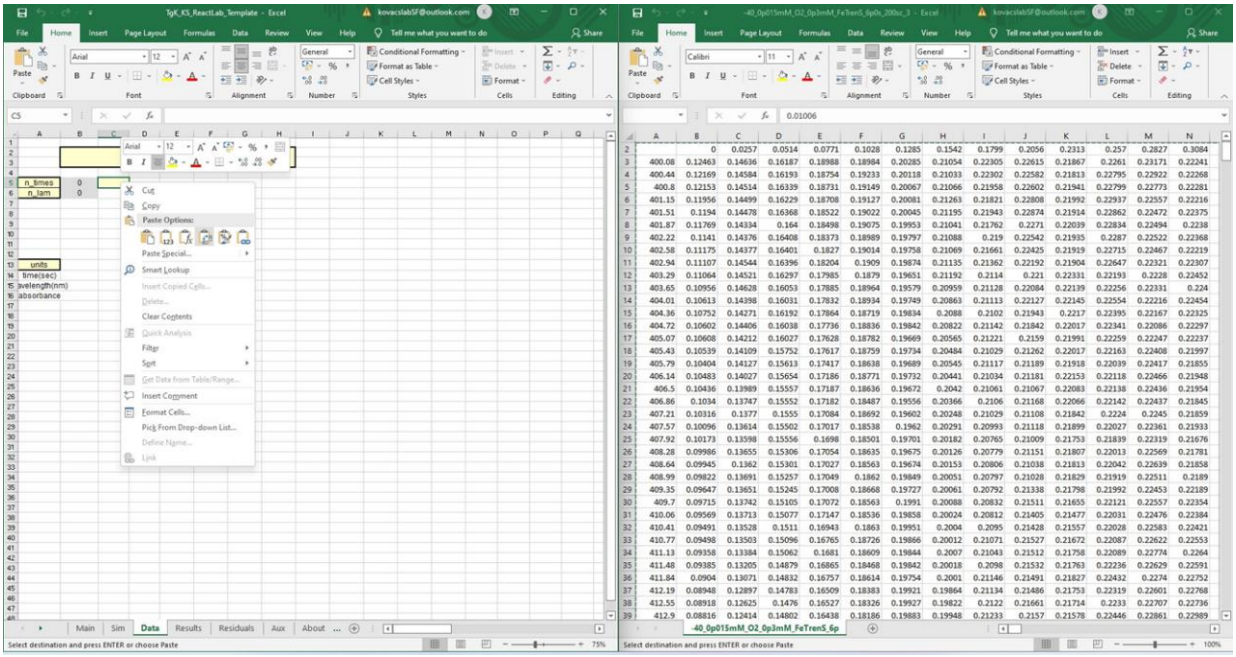

Figure A.2 Transposing the EAS data from the .CSV generated into the ReactLab™ workbook under the data tab. Right click in the yellow box and click on transpose under paste options to ensure that the wavelengths are in the row 5 and the time points are in column C.

A.1.2 Launching ReactLab™ and Opening Workbook

To open the graphic user interface (GUI) and to interact with the workbook that has been saved with the EAS data, launch the *ReactLab™ KINETICS* software, which will bring up a screen that has four blank windows and multiple buttons most of them will be greyed out. Click on *Load Excel File* and open the pre-populated workbook, **Figure A.3**. Three windows should be displayed, the Excel workbook that contains the experimental EAS in the Data tab, the ReactLab™ KINETICS interface and a pop-up window of the experimental spectrum with axis of absorbance, time, and

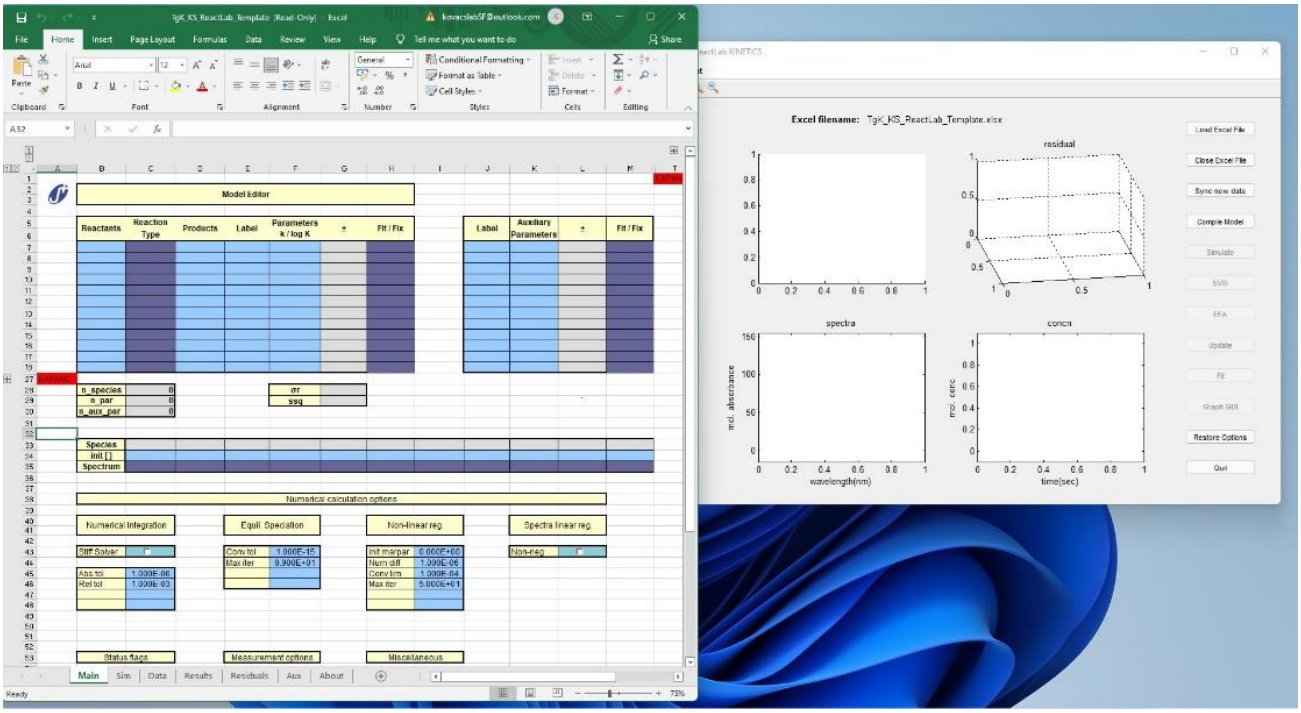

Figure A.3 Opening up ReactLab™ workbook through the interface by clicking on Load Excel file. Workbook opens to the main tab that the user interacts with mainly.

wavelength. The data display also has functions such as zooming and rotating tools for the plots and editing access. To close the Excel workbook, select the *Close Excel File* button on the GUI, and a prompt to save changes will appear on the workbook. If at any time the data is changed in the Excel workbook the GUI won't reflect these changes unless the workbook is synchronized, to achieve this the button *Sync New Data* will synchronize the new data. This prevents having to save and re-load the workbook to apply edits.

A.1.3 Compile a Reaction Model

To analyze the data, a model of the reaction that is being fitted needs to be compiled. The "Model Editor" of the Main tab is where the reaction scheme is entered. The species names, which are arbitrary, are entered under the "Reactants" column, such as A, A + B. There are two reaction

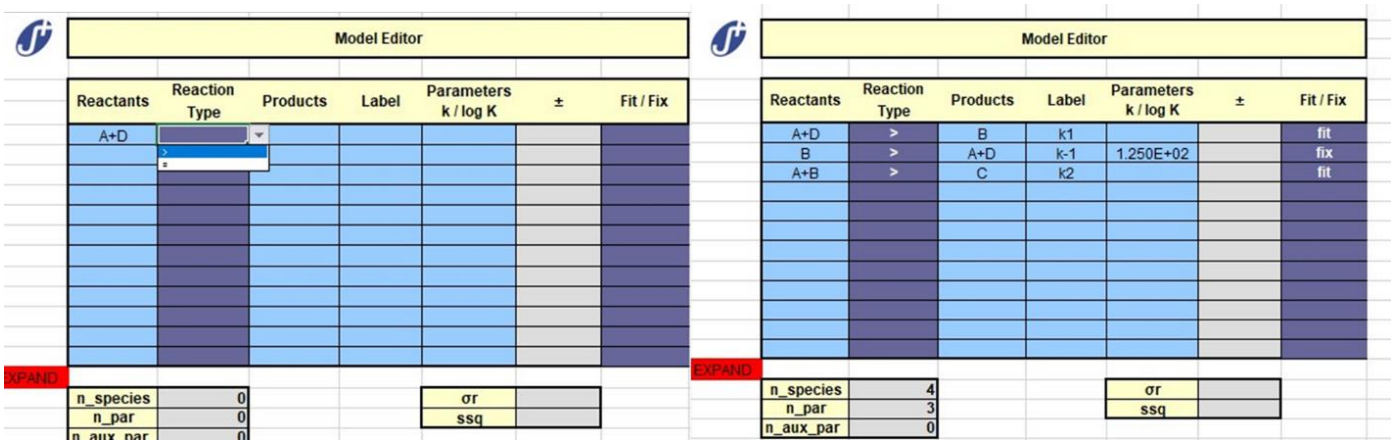

Figure A.4 Entering a plausible model of the reaction for the data to be fitted. Shown is a two-step reaction with a reversible first step. Labels are arbitrary and are named based on user discretion. Parameters are entered based on kinetic data or chemical intuition of the reaction being model. The user decides which parameters will be fitted, calculated by the program, or fixed, not changing, usually based on literature or kinetic data obtained from experiments. Shown above the "k_{-1}" term is fixed as the data was obtained by the estimate of the y-intercept from a plot of k_{obs} (s^{-1}) versus excess changing [O_2].

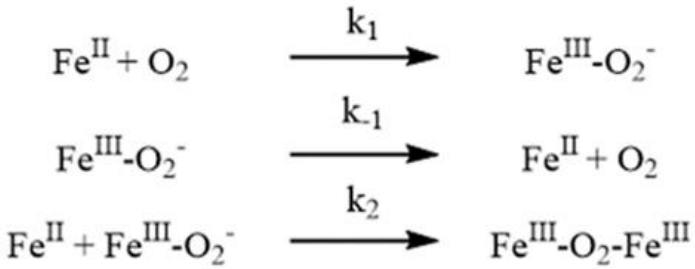

Scheme A. 1 Three step mechanism model employed for global fitting of time resolved spectra from reactions of Fe^{II} and dioxygen.

types to choose from, ">" or "=". The first is a forward reaction, and the second is syntax for a rapid equilibrium step. To enter in a reversible step the input would be the opposite of the forward reaction. Below in **Scheme A.1** is an example model for FeTrenS (**A**) reacting with O_2 (**D**) to form Fe^{III}-superoxo (**B**) and the reverse reaction. Then a 2^{nd} step of Fe^{III}-superoxo (**B**) reacting with another molecule of FeTrenS (**A**) to form the peroxo-bridged dinuclear complex (**C**). As you can see the reaction is broken into three stepwise reactions. Labeling each step is determined by the user, in the example below, the first step is k_1, the reverse of step one is k_{-1}, and the last step to form the product is k_2. An example of the input described above into the Model Editor is shown in **Figure A.4**.

Note: When entering in the model that leading numbers prefixing a species letter or string will be interpreted as stoichiometry coefficient for the species, 2A > B is A + A goes to B. Similarly trailing numbers are used to represent multiple species in a particular complex, ML, ML2, ML3, etc.

Note: Make sure that each entry in the Excel workbook is properly completed, to do so make sure to take focus away from the cell in question by removing the cursor or hitting the return key. Failure to do so will result in an error message of "Incomplete worksheet entry" when syncing or compiling the model.

Once the model entry is complete press the *Compile Model* button on the GUI window. Doing so results in ReactLab™ translating the model into internal coefficient form necessary for the subsequent numerical calculations of the concentration profiles of all participating species. At the same time the "Reactants" species names are extracted and populates the table below the "Model Editor" to input initial concentrations of each species and designate which species contributes to the absorption spectrum which will be discussed in the "Setting Parameters" section. Other fields,

"Sim" and "Results" tab of the worksheet, where excel tables of each of the GUI windows are located. Certain key values are also calculated automatically by Excel and are required by ReactLab™ in locked cells that cannot be edited.

A.1.4 Setting Parameters

Prior to fitting, numerical parameters known or estimated values are entered in their respective fields. Rate constants are entered as absolute values, and may be obtained from literature values, experimental data, as shown in the example, or initial guesses. A value must be entered, and the user must decide whether the parameters will be fixed or fitted, **Figure A.4**. Another parameter that needs to be set before fitting are the initial concentrations of the species in the reaction model, the units should be in molarity (M) and the spectral status of each assigned, "colored", "non-abs" or "known" using the drop-down box. If a species has a known spectrum, the EAS data can be placed in the "Aux" tab of the Excel workbook.

Species	A	D	B	C	
init [ ]	3.00E-04	1.50E-05	0.00E+00	0.00E+00	
Spectrum	non-abs	non-abs	colored	colored	

Figure A.5 Setting initial concentration conditions for reactants in molarity. Example is of excess Fe^{II}TrenS (**A**) with limiting dioxygen (**D**). Species A and D are set to "non-abs" as they don't contribute to the spectrum. Fe^{III}-superoxo (**B**) and dimeric Fe^{III}-peroxo (**C**) initially have no concentration and are the predicted two-colored species observed in the collected experimental data.

The example shown is for [Fe^{II}TrenS] = 0.3 mM (3 x 10^{-4} M) reacting with [O_2] = 0.015 mM (1.5 x 10^{-5} M) and the concentration of the superoxo and peroxo species initially is zero. Fe^{II}TrenS and dioxygen are set to "non-abs" as Fe^{II}TrenS is colorless from 400 to 700 nm, and dioxygen is also colorless, while the superoxo and peroxo both participate in the absorption spectrum and are set to "colored", **Figure A.5**.

To ensure all entries are completed properly, *Sync New Data* will populate the GUI of initial spectra, concentration profiles, and residual windows, **Figure A.6**. At this time, the data is not

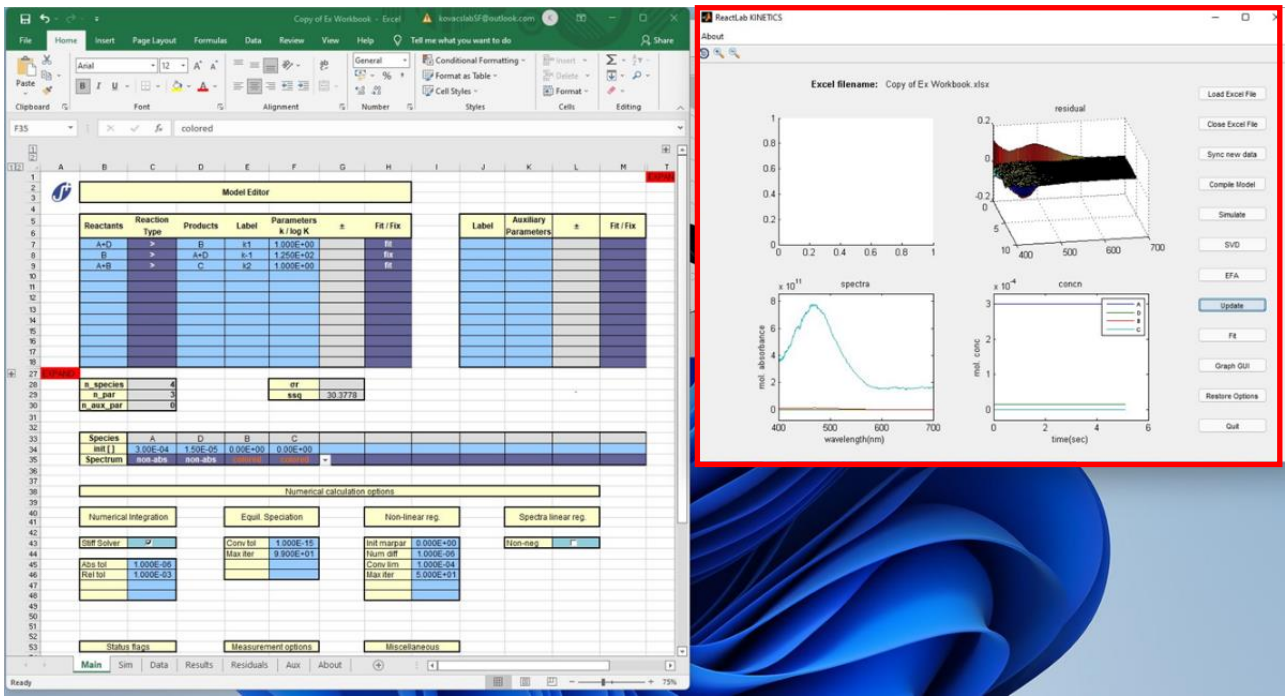

Figure A.6 Once all data is entered properly, *Update* with the GUI to see the three windows populate with the entered information. Data is not fit at this time; this is just a check to make sure that the workbook and GUI are complete and interacting with one another without and errors.

fitted to the model. If entries are not completed properly, and error message of incomplete dataset will appear. Typical this error occurs if a cell containing data is selected when updating the GUI, make sure to press *Enter* on the keyboard or click out of cells before syncing with the GUI.

A.1.5 Fitting the Model to Experimental Data

Selecting *Fit* on the GUI initiates the data fitting algorithm, **Figure A.7**, which proceeds to attempt to minimize the residual square sum (ssq), which is a measure of the difference between the real data and that predicted by the current model and prevailing parameters. The default number of iterations the algorithm will go through is 50 with a convergence limit of 0.0001. The algorithm refines the free parameters of the model using an adaptation of a Marquardt-Levenberg algorithm and adjusting the "colored" spectra, according to a least square criterion. Details of the Marquardt-Levenberg algorithm are described in more detail in the manual, these parameters may be changed at the user's discretion.

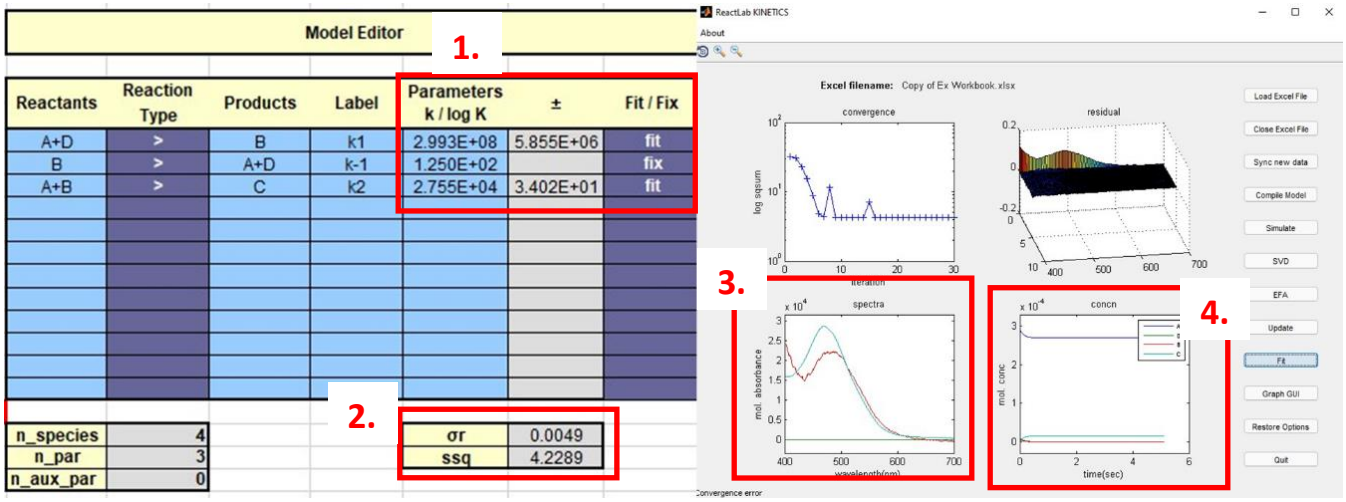

Figure A.7 Example of a fitting that has converged. **1.** The fitted parameters are updated with rates and associated error. **2.** The residual and ssq are updated when the fitting has converged, the closer to zero the better the fit. **3.** The calculated spectra color coded to the reactant labels used. **4.** Concentration profile of the fitted data.

The progress of fitting can be monitored graphically in the ReactLab™ GUI which displays both intermediate concentration profiles and spectra as well as the 3D residual surface of the whole dataset. Iterations stop according to specific convergence limit for a true minimum, if the fit is not converging then at the pre-set iteration maximum is reached.

Once fitted statistical output includes standard deviations for each fitted parameter, the sum of squares, ssq, and the standard deviation $\sigma_{(r)}$. The concentration and spectra matrices are

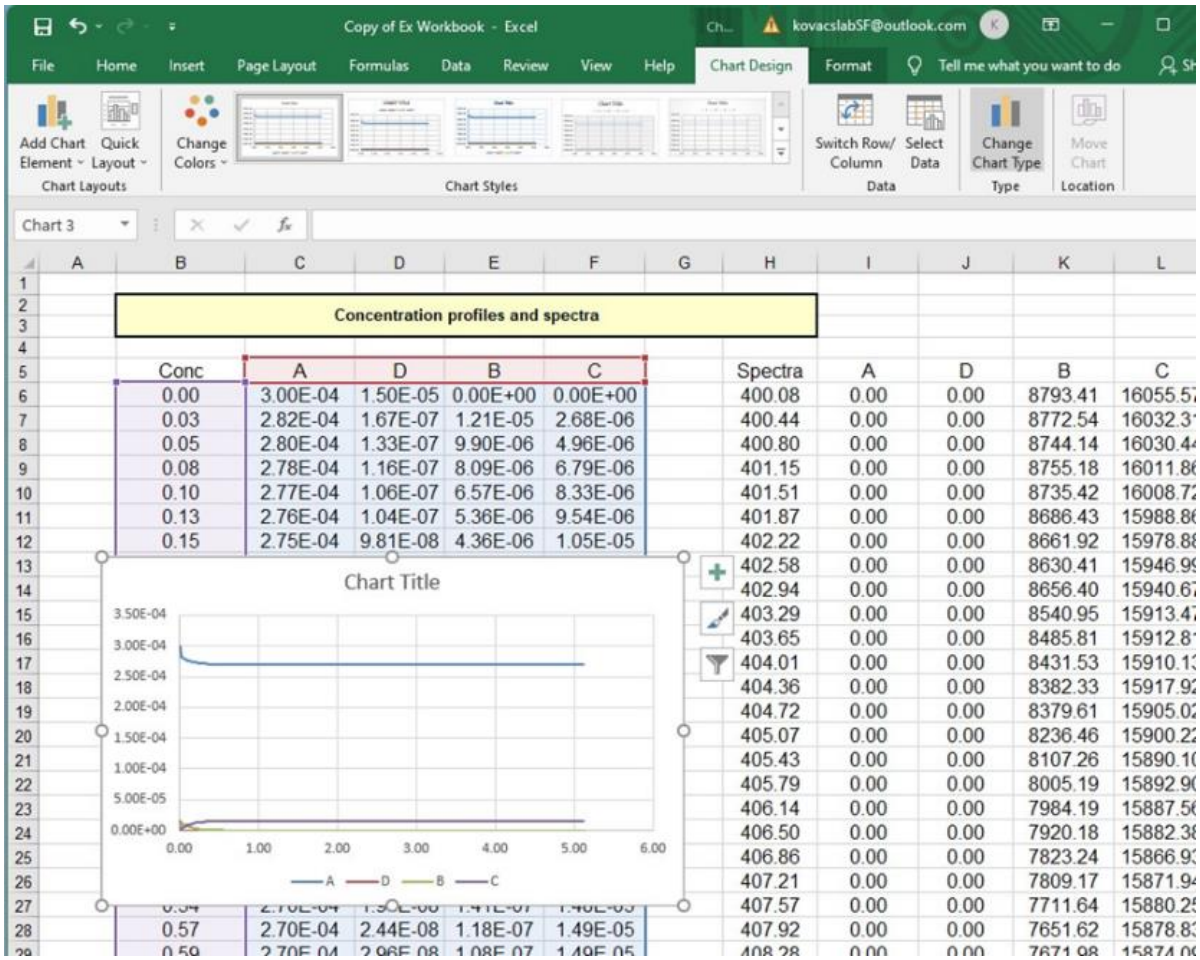

Figure A.8 Results tab of the workbook holds all the fitted data. The first set of data is the concentration profile, and the second is the calculated spectra. Use of excel allows to graphically display the data at the user's discretion. The workbook can be saved and opened outside of the ReactLab™ GUI and edited.

automatically updated in the "Results" tab of the workbook, **Figure A.8**. Any Excel graphs linked to these data ranges will be updated accordingly. Good fits result in non-negative absorption spectra, and small ssq values, as well as good chemical intuition of fitness to the experimental data.

Another useful tool is the *Update* function, which allows checking of a model and the starting parameters without executing a fit which attempts to iteratively optimize parameters. The results of these calculations along with the residuals are shown graphically and will indicate whether the model of the initial parameter values is remotely consistent with the current data or have been entered incorrectly. If the discrepancy between measured and calculate data is excessive it is improbably that a fit will converge. Experimenting with different initial guesses or models may result in more reasonable fits. Example of this is changing the initial values of k_1 and k_2 and updating the GUI. When k_1 is larger than k_2, **Figure A.9 Left**, the calculated spectra result in the peroxo (C) being the more intense band at 465 nm, and the superoxo (B) intermediate is the low absorbing broad band. When these parameters are switched, **Figure A.9 Right**, B becomes the more intense band, while C is now the low absorbance band. The second case is not consistent with the experimentally data obtained and would not result in accurately fitted data.

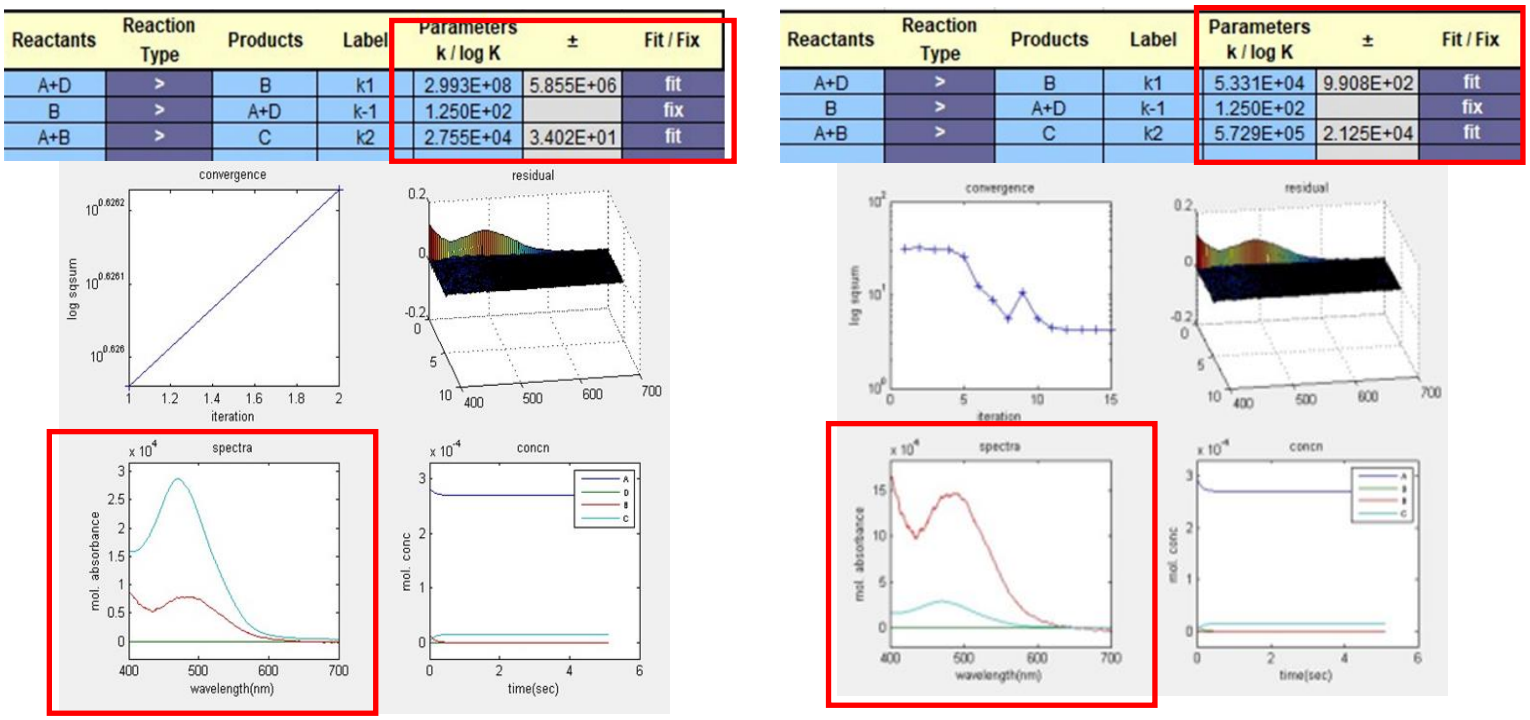

Figure A.9 Utilizing the *Update* function on the GUI to test the parameters for the model against the experimental spectrum observed. **Left:** k_1 is larger than k_2 which is in good agreement with experimental observations of the identity of species B and C. **Right:** k_2 is larger than k_1 which is not in agreement with experimental observations. Testing the initial guess of the fit will lead the user to adjusting parameters consistent with the experimental results instead of running calculations on fits that don't represent the data.

Chapter 3: Cryogenic Stopped-Flow Kinetic Studies Involving the Formation of a Thiolate-Ligated Fe^{III}-Superoxo

Portions of this chapter have been republished or adapted with permission of the Journal of American Chemical Society from, "Cryogenic Stopped-Flow Kinetic Studies Involving the Formation of a Thiolate-Ligated FeIII-Superoxo" Greiner, Maria B.; Downing, Alexandra N.; Blakely, Maike N.; Piquette, Marc C.; Kovacs, Julie A. J. *Manuscript Submitted*

As well as from "Formation of a Reactive, Alkyl Thiolate-Ligated Fe^{III}-Superoxo Intermediate Derived from Dioxygen" Blakely, Maike N.; Dedushko, Maksym A.; Poon, Penny Chaau Yan; Villar-Acevedo, Gloria; Kovacs, Julie A. *J. Am. Chem. Soc.* **2019**, 141, 5, 1867 – 1870. DOI: 10.1021/jacs.8b12670

3.1 Introduction

As described in the introduction the mechanisms of enzymes start with an aquo- species and undergo a geometric rearrangement to displace the water and have an open site for dioxygen (O_2) to bind, as well as a spin-state change. The difference between an aprotic versus protic environment would contribute to how well dioxygen would bind leading to the formation of the first intermediate ferric-superoxo (Fe^{III}-superoxo) and the reactivity of the oxidative species. In small molecules the solvent is varied to best mimic the protein environment, specifically tetrahydrofuran (THF) for aprotic, and methanol (MeOH) for protic environments. Studying the effects of these solvents of dioxygen binding have been qualitatively investigated, and herein we have made efforts to quantitatively evaluate the difference between the two environments for dioxygen binding.

Only six well-characterized examples of small molecule, non-heme Fe^{III}-superoxo complexes have been reported.[1-6] For those generated from O_2, the reversibility of the reaction was qualitatively evaluated by purging a solution with an inert gas and monitoring the intensity of the Fe^{III}-superoxo electronic absorption bands. A decrease in intensity, followed by an increase to the

Fe^{III}-superoxo's original value upon the reintroduction of O_2 over several cycles provides qualitative evidence for reversible O_2 binding. Using this method, synthetic small-molecule complexes, [Fe^{II}(BDPP)] and [$Fe^{II}(L^{Ph})(Tp^{Me2})$], have been shown to reversibly bind O_2 in tetrahydrofuran (THF) at -80 °C and -60 °C, respectively.[4,7] In contrast, the arylthiolate-ligated complex, [$Fe^{II}(Tp^{Me2})$(2-ATP)] was qualitatively shown to irreversibly bind O_2 in THF at -80 °C.[8] An S = 2 ground state indicates that the electronic structure of [$Fe^{III}(O_2)(Tp^{Me2})$(2-ATP)] is best described as a high-spin S = 5/2 Fe^{III} center antiferromagnetically coupled to a superoxide radical.[8] Another example of irreversible O_2 binding to a thiolate-ligated first row transition-metal, [$Co^{II}(Me_3TACN)(S_2SiMe_2)$]; revealed through EPR, XAS, and DFT computational studies that the cobalt ion maintains electron density consistent with an oxidation state of Co^{II} throughout the reaction with dioxygen, suggesting that the thiolate is redox active.[9] These examples illustrate differing metal- and ligand-dependent reactivities with respect to O_2 binding and the transfer of electron density onto the O_2 moiety, however limited information can be obtained from qualitative studies.

Previously in the Kovacs group, a crystallographically characterized, five-coordinate, reduced alkyl thiolate-ligated complex, [$Fe^{II}(S_2{}^{Me2}N_2N^H$(Pr,Pr))] (**1**) that reacts with O_2 to form a well characterized, metastable ferric superoxo species, [$Fe^{III}(S_2{}^{Me2}N_2N^H$(Pr,Pr))($O_2$)] (**2**).[1] Vibrational resonance Raman (rR) data, computational studies, EPR, and ^{1}H NMR spectroscopic data established that the electronic structure of superoxo **2** consists of a low-spin Fe^{III} (S = 1/2) ion strongly coupled antiferromagnetically (J^{calc} = -450 cm^{-1}) to an S = 1/2 superoxo radical,[1] indicating that an electron is transferred from the reduced Fe^{II} ion to O_2 during the formation of **2**, **Scheme 3.1.** The time-dependent DFT (TD-DFT) calculated electronic absorption spectrum of **2** reproduced the experimental spectrum, and shows that the superoxo π^*(O-O) → d_{xy}(Fe) charge

transfer transitions are responsible for the higher energy bands, and the thiolate RS^- → Fe-$O_2^{\bullet-}$ charge transfer transition for the lower energy band.[1] Both the calculated and experimental spectrum of **2** are similar to that of the putative IPNS superoxo intermediate.

The focus of **Chapter 3** examines the quantitatively investigation of the barrier to, and reversibility of, O_2 binding to **1** of the corresponding **2** complex in aprotic versus protic solvents, THF and MeOH using variable temperature stopped-flow kinetics. As well as explores the mechanism of formation of metastable superoxo **2** via two distinct pathways, **Scheme 3.1**: dioxygen binding and inner-sphere electron transfer from five-coordinate **1**, and outer-sphere electron transfer of oxidized **1**, $[Fe^{III}(S_2{}^{Me2}N_2N^H(Pr,Pr))]BF_4$ (**3**) with KO_2 solubilized in KryptoFix222® maintain at a constant ionic strength. Time-resolved electronic absorption

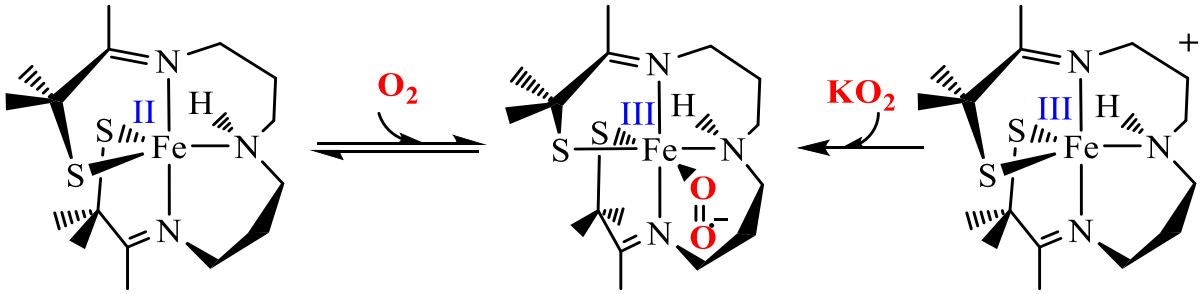

Scheme 3.1 Formation of **2** via two distinct pathways. **Left**: **1** plus dioxygen forms **2** via inner sphere electron transfer. **Right**: **3** plus potassium superoxide forms **2** through outer sphere electron transfer.

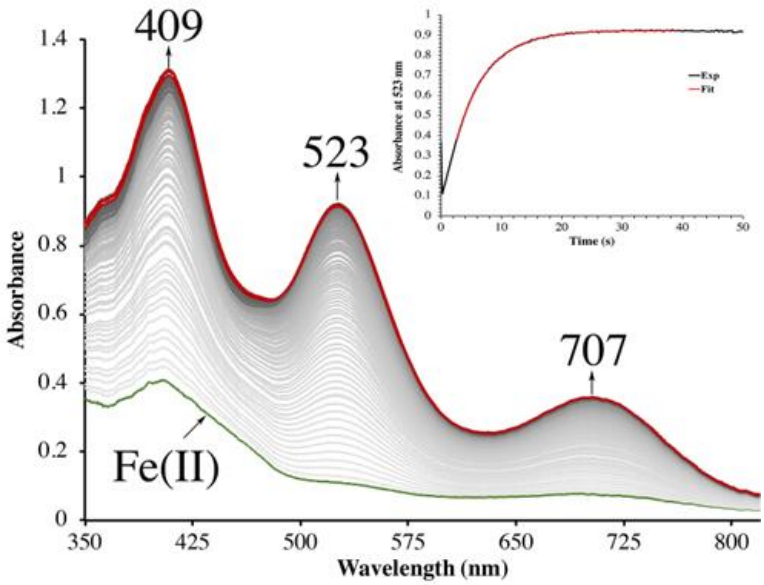

Figure 3.1 Time-resolved spectral changes obtained upon mixing THF solutions of **1** (0.25 mM) and O_2 (3.95 mM) at -40 °C. **Insert**: Kinetic trace (λ= 523 nm) showing the formation of **2** intermediate. All reported concentrations are after mixing in the stopped-flow cell.

spectroscopy was used to monitor both reactions using a TgK scientific cryogenic stopped-flow instrument. The growth of spectral features associated with **2** in THF and MeOH were monitored using a CCD detector. Kinetics were monitored at λ = 523 nm under pseudo first-order conditions with excess reagent (O_2 or $O_2^{\bullet-}$). As illustrated in the time-resolved absorption spectrum and kinetic trace of **Figure 3.1** , superoxo **2** forms in ~20 seconds at -40 °C in THF. The kinetic trace (**Figure 3.1**, **insert**) can be fit to the single exponential **Eq 1** with very small residuals.

$$A_t = A_\infty - (A_\infty - A_0)e^{-k_{obs}t} \qquad \textbf{Eq 1}$$

Activation barriers of O_2 binding will be compared to another thiolate-ligated non-heme Fe^{II} complex, $[Fe^{II}(S^{Me2}N_4(tren))]^+$ (**5**), and insights into difference in O_2 binding rates as well as ligand constraints will be discussed.

3.2 Results and Discussion

3.2.1 Mechanism of Dioxygen Activation for Superoxo

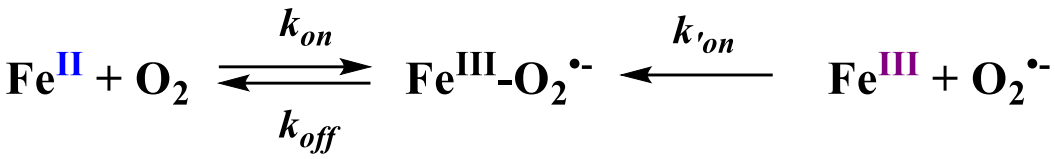

Scheme 3.2 General Kinetic scheme for formation of **2** from **1** and dioxygen and oxidized **3** and superoxide.

The proposed kinetic scheme of **1** reacting with dioxygen, **Scheme 3.2**, results in the formation of relatively meta-stable **2**. Over time **2** results in the formation of $[Fe^{III}(\eta^2\text{-}S^{Me2}O)(S^{Me2})N_2N^H(Pr,Pr)]^+$ **4** in various solvents[11], and the decay of the **2** preliminary depends on the strength of C-H bonds present in solution. The complex **1** does not yield a binuclear species along the reaction pathway unlike other non-heme small molecules. The overall rate of formation of superoxo **2** is dependent on dioxygen binding rate constant (k_{on}) and the reverse, dissociation rate constant (k_{off}) in **Eq 2**. Since **1** does not form binuclear species, the derived rate law uses the

$$Fe^{II} + O_2 \underset{k_{off}}{\overset{k_{on}}{\rightleftharpoons}} Fe^{III}O_2 \qquad (2)$$

$$\frac{d[Fe^{III}O_2]}{dt} = k_{on}[Fe^{II}]_t[O_2] - k_{off}[Fe^{III}O_2]_t \qquad (3)$$

$$[Fe^{II}]_0 = [Fe^{II}]_t + [Fe^{III}O_2]_t \qquad (4)$$

$$[Fe^{III}O_2]_t = [Fe^{II}]_0 - [Fe^{II}]_t \qquad (5)$$

$$\frac{d[Fe^{III}O_2]}{dt} = k_{on}[Fe^{II}]_t[O_2] - k_{off}([Fe^{II}]_0 - [Fe^{II}]_t) \qquad (6)$$

$$= k_{on}[Fe^{II}]_t[O_2] + k_{off}[Fe^{II}]_t - k_{off}[Fe^{II}]_0 \qquad (7)$$

$$= [Fe^{II}]_t(k_{on}[O_2] + k_{off}) - k_{off}[Fe^{II}]_0 \qquad (8)$$

$$\frac{d[Fe^{III}O_2]}{dt} = k_{obs}[Fe^{II}]_t - C \qquad (9)$$

$$k_{obs} = k_{on}[O_2] + k_{off} \qquad (10)$$

assumption of mass balance, that the concentration of **2** at any given time, $[FeO_2]_t$, is equal to the initial concentration of **1**, $[Fe^{II}]_0$, plus the concentration of **1** at any given time, $[Fe^{II}]_t$, **Eq 4**. Solving for the concentration of **2** yields **Eq 5** in terms of [**1**], and substituting this into **Eq 2**, yields **Eq 6**, and simplified to **Eq 8**. Under pseudo-first order kinetics with excess dioxygen, the rate expression simplifies to **Eq 9**, with the observed rate constant (k_{obs}) defined in a linear equation with k_{on} being the slope, and k_{off} as the y-intercept, **Eq 10**. For a reversible process under pseudo first-order conditions with excess O_2, k_{obs} would be dependent on both k_{on} and k_{off}.[11] The term $k_{off}[Fe^{II}]_0$ is constant and represented as *C* in **Eq 9**, which does not change with time, therefore it does not affect the measured rate constants k_{obs}. Also important to note is that the magnitude of *C* is small relative to the other terms when working with sub-mM concentrations of $[Fe^{II}]_0$, and thus is dropped from **Eq 9**.[11]

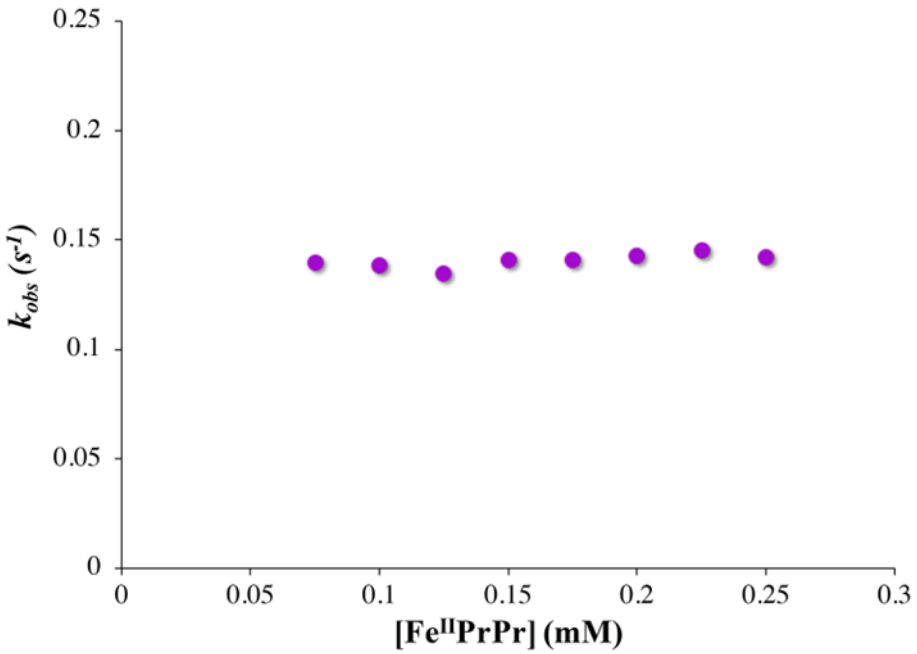

Figure 3.2 Plot of observed rate constants (k_{obs}) for the formation of **2** versus **1** concentration at -40 ˚C in THF. $[O_2]$ after mixing = 3.95 mM. This would be consistent with 1st order dependence on Fe^{II} overall.

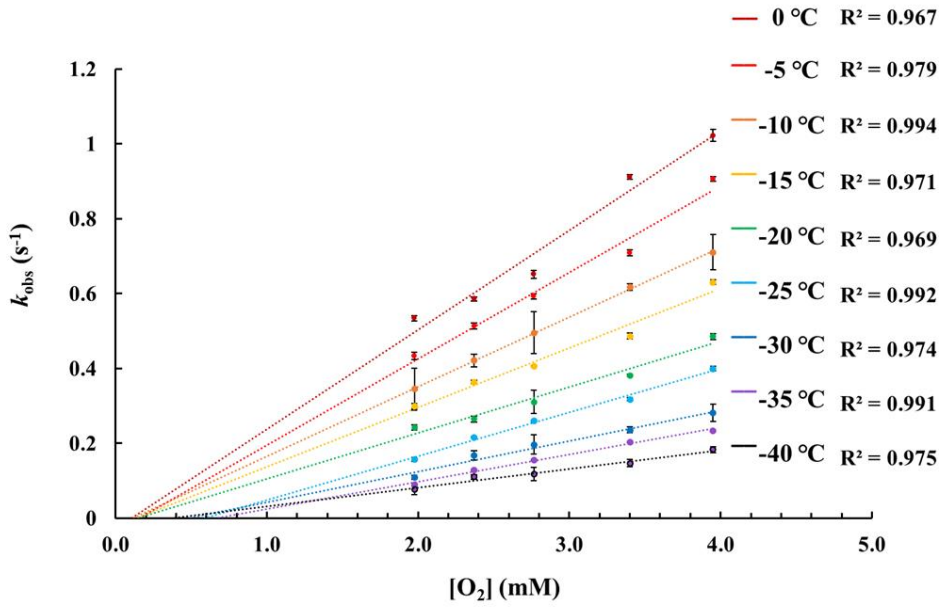

Figure 3.3 Temperature-dependent rate constants k_{obs} for the formation of superoxo **2** in the reaction between **1** (0.25 mM) and O_2 in THF plotted against [O_2]. The intercept of approximately 0.0 would be consistent with irreversible O_2 binding.

Table 3.1 Temperature-Dependent Rate Constants for Irreversible O_2 Binding to [$Fe^{II}(S_2{}^{Me2}N_2N^H(Pr,Pr))$] (**1**) in THF, and Reversible O_2 Binding to **1** in MeOH.

Temperature (K)	k_{on} ($M^{-1}s^{-1}$) **THF**	k_{on} ($M^{-1}s$-1) **MeOH**	k_{off} (s^{-1}) **MeOH**
273.15	2.66(19) x 10^2	4.4(2)	4(2) x 10^{-3}
268.15	2.31(10) x 10^2	3.4(1)	3.4(8) x 10^{-3}
263.15	1.86(1) x 10^2	2.3(1)	2.5(4) x 10^{-3}
258.15	1.59(8) x 10^2	1.70(4)	2.4(3) x 10^{-3}
253.15	1.23(5) x 10^2	1.20(7)	1.9(4) x 10^{-3}
248.15	1.17(4) x 10^2	1.05(5)	1.0(4) x 10^{-3}
243.15	8.2(6) x 10^1	0.79(2)	6(2) x 10^{-4}
238.15	7.3(3) x 10^1	----	----
233.15	5.0(3) x 10^1	----	----
$\Delta H^{\ddagger}$ (kJ•mol^{-1})	19.3(9)	30(2)	32(4)
$\Delta S^{\ddagger}$ (J•mol^{-1}K^{-1})	-127(3)	-123(7)	-173(15)
E_a (kJ•mol^{-1})	21.4(8)	32(2)	34(4)
$\Delta G^{\ddagger}$ (243 K, kJ•mol^{-1})	50(1)	60(3)	73(4)

3.2.2 Low Temperature Kinetics for the Reaction Between O_2 and 1

Under pseudo first-order conditions with excess O_2, k_{obs}, obtained from fits to **Eq 1** were found to be independent of the concentration of **1** in both THF and MeOH (**Figure 3.2**), confirming that the reaction is first-order overall with respect to **1.** This would be consistent with the formation of a 1:1 dioxygen adduct. Observed rate constants, k_{obs}, were found to increase linearly with increasing O_2 concentration in both THF (**Figure 3.3**) and MeOH (**Figure 3.4**) consistent with first-order dependence on O_2 (**Eq 10**). Second order rate constants (**Table 3.1**), k_{on}, were obtained from the slope of the k_{obs} versus [O_2] plot (**Figures 3.3** and **Figure 3.4**) over the temperature range -40 ˚C to 0 ˚C in THF, and -30 ˚C to 0 ˚C in MeOH, in 5 ˚C increments. In MeOH, O_2 binds to **1**,

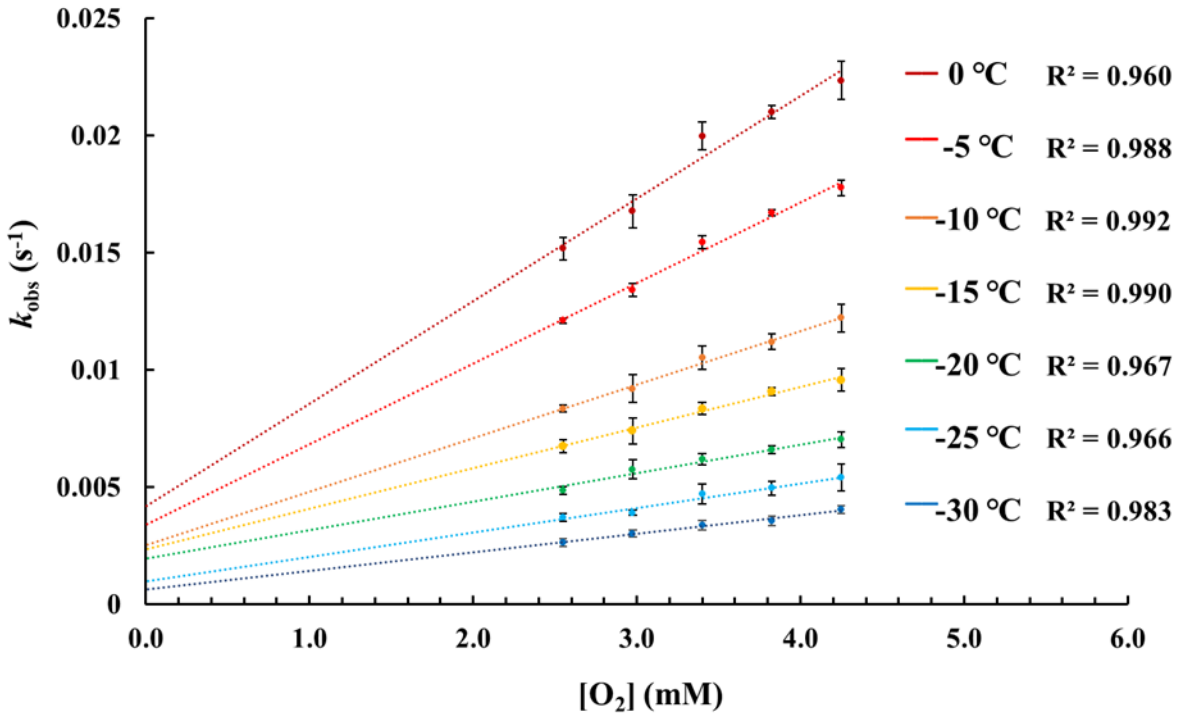

Figure 3.4 Temperature-dependent rate constants k_{obs} for the formation of superoxo **2** in the reaction between **1** (0.25 mM) and O_2 in MeOH plotted against [O_2]. The non-zero intercepts would be consistent with reversible O_2 binding in MeOH.

and is released from **2**, too slowly to collect data at temperatures below -30 ˚C using a stopped-flow instrument. Saturated dioxygen solutions were prepared by bubbling dry O_2 gas into a small round-bottom flask containing dry degassed THF or MeOH for 15 minutes at room temperature. The solution was then allowed to equilibrate over 15 minutes at 25 °C in a temperature-controlled water bath. Gas-tight syringes were loaded by inverting the flask and using a 3-way valve as described in the experimental section. The solubility of O_2 was taken as 7.9 mM in THF, and 8.5 mM in MeOH at 25 °C, respectively.[12,13] Dilutions of O_2-saturated solvents were performed in an atmosphere-free closed system, devoid of head-space using a TgK stopped-flow instrument to obtain precise O_2 concentrations, the process is explained in detail with figures in **3.4 Experimental Details**. All concentrations of reagents are reported in "after-mix" concentrations. Reaction runs were taken in triplicate and quintuplicates and analyzed using Grubb's test[14] providing a 95% confidence level on the pseudo-first order rate constants observed, k_{obs}. In THF, the intercept of k_{obs} vs $[O_2]$ was found to be approximately zero over the entire temperature range

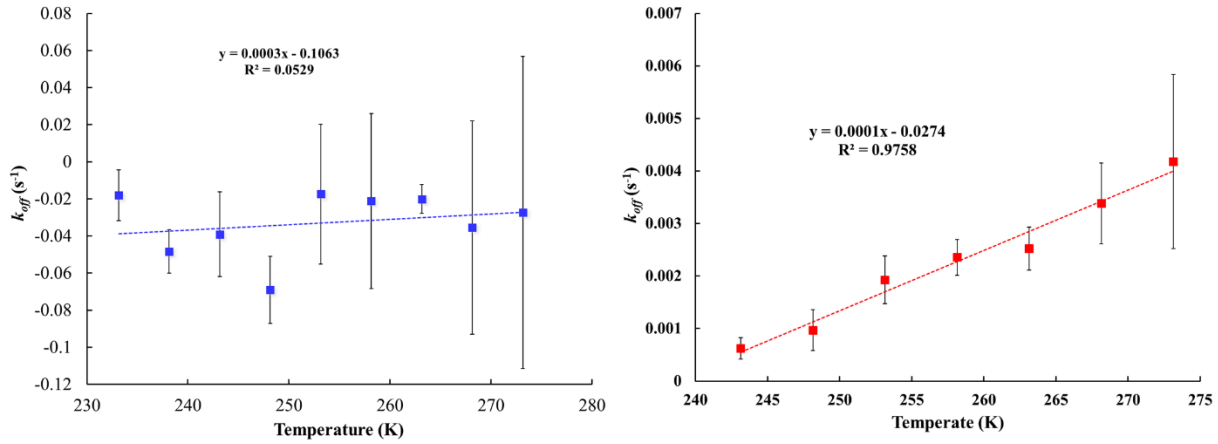

Figure 3.5 Left: The dissociate rate constant, k_{off}, obtained from the y-intercept of the k_{obs} vs $[O_2]$ plots of **Figure 3.2**, does not correlate with temperature in THF. This, coupled with the ~zero intercept of **Figure 3.2** would be consistent with irreversible O_2 binding to **1** in THF. **Right**: Correlation between temperature and rate constants for O_2 release from superoxo **2**, k_{off}, in MeOH. Dissociation rate constants, k_{off}, were obtained from the y-intercept of the k_{obs} vs $[O_2]$ plots of **Figure 3.3**.

examined (**Figure 3.3**), indicating that O_2 binds irreversibly to **1** in this solvent. This is supported by the fact that no trend in k_{off} vs temperature is observed in THF (**Figure 3.5, left**). In MeOH, the non-zero intercept (**Figure 3.4**) was found to increase with increasing temperature (**Figure 3.5, right**) consistent with reversible O_2 binding in this solvent. Dioxygen dissociation rate constants in MeOH, k_{off}, obtained from the intercept of the k_{obs} versus [O_2] plot of **Figure 3.3**, are assembled in **Table 3.1**.

3.2.3 Kinetic Barrier to O_2 Binding.

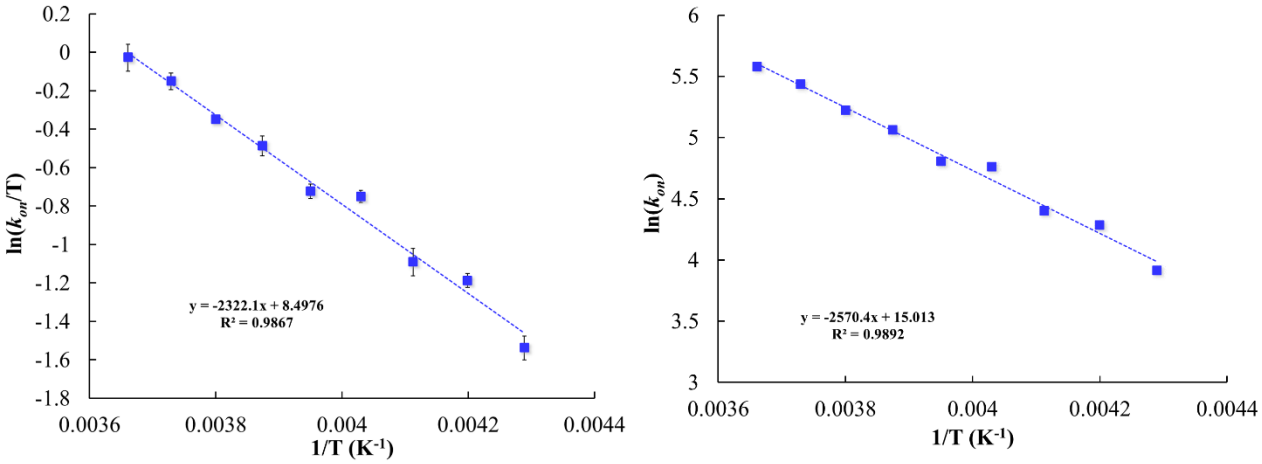

Figure 3.6 Left: Eyring plot for O_2 binding to 1 in THF. Second order rate constants, k_{on}, were obtained from the slope of k_{obs} vs [O_2] plots (**Figure 3.2**). [**1**] = 0.25 mM, after mixing.
Right: Arrhenius plot for O_2 binding to **1** in THF, from which activation parameter E_a= 21.4(8) kJ•mol^{-1} was obtained.

Comparison of the second order rate constants, k_{on}, in THF versus MeOH indicates that dioxygen binds roughly two orders of magnitude more slowly to **1** in MeOH. Activation parameters for O_2 binding were obtained from Eyring and Arrhenius plots in THF and MeOH (**Figure 3.6** and **Figure 3.7**) are assembled in **Table 3.1**. The negative entropy of activation ($\Delta S^{\ddagger}$ = -127(4) J•mol^{-1}K^{-1} in THF; $\Delta S^{\ddagger}$ = -123(7) J•mol^{-1}K^{-1} in MeOH) is consistent with an associative mechanism, as opposed to one that involves initial solvent dissociation, in both solvents. If,

however, the entropy change associated with solvent release is less than that of O_2 binding, then it is possible that solvent release is involved. We have no evidence, however for a derivative of reduced **1** containing a coordinated solvent molecule, despite crystallization from coordinating

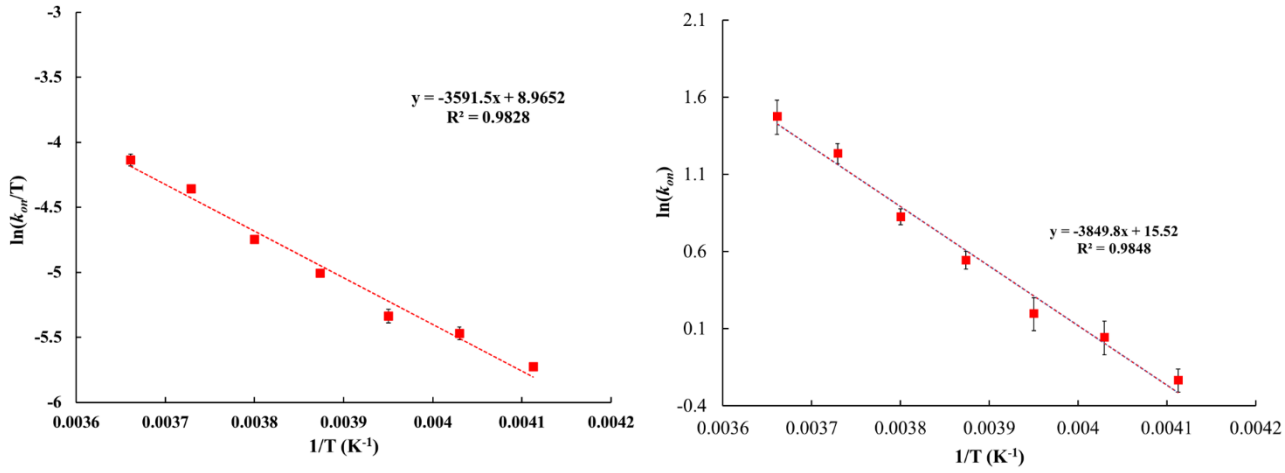

Figure 3.7 Left: Eyring plot for O_2 binding to **1** in MeOH, from which the activation parameters $\Delta H^{\ddagger}$ = 30(2) kJ•mol^{-1} and $\Delta S^{\ddagger}$ = -123(7) J•mol^{-1} K^{-1} were obtained. **Right:** Arrhenius plot for O_2 binding to **1** in MeOH, from which activation parameter E_a= 32(2) kJ•mol^{-1} was obtained.

solvents acetonitrile (MeCN) or MeOH which reproducibly affords a five-coordinate complex.

3.2.4 Low-Temperature Kinetics for the Reaction Between [Fe^{III}(S$_2^{Me2}$N$_2$N^{H}(Pr,Pr))]BF$_4$ and KO$_2$

As shown in **Scheme 3.1**, superoxo compound **2** forms both via the addition of O_2 to **1** as well as via the addition of KO_2 to **3**.[1] Evidence for this was described previously[1] where the electronic absorption spectrum identical to that of **Figure 3.1** is observed in the reaction between **3** and KO_2, **Figure 3.8**. By examining variable temperature kinetics for the reaction between KO_2 and **3** we were able to determine whether an inner sphere or outer sphere electron transfer mechanism is involved. As shown in **Figure 3.8**, the reaction between **3** and KO_2 takes ~15 seconds to go to completion at -30 °C under pseudo first-order conditions with excess KO_2, and ~27 seconds at -40

°C under the same conditions. Observed pseudo first-order rate constants k_{obs}, obtained from first to **Eq 1**, increase linearly as [KO_2] is increased (**Figure 3.9**) and are independent of the concentration of **3** (**Figure 3.10**). The latter would be consistent with first-order dependence on Fe^{III} overall. The reaction order with respect to superoxide ($O_2^{\bullet-}$) was determined by varying the

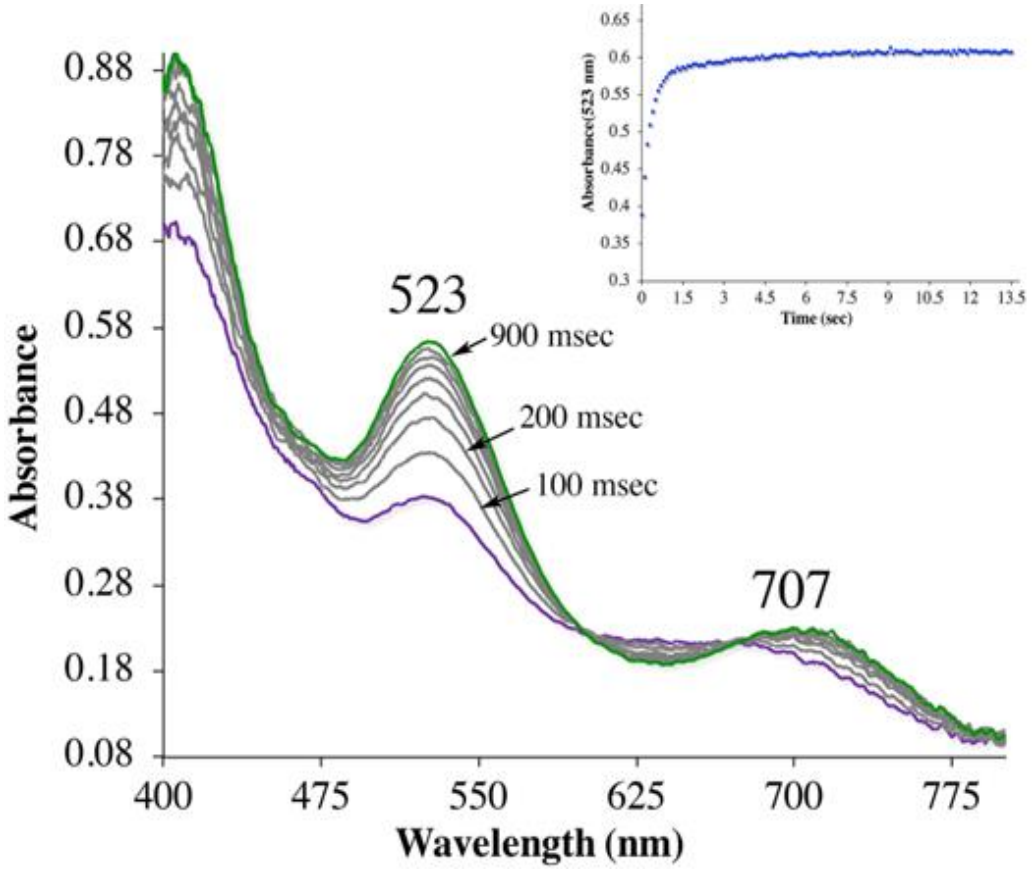

Figure 3.8 Time-resolved spectral changes observed in the reaction between **3** (0.1 mM) and KO_2 (5.0 mM; solubilized with 222-Kryptofix) in THF at -30 °C. **Insert:** Kinetic trace (λ = 523 nm) showing the formation of superoxo **2**. All reported concentrations are after mixing in the stopped-flow cell.

Table 3.2 Temperature-Dependent Second-Order Rate Constants and Activation Parameters for KO_2 Binding to **3** Under Constant Ionic Strength (0.01 M) maintained via the addition of Bu_4NPF_6.

Temperature (K)	k'_{on} ($M^{-1}s^{-1}$) KO_2 THF
253.15	298(11)
248.15	235(24)
243.15	142(17)
238.15	95(12)
233.15	58(3)
228.15	46(7)
223.15	29(2)
218.15	20(2)
213.15	11.6(5)
$\Delta H^{\ddagger}$ ($kJ•mol^{-1}$)	34.3(9)
$\Delta S^{\ddagger}$ ($J•mol^{-1}K^{-1}$)	-61(4)
E_a ($kJ•mol^{-1}$)	36.3(9)

concentration of KO_2 (**Figure 3.9**) over the range 1.0 mM to 5.0 mM. Second-order rate constants, $k_{superoxide}$, were obtained from the slope of k_{obs} vs [KO_2] plot of Figure X and are assembled in **Table 3.2**. Activation parameters for $O_2^{\bullet-}$ binding to **3** in THF (E_a = 36.3(9) $kJ•mol^{-1}$; **Table 3.2**)

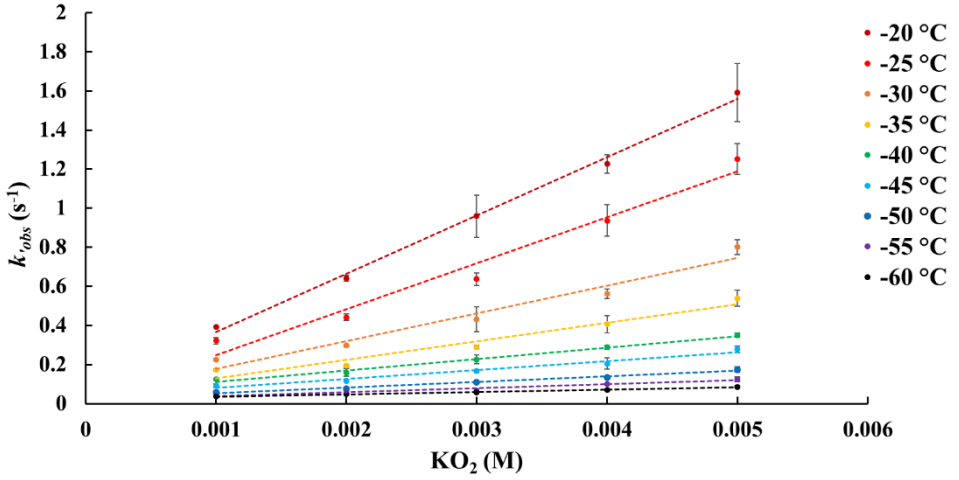

Figure 3.9 Temperature-dependent rate constants, k_{obs}, for the formation of superoxo **2** in the reaction between **3** and KO_2 (solubilized with KryptoFix) in THF, plotted against [KO_2]. The ~zero intercepts would be consistent with irreversible $O_2^{\bullet-}$ binding. [**3**] = 0.1 mM. Concentrations listed correspond to after mixing in the stopped-flow cell.

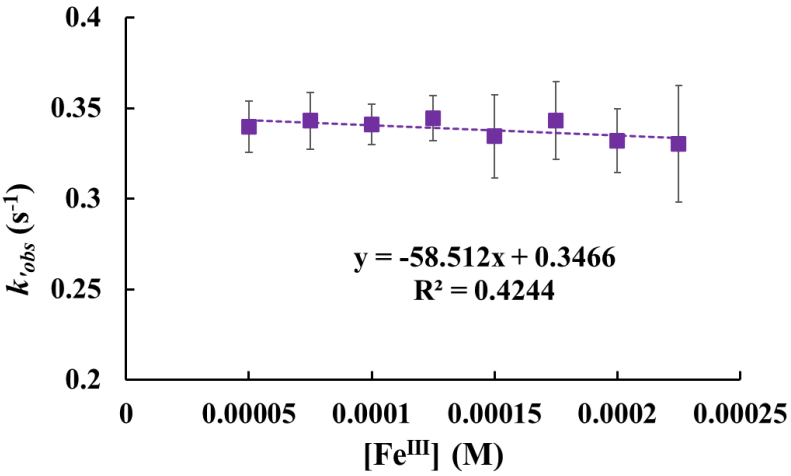

Figure 3.10 Zero order dependence of k_{obs} on Fe^{III} concentration under pseudo first order conditions with excess KO_2 (5 mM). This would be consistent with 1st order dependence on Fe^{III} overall.

under constant ionic strength conditions (0.01 M; maintained with Bu_4NPF_6) were obtained from Eyring and Arrhenius plots, **Figure 3.11**. The Arrhenius parameter, E_a, for KO_2 binding to **3** (**Table 3.2**) is 14.9 kJ•mol^{-1} greater than the barrier (E_a = 21.4(8) kJ•mol^{-1}) to O_2 binding to **1** (**Scheme 3.1**, **Table 3.1**) in the same solvent. This has implications about the mechanism of the reaction between **1** and O_2 (*vide infra*). The negative entropy of activation, $\Delta S^{\ddagger}$, (**Table 3.2**) is

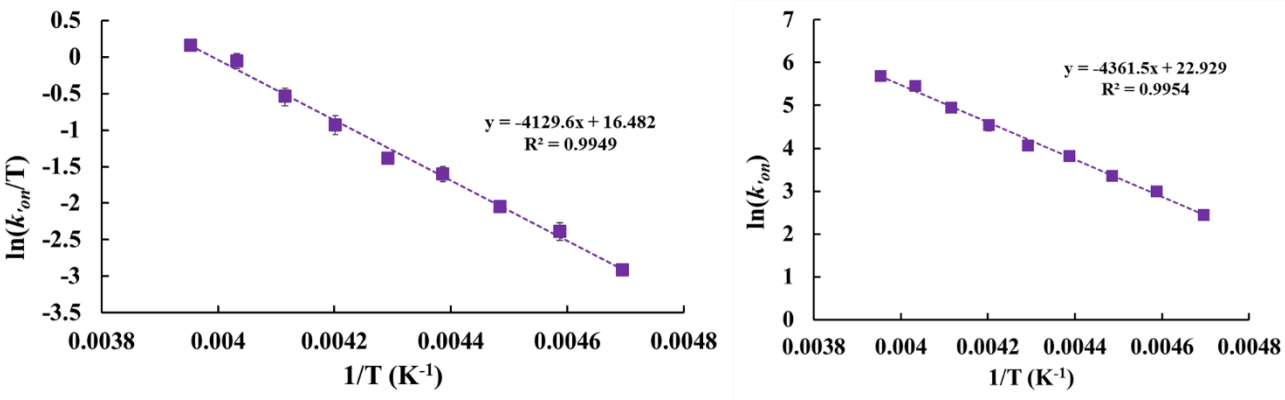

Figure 3.11 Left: Eyring plot for superoxide (KO_2 solubilized with KryptoFix) binding to **3** in THF. **Right**: Arrhenius plot for superoxide (KO_2 solubilized with KryptoFix) binding to **3** in THF.

consistent with an associative process involving KO_2 binding to **3**. The smaller (**Table 3.2**) magnitude of $\Delta S^{\ddagger}$ for the KO_2 reaction relative to the O_2 reaction (**Table 3.1**) is likely due to the release of solvent from the superoxide anion.

As shown in **Figure 3.12**, possible mechanism for the formation of **superoxo-2** via the reaction between **1** and O_2 include (1) outer-sphere electron transfer (ET) to afford oxidized **3** and superoxo ($O_2^{\bullet-}$), followed by $O_2^{\bullet-}$ binding to **3** to afford superoxo **2**, (**2**) dioxygen binding to **1** to afford an Fe^{II}-O_2 dioxygen intermediate followed by inner-sphere electron transfer (ET) to afford superoxo **2**, or, (**3**) a concerted mechanism across the diagonal. The latter two are indistinguishable. The fact that the activation barrier to, E_a, to $O_2^{\bullet-}$ binding to **3** was experimentally determined to be 14.9 $kJ \bullet mol^{-1}$ higher than E_a for dioxygen binding to **1** implies that mechanism (**2**) or (**3**), involving inner-sphere ET, are the most likely mechanisms. The unfavorable thermodynamics of electron

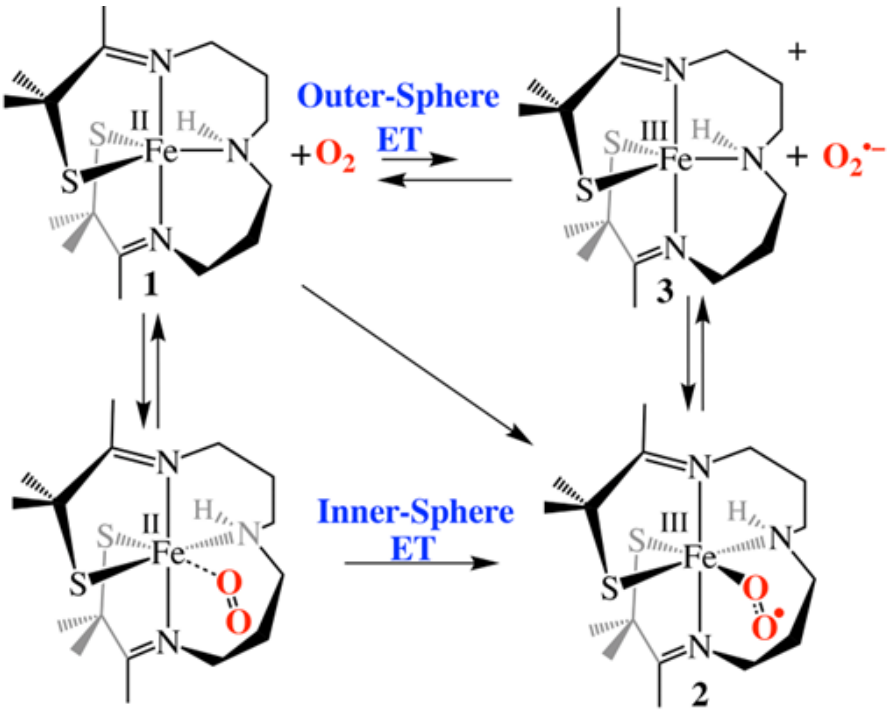

Figure 3.12 Possible mechanisms for the reaction between **1** and O_2 involving either outer-sphere electron transfer (ET) followed by superoxide ($O_2^{\bullet-}$) binding to oxidized **3**, O_2 binding followed by inner-sphere ET, or a concerted mechanism (diagonal).

transfer from **1** to O_2 (K_{eq} = 1.6 x10^{-8} M^{-1} calculated using $E^{1/2}$(**Fe^{II}-1**/**Fe^{III}-3**) = -0.40 V and $E_{1/2}(O_2^{\bullet-}/O_2)$ = -0.86 V vs SCE in THF),[15] provides additional support for this conclusion.

3.2.5 Contributions to the Kinetic Barrier for O_2 Release from 2

In MeOH, O_2 binds reversibly to **1**, in contrast to the irreversible binding in THF as evident by the lack of y-intercept observed in the observed rate constant (k_{obs}) versus excess [O_2]. The

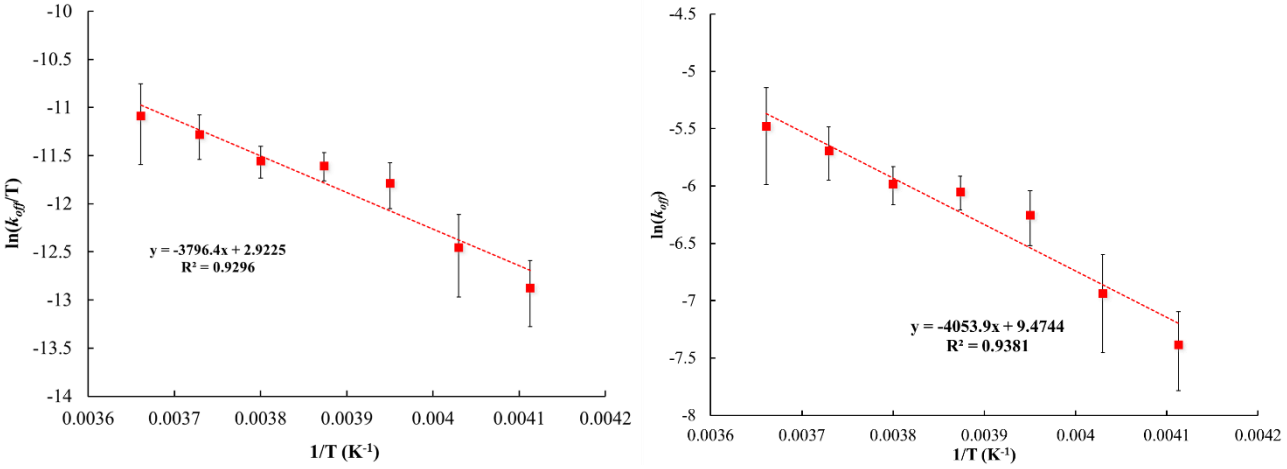

Figure 3.13 Left: Eyring plot for O_2 release from superoxo **2** in MeOH, from which the activation parameters $\Delta H^{\ddagger}$ = 32(4) kJ•mol^{-1} and $\Delta S^{\ddagger}$ = -170(2) J•mol^{-1} K^{-1} were obtained. First order rate constants, k_{off}, were obtained from the intercept of k_{obs} versus [O_2] plots (**Figure 3.4**). **Right:** Arrhenius plot for O_2 release from superoxo **2** in MeOH, from which the activation parameter E_a= 34(4) kJ•mol^{-1} was obtained.

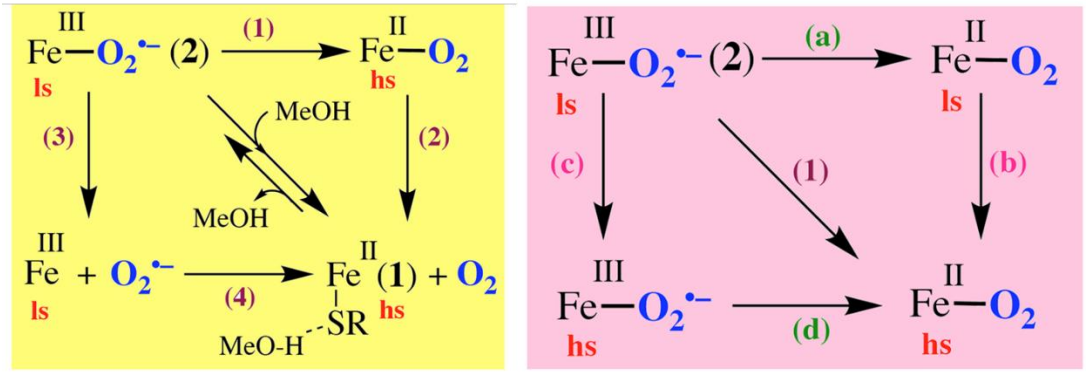

Figure 3.14 Dissecting the steps involved in O_2 release from ferric superoxo **2** to afford reduced 1, into the individual redox and spin-state changes involved, as well as H-bonded MeOH.

reversible nature of O_2 binding in **1** in MeOH is analogous to that observed with thiolate-ligated **5** in MeOH.[16] Activation parameters for O_2 release from superoxo **2** in MeOH ($\Delta H^{\ddagger}$ = 32(4) kJ•mol^{-1}, $\Delta S^{\ddagger}$ = -170(2) J•mol^{-1}K^{-1}, E_a = 34(4) kJ•mol^{-1}) were obtained from Eyring and Arrhenius plots (**Figure 3.13**) and are assembled in **Table 3.1**. The negative entropy of activation for release of O_2 is unexpected given the dissociative nature, unless one considers the requisite spin-state and oxidation state changes, in addition to oxidation state-dependent H-bonding to solvent in reduced **1** versus oxidized **2**. The first two contributions can be broken down into steps as shown in **Figure 3.14**. Steps (**1**) and (**4**) involve electron transfer from $O_2^{\bullet-}$ to Fe^{III} via inner- and outer-sphere mechanisms, respectively. Steps (**2**) and (**3**) involve the dissociation of O_2 or $O_2^{\bullet-}$, respectively, both of which would contribute towards a positive $\Delta S\ddagger$. The relative redox potential of **1** (-400 mV vs SCE)[10] and O_2 in THF (800 mV vs SCE)[15], and the principle of microscopic reversibility would suggest that a pathway involving steps (**3**) then (**4**) is unlikely. Step (**1**) can be broken down further (**Figure 3.14, right**) into sequential steps involving (**a**) electron transfer followed by (**b**) a spin-state change(**Figure 3.14 right**, clockwise), or (**c**) a spin-state change followed by (**d**) an electron transfer (**Figure 3.14 right**, counterclockwise). Step (**c**) would require that the strong antiferromagnetic coupling (J = -450 cm^{-1}, or 5.38 kJ•mol^{-1})[1] between the *S* = 1/2 Fe^{III} ion and *S* = 1/2 $O_2^{\bullet-}$ be broken. We know that a spin-state change is required upon O_2 release to return to the inactivated triplet state, and because **1** is high-spin *S* = 2 (μ_{eff} = 4.69 BM), whereas superoxo **2** contains a low-spin *S* = 1/2 Fe^{III} ion. A more ordered state involving adjusted Fe-L bond lengths is required in preparation for electron transfer. This would contribute to a negative $\Delta S^{\ddagger}$ term that could potentially offset the positive $\Delta S^{\ddagger}$ term typically associated with O_2 dissociation.

3.2.6 Influence of H-bonds on Kinetic Barriers

Contributions from oxidation state-dependent H-bonding to solvent would also affect $\Delta S^{\ddagger}$. The DFT calculated structure (**Figure 3.15, left**), calibrated to the electronic absorption spectrum,

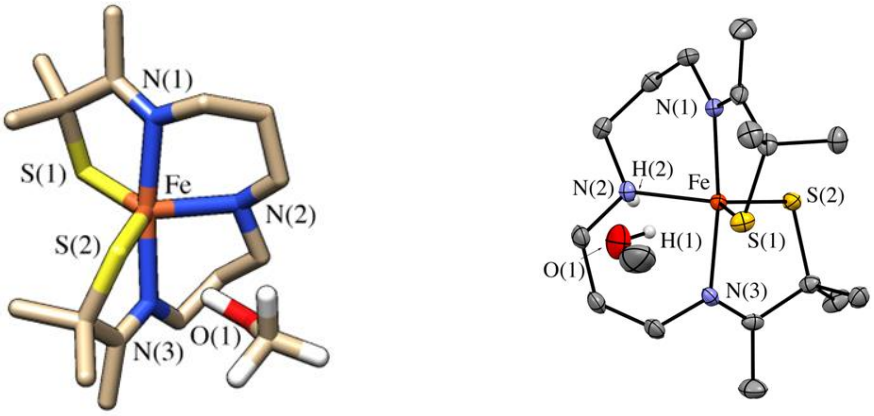

Figure 3.15 Left: DFT optimized structure of $[Fe^{II}(S_2{}^{Me2}N_2N^{H}(Pr,Pr)]$•••H-OMe (**1**) containing a MeOH solvent molecule H-bonded to one of the thiolate sulfurs, S(2). Calculated MeO(1)-H•••S(2) distance is 2.211 Å. **Right:** ORTEP diagram of **1** crystallized from MeOH showing the MeOH that is H-bonded to one of the thiolate sulfurs, S(1).

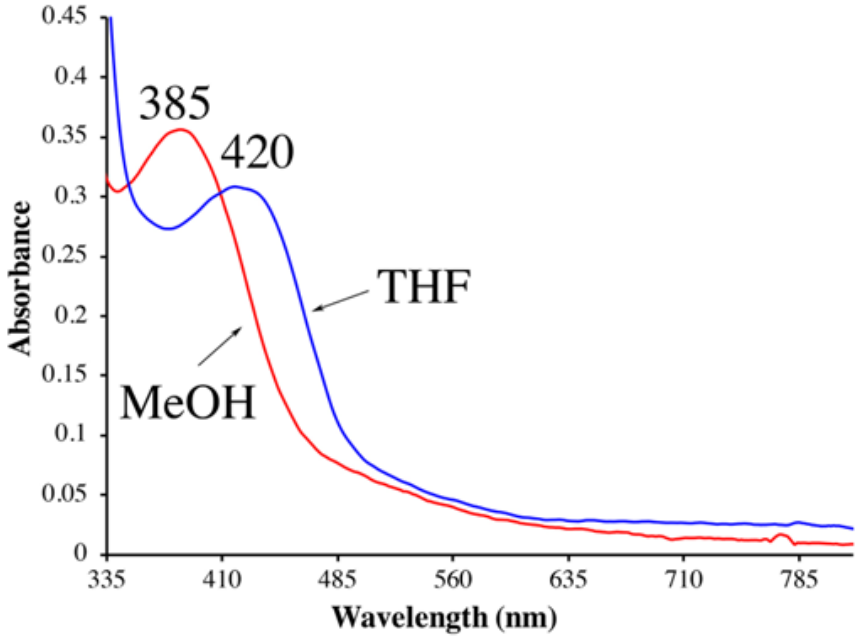

Figure 3.16 H-bonding to MeOH causes the RS→Fe band of reduced **1** (0.238 mM) to blue-shift relative to its energy in THF.

Table 3.3 DFT calculated (using PBE0 functional and def2-TZVP basis set) Mulliken charges for the optimized structure of [$Fe^{II}(S_2{}^{Me2}N_2N^H(Pr,Pr)$] (**1**) in THF and [$Fe^{II}(S_2{}^{Me2}N_2N^H(Pr,Pr)$]•••H-OMe (**1**•••H-OMe), containing a MeOH solvent molecule H-bonded to one of the thiolate sulfurs, S(2) (**1**).

Atom	[$Fe^{II}(S_2{}^{Me2}N_2N^H(Pr,Pr)$] (1)	[$Fe^{II}(S_2{}^{Me2}N_2N^H(Pr,Pr)$]•••H-OMe (1•••H-OMe)
Fe	+0.421	+0.373
S(1)	-0.675	-0.525
S(2)	-0.678	-0.543
N(1)	-0.130	-0.131
N(2)	-0.318	-0.331
N(3)	-0.140	-0.144
O(1)	-----	-0.484
H(1)	-----	+0.277

shows that the thiolate sulfurs of reduced **1** have an average Mulliken charge of -0.676 (**Table 3.3**), whereas the thiolate sulfurs of oxidized superoxo **2** have Mulliken charges of -0.395 and -0.305, for the *trans* RS- and *cis* RS-, respectively (**Table 3.3**). Methanol (MeOH) can potentially H-bond to one of both thiolate sulfurs of **1**. Hydrogen-bonding would be less likely, or involve fewer MeOH molecules, with **2**, given that there is less negative charge on the thiolate sulfurs (-0.676 for **Fe^{II}-1** vs 0.395 for **superoxo-2**). Release of one or more H-bonded MeOH molecules from **1** upon O_2 binding and metal ion oxidation (**Figure 3.14**) would contribute a positive $\Delta S^{\ddagger(\text{solvent release})}$ term that slightly offsets the negative $\Delta S^{\ddagger(\text{O2 binding})}$ term associated with O_2 binding. Conversely, O_2 release from **2** would involve the addition of at least one H-bonding MeOH to **1** (**Figure 3.14**) offsetting the favorable entropy of activation term associated with O_2 release. Evidence to support RS•••H-OMe H-bond in **1** was obtained by crystallizing **1** from MeOH. As shown in the ORTEP diagram of **Figure 3.15, right,** a MeOH sits nestled in the O_2 binding pocket and the MeOH proton, H(1), points towards S(1) with a H(1)•••S(1) distance of 2.318 Å. Previous structures have shown that exogenous ligands such as N_3^- and NO bind to Fe in the pocket that lies opposite to the secondary amine proton,[17,18] H(2), in the more open N(2)-Fe-S(1) angle, thus we

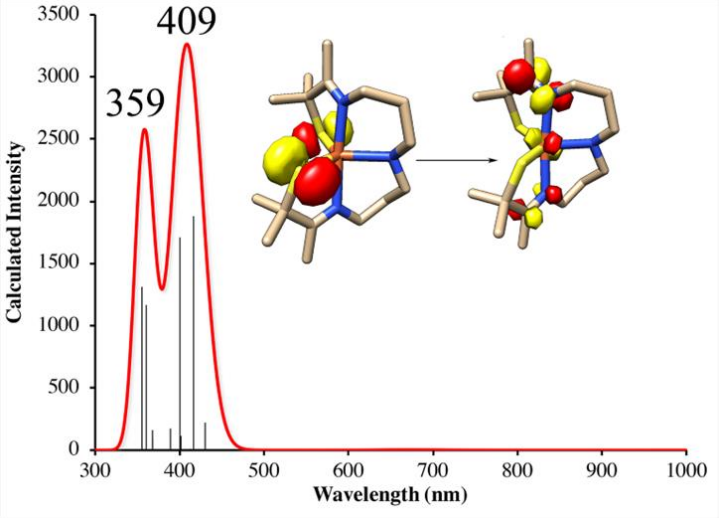

Figure 3.17 Time-dependent DFT (TD-DFT) calculated electronic absorption spectrum for **1** in THF solvent.

refer to this as the O_2 binding site. Additional evidence to support H-bonding to the thiolates of **1** is the observed blue-shift of the RS → Fe charge transfer transitions,[19] from 420 nm in THF to 385 nm in MeOH (**Figure 3.16**). This blue-shift is reproduced in the time-dependent DFT (TD-DFT) calculated electronic absorption spectra in THF (**Figure 3.17**) versus MeOH (**Figure 3.18, left**).

Table 3.4 DFT optimized bond lengths (using the B3LYP functional and def2-TZVP basis set) versus experimental distances for $[Fe^{II}(S_2{}^{Me2}N_2N^H(Pr,Pr)]$•••H-OMe (**1•••H-OMe**) containing a MeOH solvent molecule H-bonded to one of the thiolate sulfurs, S(2).

Bond	Calcd Bond Length (Å)	Exptl Bond Length (Å)
Fe-S(1)	2.316	2.3103(7)
Fe-S(2)	2.341	2.3372(8)
Fe-N(1)	2.176	2.1802(19)
Fe-N(2)	2.217	2.154(2)
Fe-N(3)	2.198	2.153(2)
S(2)•••H	2.211	2.318
O(1)-H	0.985	0.840
τ	0.79	0.76

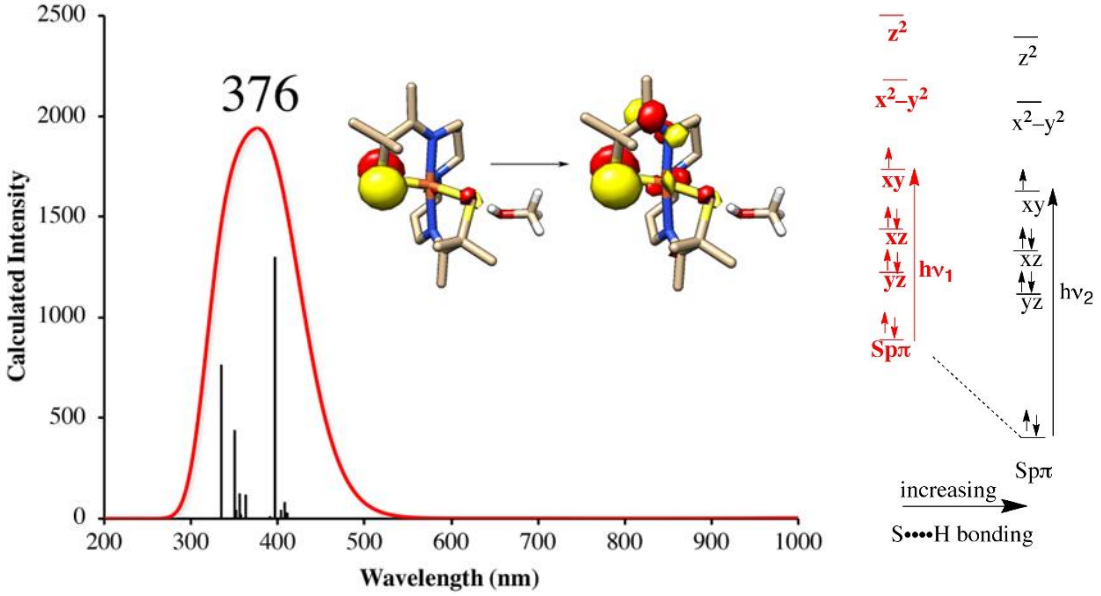

Figure 3.19 Left: Time-dependent DFT (TD-DFT) calculated electronic absorption spectrum for [$Fe^{II}(S_2{}^{Me2}N_2N^H(Pr,Pr)$]•••H-OMe (**1**) containing a MeOH solvent molecule H-bonded to one of the thiolate sulfurs, showing that H-bonding causes the S→Fe charge transfer band to blue shift relative to that shown in **Figure 3.17**. **Right**: Influence of H-bonds on the the **π**-symmetry sulfur orbitals and the RS→Fe^{II} charge transfer (CT) band.

The blue-shift can be explained by the decrease in Mulliken charge on the sulfurs (-0.676 in THF to -0.525 in MeOH (**Table 3.3**)) according to the calculate structure for **1**•••HOMe (**Figure**

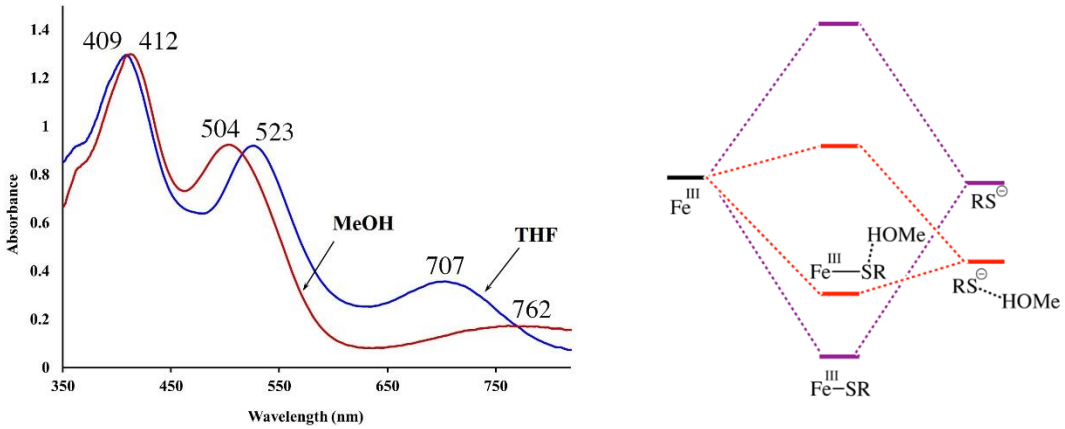

Figure 3.18 Left: Electronic absorption spectrum of Fe^{III}-superoxo **2** (0.25 mM) in THF vs MeOH. **Right:** Influence of H-bonds on the energy of the **π**-symmetry sulfur orbitals and the stabilization of the resulting Fe^{III}-SR (purple) versus H-bonded Fe^{III}-SR bonds (red).

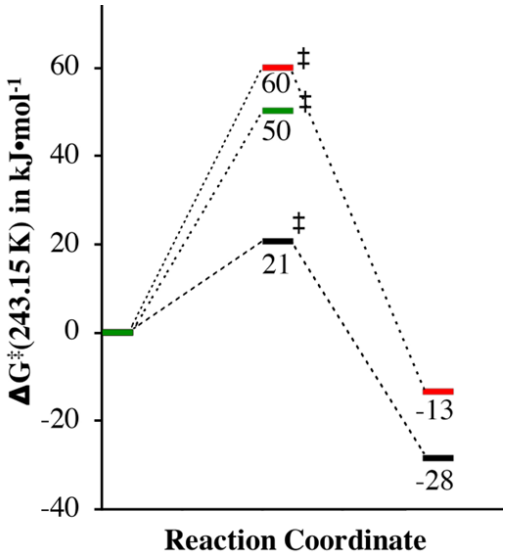

Figure 3.20 Comparison of the barrier to O_2 binding to **1** in THF (green) and MeOH (red) and **5** in MeOH (black), as well as the release of O_2 from **2** and **6** in MeOH.

3.15,left), and reflects the stabilization of the Fe-SR molecular orbitals involved in the RS → Fe charge transfer band (**Figure 3.18, right**).[19] The DFT optimized RS•••H-OMe distance is 2.211 Å with the MeOH H-bonded to one of the sulfurs (**Table 3.4**). The ramifications of this on the kinetic barrier to O_2 and release are significant (*vide infra*).

Table 3.5 Dependence of Activation Parameters on Solvent and Ligand Constraints.

Reaction	$\Delta G^{\ddagger}$(243.15K, kJ•mol^{-1})	$\Delta H^{\ddagger}$ (kJ•mol^{-1})	$\Delta S^{\ddagger}$ (J•mol^{-1}K^{-1})	Solvent	$\Delta\phi$*
1 + O_2	50(1)	19.3(8)	-127(4)	THF	19.5°
1 + O_2	60(3)	30(2)	-123(7)	MeOH	19.5°
5 + O_2	21(2)	34(150	55(68)	MeOH	N/A
3 + KO_2	49(1)	34.3(9)	-60(4)	THF	25°
O_2 dissociation from **2**	73(4)	32(4)	-170(2)	MeOH	19.5°
O_2 dissociation from **5**	49(7)	15(5)	-140(20)	MeOH	N/A

*$\Delta\phi$ is defined as the difference in helical twist angle, ϕ, between the reactant and the product formed in the reaction listed. The helical twist angle, ϕ, is defined as the angle separating the least squared plane containing the Fe center, the two carbons flanking the equatorial nitrogen, N(2), and the equatorial nitrogen (C(6)N(2)C(7)Fe) from the mean plane containing N(1)FeN(3)

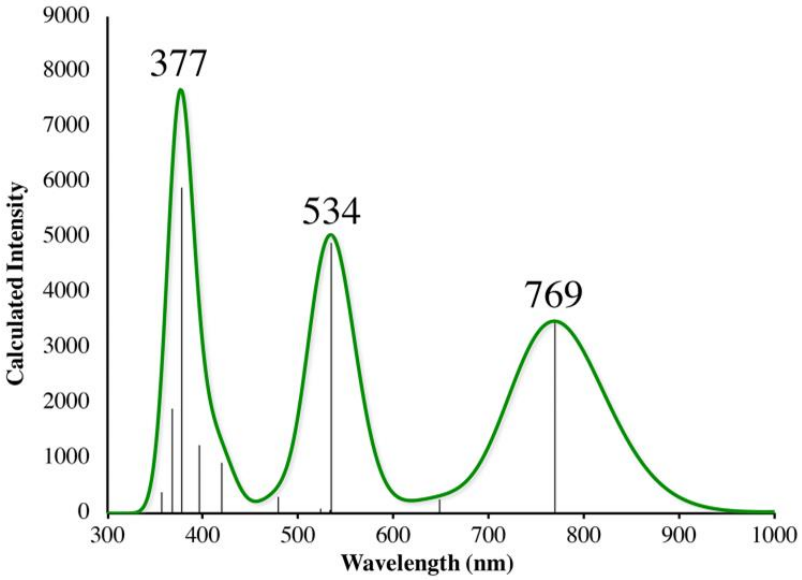

Figure 3.21 TD-DFT calculated spectrum (of superoxo complex $[Fe^{III}(S_2{}^{Me2}N_2N^H(Pr,Pr)(O_2)]^+$ (**2**) in MeOH using a polarizable MeOH continuum model. The calculated 534 nm (18,727 cm^{-1}) band is blue shifted by 741 cm^{-1} relative to the TD DFT calculated band at 556 nm (17,986 cm^{-1}) in THF.[1]

Thiolates have previously been shown by the Solomon group to lower the activation barrier to O_2 binding to Fe^{II} site of IPNS.[20] Thiolates have also been shown by our group to form highly covalent Fe^{III}-SR bonds[21] thereby stabilizing oxidized products such as **2**,[1,16] and any transition states with developing Fe^{III}-SR character. If, on the other hand, the thiolate sulfur is involved in H-bonding to a protic solvent, in this case MeOH),[19] then the incipient Fe^{III}-SR bond of the transition-state would be less stable than it would be otherwise **Figure 3.19**, resulting in slower

reaction rates as is experimentally observed with O_2 addition to **1** in MeOH (**Table 3.1**). This is consistent with the experimentally measured free energy of activation, $\Delta G^{\ddagger}$, for dioxygen binding to **1** in MeOH (60(3) kJ•mol^{-1}) versus THF (50(1) kJ•mol^{-1} at 243.15 K, which is 10 kJ•mol^{-1} higher in the protic solvent (**Figure 3.19, Table 3.5**), and is caused by the poor energy match between a thiolate sulfur that is engaged in H-bonding and the Fe^{III} d-orbitals (**Figure 3.20, right**). Evidence to support H-bonding to the thiolates of **2** is observed blue-shift of the RS → Fe charge transfer transition,[19] from 523 nm in THF to 504 nm in MeOH (**Figure 3.20, left**). This is in good agreement with the TD-DFT calculated blue shift of 7.41 nm (**Figure 3.21**) and is significantly smaller than what is observed with **1** implying that H-bonding play a less significant role with oxidized superoxo **2**.

3.2.7 Influence of Ligand Constraints on Kinetic Barriers

Comparison of the free energy of activation, $\Delta G^{\ddagger}$(243.15 K), for O_2 release from superoxo **2** (73(4) kJ•mol^{-1}) in MeOH at 243.15 K **Table 3.5** relative to that for $[Fe^{III}(S^{Me2}N_4(tren))(O_2)]^+$ (**5**, **Scheme 3.3**, 49(7) kJ•mol^{-1})[16] under the same conditions, we find that the barrier to O_2 release is

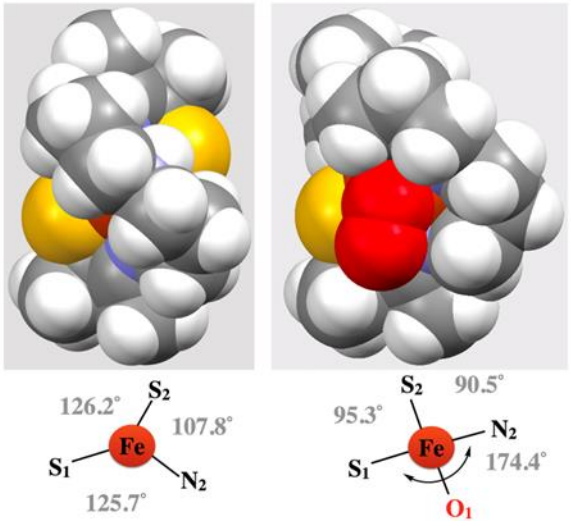

Figure 3.22 Space-filling depiction of the crystallographic structure of **1** versus the DFT calculated structure of superoxo-bound **2** showing the extensive reorganizational barrier caused by the single chain ligand backbone.

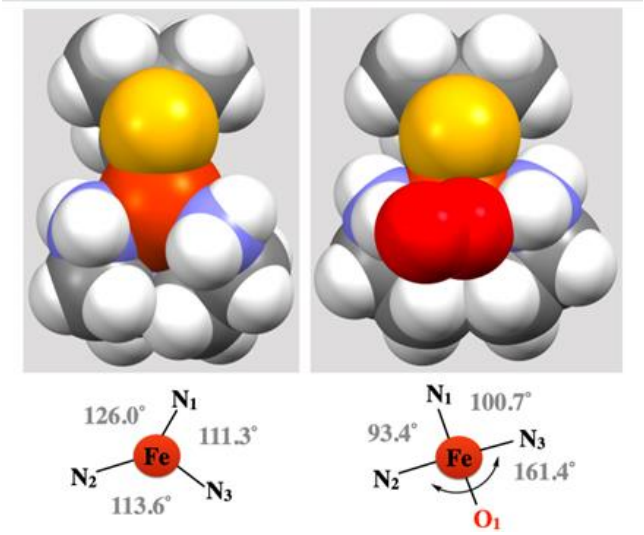

Figure 3.23 Space-filling depiction of the crystallographic structure of **5** versus the DFT calculated structure of superoxo-bound **6** showing the minimal ligand rearrangement required to bind and release O_2 given the less constraining ligand.

24 kJ•mol^{-1} higher for **2**. This likely reflects ligand constraints[17,22,23] **Figure 3.22** and the ligand rearrangement required to form the transition-state necessary for O_2 release. The multidentate ligand of **1** and superoxo **2** consists of a single chain that wraps around the metal ion in a helical fashion **Figure 3.22**.[25] Even minor angle changes at the metal ion in preparation for O_2 release translate into significant unwinding of the single chain ligand backbone. This reorganizational barrier would be mostly entropic in nature. The entropy of activation for O_2 binding to **1** in MeOH ($\Delta S^{\ddagger}$ = -123(7) J•mol^{-1}K^{-1}), is 178 J•mol^{-1}K^{-1} less favorable than for O_2 binding to **5** (+55(68) J•mol^{-1}K^{-1}).[16] This factor dominates and is responsible for the large differences in $\Delta G^{\ddagger}$. The lower

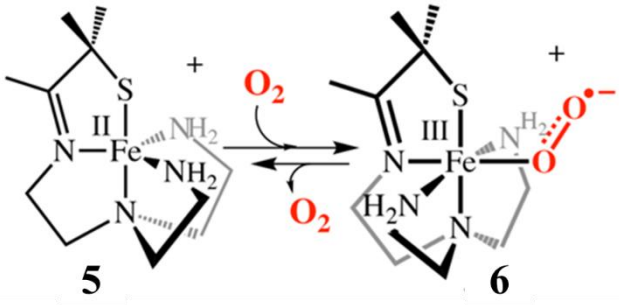

Scheme 3.3 Fe^{II} **5** reacts with dioxygen to form a short lived Fe^{III}-superoxo **6** in MeOH.[15]

barrier for O_2 release from **6**, relative to **3**, likely reflects its less constraining tripodal ligand with its three independent arms **Figure 3.23**, **Scheme 3.2**. This is also reflected in the free energy of activation for dioxygen binding to **1** in MeOH at 243.15 K (60(3) kJ•mol^{-1}), $\Delta G^{\ddagger}$(243.15 K), versus $[Fe^{II}(S^{Me2}N_4(tren))]^+$ (**5**, **Scheme 3.3**, 21(2) kJ•mol^{-1}) in the same solvent,[16] which is 39 kJ•mol^{-1} higher **Figure 3.19** for the more constrained helical ligand of **1**.

3.2.8 Understanding Why the Kinetic Barrier to O2•- Binding is Higher than the Kinetic Barrier to O2 Binding

Given that oxidized **3** is cationic, one might expect electrostatic attraction to lower the barrier to $O_2^{\bullet-}$ binding to **3,** relative to O_2 binding to neutral **1** (**Figure 3.24**). This likely would be the case, if it weren't for the oxidation state-dependent ligand constraints imposed by the single chain helical ligand.[16,23] With five-coordinate **3**, the helical twist is "tighter" relative to five-coordinate **1** due to

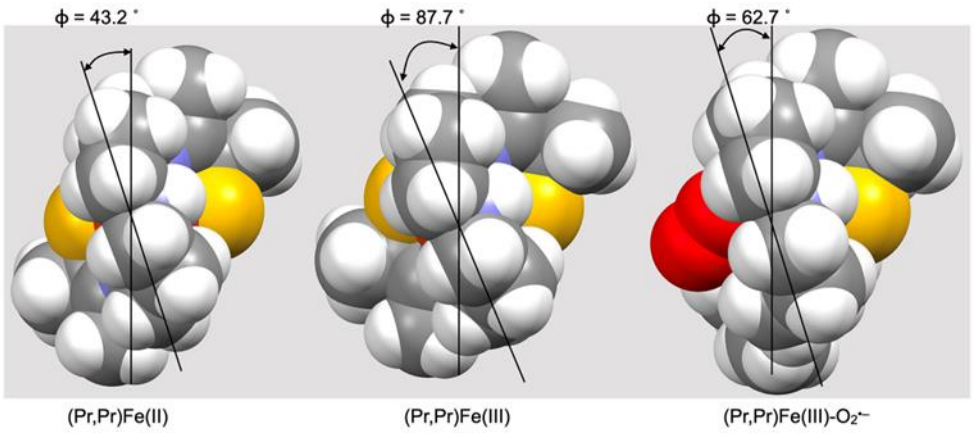

Figure 3.24 Space-filling models generated from the crystallographically-determined structure of **1** (left) and **3** (middle), and the DFT-optimized geometry of **2** (right) displaying differences in the helical wrapping angle, ϕ, and the larger amount of structural rearrangement required for $O_2^{\bullet-}$ binding to **3**.

the shorter Fe^{III}-L bond lengths. The bond lengths expand upon binding a sixth ligand.[17] This difference can be quantified by comparing the helical twist angle, ϕ **Figure 3.24**.[23] The angle phi

is defined as the angle separating the least squared plane containing the Fe center, the two carbons flanking the equatorial nitrogen, N(2), and the equatorial nitrogen (C(6)N(2)C(7)Fe) from the

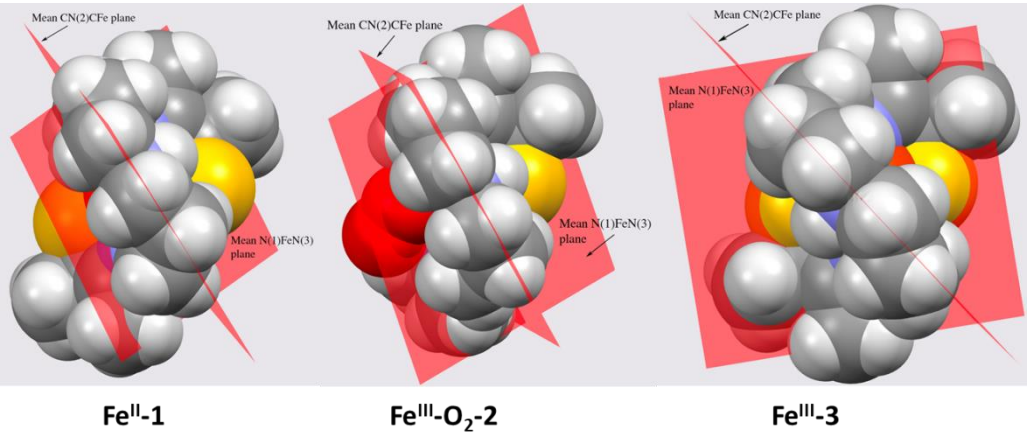

Figure 3.25 Defining the mean CN(2)CFe plane and the mean plane containing N(1)FeN(3) for Fe^{II}-**1** (left), Fe^{III}-superoxo **2** (middle), and Fe^{III}-**3** (right).

mean plane containing N(1)FeN(3) (**Figures 3.25**). One can see in **Figure 3.24**, that the twist angle increases, and the ligand wraps more tightly around the metal ion, when O_2 binds to Fe^{II} causing the oxidation to Fe^{III} and a decrease in metal-ligand bond lengths. In contrast, the twist angle decreases, and the ligand partially uncoils when $O_2^{\bullet-}$ binds to **Fe^{III}-3** (**Figure 3.24**). The change to this angle is larger for **Fe^{III}-3 → Fe^{III}-O$_2^{\bullet-}$-2** (87.7 ° - 62.7 ° = 25 °) relative to **Fe^{II}-1 → Fe^{III}-O$_2^{\bullet-}$-2** (62.7 ° - 43.2 ° = 19.5 °). This translates into a larger reorganizational barrier for the KO_2 + **3** reaction relative to the O_2 + **1** reaction (**Figure 3.24**; **Table 3.5**).

3.3 Conclusion

Low-temperature stopped-flow kinetics have been used to determine the most likely mechanism, and reversibility of O_2 binding to [$Fe^{II}(S_2{}^{Me2}N_2N^H(Pr,Pr)$] (**1**) to afford a well-characterized, reactive, thiolate-ligated ferric superoxo compound, [$Fe^{III}(S_2{}^{Me2}N_2N^H(Pr,Pr)(O_2)$] (**2**).[1] Thiolates have been previously shown to increase the oxidative potency of iron superoxo and high-valent iron oxo compounds, and their ability to cleave strong C-H bonds.[1,16,24] These

exceptional properties are critical in the biosynthesis of β-lactam antibiotics by isopenicillin N synthase (IPNS). The complexity of O_2 binding to **1** and O_2 release from **2** was analyzed in terms of contributions from requisite spin-state changes and electron transfer steps, in addition to oxidation state-dependent H-bonding to solvent. Comparison of the kinetics of formation of **2** via the addition of KO_2 to oxidized $[Fe^{III}(S_2{}^{Me2}N_2N^H(Pr,Pr)]^+$ (**3**) versus the addition of O_2 to **1** provided evidence for a mechanism involving O_2 binding to Fe^{II} followed by inner-sphere electron transfer, as opposed to outer-sphere electron transfer followed by $O_2^{\bullet-}$ binding. Dioxygen was shown to bind two orders of magnitude more slowly to **1** in MeOH, relative to THF, and to bind reversibly to **1** in MeOH, but irreversibly in THF. Dissociation rate constants, k_{off}, in MeOH were obtained from the intercept of a k_{obs} versus $[O_2]$ plot. The kinetic barrier to O_2 binding was shown to be 10 kJ mol^{-1} higher in MeOH relative to THF, indicating that the transition-state is destabilized in the presence of H-bond donors. Evidence for H-bonding to the thiolate sulfur of **1** was obtained via the presence of a MeOH with an H(1)••••S(1) distance of 2.318 Å when **1** is crystallized from MeOH, and an observed blue-shift (by 21.64 nm) of the RS→Fe charge transfer transition in THF relative to MeOH. Oxidation state-dependent ligand constraints imposed by the single chain helical ligand of **1** and **3** were also shown to dramatically influence O_2 binding kinetics, relative to previously reported thiolate-ligated $[Fe^{II}(S^{Me2}N_4(tren))]^+$ (**5**)[17] which contains a tripodal ligand with three independent arms. Constraints were quantified by comparing the helical twist angle, ϕ, for **1**, **2**, and **3**. The twist angle was shown to increase as the ligand wraps around the metal ion more tightly in response to oxidation of the metal ion, i.e., **Fe^{II}-1→ Fe^{III}-3**, and decrease in response to the partial uncoiling that occurs when a sixth ligand binds and **3** is converted to **2**. The change in twist angle, $\Delta\phi$, was shown to be larger for the conversion of **3** to

2 (25˚), than for the conversion of **1** to **2** (19.5˚), thus explaining the larger kinetic barrier to KO_2 binding to **3.**

3.4 Experimental Details

3.4.1 General Methods

Reagents purchased from commercial vendors were of the highest purity available and used without further purification. [$Fe^{II}(S_2{}^{Me2}N_2N^H(Pr,Pr)$] (**1**) and [$Fe^{III}(S_2{}^{Me2}N_2N^H(Pr,Pr)]BF_4$ (**3**) were synthesized as previously described.[1,17] Methanol (MeOH) was distilled over magnesium turnings and iodine and degassed prior to use. Un-stabilized tetrahydrofuran (THF) was rigorously degassed and purified using solvent purification columns housed in a custom stainless-steel cabinet, dispensed via a stainless steel Schlenk line (GlassContour). All manipulations were performed using Schlenk line techniques or under an N_2 atmosphere in a glovebox.

3.4.2 Evans Method of [$Fe^{II}(S_2{}^{Me2}N_2N^H(Pr,Pr)$] (1)

^{1}H-NMR spectra were recorded on Bruker AV 301 FT-NMR spectrometers and are referenced to residual protio-solvent. Chemical shifts are reported in ppm. The magnetic moment of **1** was determined to be μ_{eff} = 4.69 B.M (MeOH), and μ_{eff} =4.08 B.M. (THF) using the Evans method.

3.4.3 Kinetic Measurements

Solutions were prepared in a N_2-filled anaerobic glove-box ([O_2] <1 ppm) and placed in Hamilton gastight® syringes equipped with three-way valves. Time-resolved spectra (350−820 nm) were acquired at low temperatures using a TgK Scientific (U.K.) CSF-61DX2 Multi-Mixing CryoStopped-Flow Instrument equipped with a tungsten visible light source. The stopped-flow instrument is equipped with PEEK tubing fitted inside stainless-steel plumbing, a 1.00 cm^3 quartz mixing cell, and an anaerobic kit purged with an inert gas. The temperature in the mixing cell was

maintained to ± 0.1 °C, and the mixing time was 2-3 ms. All flow lines of the instrument were extensively washed with degassed, anhydrous THF before charging the driving syringes with solutions containing the reactants. The reactions were studied by rapid scanning spectrophotometry under pseudo-first order conditions with excess oxygen or superoxide. Saturated solutions of O_2 were prepared as described below. The O_2 concentration was assumed not to change upon cooling, given that the system is closed, and the solutions were not in contact with the gas phase (small variations in the solvent density were not taken into account). Dilutions of the O_2-saturated solvent were performed anaerobically to obtain the desired [O_2]. Potassium superoxide solutions were prepared as described below. All concentrations reported in stopped-flow experiments refer to the "after mixing" conditions. Experiments were performed in single-mixing mode, with a 1:1 (v/v) mixing ratio. A series of three or four measurements gave an acceptable standard deviation (within 10%). Rates reported for the oxygen dependence are the average of at least three different experiments. Data analysis was performed with Kinetic Studio software from TgK Scientific.[33] Data was fit at a single wavelength (523.5 nm) using the following equation:

$$A_t = A_\infty - (A_\infty - A_0)e^{-k_{obs}t}$$

The reaction order with respect to O2 was determined by varying the O_2 concentration over the range of 1.975 mM to 3.95 mM in THF, and 2.55 mM to 4.25 mM in MeOH, while maintaining a constant Fe^{II} concentration of 0.1 mM.

Kinetics for the formation of superoxo-2 via an alternate route involving KO_2 + Fe^{III}-3 were monitored at λ = 523 nm under pseudo first order conditions with excess KO_2, 1 mM to 5 mM (solubilized with KryptofixR 222) using a TgK stopped-flow instrument and CCD detector.

Constant ionic strength or 10 mM conditions were maintained by adding an appropriate amount of Bu4NPF6. Kinetics traces were fit to the single exponential of **Eq 1** with very small residuals.

3.4.4 Grubb's Test Calculation

Trial	Value	Grubbs	Excluded
1	0.30294	1.440468	
2	0.29614	0.068387	
3	0.29844	0.441961	
4	0.29326	0.707431	
5	0.291461	1.106611	
6		65.77898	
7		65.77898	
8		65.77898	
9		65.77898	
10		65.77898	
Average	0.296448		
Std dev	0.004507		
95% CI	0.005596		
T	2.776445		
count	5		

Count	Grubb value 0.05
3	1.153
4	1.463
5	1.672
6	1.822
7	1.938
8	2.032
9	2.11
10	2.176

Figure 3.26 Example of a Grubb's test calculation in Excel, using a 5-point data set and a Grubb's confidence level of 95%.

The Grubb's test is a statistical method to find a single outlier in a normally distributed data set. The test only finds a single outlier in the data set; once found, the outlier is removed, and the data set compared to the critical G-value determined for the data set. To start, calculate the average, standard deviation, and the population of the data set, **Figure 3.26**. The Grubb's value for each point is calculated by taking the absolute value of the average minus the value divided by the standard deviation. The Grubb's value for each data point is then compared to the known Grubb's values for a specific count and difference confidence intervals, in this case for 5% for a count of 5 is a Grubb's value of 1.672. Since all of the data points individual Grubb's values fall below the 1.672, none of the data points are excluded and included in a 95% confidence interval.

3.4.5 Preparation of Saturated Dioxygen Solutions

Degassed solvent (THF or MeOH) was added to a round bottom flask fitted with a septum cap under a nitrogen atmosphere in the glovebox. Dry O_2 (from a gas cylinder) was bubbled through

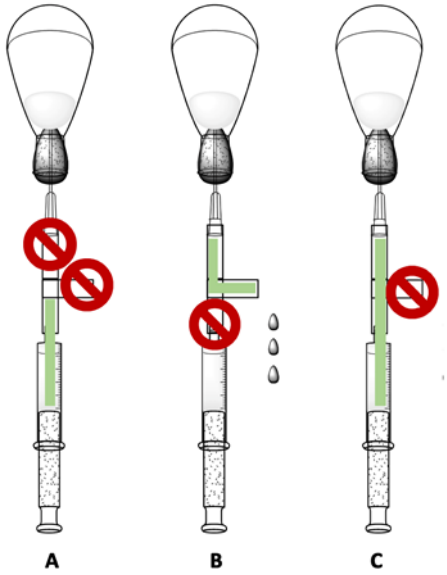

the solvent at 1 atm for 15 min. The solution was then allowed to equilibrate over 15 minutes at 25 °C in a temperature-controlled water bath. To load the syringe, the flask containing O_2 saturated THF or MeOH was inverted, and a gastight syringe equipped with a 3-way valve and needle was inserted through the septum (**Position A** in the Figure to the right). The valve was then turned to allow the saturated solution to flow through the open arm of the 3-way valve, leaving no headspace in the needle (**Position B**). The valve was then closed, and the dioxygen solution drawn into the syringe (**Position C**). The concentration of O_2 was taken as 8.5 mM in MeOH, and 7.9 mM in THF both at 25 °C.[12,13] Dilutions of the O_2-saturated solvent were performed anaerobically as described above with a prefilled syringe of solvent to obtain the desired [O_2].

3.4.5 Dilution of Dioxygen Solutions

Dilutions of the O_2-saturated solvent were performed anaerobically by attaching a second syringe filled with an excess of an appropriate

quantity of deoxygenated solvent to the open arm of the 3-way valve (**Position D** in Figure below). Air bubbles trapped in the valve by this process were purged by flowing the excess solvent through the needle down to the quantity of solvent necessary for the desired O_2 concentration (**Position E**). The valve was then turned to allow the two needles to communicate, and the saturated O_2 solution was drawn into the deoxygenated solvent until the desired O_2 concentration is met (**Position F**). The dilute O_2 solution was then allowed to equilibrate for 30 min after which time it was ready for

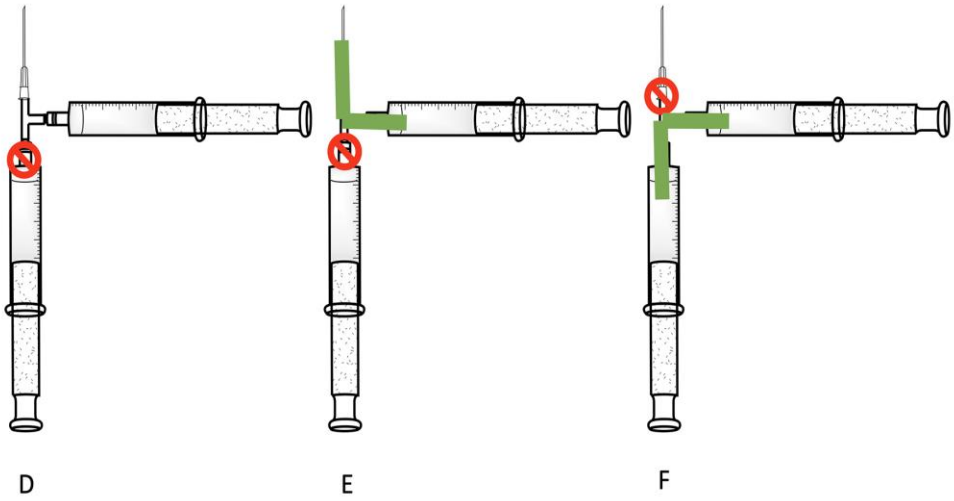

use. This dilution process can be repeated in the same manner if it is not practical to attain the desired O_2 concentration via one dilution.

3.4.6 Preparation of Potassium Superoxide Solutions

A very fine powder of KO_2 was weighed out on an analytical balance, and then 1 eq. of Kyrptofix®222 was added to solubilize the KO_2 in THF and vigorously stirred at RT in a glovebox for at least 20 mins and used within 6 hours of preparation. An appropriate amount of Bu_4NPF_6

([Bu_4NPF_6] = 11.8 – 17.8 mM (pre-mix concentrations)) weighed out on an analytical balance, was added to maintain a constant ionic strength of 10 mM (post-mix concentration).

3.4.7 Computational Details

Calculations were performed using the ORCA v. 4.2.1 quantum chemistry package developed by Neese and coworkers,[25] and employed a polarized triple-zeta def2-TZVP basis set, the def2/J auxiliary basis set for Coulomb fitting, and the atom-pairwise dispersion correction of Grimme (D3BJ).[26] Tight convergence criteria were required for self-consistent field (SCF) solutions. The Grid4 (GridX4) integration grid size, and the conductor-like polarizable continuum model with the dielectric constant $\varepsilon = 7.25$ for tetrahydrofuran solvent (CPCM(THF)), or the dielectric constant $\varepsilon = 32.63$ for methanol solvent (CPCM(MeOH)), were used for geometry optimizations.[27] Geometry optimizations and analytical frequency calculations were performed using the PBE0 functional, with the resolution of identity (RI) chain-of-spheres (RIJCOSX) approximation,[28,29] and initiated from the crystallographic coordinates when available. Analytical frequency calculations were performed on all optimized structures to determine whether the obtained stationary points corresponded to local minima.

Calculations for the Fe^{III}-superoxo complex, $[Fe^{III}(S_2{}^{Me2}N_3(Pr,Pr)(O_2)]^+$ (**2**) employed the broken-symmetry formalism to model coupled paramagnetic sites. The previously reported[1] DFT optimized structure of superoxo $[Fe^{III}(S_2{}^{Me2}N_3(Pr,Pr))(O_2)]$ (**2**) was used as a starting point for the calculated structure in a polarizable continuum model in MeOH. Hybrid time-dependent DFT (TD-DFT) calculations employed the RIJCOSX and the Tamm-Dancoff approximations (TDA).[30,31] The Fermi level, i.e., the halfway between the calculated HOMO and LUMO energies, was set to 0 eV in molecular orbital (MO) analysis. Excited states from TD-DFT calculations were analyzed using Natural Transition orbitals (NTOs) and by visualizing their

difference densities between the ground and excited states. Canonical molecular orbital isosurfaces and natural transition orbitals in the TD-DFT calculations were visualized at an isovalue of 0.05 a_0^3 using UCSF Chimera.[32]

3.5 Chapter 3 References

(1) Blakely, M. N .; Dedushko, M. A.; Poon, P. C. Y.; Villar-Acevedo, G.; Kovacs, J. A. , Formation of a Reactive, Alkyl Thiolate-Ligated FeIII-Superoxo Intermediate Derived from Dioxygen. *J. Am. Chem. Soc.* **2019,** *141*, 1867-1870. DOI: 10.1021/jacs.8b12670

(2) Fischer, A. A.; Lindeman, S. V.; Fiedler, A. T., A synthetic model of the nonheme iron–superoxo intermediate of cysteine dioxygenase. *Chem. Comm.* **2018,** *54*, 11344-11347. DOI: 10.1039/C8CC06247A

(3) Hong, S.; Sutherlin, K. D.; Park, J.; Kwon, E.; Siegler, M. A.; Solomon, E. I.; Nam, W., Crystallographic and spectroscopic characterization and reactivities of a mononuclear non-haem iron(III)-superoxo complex. *Nature Comm.* **2014,** *5*, 5440-5446. DOI: 10.1038/ncomms6440

(4) Chiang, C. -W.; Kleepsies, S. T.; Stout, H. D.; Meier, K. K.; Li, P. -Y.; Bominaar, E. L.; Que, L., Jr.; Munck, E.; Lee, W. -Z., Characterization of a Paramagnetic Mononuclear Nonheme Iron- Superoxo Complex. *J. Am. Chem. Soc.* **2014,** *136*, 10846-10849. DOI: 10.1021/ja504410s

(5) O'ddon, F.; Chiba, Y.; Nakazawa, J.; Ohta, T.; Ogura, T.; Hikichi, S., Characterization of Mononuclear Non-heme Iron(III)-Superoxo Complex with a Five-Azole Ligand Set. *Angew. Chem. lnt. Ed.* **2015,** *54*, 7336-7339. DOI: 10.1002/anie.201502367.

(6) Winslow, C.; Lee, H. B.; Field, M. J.; Teat, S. J.; Rittle, J., Structure and Reactivity of a High-Spin, Nonheme Iron(III)- Superoxo Complex Supported by Phosphinimide Ligands. *J. Am. Chem. Soc.* **2021,** *143*, 13686-13693. DOI: 10.1021/jacs.1c05276

(7) Hong, S.; Sutherlin, K. D.; Park, J.; Kwon, E.; Siegler, M. A.; Solomon, E. I.; Nam, W. A mononuclear nonheme iron(III)-superoxo complex: Crystallographic and spectroscopic characterization and reactivities. *Nat. Commun*. **2014**, 5 (25), 7336–7339. DOI: 10.1038/ncomms6440.

(8) Fischer, A. A.; Lindeman, S. V.; Fiedler, A. T. A Synthetic Model of the Nonheme Iron–Superoxo Intermediate of Cysteine Dioxygenase. *Chem. Commun*. **2018**, 11344–11347. DOI: 10.1039/C8CC06247A.

(9) Gordon, J. B.; Vilbert, A. C.; Siegler, M. A.; Lancaster, K. M.; Goldberg, D. P.; Moe, P.; Moënne-Loccoz, P.; Goldberg, D. P. A Nonheme Thiolate-Ligated Cobalt Superoxo Complex: Synthesis and Spectroscopic Characterization, Computational Studies, and Hydrogen Atom Abstraction Reactivity. *J. Am. Chem. Soc*. **2019**, 141 (8), 3641–3653. DOI: 10.1021/jacs.8b13134

(10) Villar-Acevedo, G.; Lugo-Mas, P.; Blakely, M. N.; Rees, J. A.; Ganas, A. S.; Hanada, E. M.; Kaminsky, W. Kovacs, J. A. Metal-Assisted Oxo Atom Addition to an Fe(III) Thiolate. *J. Am. Chem. Soc.* **2017**, 139, 1, 119-129, DOI: 10.1021/jacs.6b03512

(11) Espenson, J. H. *Chemical Kinetics and Reaction Mechanisms*; McGraw-Hill Book Company: New York, **1981**.

(12) Kryatov, S. V. ; Rybak-Akimova, E. V.; Schindler, S., Kinetics and Mechnisms of Formation and Reactivity of Non-heme Iron Oxygen Intermediates. *Chem. Rev.* **2005,** *105,* 2175-2226. DOI: 10.1021/cr030709z

(13) Battino, R.; Clever, H. L.; Young, C. L., *Oxygen and Ozone*. Elsevier: 1981; Vol. 7, p xiii–xviii.

(14) Grubbs, Frank E., Procedures for Detecting Outlying Observations in Samples. *Technometrics* **1969,** *11* (1), 1-21, DOI: 10.1080/00401706.1969.10490657

(15) Dedushko, M. A.; Pikul, J.; Kovacs, J. A., Superoxide Oxidation by a Thiolate-ligated Iron Complex and Anion Inhibition. *Inorg. Chem.* **2021,** *60*, 7250-7261. DOI: 10.1021/acs.inorgchem.1c00336

(16) Dedushko, M. A.; Greiner, M. B.; Downing, A. N.; Coggins, M. K.; Kovacs, J. A., Electronic Structure and Reactivity of Dioxygen-Derived Thiolate-Ligated Fe-Peroxo and Fe(IV) Oxo Compounds. *J. Am. Chem. Soc.* **2022,** *144* (19), 8515-8528. DOI: 10.1021/jacs.1c07656

(17) Ellison, J. J.; Nienstedt, A.; Shoner, S. C.; Barnhart, D.; Cowen, J. A., Kovacs, J. A., Reactivity of Five-Coordinate Models for the Thiolate-Ligated Fe Site of Nitrile Hydratase. *J. Am. Chem. Soc.* **1998,** *120* (23), 5691-5700. DOI: 10.1021/ja973129q

(18) Schweitzer, Dirk; Ellison, Jeffrey J.; Shoner, Steven C.; Lovell, Scott; Kovacs, Julie A., A Synthetic Model for the NO-Inactivated Form of Nitrile Hydratase. *J. Am. Chem. Soc.* **1998,** *120* (42), 10996-10997. DOI 10.1021/ja973129q:

(19) Jackson, H. L.; Shoner, S. C.; Rittenberg, D.; Cowen, J. A.; Lovell, S.; Barnhart, D.; Kovacs, J. A., Probing the Influence of Local Coordination Environment on the Properties of Fe-Type Nitrile Hydratase Model Complexes. *Inorg. Chem.* **2001,** *40* (7), 1646-1653. DOI: 10.1021/ic001271d

(20) Brown, C. D.; Neidig, M. L.; Neibergall, M. B.; Lipscomb, J. D.; Solomon, E. I., VTVH-MCD and DFT Studies of Thiolate Bonding to {FeNO}7/{FeO2}8 Complexes of Isopenicillin N Synthase: Substrate Determination of Oxidase versus Oxygenase Activity

in Nonheme Fe Enzymes. *J. Am. Chem. Soc.* **2007,** *129* (23), 7427-7438. DOI: 10.1021/ja071364v

(21) Kennepohl, P. ; Neese, F.; Schweitzer, D.; Jackson, H. L.; Kovacs, J. A; Solomon, E. I., Spectroscopy of Non-Heme Iron Thiolate Complexes: Insight into the Electronic Structure of the Low-Spin Active Site of Nitrile Hydratase. *Inorg. Chem.* **2005,** *44*, 1826-1836. DOI: 10.1021/ic0487068

(22) Schweitzer, D.; Shearer, J.; Rittenberg, D. K.; Shoner, S. C.; Ellison, J. J.; Loloee, R.; Lovell, S.; Barnhart, D.; Kovacs, J. A., Enhancing reactivity via structural distortion. *Inorganic chemistry* **2002,** *41* (12), 3128-36. DOI: 10.1021/ic0109187

(23) Guo, Cunlan; Yu, Jingxian; Horsley, John R.; Sheves, Mordechai; Cahen, David; Abell, Andrew D., Backbone-Constrained Peptides: Temperature and Secondary Structure Affect Solid-State Electron Transport. *The Journal of Physical Chemistry B* **2019,** *123* (51), 10951-10958. DOI: 10.1021/acs.jpcb.9b07753

(24) Green, M. T., C–H bond activation in heme proteins: the role of thiolate ligation in cytochrome P450. *Curr. Op. Chem. Biol.* **2009,** *13,* 84-88. DOI: 10.1016/j.cbpa.2009.02.028

(25) Neese, Frank. Software update: The ORCA program system – Version 5.0. *WIREs Computational Molecular Science.* **2022**, 12, 5 e1606, DOI: 10.1002/wcms.1606

(26) Grimme, Stefan; Ehrlich, Stephan; Goerigk, Lars. Effect of the damping function in dispersion corrected density functional theory. *J. Compt. Chem.* **2011**, 32, 7, 1456-1465, DOI: 10.1002/jcc.21759

(27) Barone, V.; Cossi, M., Quantum Calculation of Molecular Energies and Energy Gradients in Solution by a Conductor Solvent Model. *J. Phys. Chem.* **1998,** *102*, 1995 -2001. DOI: 10.1021/jp9716997

(28) Adamo, Carlo and Barone, Vincenzo. Toward reliable density functional methods without adjustable parameters: The PBE0 model. *J. Chem. Phys.* **1999**, 110, 6158-6170, DOI: 10.1063/1.478522

(29) Neese, Frank. Efficient, approximate, and parallel Hartree-Fock and hybrid DFT calculations. A 'chain-of-spheres' algorithm for the Hartree-Fock exchange. *Chemical. Physics.* **2009**, 356, 1-3, 98-109, DOI: 10.1016/j.chemphys.2008.10.036

(30) Hirata, So and Head-Gordon, Martin. Time-dependent density functional theory within the Tamm-Dancoff approximation. *Chemical Physics Letters.* **1999**, 314, 3-4, 291-299, DOI: 10.1016/S0009-2614(99)01149-5

(31) Neese, F., and Olbrich, G. Efficient use of the resolution of the identity approximation in time-dependent density functional calculations with hybrid density functionals. *Chemical Physics Letters.* 2002, 362, 1-2, 170-178, DOI: 10.1016/S0009-2614(02)01053-9

(32) Pettersen, Eric F.; Goddard, Thomas D.; Huang, Conrad C.; Couch, Gregory S.; Greenblatt, Daniel M.; Meng, Elaine C.; Ferrin, Thomas E. UCSF Chimera—a visualization system for exploratory research and analysis. *J. Compt. Chem.* **2004**, 25, 13, 1605-1612, DOI: 10.1002/jcc.20084

(33) ReactLab^{TM} Kinetics – Global Analysis and Reaction Modeling for Kinetic Processes. Jplus Consulting Pty Ltd, United Kingdom, **2023**.

Chapter 4: Dioxygen Reactivity with Thiolate-Ligated Iron Biomimetic Model Related to IPNS

Portions of this chapter have been republished or adapted with permission of the Journal of American Chemical Society from, "Reactivity of Five-Coordinate Models for the Thiolate-Ligated Fe Site of Nitrile Hydratase" Ellison, Jeffrey, J.; Nienstedt, Andrew; Shoner, Steven C.; Barnhart, David; Cowen, Jerry A.; Kovacs, Julie A. *J. Am. Chem. Soc.* **1998**, 120, 23, 5691-5700. DOI: 10.1021/ja973129q

4.1 Introduction

Most non-heme iron enzymes that bind dioxygen to form superoxos are capable of an array of reactions such as, hydrogen atom abstraction, sulfur oxidation, oxo atom transfer, and more. Many components govern the specific reaction the superoxo undergoes including the substrate, orientation of substrate, and protein binding pocket environment.[1-4] One aspect of protein environments that affects their reactivity, aprotic versus protic residues, was explored in **Chapter 3** with [$Fe^{II}(S_2{}^{Me2}N_2N^H(Pr,Pr))$]. Another aspect is the folding and configuration of the active site and the orientation of the substrate binding, which also affects the specific reactivity.[5,6] The Solomon group performed computational studies on the enzymes of IPNS and CDO superoxo structures to investigate the activation barrier and preference of hydrogen atom abstraction (HAA) over electrophilic sulfur attack (SOX). These studies found that the protein binding pocket that holds the tripeptide substrate (β (L-alpha-aminoadipoyl)-L-cysteinyl-D-valine) ACV keeps the Val side chain in place through van der Waals interactions. The energy barrier of HAA was found to be 6.7 kcal/mol lower than that of SOX.[9,10] If the ACV substrate isn't constrained, then the SOX reaction becomes energetically favored.

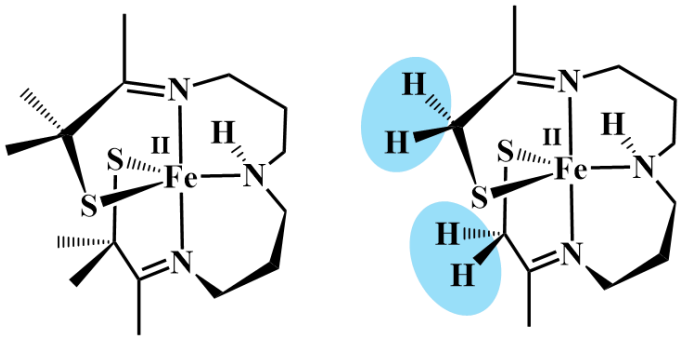

Figure 4. 1 ChemDraw of [$Fe^{II}(S_2{}^{Me2}N_2N^H(Pr,Pr))$] (**1**)[16], and [$Fe^{II}(S_2{}^{\beta\text{-}H2}N_2N^H(Pr,Pr))$] (**4**)[22], highlighted are the difference between the gem-dimethyl and hydrogens on the alkyl thiolate arm.

Chapter 4 will be focusing on a model relevant to IPNS, whose proposed enzymatic mechanism was laid out in section *1.3.2.1.* A main feature of this mechanism is that the Fe^{III}-superoxo's distal oxygen is in close proximity to a *β*-hydrogen, which is supported by the dioxygen mimic, NO-bound form of IPNS.[7,11] Small molecule analogues of metalloenzyme active sites can be used to study the mechanism of dioxygen activation and provide insights into the metal-centered intermediate's oxidation state and electronic structure.[1,12,13] The first intermediate in dioxygen activation pathways is a metal-superoxo. The degree of electron transfer is variable and the formal oxidation of first-row transition-metal superoxo complexes (Fe^{II}-O_2 or Fe^{III}-O_2^-) has been debated.[14,15]

Previously, in the Kovacs group, a bio-inspired small molecule model of the active site of IPNS was synthesized that supports an Fe^{III}-superoxo, [$Fe^{II}(S_2{}^{Me2}N_2N^H(Pr,Pr))$] (**1**), **Figure 4.1 left**.[16] The scaffold includes a *bis* propylamine backbone, along with two alkyl thiolates bound to an iron metal ion in a square pyramidal fashion. Modifications to this scaffold include shortening the amine backbone and substitutions of the imine hydrogens or *gem*-dimethyl groups on the thiolate portion. To create a better mimic of the active sites of IPNS, the *gem*-dimethyl groups were

switched out for hydrogens to form [$Fe^{II}(S_2{}^{\beta\text{-}H2}N_2N^H(Pr,Pr))$] (**4**) (**Figure 4.1, right**). The small molecule model now contained similar strength cysteine C—H bond strength (93 kcal/mol)[17] as the native enzyme. EAS (**Figure 4.10**) and time dependent DFT (**Figure 4.11**) experiments demonstrated that **4** is capable of forming a superoxo, [$Fe^{III}(S_2{}^{\beta\text{-}H2}N_2N^H(Pr,Pr))\text{-}O_2$] **5**.

The focus of **Chapter 4** explores the reactivity of dioxygen with **4**, a non-heme iron complex with a structure capable of a β-hydrogen abstraction, and insights into whether a thiolate-ligated metal-superoxo can abstract such a high energy C-H bond. Proposed mechanisms of both an intra- and intermolecular HAT will be explored. Density functional theory will (DFT) also be utilized to understand properties of the short-lived metastable intermediates that accompany dioxygen reactivity with **4**.

4.2 Results and Discussion

4.2.1 Probing the Reactivity of [$Fe^{II}(S_2{}^{\beta\text{-}H2}N_2N^H(Pr,Pr))$] (4) with Dioxygen Inhibitors and Mimics

Dioxygen mimics have been utilized to probe the substrate binding site of enzymes that activate dioxygen and biomimetic models. Since dioxygen can oxidize ligands or thiolates around the metal center, investigating whether the substrate binds to the metal is essential for evaluating the functionality of the small model molecule to be related back to the native enzyme's reactivity. Dioxygen inhibitors such as carbon monoxide (CO) and azides (N_3^-) can bind to the metal center at various oxidation states, Fe^{II} and Fe^{III} respectively, and bind reversibly. Nitric oxide (NO•) acts as a dioxygen mimic binding to the metal, and since NO has one less electron, makes a stable metal nitrosyl complex that allows for observation of analogous dioxygen binding without going on to form other oxidation products.[18-21]

4.2.1.1 Addition of Carbon Monoxide to ***[Fe^{II}(S$_2^{\beta\text{-}H2}$N$_2$N^H(Pr,Pr))] (4)***

Previously in the Kovacs group, **4ox,** [Fe^{III}(S$_2^{\beta\text{-}H2}$N$_2$N^H(Pr,Pr))] was not able to be isolated as a stable product, thus the reactivity of reduced **4** was investigated with carbon monoxide (CO), **Figure 4.2**. The variable-temperature EAS spectra in **Figure 4.2**, demonstrates that CO-bound **4** does not form unless the temperature is near or below 0 °C. As the solution is cooled to -97 °C the

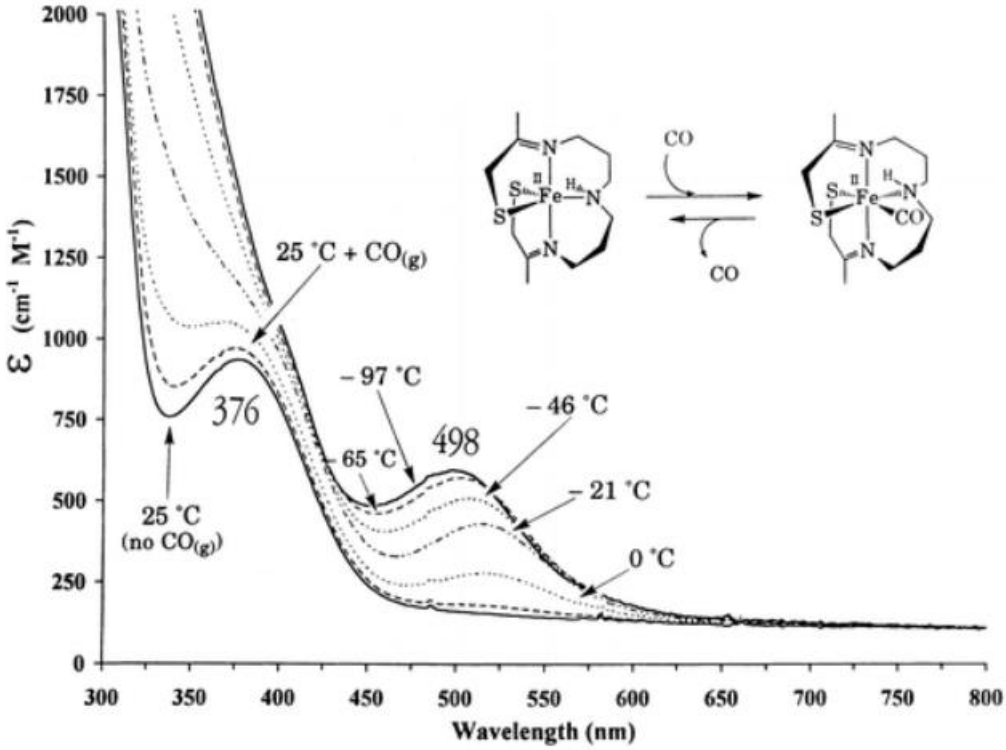

Figure 4. 2 Variable-temperature EAS spectrum of **4** (0.0916 mM) and excess CO in MeOH.[22]

band at 498 nm grows in appreciably, and the solution changes from a chartreuse green to intense red solution. As the temperature is raised, the spectrum shifts back to unbound **4**, as the 376 nm band. The formation of CO-bound **4** is also supported by IR with υ_{CO} stretch as 1929 cm^{-1}.[22] Reversible CO binding is common among Fe^{II} complexes[23-26], and the lower energy υ_{CO} stretch of **4** suggests significant π back donation due to the thiolate. The 6th coordinate Fe^{II} **4** with an

absorption band at 498 nm is of importance later in this chapter when discussing the intramolecular mechanism of IPNS, as an Fe^{II} 6th coordinate species is proposed.

4.2.1.2 Addition of Tetrabutylammonium azide to ***[$Fe^{II}(S_2^{\beta\text{-}H2}N_2N^H(Pr,Pr)$)] (4)***

Azides are known as dioxygen inhibitors as they bind to the 6th position of the metal center, and provide evidence that dioxygen activation is metal mediated, instead of being an outer-sphere oxidant.[27,28] Azides do not react with Fe^{II}, thus **4** needed to be oxidized *in situ* using a known outer

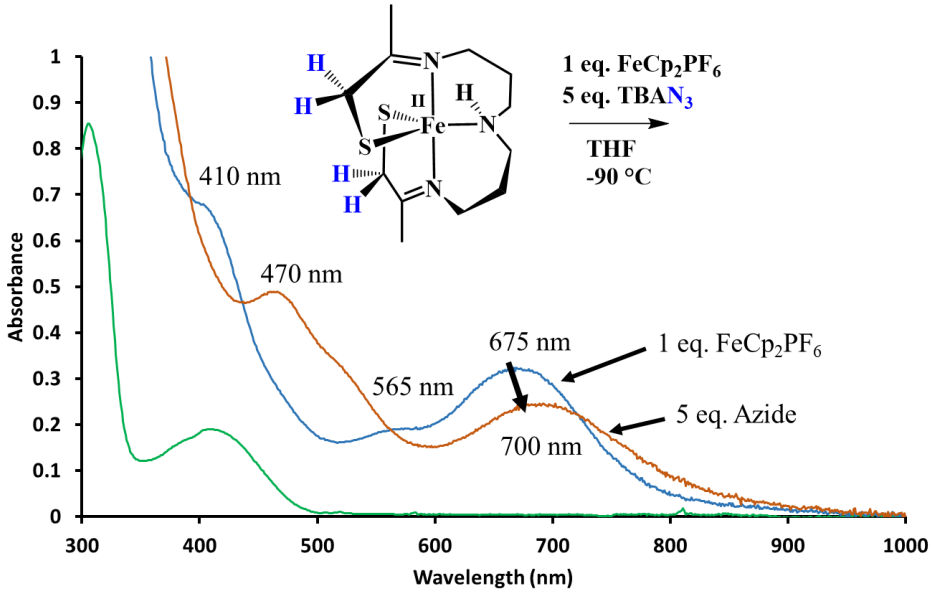

Figure 4. 3 EAS observation of 0.5 mM of **4** (green) oxidized with 1 equivalent of ferrocenium hexafluorophosphate (blue) then addition of 5 equivalents of tetrabutylammonium azide(red) THF at -90 °C.

sphere oxidant ferrocenium hexafluorophosphate ($FeCp_2PF_6$) forming **4-ox**. The addition of tetrabutylammonium azide ($TBAN_3$) to oxidized (*in situ*) **4** (λ_{max} = 410, 565, and 675 nm) resulted in formation of a new species with λ_{max} = 470 and 700 nm in THF at -90 °C, **Figure 4.3**. Dioxygen was introduced after the new species was formed, and showed no reactivity, providing evidence that the new species has azide coordinated. At low temperature the stability of the species last for

4 hours and attempts of crystallization have been unsuccessful. Previously, Fe^{II} **4** was reacted with azide and no reaction was observed.[22] Thus the new species is proposed as the azide bound **4** and is consistent with other alkyl thiolate azide bound Fe^{III}.[29,30] Further investigations with EPR will help to characterize the proposed azide bound species **4**-N_3.

4.2.1.3 Nitric Oxide Reactivity with ***[$Fe^{II}(S_2^{\beta\text{-}H2}N_2N^H(Pr,Pr))$] (4)***

Analogous to the enzymatic studies done on IPNS with NO to probe the O_2 binding site and obtaining a crystal structure with NO bound and in the vicinity of the β-hydrogen on the thiolate, which is consistent with the proposed mechanism of HAA. Complex **4** was reacted with nitric

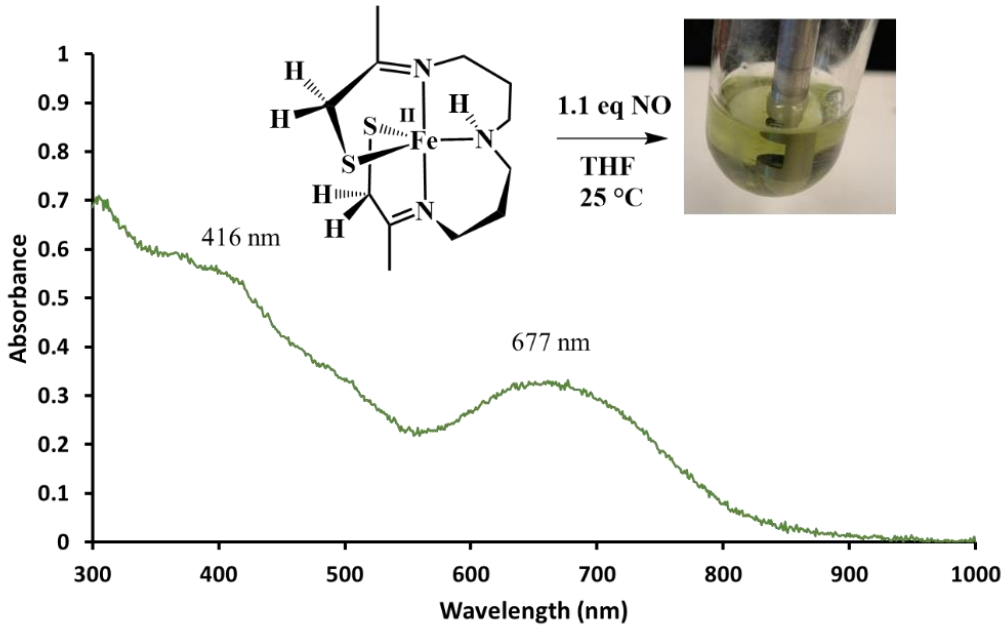

Figure 4. 4 EAS observation of 0.5 mM of **4** reacting with 1.1 equivalents of NO gas in THF at 25 °C.

oxide to generate a proposed NO bound Fe^{III} species. To a frozen solution of **4,** 1.1 equivalents of NO gas was given through a high-vacuum line and allowed to thaw at room temperature and brought back into the glovebox under an inert atmosphere. As the solution thawed a color change was observed from chartreuse green to forest green. An aliquot was taken and diluted to 0.5 mM

and observed by EAS to have a shoulder at 416 nm and one broad band feature at 677 nm (**Figure 4.4**). This solution was exposed to O_2 and did not react or decay in appreciable timeframe. Previous DFT calculations support the assignment of a band from the 600-700 nm as the complex in the Fe^{III} state with a sixth ligand bound. Preliminary IR experiments were completed and showed two new peaks at 1764 and 1720 cm^{-1} which can likely be attributed to symmetric and antisymmetric υ_{NO} stretches, as well as a υ_{NH} stretch at 3268 cm^{-1} from the amine backbone. Attempts to obtain a crystal structure are ongoing, and an effort to elucidate structural and electron details of the NO-bound complex via density functional theory (DFT) were performed.

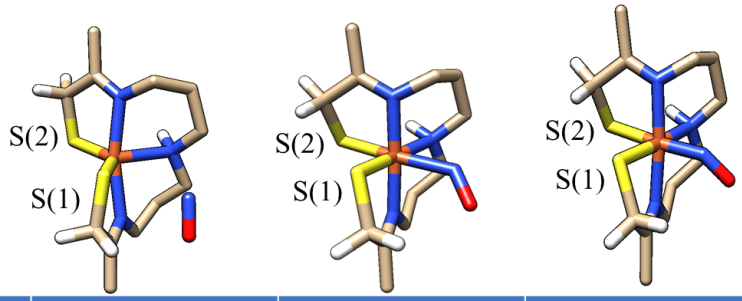

Bond/Angle	High Spin S = 5/2	Intermediate Spin S = 3/2	Low Spin S = 1/2
Fe-S(1)	2.36505	2.22509	2.30622
Fe-S(2)	2.33540	2.34990	2.37758
Fe-N1	2.19047	1.99731	2.01857
Fe-N2	2.24455	2.14069	2.12117
Fe-N3	2.16412	1.99510	2.01180
Fe-N4	3.65454	2.08993	1.80048
N4-O	1.16748	1.20458	1.19341
N-O angle	180°	129.783°	138.047°
O---H	2.45311	2.66530	3.08435

Figure 4. 5 Calculated bond lengths and Fe-N-O angles of Fe^{III} high spin S = 5/2, intermediate spin S = 3/2, and low spin S = 1/2 , with their respective geometry optimized structure.

Nitric oxide is a linear molecule that has one unpaired electron that reacts with transition metals to yield metal nitrosyls. Binding to the metal center causes the unpaired electron to delocalize changing the metal-N-O angle from 180°. Due to the delocalization, determination of the oxidation of the metal center is supported by a crystal structure to analyze the M-N-O angle.[31-33] DFT was performed on multiple spin states for an Fe^{III} metal center (S = 1/2, 3/2, 5/2) to accommodate the d^6 or d^7 electron configuration of the Fe-NO bound of **4**. The starting point for the geometry optimization was the crystal structure of **4**, with a linear NO molecule bound in the 6th ligand position (**Figure 4.5**).

The results of the DFT calculations for bonds, N-O angle, and the distance of the β-hydrogen and distal oxygen are summarized in **Figure 4.5**. For the high spin S = 5/2 case, the geometry optimized structure has the NO ligand unbound, which does not make a viable intermediate for the species observed in the EAS. Both low spin S = 1/2 and intermediate spin S = 3/2 are reasonable configurations of the species observed, and time-dependent DFT was performed on these two options. The TD-DFT for the intermediate spin was the closest to the experimental spectrum with a band at 666 nm, **Figure 4.6**. Detailed natural transition orbitals are shown with the percentages of the two major transitions, sulfur to ligand charge transfers, and sulfur to a mixture of metal and NOπ* charge transfers. Calculated IR was performed on the intermediate spin structure and revealed to have a major stretch at 1548 cm^{-1} which is not in agreement with the experimental IR obtained. The experimental IR is more consistent with a linear NO structure, than the theoretical bend NO for the Fe^{III} S = 3/2 structure.

Preliminary results of **4** reacting with NO resulted in generation of a new species with bands at 416 and 677 nm via EAS and IR stretches at 1764 and 1720 cm^{-1}. Calculated structures of varying spin state reveal that an Fe^{III} S = 3/2 to be most like the experimental species, however the

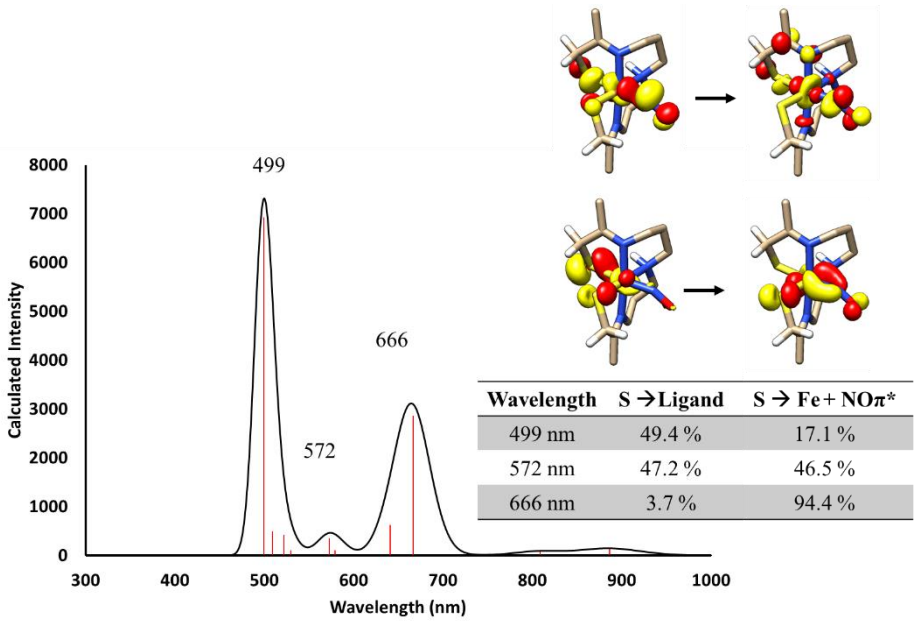

Wavelength	S →Ligand	S → Fe+ NOπ*
499 nm	49.4 %	17.1 %
572 nm	47.2 %	46.5 %
666 nm	3.7 %	94.4 %

Figure 4. 6 TD-DFT simulated EAS of geometry optimized NO bound Fe^{III} S = 3/2 . The three prominent transitions have been labeled. Natural tranistion orbitals (NTO) describing the charge transfer (CT) tranistions. Transition at 499 nm is majorily sulfur to ligand, while transition 572 has both sulfur to ligand and sulfur to Fe and NOπ* CT character. Transition 666 nm mostly has sulfur to Fe and NOπ* CT character.

calculated IR does not agree with experimental, and further investigation is needed. Another technique that would give more information as to the identity of the NO generated species is EPR. However, due to the nature of the electron delocalization, EPR may not be as conclusive as for other Fe^{III} paramagnetic species.

4.2.2 Dioxygen Reactivity with [$Fe^{II}(S_2{}^{\beta\text{-}H2}N_2N^{H}$(Pr,Pr))] (4)

Previous work with **1** revealed that the rate of formation of **3** is approximately 60 times faster in THF than MeOH, suggesting that hydrogen bonding facilitates the ligand rearrangement required for O_2 to bind.[1] Applying this observation to **4**, one would expect that the rate of formation of **5** would be more easily observed via EAS in MeOH. However, the reactivity of **4** with O_2 is different in aprotic versus protic solvents, in that the O_2 binds to the Fe center to form an observable Fe^{III}-superoxo in THF at low temperatures, but at low temperatures in MeOH, O_2 behaves as an

outer sphere oxidant and forms a putative solvent-bound [$Fe^{III}(S_2{}^{\beta\text{-}H2}N_2N^{H}(Pr,Pr))(OMe)$]species (**4-OMe**).

4.2.2.1 Dioxygen Reactivity in Protic Methanol (MeOH)

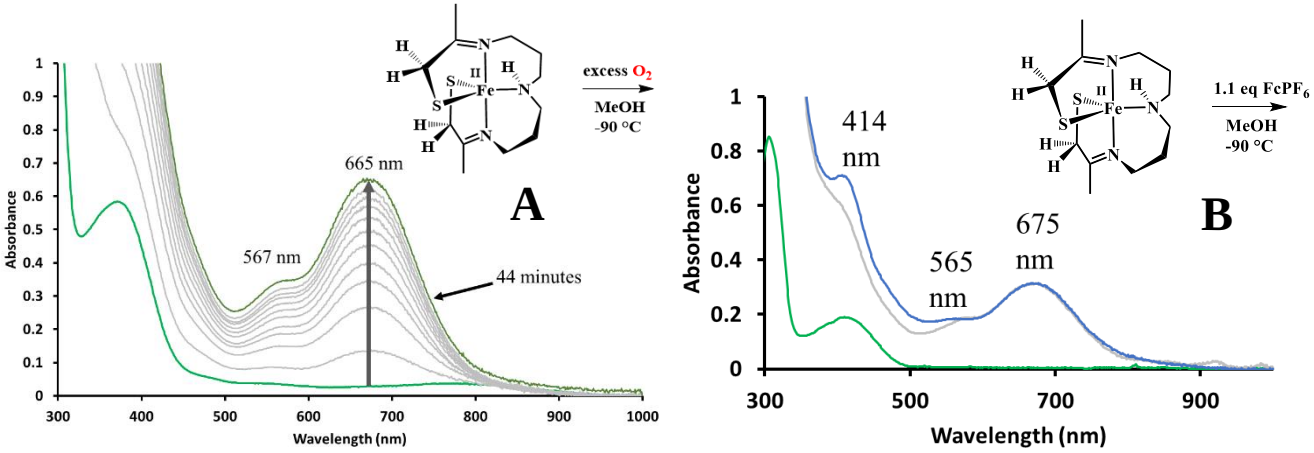

Figure 4. 7 A: EAS of an intermediate at 567 nm, and 675 nm formed from **4** and the addition of excess O_2 in MeOH at -90 ° **B:** EAS of a similar intermediate seen in **A** formed from **4** and addition of 1.1 eq of Cp_2FePF_6 in MeOH at -90 °C.

Spectral features of an Fe^{III}-solvent bound species include a band at 675 nm and a shoulder at 567 nm that grow in over 44 minutes when **4** is reacted with excess O_2 in MeOH at low temperatures, **Figure 4.7, A**. An identical species is generated when **4** is oxidized in MeOH by a standard outer-sphere oxidant ferrocenium hexafluorophosphate (Cp_2FePF_6) in MeOH (**Figure 4.7, B**). When the oxidant is dissolved in acetonitrile (MeCN) and added to **4** in THF at -78° C the main absorption band at 675 nm shifts to 670 nm. Further characterization is required to confirm the identity of this species and attempts with EPR have been unsuccessful. DFT was also used to aid in the identification and geometry optimized structures of Fe^{III}-methoxy (Fe^{III}-OMe) at various spin states (S = 5/2, 3/2, 1/2) were employed to reproduce the EAS spectrum, **Figure 4.9**. The TD-

DFT calculated spectra did not match with the experimentally observed putative solvent bound Fe^{III} species and requires further fine-tuning.

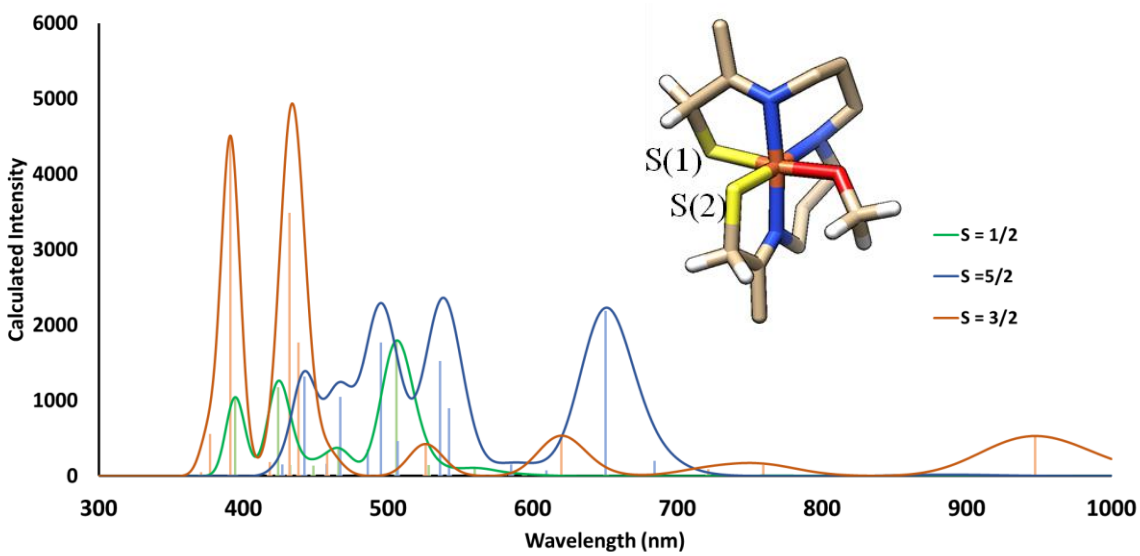

Figure 4. 9 TD-DFT calculate spectra with B3LYP functional for proposed solvent bound Fe^{III}-OMe species with spin states of *S* = 5/2 (blue), *S* = 3/2 (red), and *S* = 1/2 (green).

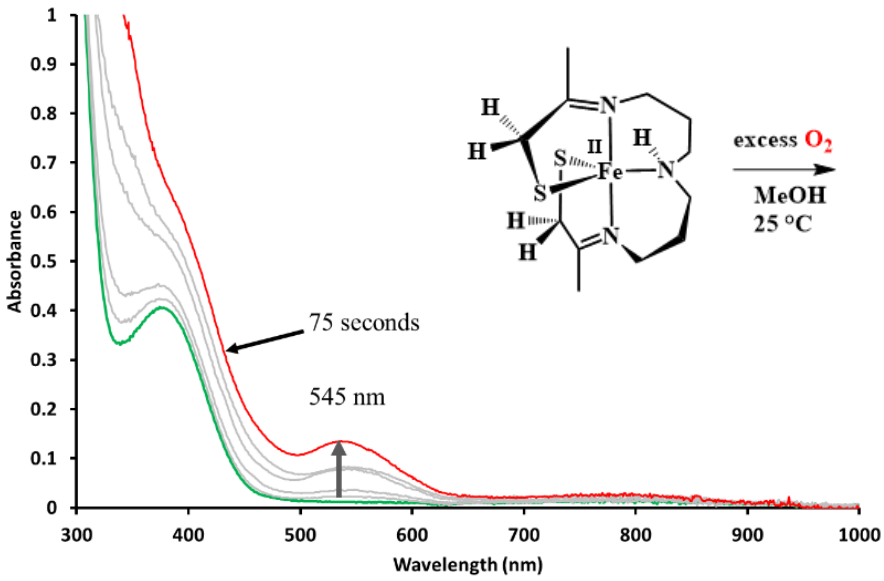

Figure 4. 8. EAS of an intermediate at 545 nm formed from **4** and addition of excess O_2 in MeOH at 25 °C.

Table 4. 1 DFT geometry optimizations with B3LYP functional for proposed Fe^{III}-sulfenate (*S* = 5/2, 3/2, and 1/2) compared to crystal structure of **6**.

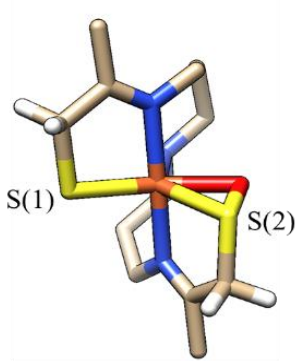

Bond (Å)	Crystal 6 *S* = (1/2)	*4-sulfenate* *S* = 5/2	*4-sulfenate* *S* = 3/2	*4-sulfenate* *S* = 1/2
Fe-S(1)	2.142	2.29048	2.19172	2.15828
Fe-S(2)	2.148	2.43551	2.46079	2.20268
Fe-O	2.115	2.04477	1.99068	2.26422
S(2)-O	1.447	1.60132	1.59317	1.55224

When **4** is reacted with O_2 at room temperature in MeOH; a species at 545 nm grows in shortly, before converting to a featureless spectrum (**Figure 4.9**). Comparing the reactivity of O_2 at room temperature with other complexes in the propyl, propyl amine family (Pr,Pr) this species is most likely an Fe^{III}-sulfenate. Complexes, $Fe^{III}(\eta^2S^{Me2}O)(S^{Me2)}N_2N^H(Pr,Pr)]^+$, $[Fe^{III}(\eta^2$-$S^{Me2}O)(S^{Me2)}N_2N^{Me}(Pr,Pr)]^+$, $[Fe^{III}(\eta^2$-$S^{Me2}O)(S^{Me2)}N_2N^H(Et,Pr)]^+$ have been characterized with X-ray crystal structures and all three display absorption bands in the 500-550 nm region.[30,34,57] The use of DFT geometry optimized structures of a sulfenate species generated from **4** compared to the crystal structure of $[Fe^{III}(\eta^2$-$S^{Me2}O)(S^{Me2})N_2N^H(Pr,Pr)]^+$ (**6**),[34] reveal that the sulfenate species derived from **4** may be *S* = 5/2 or 1/2 (**Table 4.1**). The TD-DFT of each of the spin states, however, did not reproduce the experimental spectrum, and require further geometry optimizations with different basis sets and functionals. Further characterization via EPR and mass spectroscopy are difficult due to the short life span, 45 seconds, of the species. A trend is

occurring with **4** in that the lifespan of intermediates and reactions are much shorter relative to the gem-dimethyl systems.

4.2.2.2 Dioxygen Reactivity in Aprotic Tetrahydrofuran (THF)

The reaction of **4** with dioxygen results in the growth of bands at 400, 530, and 704 nm in the electronic absorption spectrum (**Figure 4.10**). The EAS spectrum is similar to that found for superoxo **3** (**(**$[Fe^{III}(S_2{}^{Me2}N_2N^H(Pr,Pr))\text{-}O_2]$) (409, 520, 707 nm). The proposed Fe^{III}-superoxo formed from complex **4**, $[Fe^{III}(S_2{}^{\beta\text{-}H2}N_2N^H(Pr,Pr))\text{-}O_2]$ (**5**), has a lifetime of 90 seconds and is significantly shorter-lived than **3**, that has a lifetime of 10 minutes. By exchanging the *gem*-dimethyls for *β*-hydrogens, **4** has a more positive reduction potential of -270 mV (vs. SCE)[35] compared to that **1** at -425 mV (vs. SCE)[35] indicating that **4** is more difficult to oxidize to Fe^{III}, likely because the +3 oxidation state is less stable. The *gem*-dimethyls of **1** may donate electron

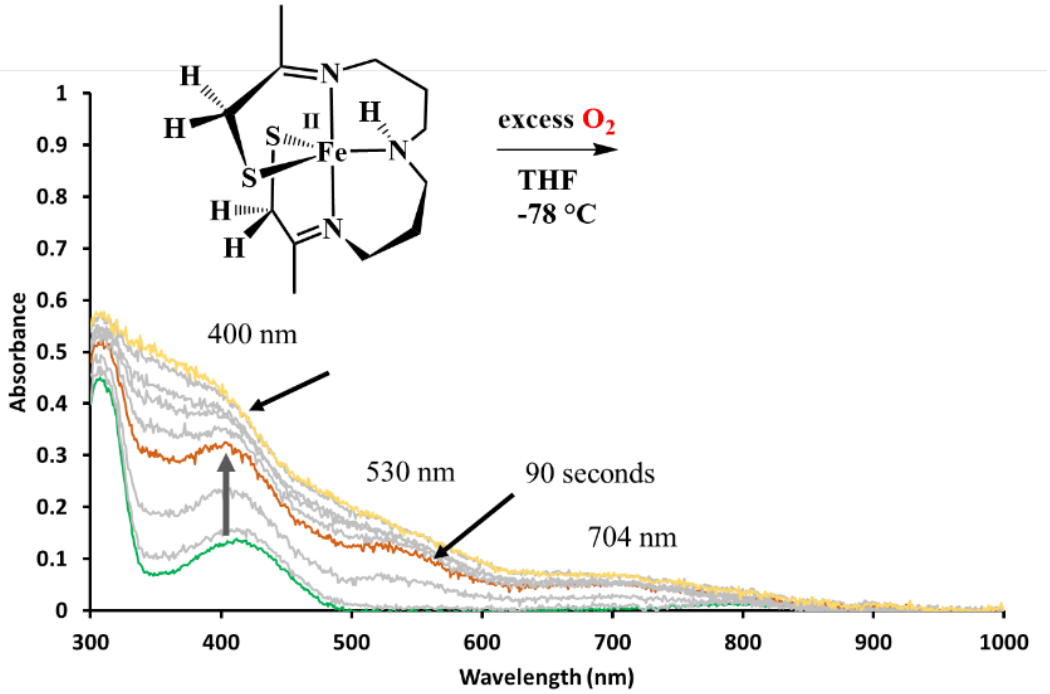

Figure 4. 10 EAS of short-lived proposed Fe^{III}-superoxo of complex **5**, through the addition of excess O_2 in THF at -78 °C over 90 seconds.

density onto the thiolates allowing the +3oxidation state of Fe to be more stable. The difference in reduction potential supports an understanding of why **4** forms a much a shorter-lived putative Fe^{III}-superoxo intermediate, which can only be observed at lower temperatures. The oxidation potentials also reflect the HOMO/LUMO energetic gap of a complex, where a less negative reduction potential indicates that the HOMO is lower in energy with **4**, and therefore also likely lower for species **5**, which would cause the sulfur to metal charge transfer band to shift to lower energies, explaining the slight red-shift in its absorption bands relative to **3**.

4.2.3 Computational Experiments for Superoxo Intermediates

Density functional theory (DFT) geometry optimizations were performed with the PBE0 functional and the polarized triple-zeta def2-TZVP starting from the crystal structure previously reported for azide-bound $[Fe^{III}S_2{}^{Me2}N_2N^H(Pr,Pr)(N_3)]$ (**7**),[35] since azide is structurally similar to O_2

Table 4. 2. Bond distances for core atoms of the $[Fe^{II}(S_2{}^{\beta\text{-}H2}N_2N^H(Pr,Pr))]$ (**4**) and calculated $[Fe^{III}(S_2{}^{B\text{-}H2}N_2N^H(Pr,Pr))\text{-}O_2)$ (**5**).

Bond (Å)	Crystal 4	*Calc. 4*	*Calc. 3*	*Calc. 5*
Fe-S(1)	2.35412(4)	2.341	2.203	2.224
Fe-S(2)	2.3453(4)	2.345	2.256	2.305
Fe-N(1)	2.1519(11)	2.158	1.981	1.996
Fe-N(2)	2.1612(11)	2.200	2.111	2.121
Fe-N(3)	2.1670(11)	2.158	1.981	1.996
Fe-O	N/A	N/A	1.947	1.947
O-O	N/A	N/A	1.289	1.306

and used to probe activation sites of enzymes instead of O_2.[12] The structure of **7** was modified to fit the structure of **5** by removing the *gem*-dimethyls and replacing them with hydrogens, and the O-O bond position replaced the proximal and middle nitrogen atoms of the azide while the terminal nitrogen was removed. The Fe^{III} metal center was assumed to be $S = 1/2$, based on previous knowledge that thiolates tend to stabilize low spin-state species due to the nephelauxetic effect.[13] The calculated structure of putative Fe^{III}-superoxo **5** contains an O_2 moiety *cis* to one of the thiolate sulfurs with an O-O bond length of 1.306 Å, consistent with a superoxo. The bond lengths for crystallographically characterized **4** are compared with DFT-calculated **5** in **Table 4.2**. The Fe-S bond (Fe-S(1) = 2.224 Å) for the thiolate that is *trans* to the superoxo moiety, O_2 is shorter than the *cis* Fe-S bond (Fe-S(2) = 2.305 Å). One would expect that the binding of O_2 would have a push effect on the *trans* thiolate and elongate the (Fe-S(1)) bond, but that does not appear to be the case. The shorter Fe-S bond indicates that the bond is more covalent and pushes the thiolate's electron density back onto the metal center, which may be contributing to the strength of the Fe^{III}-superoxo and the C-H bond activation capability. Broken symmetry geometry optimizations[14,16] were used

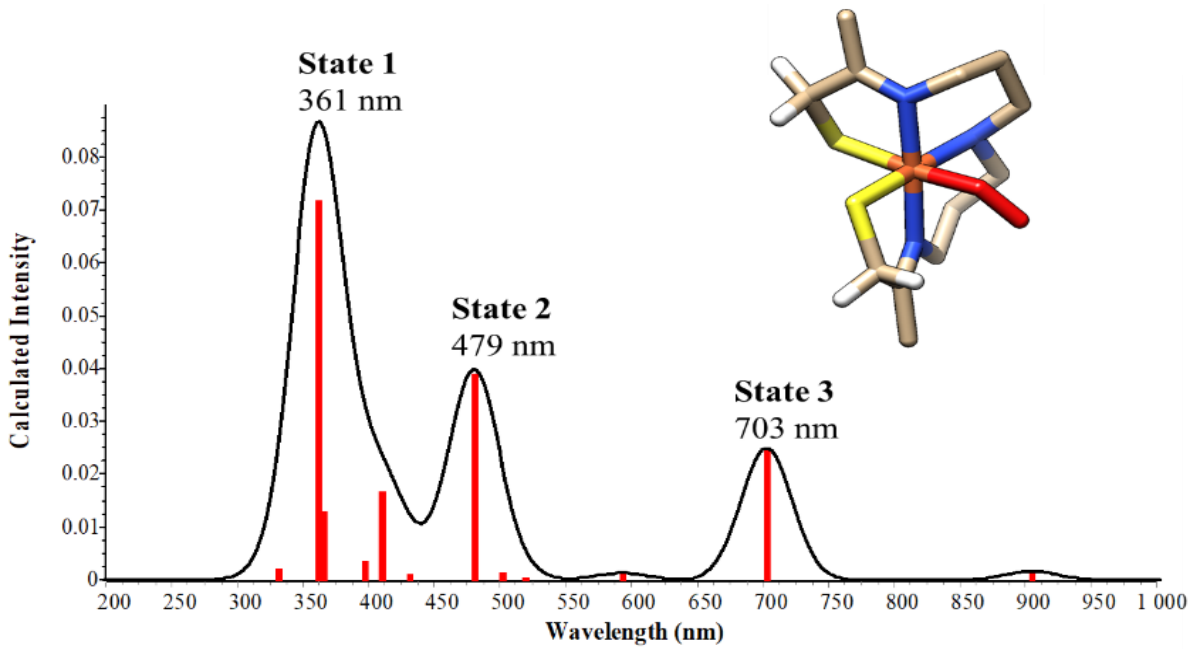

Figure 4. 12 TD-DFT simulated EAS of broken symmetry geometry optimized **5**. The three prominent transitions have been labeled.

in order to model coupled paramagnetic sites, as previously seen with **3**, where the high-spin (HS) case was calculated for Fe^{III}(S = 1/2 ↑)-$O_2^{\bullet-}$ (S = 1/2 ↑) as well as the low-spin (LS) case in which the spin on the Fe^{III} metal center is flipped to give a final total spin of S = 0; Fe^{III}(S = 1/2 ↓)-$O_2^{\bullet-}$

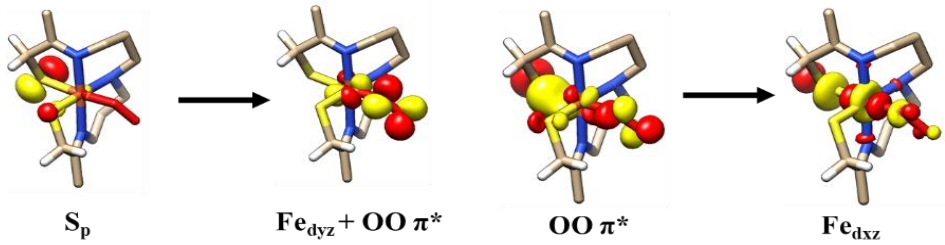

	S_p → Fe_{dyz} + OO π*	OO π* → Fe_{dxz}
State 1	54.7 %	33.6 %
State 2	92.7 %	6.0 %
State 3	94.9 %	0 %

Figure 4. 11. Natural tranistion orbitals (NTO) describing the charge transfer (CT) tranistions. State 1 and 2 have both S_p to Fe_d and OOπ* CT character. State 3 only has S_p to Fe_d and OOπ* CT character.

(S = 1/2 ↑).[14,15] Finally, the energies from the HS and LS broken symmetry states were used to estimate the coupling constant, J, using the equation $J = -(E_{HS} - E_{LS})/(\langle S^2\rangle_{HS} - \langle S^2\rangle_{LS})$,[15] which is valid over the entire coupling strength regime. E_{HS} and E_{LS} are the energies of the HS and LS states, and $\langle S^2\rangle$ are the expectation values of the squared spin operator for the HS and LS states, respectively. The coupling constant of $J^{calc} = -580\ cm^{-1}$, was obtained for putative **5**, compared to the $J^{calc} = -450\ cm^{-1}$ for **3**,[16] in which 2J is the energy required for the electron to go from the LS to HS. The more negative J value indicates that the unpaired spins are strongly antiferromagnetically coupled.

Time dependent DFT (TD-DFT) was performed on **5** with the broken symmetry geometry optimized structure and employed the CAM-B3LYP functional, a polarized triple-zeta def2-TZVP basis set, the def2/J auxiliary basis set and RIJONX approximation for Coulomb fitting. The simulated EAS excited state of **5** (**Figure 4.11**) has three prominent natural transition orbitals

Table 4. 3. Mulliken charges for calculated core atoms of superoxo **3** and **5**.

Mulliken Charges	***Calc. 3***	***Calc. 6***
Fe	-0.062	-0.035
***trans*-Sulfur**	-0.395	-0.337
***cis*-Sulfur**	-0.305	-0.324
Proximal Oxygen	-0.095	-0.078
Distal Oxygen	-0.262	-0.280

(NTO) describing the charge transfer (CT) transitions at 361 nm, 480 nm, and 703 nm that are in good agreement with the experimentally observed **5** (**Figure 4.10**). States 1 and 2 are comprised mostly of S_p to Fe_d and O-Oπ* and O-Oπ* to Fe_d charge transfers, while State 3 is comprised of S_p to Fe_d and O-Oπ* (**Figure 4.12**). The trend that the RS^- character contributions to CT transitions increases as the energy increases is consistent with the previously reported DFT of **3**.[16] Investigation of the local electron density via Mulliken charges of **3** and **5**, have shown that the *trans*-thiolate (-0.337) has slightly more electron density than the *cis*-thiolate (-0.324) (**Table 4.3**), as well as, an increase in negative charge on the distal oxygen consistent of the superoxo. The increased electron density on the distal oxygen also supports thiolate donation of electron density into the metal ion and then into the O-Oπ* bond of the Fe-superoxo aiding in the reactivity and cleavage C-H bonds of 93 kcal/mol. Overall, the computational experiments provided are consistent with **5** being assigned as a short-lived Fe^{III}-superoxo.

4.2.4 Proposed Mechanisms

Possible reactions to consider following the formation of Fe^{III}-superoxo via hydrogen atom transfer (HAT) are either intermolecular HAT from either substrate or solvent, as shown previously with **3**,[16] (**Scheme 4.1**) or intramolecular HAT from the β C-H bond of the alkyl thiolate (**Scheme 4.2**), as closely mimics the proposed mechanism of IPNS. In both scenarios, the Fe^{III}-hydroperoxo species would form and then could undergo homolytic or heterolytic O-O bond cleavage to form a high valent Fe^{IV}-oxo or Fe^{V}-oxo species, respectively, and proceed to perform another HAT.

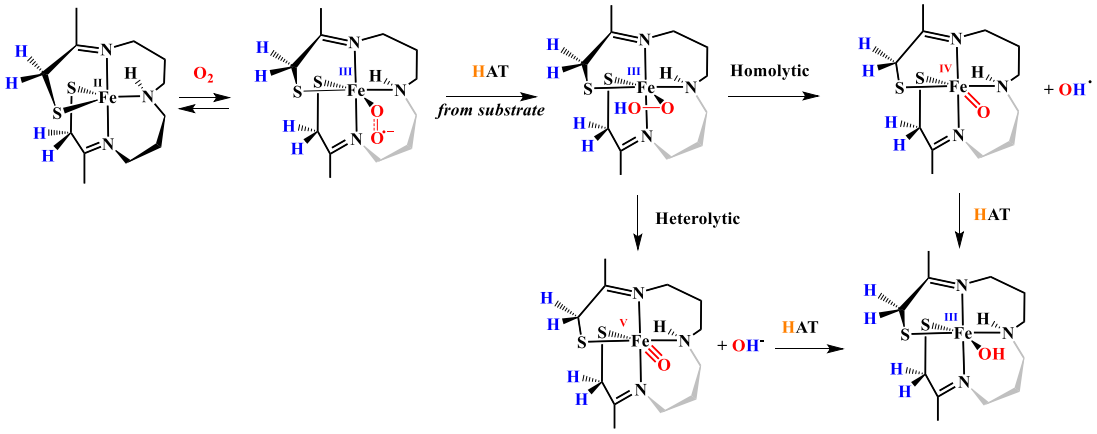

Scheme 4. 1 Proposed intermolecular hydrogen atom transfer (HAT) ~93 kcal/mol from bulk solvent, or substrate. Formation of a Fe^{III}-OOH that undergoes either homolytic or heterolytic O-O cleavage to form a high valent Fe-oxo that would undergo another HAT to form a Fe^{III}-hydroxide.

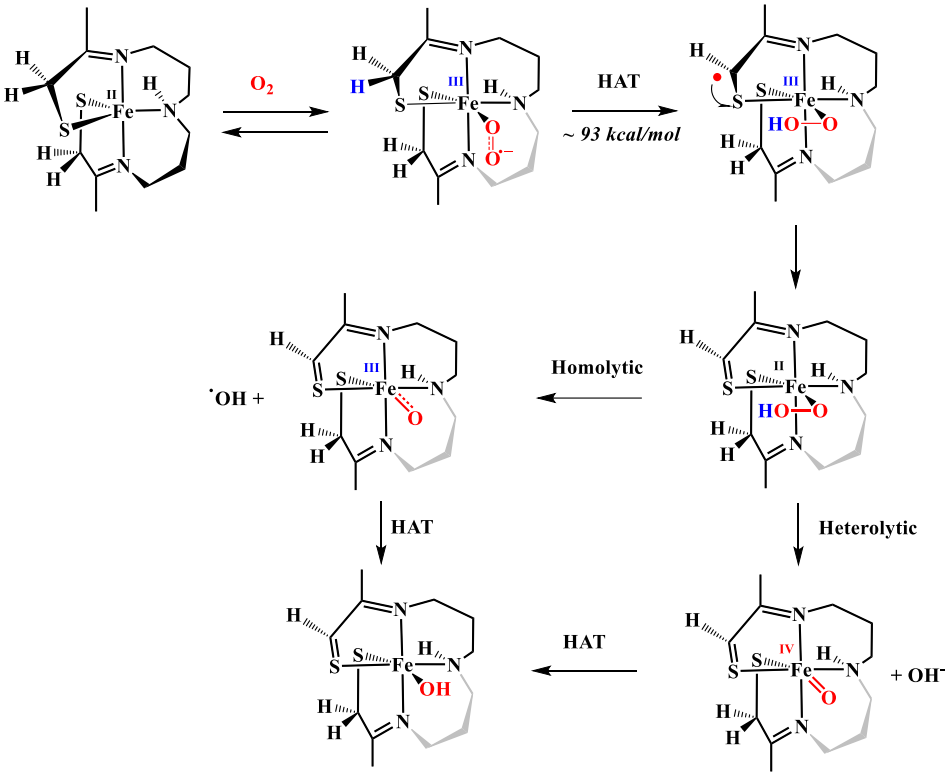

Scheme 4. 2 Proposed intramolecular hydrogen atom transfer (HAT) of ~93 kcal/mol of the *β*-hydrogen of the alkyl thiolate ligand. Formation of the Fe^{II}-OOH and thioaldehyde as proposed for the IPNS mechanism. Formation of a Fe^{II}-OOH that undergoes either homolytic or heterolytic O-O cleavage to form a high valent Fe-oxo that would undergo another HAT to form a Fe^{II}-hydroxide.

4.2.4.1 Intermolecular HAT Evidence

In order to test for the intermolecular HAT a weak H-atom donor, TEMPO-H (BDFE = 70 kcal/mol[36]) was added to the reaction in order to push the mechanism to favor intermolecular over intramolecular, lower the activation barrier, and build up a large enough concentration of a putative Fe^{III}-OOH (λ_{max} = 664 nm) so that it could be spectroscopically observed prior to O-O bond cleavage. When O_2 is added to **4** in the presence of TEMPO-H at low temperatures in THF, a new species was observed via EAS at λ_{max} = 664 nm that then goes on to form another species at 565 nm. The addition of TEMPO-H to the initially formed Fe^{III}-superoxo **5** produced the same results (**Figure 4.13**). The reactivity is consistent with the formation of a putative $Fe^{(III)}$-OOH.

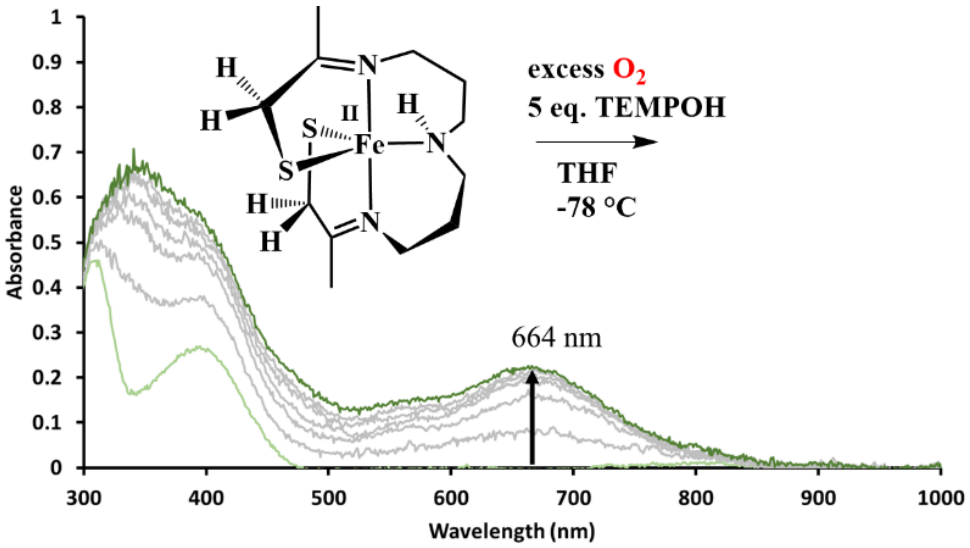

Figure 4. 13. EAS of **5** and addition of 5 equivalents TEMPOH to push the intermediate to form a proposed Fe^{III}-OOH in THF at -78 °C.

Another experiment to support an intermolecular HAT mechanism was to observe if the formation of the Fe^{III}-superoxo were to slow down when the bulk solvent was d_8-THF, thereby demonstrating a kinetic isotope effect (KIE). Complex **3** was observed to have a KIE = 4.8 in THF/d_8-THF.[16] However, the addition of dioxygen to **4** in d_8-THF solution did not result in a

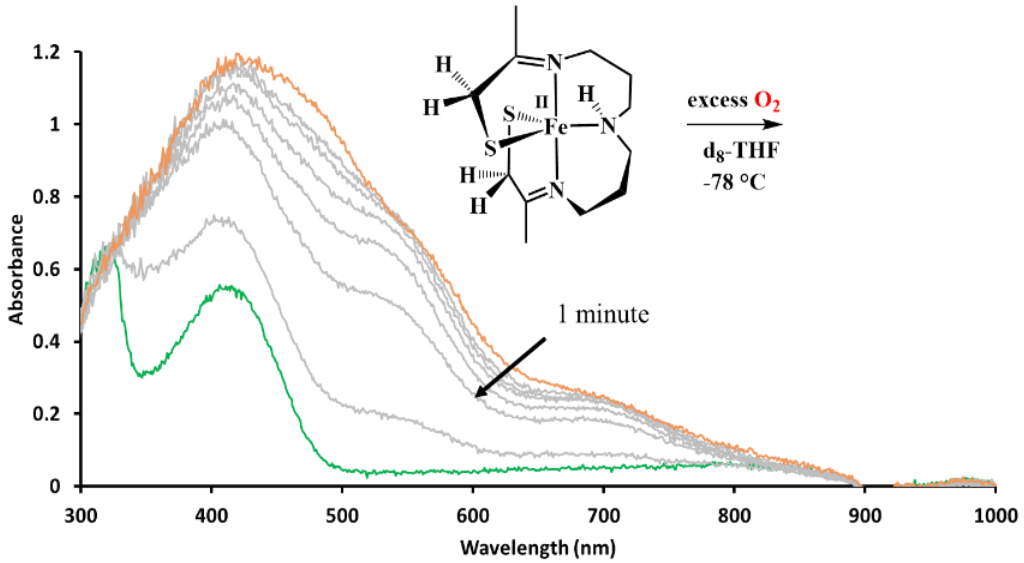

Figure 4. 14 Figure 4.14. EAS 3.16 mM **4** and excess O_2 in deuterated THF at -78 °C testing the intermolecular mechanism of solvent HAT.

longer lived intermediate which had the same spectral features as **5**, and further continued to produce a featureless spectrum (**Figure 4.14**).

4.2.4.2 Intramolecular HAT Evidence

The intramolecular HAT reaction mechanism is of interest in that it closely mimics the mechanism of the IPNS enzyme (**Scheme 4.2**). The DFT calculated structure of **5** shows that the terminal oxygen is 3.273 Å away from the *β*-hydrogen, however with rotation about the Fe-O bond, the distance could decrease to 2.271-1.764 Å. Molecular mechanics calculations using Avogadro, resulted in the *β*-hydrogen being within the range of feeling a strong, mostly covalent force from the distal oxygen.[37] Intramolecular abstraction of a H-atom from the *β* C-H bond would lead to the formation of a Fe^{III}-hydroperoxo intermediate. After which, the *β*-carbon radical may form a thioaldehyde and reduce the Fe^{III} center to Fe^{II} if the mechanism were analogous to IPNS. This mechanistic pathway agrees more with what we observe experimentally since the observed HAT is relatively fast, 90 seconds, and is not influenced by bulk solvent. The rearrangement and formation of an Fe^{II}-hydroperoxo would shift the sulfur-to-metal charge transfer band to the ultraviolet region making observation by EAS difficult. The resulting Fe^{II}-hydroperoxo could either undergo homolytic or heterolytic O-O bond cleavage to form an Fe^{III}-oxo or an Fe^{IV}-oxo. A key feature of this mechanism is the formation of a thioaldehyde. Thioaldehydes have largely been considered as intrinsically unstable and transient intermediates since their calculated π bond energies decrease to an extent of 30-40 kcal/mol less than second row organic counterparts.[38] Observing the reactivity of thioaldehydes are usually carried out via *in situ* chemical trapping such as Diels-Alder cycloadditions or reacting with amines to generate their corresponding imines.[39] Generation of more stable aliphatic and aromatic thioaldehydes have been previously synthesized using bulky mesomeric stabilization to allow for characterization by NMR (C^{13}: 230-255 δ), EAS

(500-600 nm), and IR (1275-1030 cm^{-1}) in mild conditions.[38] Future experiments would be to add substrates to trap the proposed thioaldehyde proposed to form via an intramolecular HAT mechanism.

4.2.5 Deuterating the Ligand Framework

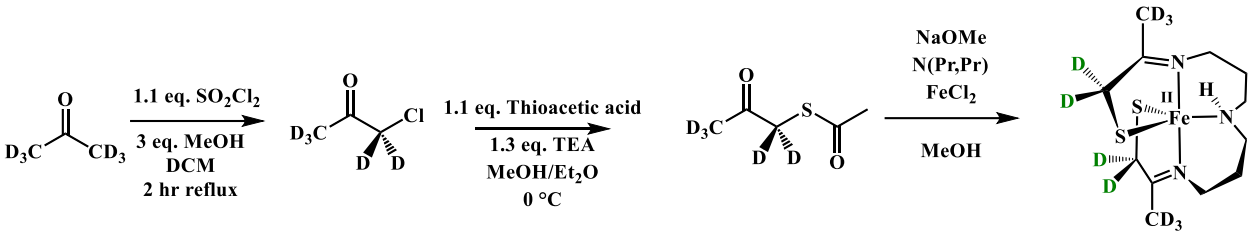

Scheme 4. 3 Overall synthetic route to the deuterated complex $[Fe^{II}S_2{}^{D\text{-}\beta2}N_2N^H(Pr,Pr)]$ (**8**).

The next step in investigating the intramolecular mechanism was to deuterate the β-hydrogen positions of complex **4**. By doing so the rate of formation of the proposed Fe^{III}-superoxo intermediate would be expected to experience a kinetic isotope effect, allowing the Fe^{III}-superoxo to be longer lived, relative to the undeuterated complex, **4**. In order to deuterate the β-hydrogen position, a new ligand, d_5-(1-mercaptoacetone, acetate) (**Scheme 4.3**), was synthesized. The formation of d_5-chloroacetone is light sensitive and with the addition of the moderator MeOH the reaction required no further purification as the side product d_4-(1,3-dichloroacetone) is produced in trace amounts. [40] The use of thioacetic acid to replace the halogen was used to protect the thiolate, as thiolates are known to form disulfide bonds or become oxidized. The metal templated Schiff base condensation with additional base deprotects the thiolate then the condensation to yield crude $[Fe^{II}S_2{}^{D\text{-}\beta2}N_2N^H(Pr,Pr)]$ (**8**).

4.2.6 Dioxygen Reactivity with [$Fe^{II}(S_2{}^{\beta\text{-}D2}N_2N^H(Pr,Pr))$] (8)

The addition of excess dioxygen to crude [$Fe^{II}(S_2{}^{\beta\text{-}D2}N_2N^H(Pr,Pr))$] (**8**) in MeOH and THF at 25 °C (**Figure 4.15**) results in the formation of a fleeting dioxygen sensitive intermediate. The intermediate is formed and decayed around 45 seconds, on par with the protonated complex. Further purification and repeat experiments at lower temperatures are needed to be confident in that the proposed deuterated Fe^{III}-superoxo intermediate is longer lived compared to the Fe^{III}-

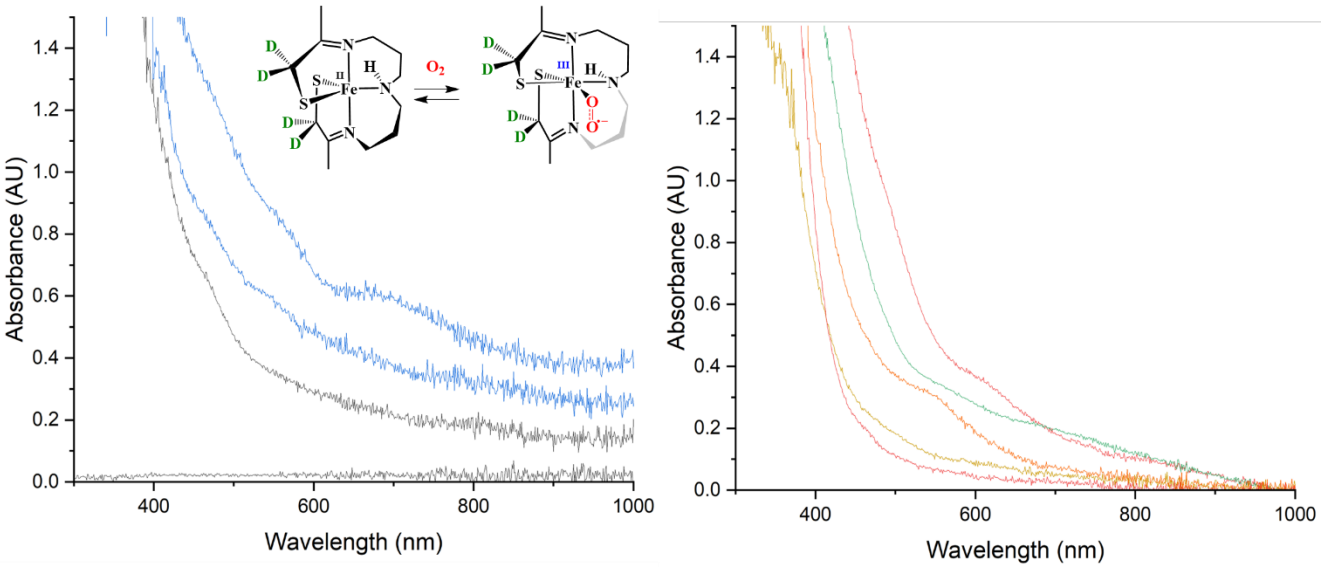

Figure 4. 15 Preliminary EAS spectrum addition of excess dioxygen to [$Fe^{II}(S_2{}^{\beta\text{-}D2}N_2N^H(Pr,Pr))$] (**8**) in MeOH (**Left**) THF (**Right**) at 25 °C.

superoxo of **5**, and if so, provides direct evidence that **4** proceeds through an intramolecular mechanism analogous to IPNS mechanism, and thiolate ligated Fe^{III}-superoxos are capable of abstracting C-H bonds of 93 kcal/mol.

4.2.7 Reactivity of [$Fe^{II}(S_2{}^{\beta\text{-}H2}N_2N^H(Pr,Pr))$] (4) with Oxo Atom Donors

In order to investigate the second active oxidant of the IPNS mechanism, a high valent Fe^{IV}-oxo, oxo atom donors were employed. Oxo atom donor such as iodosylbenzene (PhIO) are a two-electron oxidant that provide an alternative route to produce high valent Fe-oxos, and by-passes

dioxygen-produced radicals (e.g., OH•) that could compete for reactivity. The Kovacs group have found that oxo atom donors form oxo atom adducts and sulfenates.[30,34,43,44,57] Oxo atom donors were shown to react with complex **4** as indicated by the formation of new metastable intermediates with charge transfer bands in the 600-700 nm region (**Figure 4.16**). These transitions are in good agreement with the DFT calculated RS^--to- metal charge transfer band for the formation of an oxo atom donor Fe^{III} species.[34] In addition, λ_{max} is dependent on the type of oxo atom donor, indicating that they bind to the iron's 6th position. After the addition of iodosylbenzene (PhIO) to **4**, the metastable intermediate at 704 nm converts to a new intermediate at 520 nm. The new intermediate could be a sulfenate similar to the *gem* di-methyl **6**[34], a high valent Fe-oxo[42-44], or a Fe-OH species that forms following the formation of a high valent oxo.

The difference in reactivity between dioxygen and oxo atom donors with **4**, is the ability to form the sulfenate. Dioxygen reactivity results in the formation of a superoxo capable of abstraction the β hydrogen from the ligand backbone, and the proposed thioaldehyde that forms

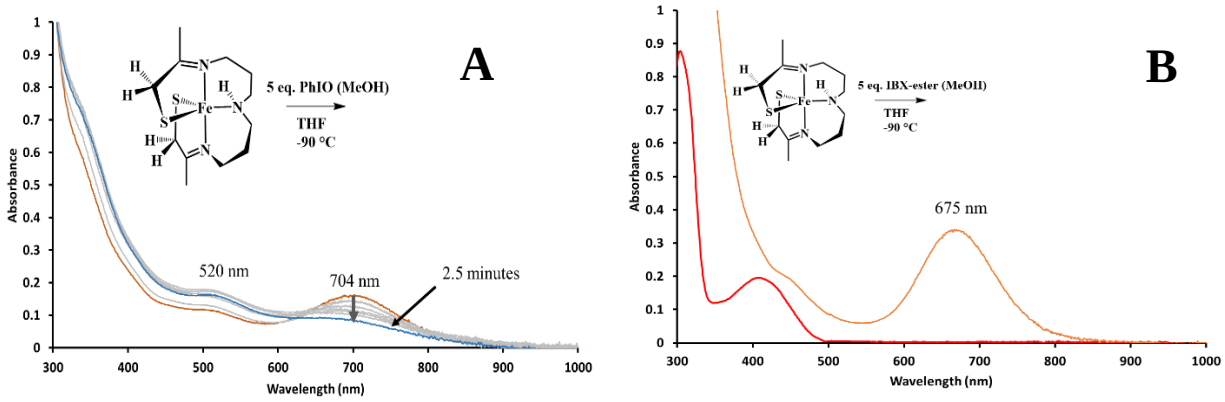

Figure 4. 16. A. EAS of **4** in bulk THF reacting with 5 equivalents of PhIO dissolved in MeOH at -90 °C forming a proposed oxo atom donor metastable intermeidate at 704 nm, and converts to a new intermediate at 520 nm. **B**. EAS of **4** in bulk THF reacting with 5 equivalents of IBX-ester dissolved in MeOH at -90 °C and forming a new intermeidate at 675 nm.

captures electron density on the thiolate resulting in no further reaction with the remaining oxygen to form the sulfenate bond. Whereas during a reaction with oxo atom donors, the distance to the β hydrogen is much greater, and the adjacent thiolate has lone pairs that are accessible to react with the oxo, once donated. Another possibility for the identity of the new intermediate at 520 nm is that it is a high valent Fe-oxo. A high valent Fe-oxo would be expected to be highly reactive and capable of cleaving C-H bonds of up to 100 kcal/ mol.[45] Bulk THF or MeOH have C-H bonds of 93.6 and 95.6 kcal/mol,[46] respectively. If HAT is occurring after the formation of a high valent Fe species, then the next species to be formed would be an Fe^{III}-hydroxide, which can be generated authentically by reacting **4** with a hydroxide source in the presence of an outer sphere oxidant (e.g. Cp_2Fe^+) to get obtain a benchmark of where this species would be observed via EAS. Preliminary results of forming an authentic $[Fe^{III}(S_2{}^{\beta\text{-}H2}N_2N^H(Pr,Pr))(OH)]$ (**4-OH**) was generated by reacting

4-ox with 1 equivalent of tetrabutylammonium hydroxide (TBAOH) solubilized in MeOH which resulted in a new species at 574 nm, **Figure 4.17**.

4.3 Conclusions

The generation of an electronically similar, but shorter-lived (~90 sec) Fe^{III}-superoxo **5,** capable of abstracting hydrogen atoms of BDFE of ~93 kcal/mol either from solvent (intermolecular) or from the *β*-hydrogen on the complex (intramolecular) was discussed. The mechanism of HAT was explored with investigations of intermolecular HAT by addition of weak

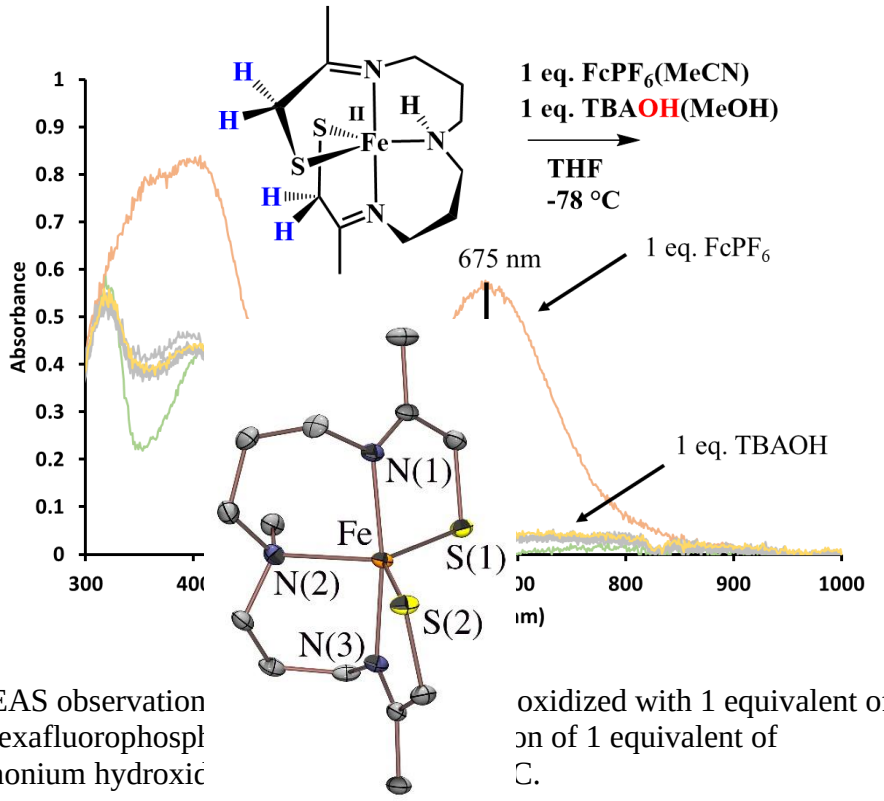

Figure 4. 17 EAS observation oxidized with 1 equivalent of ferrocenium hexafluorophospl on of 1 equivalent of tetrabutylammonium hydroxic C.

Figure 4. 18 ORTEP diagram of [$Fe^{III}(S_2{}^{\beta\text{-}H2}N_2N^{Me}$(Pr,Pr))] (**9**) with hydrogens removed, showing thermal ellipsoids at the 50% probability level.

hydrogen donors (TEMPOH) or deuterated solvent (d_8-THF) to trap or slow down the short-lived **5** to the next proposed intermediate Fe^{III}-OOH. No observation of a change in rate in bulk deuterated solvent provided evidence that the mechanism is most likely intramolecular HAT, similar to the IPNS mechanism. A motivation to investigate the intramolecular HAT mechanism led to the formation of the deuterated complex **8** and preliminary reactivity with O_2 to produce a relatively longer lived Fe^{III}-superoxo compared to **5**. Further characterization with EPR and X-ray crystallography, and trapping a thioaldehyde with external reagents of various intermediates is needed to comment on their identity and are difficult due to the short lifespan of the intermediates. Fine-tuning of DFT calculations to verify the species and interrogate the unique electronic structure that the β hydrogen system of **4** provides.

The intramolecular mechanism also mimics the IPNS mechanism of forming a thioaldehyde that may have importance for directing the reactivity of the second active oxidant, a high valent Fe-oxo to close the β -lactam ring. Oxo-atom donors were employed with complex **4** in order to generate an oxo-atom adduct, which may perform HAT from the β-H on the ligand or from solvent producing a putative Fe^{III}-OH, **4-OH**. The β-hydrogen scaffold is very open to further investigations or other modifications to compare sterics and electronics of forming dioxygen active intermediates. One such complex that has been synthesized is $[Fe^{III}(S_2{}^{\beta\text{-}H2}N_2N^{Me}(Pr,Pr))]$ (**9**) **Figure 4.18**, and has preliminary results of dioxygen reactivity on par with $[Fe^{III}(S_2{}^{Me2}N_2N^{Me}(Pr,Pr))]$.

4.4 Experimental Details

4.4.1 General Methods

All reactions were performed under dinitrogen atmosphere in a glovebox, standard Schlenk techniques, or using a custom-made solution cell with a threaded glass connector to fit a dip probe. Reagents purchased from commercial vendors were of the highest purity and used without further purification. Acetonitrile (MeCN), toluene, diethyl ether (Et_2O), tetrahydrofuran (THF), dichloromethane (DCM) were rigorously degassed and purified using solvent purification columns housed in a custom stainless-steel cabinet, dispensed via a stainless steel Schlenk-line (GlassContour). Methanol (MeOH) was distilled from magnesium methoxide and degassed prior to use. The synthesis of 3-methyl-3-mercapto-2-butanone and $[Fe^{II}S_2{}^{\beta\text{-}H2}N_2N^H(Pr,Pr)]$•MeOH were done according to literature precedent.[35]

^{1}H-NMR and ^{2}H-NMR spectra were recorded on Bruker AV 300 or AV 301 FT-NMR spectrometers and are referenced to an internal standard of tetramethylsilane (TMS). Chemical shifts are reported in ppm and coupling constants (J) in Hz. Electrospray ionization mass spectrometry (ESI-MS) was performed on a Bruker Esquire LC-Ion Trap. Gas chromatography-mass spectrometry (GM-MS) was performed on an Agilent 5973 inert gas chromatograph/mass spectrometer (GC/MS). Infrared spectroscopy (IR) was performed on a Perkin Elmer FT-IR/FIR spectrometer with nujol mull on KBr.

Low-temperature electronic absorption spectra were recorded using a Varian Cary 50 or 60 spectrophotometers equipped with a fiber optic cable connected to a “dip” attenuated total reflection probe (C-technologies), with a custom-built two-neck solution sample holder with a threaded glass connector (sized to fit the dip probe) purged with argon gas. Modeling and

molecular mechanics were performed on Avogadro (version 1.2.0).[47] Cyclic voltammograms were recorded in MeCN (0.1 M tetrabutylammonium(PF_6) solution) using a CH instruments (CHI600E) potentiostat with a glassy carbon working electrode, a $Ag/AgNO_3$ working electrode, and a platinum auxiliary electrode. Magnetic susceptibility data were acquired by Evan's method as modified for a superconducting solenoid.[48] Temperatures were obtained using Van Geet's method.[49]

Calculations were performed using the ORCA v. 4.1. quantum chemistry package developed by Neese and coworkers,[50] and employed a polarized triple-zeta def2-TZVP basis set, the def2/J auxiliary basis set for Coulomb fitting, and the atom-pairwise dispersion correction of Grimme (D3BJ).[51] Tight convergence criteria were required for self-consistent field (SCF) solutions. The Grid4 (GridX4) integration grid size, and the conductor-like polarizable continuum model with the dielectric constant e = 7.25 for tetrahydrofuran solvent (CPCM(THF)), were used for geometry optimizations.[52] Geometry optimizations and analytical frequency calculations were performed using the CAM-B3LYP functional, with the resolution of identity (RI) chain-of-spheres (RIJCOSX) approximation,[53,54] and initiated from the crystallographic coordinates when available. Analytical frequency calculations were performed on all optimized structures to determine whether the obtained stationary points corresponded to local minima. Chemcraft was used to visualize calculated EAS and IR spectra.[55] Excited states from TD-DFT calculations were analyzed using Natural Transition orbitals (NTOs) and by visualizing their difference densities between the ground and excited states. Canonical molecular orbital isosurfaces and natural transition orbitals in the TD-DFT calculations were visualized at an isovalue of 0.05 a03 using UCSF Chimera.[56]

4.4.2 Synthesis of [$Fe^{II}(S_2{}^{\beta\text{-}H2}N_2N^H(Pr,Pr))$]•MeOH (4)

Sodium methoxide (0.324 g, 6 mmol) was added to 10 mL MeOH in a 20 mL scintillation vial with a stir bar. 2,5-dihydroxy-2,5-dimethyl-1,4-dithiane (0.541 g, 3 mmol) was added to the reaction mixture and stirred at room temperature for 10 minutes and chilled at -30 °C for 30 minutes. In an additional scintillation vial iron(II) chloride (0.380 g, 3 mmol) was dissolved in 10 mL MeOH and chilled at -30 °C for 30 minutes. The iron solution was slowly added, over thirty minutes while stirring at room temperature, and storing the iron solution in the freezer between pipet additions, to afford a translucent green solution. The reaction is stirred for 1 hour. 3,3'-Iminobis(propylamine) (0.394 g, 3 mmol) was added dropwise to the green solution and stirred for an additional three hours before being placed in the -30 °C freezer overnight. The solvent was reduced to ~4 mL by vacuum and filtered over celite. The solution was completely dried under vacuum and dissolved in minimal MeOH and filtered over a bed of wet celite. The solids were recrystallized from MeOH/Ether layering to afford green crystals (0.452 g, 1.25 mmol, 42% yield). Electronic absorption (MeOH) λ_{max} (ε, $M^{-1}cm^{-1}$) = 376 (930) nm; (THF) λ_{max} (ε) = 420 (970) nm; (H2O) λ_{max} (ε) =359 (820) nm; (MeCN) λ_{max} (ε) = 396 (860) nm. Ambient temperature (297 K) μeff) 5.15 μB in MeOH solution. IR ν (cm^{-1}): 1637 (imine). Anal. Calcd for FeC12H23N3S2: C, 43.77; H, 7.04; N, 12.76. Found: C, 43.36; H, 6.95; N, 12.63.26

4.4.3 Synthesis of d_5-(chloroacetone)

Adapted from the patent: US4310702A.[40] In a 100 mL round bottom schlenk flask fitted with a stir bar, d_6-acetone (4.375 g, 100 mmol, 1 equivalent), and methanol (300 mmol, 3 equivalent) were dissolved in 50 mL of DCM. Sulfuryl chloride (8.181 g, 110 mmol, 1.1 equivalent) were added dropwise over 10 minutes. After gaseous evolution of HCl, SO_2, and chloromethane has stopped, the reaction was refluxed for 2 hours, washed with saturated $NaHCO_3$, H_2O, and dried over Na_2SO_4. The solvent removed under vacuum to yield d_5-chloroacetone as a slight yellow liquid (1.148 g, 3.13 mmol, 67% yield). ^{13}C-NMR (300 MHz, $CDCl_3$): δ = 199.65, 47.97, 25.90. GC-MS calcd for $[C_3D_5OCl]^+$ 97 found: 97.

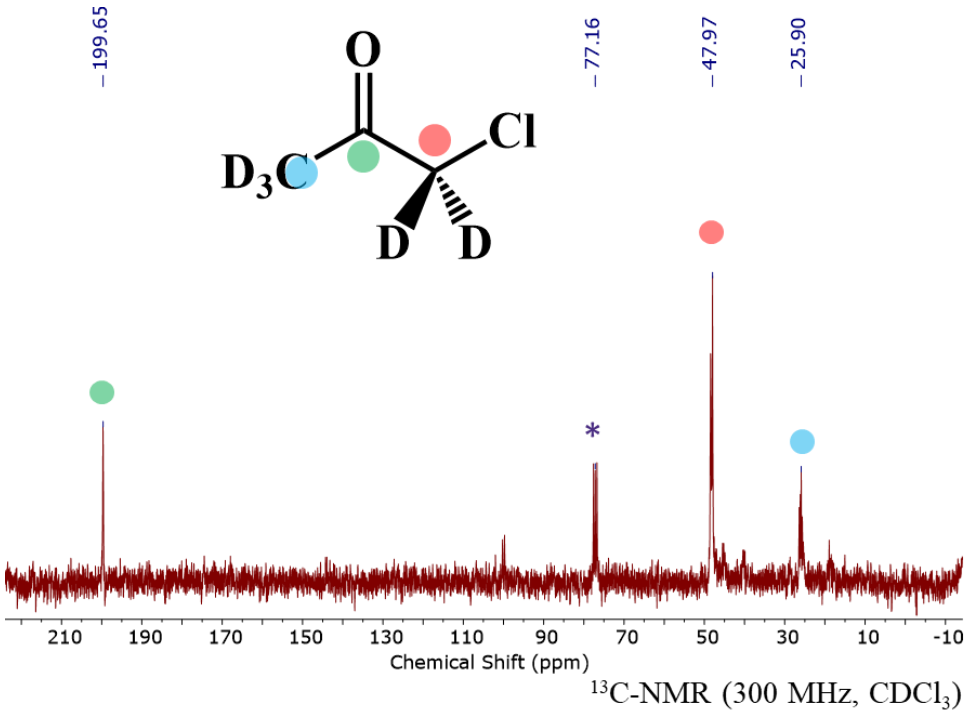

Figure 4. 19 ^{13}C-NMR (300 MHz, $CDCl_3$) spectrum of d_5-(chloroacetone). The * denotes solvent peak.

4.4.4 Synthesis of d_5(1-mercaptoacetone, acetate)

In a 100 mL round bottom Schlenk flask fitted with a stir bar, thioacetic acid (4.719 g, 68.2 mmol 1.1 equivalent) and triethylamine (7.529 g, 74.4 mmol, 1.2 equivalent) were cooled to 0 °C. D_5-(chloroacetone) (6.049 g, 62 mmol, 1 equivalent) was added dropwise over 30 minutes to yield a dark orange gel. The reaction mixture was stirred overnight under inert atmosphere. Next, the gel was dissolved in 1:3 ethyl acetate:hexanes and run through a silica plug to obtain a foul smelling dark orange liquid. The solution was removed with vacuum evaporation to yield the

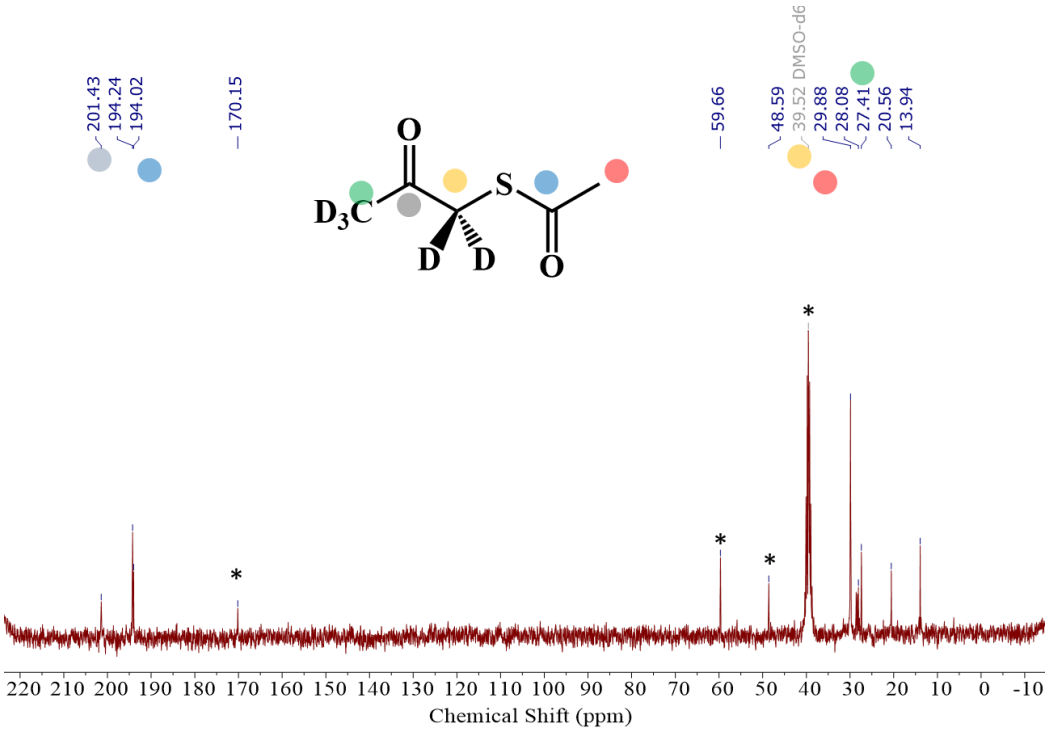

Figure 4. 20 ^{13}C-NMR (300 MHz, DMSO-d_6) spectrum of d_5-(1-mercaptoacetone, acetate). The * denotes solvent peak, and acetic acid.

desired product as a dark orange foul-smelling liquid. ^{13}C-NMR (300 MHz, $CDCl_3$): δ = 203, 194, 37, 30, 27.

4.4.5 Synthesis of [$Fe^{II}(S_2^{\beta\text{-}D2}N_2N^H(Pr,Pr))$]•MeOH (8)

Sodium methoxide (0.324 g, 6 mmol) was added to 10 mL MeOH in a 20 mL scintillation vial with a stir bar. D_5(1-mercaptoacetone, acetate) (0.541 g, 3 mmol) was added to the reaction mixture and stirred at room temperature for 10 minutes. Next, 3,3'-Iminobis(propylamine) (0.394 g, 3 mmol) was added dropwise and stirred for 20 minutes, then chilled at -30 °C for 30 minutes. In an additional scintillation vial iron(II) chloride (0.380 g, 3 mmol) was dissolved in 10 mL MeOH and chilled at -30 °C for 30 minutes. The iron solution was slowly added, over thirty minutes while stirring at room temperature, and storing the iron solution in the freezer between pipet additions, to afford a translucent green-brown solution. The reaction is stirred for three hours before being placed in the -30 °C freezer overnight. The solvent was reduced to ~4 mL by vacuum and filtered over celite. The solution was completely dried under vacuum and dissolved in minimal MeCN and filtered over a bed of wet celite and dried under vacuum. The solids were recrystallized from MeOH/Ether layering to afford green crystals in black liquid. Yield has not been calculated. Electronic absorption and extinction coefficients needed for MeOH and THF.

4.4.6 Generation of proposed [$Fe^{III}(S_2^{\beta\text{-}H2}N_2N^H(Pr,Pr))(O_2)$] 5 with excess O_2

A 0.5 mM solution of (**4**) was prepared in 5 mL of THF under an inert atmosphere in a drybox. The solution was transferred via gastight syringe to a custom-made dip probe cell, previously purged with argon, and cooled to -78 ˚C. The solution had O_2 bubbled through the solution and the formation of a short-lived intermediate formed and was characterized by EAS with λ_{max} = 400 nm, 530 nm, 704 nm.

4.4.7 Generation of proposed [$Fe^{III}S_2^{\beta\text{-}H2}N_2N^H(Pr,Pr)(OMe]$ with excess O_2

A 0.5 mM solution of (**4**) was prepared in 5 mL of MeOH under an inert atmosphere in a drybox and transferred to a long neck quartz cuvette with an airtight cap. The resulting solution

was cooled to -90 °C via liquid nitrogen temperature-controlled cryostat. A gastight syringe was filled with pure O_2 from a purged round bottom flask and added to the cooled solution. Formation of an intermediate species characterized by EAS with the λ_{max} = 665 and a shoulder at 567 nm.

4.4.8 Generation of solvent bound [$Fe^{III}S_2^{\beta\text{-}H2}N_2N^H$(Pr,Pr)(MeOH)].

A 0.5 mM of solution of (**4**) was prepared in 5 mL of MeOH under an inert atmosphere in a drybox and transferred to a long neck quartz cuvette with an airtight cap. The resulting solution was cooled to -90 °C via liquid nitrogen temperature-controlled cryostat. Addition of 1.1 equivalents of ferrocenium hexafluorophosphate in 250 µL MeCN 0.55 mM to the solution generated the formation of an orange species characterized by EAS with λ_{max} = 665 nm, 414 nm, and a shoulder at 567 nm.

4.4.9 Generation of azide bound [$Fe^{III}S_2^{\beta\text{-}H2}N_2N^H$(Pr,Pr)($N_3$)].

A 0.5 mM of solution of (**4**) was prepared in 5 mL of MeOH under an inert atmosphere in a drybox and transferred to a long neck quartz cuvette with an airtight cap. The resulting solution was cooled to -73 °C. Addition of 1.1 equivalents of ferrocenium hexafluorophosphate in 250 µL MeCN 0.55 mM then 5 equivalents of tetrabutylammonium azide added. Generation of a red species characterized by EAS with λ_{max} = 470, 700 nm.

4.4.10 Addition of PhIO to [$Fe^{II}(S_2^{\beta\text{-}H2}N_2N^H$(Pr,Pr))]•MeOH (4)

A 0.5 mM solution of (**4**) was prepared in THF under an inert atmosphere in a drybox. The solution was transferred via gastight syringe to a custom-made dip probe cell, previously purged with argon. The solution was cooled to -78 °C. Addition of 5 equivalents of PhIO in 250 µL MeOH (1.25×10^{-5} mol) via gastight syringe and the formation of a green species characterized by EAS with λ_{max} = 704 nm.

4.4.11 Addition of IBX-ester to [$Fe^{II}(S_2{}^{\beta\text{-}H2}N_2N^H(Pr,Pr))$]•MeOH (4)

A 0.5 mM solution of (**4**) was prepared in THF under an inert atmosphere in a drybox. The solution was transferred via gastight syringe to a custom-made dip probe cell, previously purged with argon. The solution was cooled to -78 °C. Addition of 5 equivalents of IBX-ester in 250 µL MeOH (1.25×10^{-5} mmol) via gastight syringe and the formation of a green species characterized by EAS with λ_{max} = 675 nm.

4.4.12 Generation of hydroxide bound [$Fe^{III}(S_2{}^{\beta\text{-}H2}N_2N^H(Pr,Pr))(OH)$] (4-OH).

A 0.5 mM of solution of (**4**) was prepared in 5 mL of MeOH under an inert atmosphere in a drybox and transferred to a long neck quartz cuvette with an airtight cap. The resulting solution was cooled to -73 °C. Addition of 1.1 equivalents of ferrocenium hexafluorophosphate in 250 µL MeCN 0.55 mM then 1 equivalent of tetrabutylammonium hydroxide solubilized in MeOH in 250 µL was added. Generation of a yellow species characterized by EAS with λ_{max} = 574 nm.

4.4.13 Generation of nitrosyl bound [$Fe^{II}(S_2{}^{\beta\text{-}H2}N_2N^H(Pr,Pr))$] (4).

A 30 mM solution of **4** was prepared in THF under an inert atmosphere in a drybox and transferred to a high vacuum line in a long neck schlenk flask. The resulting solution was frozen with liquid nitrogen and 1 atmosphere of nitric oxide gas was transferred. The solution was allowed to thaw and brought back into the glovebox. The solution was diluted to 0.5 mM and 5 mL was transferred to a long neck quartz cuvette with an airtight cap. Generation of a forest green species characterized by EAS with λ_{max} = 416, and 677 nm.

4.4.14 Generation of hydroperoxo bound [$Fe^{III}S_2{}^{\beta\text{-}H2}N_2N^H(Pr,Pr)(OOH)$].

A 0.5 mM of solution of (**4**) was prepared in 5 mL of THF under an inert atmosphere in a drybox and transferred to a long neck quartz cuvette with an airtight cap. The resulting solution

was cooled to -73 °C. Addition of 5 equivalents of TEMPOH was added to **4**, then excess dry dioxygen from a tank was bubbled into solution. Generation of a green species characterized by EAS with λ_{max} = 664 nm.

4.5 Chapter 4 References

(1) Greiner, Maria; Downing, Alexandra, N.; Blakely, Maike N.; Piquette, Marc C.; Kovacs, Julia A. Cryogenic Stopped-Flow Kinetic Studies Involving the Formation of a Thiolate-Ligated FeIII-Superoxo *Manuscript Submitted*

(2) Niederhoffer, E. C.; Timmons, J. H.; Martell, A. E. Thermodynamics of Oxygen Binding in Natural and Synthetic Dioxygen Complexes. *Chem. Rev*. **1984**, 84 (2), 137–203. DOI: 10.1021/cr00060a003.

(3) Busch, D. H.; Alcock, N. W. Iron and Cobalt "Lacunar" Complexes as Dioxygen Carriers. *Chem. Rev*. **1994**, 94 (3), 585–623. DOI: 10.1021/cr00027a003.

(4) Matthews, M. L.; Neumann, C. S.; Miles, L. A.; Grove, T. L.; Booker, S. J.; Krebs, C.; Walsh, C. T.; Bollinger, M. Jr. Substrate positioning controls the partition between halogenation and hydroxylation in the aliphatic halogenase, SyrB2. *Proc. Natl. Acad. Sci. USA.* **2009**, 106, 42, 17723-17728 DOI: 10.1073/pnas.0909649106

(5) Timmins, A.; Fowler, N. J.; Warwicker, J.; Straganz, G. D.; de Visser, S. P. Does Substrate Positioning Affect the Selectrivity and Reactivity in the Hectochlorin Biosynthesis Halogenase? *Front. Chem.* **2018**, 6, 513, 1-19 DOI: 10.3389/fchem.2018.00513

(6) Rybak-Akimova, E. V. Mechanisms of Oxygen Binding and Activation at Transition Metal Centers. In Physical Inorganic Chemistry; John Wiley & Sons, Inc.: Hoboken, NJ, USA, **2010**; Vol. Vol. 2., pp 109–188 DOI: 10.1002/9780470602577.ch4.

(7) Roach, P. L.; Cllftont, J.; Fiilipt, V.; Harlost, K.; Bartont, G. J.; Hajdut, J.; Anderssontt, I.; Schofield, C. J.; Baldwin, J. E. New Structural Family of Enzymes. *Nature* **1995,** 375 353, 6533, 700-704 DOI: 10.1038/375700a0

(8) McCoy, J. G.; Bailey, L. J.; Bitto, E.; Bingman, C. A.; Aceti, D. J.; Fox, B. G.; Phillips, G. N. Structure and Mechanism of Mouse Cysteine Dioxygenase. *Proc. Natl. Acad. Sci. U. S. A.* **2006**, 103 (9), 3084–3089. DOI: 10.1073/pnas.0509262103.

(9) Goudarzi, S.; Babicz, J. T. Jr.; Kabil, O.; Banerjee, R.; Solomon, E. I. Spectroscopic and Electronic Structure Study of ETHE1: Elucidating the Factors Influencing Sulfur Oxidation and Oxygenation in Mononuclear Nonheme Iron Enzymes. *J. Am. Chem. Soc.* **2018**, 140, 44, 14887-14902 DOI: 10.1021/jacs.8b09022

(10) Solomon, E. I.; DeWeese, D. E.; Babicz, J. T. Jr. Mechanisms of O_2 Activation by Mononuclear Non-Heme Iron Enzymes. *Biochemistry* **2021**, 60, 46, 3497-3506 DOI: 10.1021/acs.bichem.1c00370

(11) Long, A. J.; Clifton, I. J.; Roach, P. L.; Baldwin, J. E.; Rutledge, P. J.; Schofield, C. J. Structural Studies on the Reaction of Isopenicillin N Synthase with the Truncated Substrate Analogues δ-(l-α-aminoadipoyl)-l-cysteinyl-glycine and δ-(l-α-aminoadipoyl)-l-cysteinyl-d-alanine. *Biochemistry*, **2005**, 44, 17, 6619-6628 DOI: 10.1021/bi047478q

(12) Lah, M. S.; Dixon, M. M.; Pattridge, K. A.; Stallings, W. C.; Fee, J. A.; Ludwig, M. L. Structure-Function in Escherichia Coli Iron Superoxide Dismutase: Comparisons with the Manganese Enzyme from Thermus Thermophilus. *Biochemistry* **1995**, 34 (5), 1646–1660. DOI: 10.2210/pdb1MNG/pdb

(13) Kovacs, J. A. and Brines L. M. Understanding How the Thiolate Sulfur Contributes to the Function of the Non-Heme Iron Enzyme Superoxide Reductase. *Acc. Chem. Res.* **2007**, *40* 501-509, DOI: 10.1021/ar600059h.

(14) Soda, T.; Kitagawa, Y.; Onishi, T.; Takano, Y.; Shigeta, Y.; Nagao, H.; Yoshioka, Y.; Yamaguchi, K. Ab Initio Computations of Effective Exchange Integrals for H–H, H–He–H and Mn2O2 Complex: Comparison of Broken-Symmetry Approaches. *Chem. Phys. Lett.* **2000**, 319 (3–4), 223–230 DOI: 10.1016/S0009-2614(00)00166-4

(15) Fontecilla-Camps, J. C. and Nicolet, Y. Metalloproteins: Methods and Protocols. *Human Press Inc.* **2004.**

(16) Blakely, M. N .; Dedushko, M. A.; Poon, P. C. Y.; Villar-Acevedo, G.; Kovacs, J. A. , Formation of a Reactive, Alkyl Thiolate-Ligated FeIII-Superoxo Intermediate Derived from Dioxygen. *J. Am. Chem. Soc.* **2019,** *141*, 1867-1870. DOI: 10.1021/jacs.8b12670

(17) McNeill, L. A.; Brown, T. J. N.; Sami, M.; Clifton, I. J.; Burzlaff, N. I.; Claridge, T. D. W.; Adlington, R. M.; Baldwin, J. E.; Rutledge, P. J.; Schofield, C. J. Terminally Truncated Isopenicillin N Synthase Generates a Dithioester Product: Evidence for a Thioaldehyde Intermediate during Catalysis and a New Mode of Reaction for Non-Heme Iron Oxidases. *Chem. – A Eur. J.* **2017**, 23 (52), 12815-12824, DOI: 10.1002/chem.201701592

(18) Gutman, C. T.; Guzei, I. A.; Brunold, T. C. Structural, Spectroscopic, and Computational Characterization of the Azide Adduct of FeIII(2,6-Diacetylpyridinebis(Semioxamazide)), a Functional Analogue of Iron Superoxide Dismutase. *Inorg. Chem.* **2013**, 52, 8909–8918. DOI: 10.1021/ic401098x

(19) Chai, S. C.; Bruyere, J. R.; Maroney, M. J. Probes of the Catalytic Site of Cysteine Dioxygenase. *J. Biol. Chem*. **2006**, 281, 15774–15779. DOI: 10.1074/jbc.M601269200

(20) Blaesi, E. J.; Fox, B. G.; Brunold, T. C. Spectroscopic and Computational Investigation of Iron(III) Cysteine Dioxygenase: Implications for the Nature of the Putative SuperoxoFe(III) Intermediate. *Biochemistry* **2014**, 53 (36), 5759–5770. DOI: 10.1021/bi500767x.

(21) Blaesi, E. J.; Gardner, J. D.; Fox, B. G.; Brunold, T. C. Spectroscopic and Computational Characterization of the NO Adduct of Substrate-Bound Fe(II) Cysteine Dioxygenase: Insights into the Mechanism of O2 Activation. *Biochemistry* **2013**, 52 (35), 6040–6051. DOI: 10.1021/bi400825c.

(22) Ellison, Jeffrey J.; Nienstedt, Andrew; Shoner, Steven C.; Barnhart, David; Cowen, Jerry A.; Kovacs, Julie, A. Reactivity of Five-Coordinate Models for the Thiolate-Ligated Fe Site of Nitrile Hydratase. *J. Am. Chem. Soc.* **1998**, 120, 23, 5691-5700 DOI: 10.1021/ja973129q

(23) Stynes, D. V.; Hui, Y. S.; Chew, V. Effects of spin change and unsaturation in the axial ligation of carbon monoxide and benzyl isocyanide to iron(II) macrocycles 14ane, 15ane, and TIM. *Inorg. Chem*. **1982**, 21, 3, 1222-1225 DOI:v10.1021/ic00133a068

(24) Matsu-ura, M.; Tani, F.; Naruta, Y. Formation and Characterization of Carbon Monoxide Adducts of Iron “Twin Coronet” Porphyrins. Extremely Low CO Affinity and a Strong Negative Polar Effect on Bound CO. *J. Am. Chem. Soc.* **2002**, 124, 9, 1941-1950 DOI: 10.1021/ja011963g

(25) Sellmann, D.; Kunstmann, H.; Knoch, F.; Moll, M. Transition-metal complexes with sulfur ligands.Part 37. Iron, molybdenum, and ruthenium complexes with pentadentate OS4 and NHS4 ligands combining thiolato, thioether, and ether or amine donor functions: synthesis, structures, and reactivity of carbon monoxide, nitric oxide, trimethylphosphine and hydrazine derivatives. *Inorg. Chem.* **1988**, 27, 23, 4183-4190 DOI: 10.1021/ic00296a019

(26) Pulukkody, R.; Kyran, S.J.; Bethel, R. D.; Hsieh, C.; Hall, M. B.; Darensbourg, D. J.; Darensbourg, M. Y. Carbon Monoxide Induced Reductive Elimination of Disulfide in an N-Heterocyclic Carbene (NHC)/ Thiolate Dinitrosyl Iron Complex (DNIC). *J. Am. Chem. Soc.* **2013**, 135, 22, 8423-8430 DOI: 10.1021/ja403916v

(27) Jackson, T. A.; Karapetian, A.; Miller, A.-F.; Brunold, T. C. Probing the Geometric and Electronic Structures of the Low-Temperature Azide Adduct and the Product-Inhibited Form of Oxidized Manganese Superoxide Dismutase. *Biochemistry* **2005**, 44, 5, 1504–1520. DOI: 10.1021/bi048639t

(28) Grove, L. E.; Hallman, J. K.; Emerson, J. P.; Halfen, J. A.; Brunold, T. C. Synthesis, X-Ray Crystallographic Characterization, and Electronic Structure Studies of a Di-Azide Iron(III) Complex: Implications for the Azide Adducts of Iron(III) Superoxide Dismutase. *Inorg. Chem*. **2008**, 47, 5762–5774. DOI: 10.1021/ic800073t.

(29) Shearer, J.; Fitch, S. B.; Kaminsky, W.; Benedict, J.; Scarrow, R. C.; Kovacs, J. A. How does cyanide inhibit superoxide reductase? Insight from synthetic $Fe^{III}N_4S$ model complexes. *Proc. Natl. Acad. Sci. U. S. A.* **2003**, 100, 7, 3671–3676. DOI: 10.1073/pnas.0637029100

(30) Downing, A. N. Effects of Ligand-Constraints on the Reactivity of Biomimetic Thiolate-Ligated Transition Metal Complexes. Ph. D. Dissertation, University of Washington, Seattle, WA, **2021**

(31) Richter-Addo, G. B.; Legndins, P.; Burstyn, J. Introduction: Nitric Oxide Chemistry. *Chem. Rev.* **2002**, 102,4, 857-860 DOI: 10.1021/cr010188k

(32) Isvoranu, C.; Wang, B.; Ataman, E.; Knudsen, J.; Schulte, K.; Andersen, J. N.; Bocquet, M.; Schnadt, J. Comparison of the Carbonyl and Nitrosyl Complexes Formed by Adsorption of CO and NO on Monolayers of Iron Phthalocyanine on Au(111). *J. Phys. Chem. C.* **2011**, 115, 50, 24718-24727 DOI: 10.1021/jp204461k

(33) McQuilken, A. C.; Ha, Y.; Sutherlin, K. D.; Siegler, M. A.; Hodgson, K. O.; Hedman, B.; Solomon, E. I.; Jameson, G. N. L.; Goldberg, D. P. Preparation of Non-heme $\{FeNO\}^7$ Models of Cysteine Dioxygenase: Sulfur versus Nitrogen Ligation and Photorelease of Nitric Oxide. *J. Am. Chem. Soc.* **2013**, 135, 38,14024-14027 DOI: 10.1021/ja4064487

(34) Villar-Acevedo, G.; Lugo-Mas, P.; Blakely, M. N.; Rees, J. A.; Ganas, A. S.; Hanada, E. M.; Kaminsky, W. Kovacs, J. A. Metal-Assisted Oxo Atom Addition to an Fe(III) Thiolate. *J. Am. Chem. Soc.* **2017**, 139, 1, 119-129, DOI: 10.1021/jacs.6b03512

(35) Shoner, S. C.; Nienstedt, A. M.; Ellison, J. J.; Kung, I. Y.; Barnhart, D.; Kovacs, J. A. Structural Comparison of Five-Coordinate Thiolate-Ligated M^{II} = Fe^{II}, Co^{II}, Ni^{II}, and Zn^{II} Ions Wrapped in a Chiral Helical Ligand. *Inorg. Chem.* **1998**, *37*, 22, 5721-5726 DOI: 10.1021/ic980882r

(36) Warren, J. J.; Tronic, T. a.; Mayer, J. M.; Bond, S. V. G. Thermochemistry of Proton-Coupled Electron Transfer Reagents and Its Implications - Chemical Reviews (ACS Publications). Chem. Rev. **2010**, 110 (12), 6961–7001 DOI: 10.1021/cr100085k

(37) Jeffrey, George A.; *An introduction to hydrogen bonding*, Oxford University Press, **1997**.

(38) Cao, P.; Yao, J.; Ren, B.; Gu, R.; Tian, Z. Surface-Enhanced Raman Scattering Spectra of Thiourea Adsorbed at an Iron electrodie in $NaClO_4$ Solution. *J. Phys. Chem. B.* **2002**, *106*, 39, 10150-10156 DOI: 10.1021/jp0257395

(39) Okazaki, R. Chemistry Synthetic Aspects: Chemistry of thioaldehydes. *O*rganosulfur. **1995**, 1, 225-258 DOI: 10.1002/chin.199622268

(40) Masilamani, D. and Rogic, M. M. Selective Monochlorination of ketones and aromatic alcohols. U.S. Patent WO 4310402A, **1982**

(41) Roach, P. L.; Clifton, I. J.; Hensgens, C. M.; Shibata, N.; Schofield, C. J. Hajdu, J.; Baldwin J. E. Structure of Isopenicillin N Synthase Complexed with Substrate and the Mechanism of Penicillin Formation. *Nature*. **1997**, *137* (6635), 827-830, DOI: 10.1038/42990.

(42) Nam, W.; Jin, S. W.; Lim, M. H.; Ryu, J. Y.; Kim, C. Anionic Ligand Effect on the Nature of Epoxidizing Intermediates in Iron Porphyrin Complex-Catalyzed Epoxidation Reactions. *Inorg. Chem.* **2002**, 41, 14, 3647-3652 DOI: 10.1021/ic011145p

(43) Nam. W.; Choi, S. K.; Lim, M. H.; Rohde, J.; Kim, I.; Kim, J.; Kim, C.; Que, L. Jr. Reversible Formation of Iodosylbenzene-Iron Porphyrin Intermediates in the Reaction of

Oxoiron(IV) Porphyrin pi-Cation Radicals and Iodobenzene. *Ang. Chem. Int. Ed.* **2003**, 42, 1, 109-111 DOI: 10.1002/anie.200390036

(44) Kundu, S.; Thompson, J. V. K.; Ryabov, A. D.; Collins, T. J. On the Reactivity of Mononuclear Iron(V)oxo Complexes. *J. Am. Chem. Soc.* **2011**, 133, 46, 18546-18549 DOI: 10.1021/ja208007w

(45) Rittle, J.; Green, M. T. Cytochrome P450 compound I: capture, characterization, and C-H bond activation kinetics. *Science*. **2010**, *330*, 933- 937, DOI: 10.1126/science.1193478

(46) Luo, Y.-R. Comprehensive Handbook of Chemical Bond Energies; CRC Press, **2007**

(47) Hanwell, M. D.; Curtis, D. E.; Lonie, D. C.; Vandermeersch, T.' Zurek, E.; Hutchison, G. R. Avogadro: An advanced semantic chemical editor, visualization, and analysis platform *Journal of Cheminformatics* **2012**, 4:17 Version 1.2.0

(48) Evans, D. A., The Determination of the Paramagnetic Susceptibility of Substances in Solution by Nuclear Magnetic Resonance. *J. Chem. Soc.* **1959**, 2003-2005. DOI: 10.1039/JR9590002003

(49) Van Geet, A. L., Calibration of the Methanol and Glycol Nuclear Magnetic Resonance Thermometers with a Static Thermistor Probe. *Anal. Chem.* **1970**, *42*, 2227-2229. DOI: 10.1021/ac50158a064

(50) Neese, Frank. Software update: The ORCA program system – Version 5.0. *WIREs Computational Molecular Science.* **2022**, 12, 5 e1606, DOI: 10.1002/wcms.1606

(51) Grimme, Stefan; Ehrlich, Stephan; Goerigk, Lars. Effect of the damping function in dispersion corrected density functional theory. *J. Compt. Chem.* **2011**, 32, 7, 1456-1465, DOI: 10.1002/jcc.21759

(52) Barone, V.; Cossi, M., Quantum Calculation of Molecular Energies and Energy Gradients in Solution by a Conductor Solvent Model. *J. Phys. Chem.* **1998,** *102*, 1995 -2001. DOI: 10.1021/jp9716997

(53) Yanai, T.; Tew, D. P.; Handy, N. C. A new hybrid exchange-correltation functional using the Coulomb-attenuating method (CAM-B3LYP). **2004** *Chem. Phys. Lett.*, **2004**, 393, 51-57 DOI: 10.1016/j.cplett.2004.06.011

(54) Neese, Frank. Efficient, approximate, and parallel Hartree-Fock and hybrid DFT calculations. A 'chain-of-spheres' algorithm for the Hartree-Fock exchange. *Chemical. Physics.* **2009**, 356, 1-3, 98-109, DOI: 10.1016/j.chemphys.2008.10.036

(55) Zhurko, G. A. Chemcraft – graphical program for visualization of quantum chemistry computations. Ivanovo, Russia, **2005**. https://chemcraftprog.com

(56) Pettersen, Eric F.; Goddard, Thomas D.; Huang, Conrad C.; Couch, Gregory S.; Greenblatt, Daniel M.; Meng, Elaine C.; Ferrin, Thomas E. UCSF Chimera—a visualization system for exploratory research and analysis. *J. Compt. Chem.* **2004**, 25, 13, 1605-1612, DOI: 10.1002/jcc.20084

(57) Rogers, D. M. Structural Effects on the Kinetics and Thermodynamics of Making and Breaking O-O Bonds. Ph. D. Dissertation, University of Washington, Seattle, WA, **2023**

Chapter 5: Investigation of Thiolate Ligated Fe^{III}-Hydroperoxo Derived from Dioxygen in Porphyrin Like Ligand Framework

Portions of this chapter have been republished or adapted with permission of the Journal of American Chemical Society from, "A Functional Model for the Cysteinate-Ligated Non-Heme Iron Enzyme Superoxide Reductase (SOR)" Kitagawa, T.; Dey, A.; Lugo-Mas, P.; Benedict, J. B.; Kaminsky, W.; Solomon, E.; Kovacs, Julie A. *J. Am. Chem. Soc.* **2006**, 128, 45, 14448-14449. DOI: 10.1021/ja064870d

5.1 Introduction

Enzyme dioxygen activation catalysis is a greener form of chemistry and more sustainable and beneficial to production of consumer products versus rare earth metal catalysis.[1,2] Investigation of the mechanism of dioxygen activation remains a focus to develop efficient catalysts utilizing inexpensive and environmentally friendly metals.[3] Dioxygen derived oxidative reactants such as transition-metal hydroperoxos are capable of oxygen atom transfer, hydrogen atom transfer, and aldehyde deformylation.[4-6] The oxidizing power of hydroperoxos has been thought to be weaker than their high-valent oxo counterparts. However, the reactivity studied involves Fe^{III}-OOH lacking thiolates in the first coordination sphere, and thiolates have been shown to enhance the strength dioxygen generated metal-oxidants.[7-10] Iron-hydroperoxo compounds can be generated from dioxygen, or through the shunt pathway via the addition of H_2O_2. The shunt pathway is an

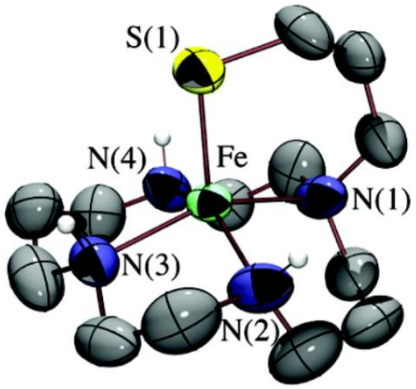

Figure 5. 1 ORTEP diagram of $[Fe^{II}CyclamPr,S]^+$ (**1**) with hydrogens removed, showing thermal ellipsoids at the 50% probability level.

alternate route to forming hydroperoxos by using organic peroxides as opposed to diatomic dioxygen and generating single oxygen active intermediates after O-O bond cleavage.[11,12]

Previous work in the Kovacs lab, has shown that the reaction between a high-spin, $S = 2$ propyl thiolate ligated cyclam complex, $[Fe^{II}CyclamPr,S]^+$ (**1, Figure 5.1**) and superoxide in the presence of an external proton source forms a well-defined high-spin, $S = 5/2$, $[Fe^{III}CyclamPr,S(OOH)]^+$ (**2**) with g-values of 2.26, 2.11, and 1.91.[14] Complex **2** has a characteristic electronic absorption band at 530 nm, **Figure 5.5**.[13] Resonance Raman revealed an $^{16}O–^{16}O$ stretch at 891 cm^{-1} , an $^{18}O–^{18}O$

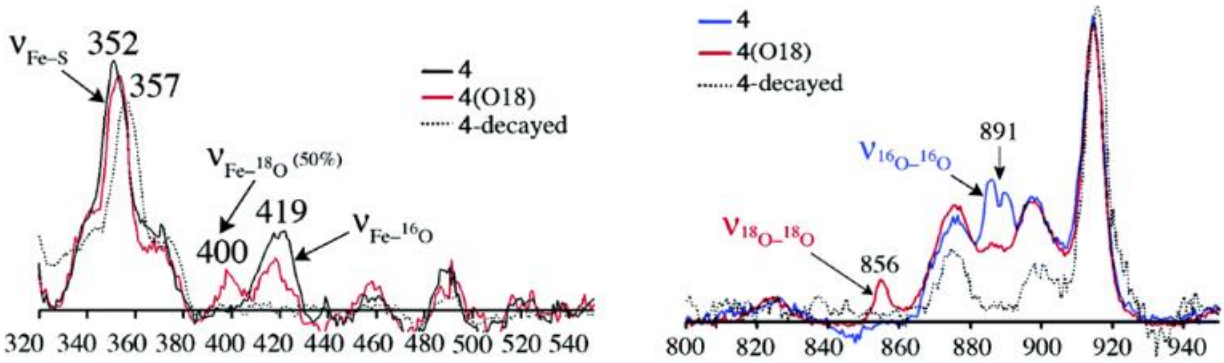

Figure 5. 2 Resonance Raman spectra of **2** generated from $^{16}O_2^-$ (blue), $^{18}O_2^-$ (red), and "decayed" product (dashed black) (571 nm excitation @ 183 K in THF/MeOH (right); at 77 K in CH_2Cl_2/THF/MeOH (left).[13]

stretch at 856 cm^{-1}, and Fe-^{16}O stretches at 419 cm^{-1} and an Fe-^{18}O stretch at 400 cm^{-1} indicating a typical end-on peroxo, **Figure 5.2**.[13] The Fe^{III}-hydroperoxo is a rare example of a high-spin species with a *trans* thiolate. A dioxygen mimic, nitric oxide gas, was also previously introduced to $[Fe^{II}CyclamPr,S]^{+}$ at low temperature to reveal an absorption band at 518 nm and a crystal structure, **Figure 5.4** was obtained to show the NO ligand *cis* to the thiolate with the macrocycle undergoing rearrangement to provide space for the NO ligand.[14] Due to the ligand rearrangement that **1** undergoes with NO, the dioxygen intermediate **2** may bind the oxygen moiety either *trans* or *cis* to the thiolate.

The emphasis of **Chapter 5** will be determining whether Fe^{III}-OOH **2** can be generated using **1** and dioxygen and utilizing density functional theory (DFT) and time-dependent DFT (TD-DFT)

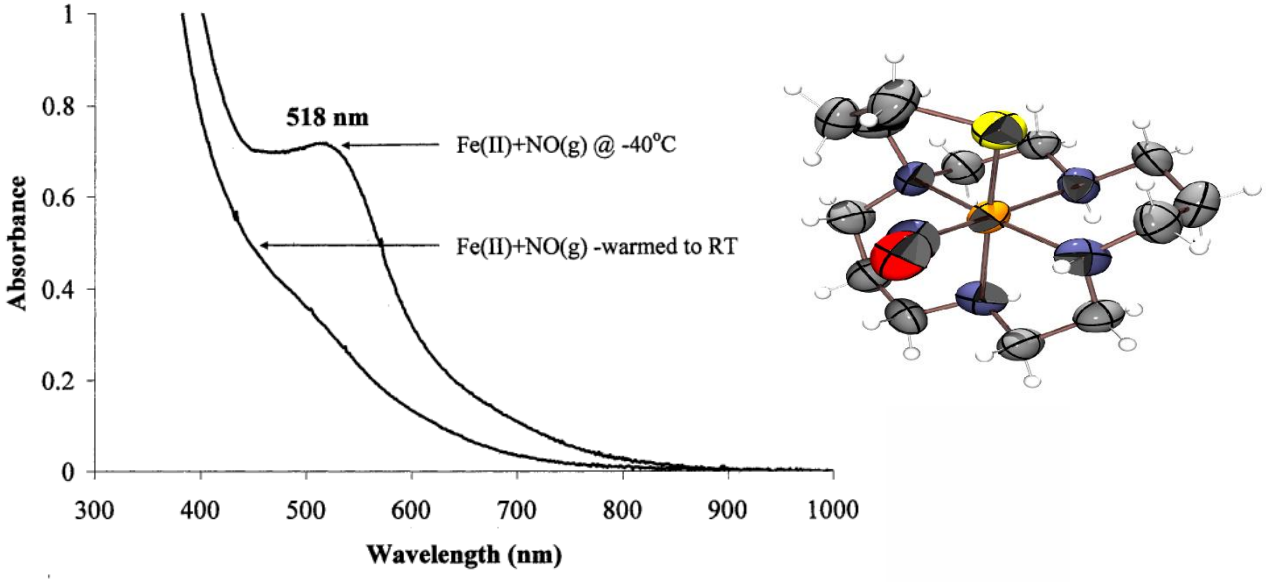

Figure 5. 4 Left: The reaction of **1** with NO(g) in MeCN. The reaction was initialized at -40 °C, and the peak at 518 nm was allowed to maximize. After the band maximized in intensity, the solution was gradually warmed to room temperature. **Right**: ORTEP diagram of $[Fe^{III}CyclamPr,S(NO)]$ (**3**). The complex is six-coordinate, with the NO binding *cis* to the thiolate moiety. The NO has bound in a bent geometry, indicating that the complex is most likely in the Fe^{III} oxidation state.[14]

to elucidate whether the hydroperoxo binds *cis* or *trans* to the thiolate. We also hoped to generate more stable alkylperoxo derivatives of **2**, Fe^{III}-OOR, in order to determine their oxidizing strength.

5.2 Results and Discussion

5.2.1 Dioxygen Reactivity

The addition of dioxygen to complex **1** affords a purple species with an absorption band at 530 nm (**Figure 5.5**) with molar absorptivity similar to hydroperoxo **2** generated from KO2 and 82 eq. of MeOH as a proton source. The dioxygen generated 530 nm species is proposed to be an Fe^{III}-OOH, generated by dioxygen activation followed by HAT from DCM solvent (BDE = 100 kcal/mol), or a Fe(III)-superoxo, DCM, with a C-H bond strength of 100 kcal/mol,[15] or hydrogen bonding to stabilize the proposed superoxo species from the hydrogens on the macrocycle. Further characterization is required such as EPR, or resonance Raman, to compare authentic samples of Fe^{III}-OOH **2** to confirm that dioxygen activation of **1** can form an Fe^{III}-OOH in a "greener" way.

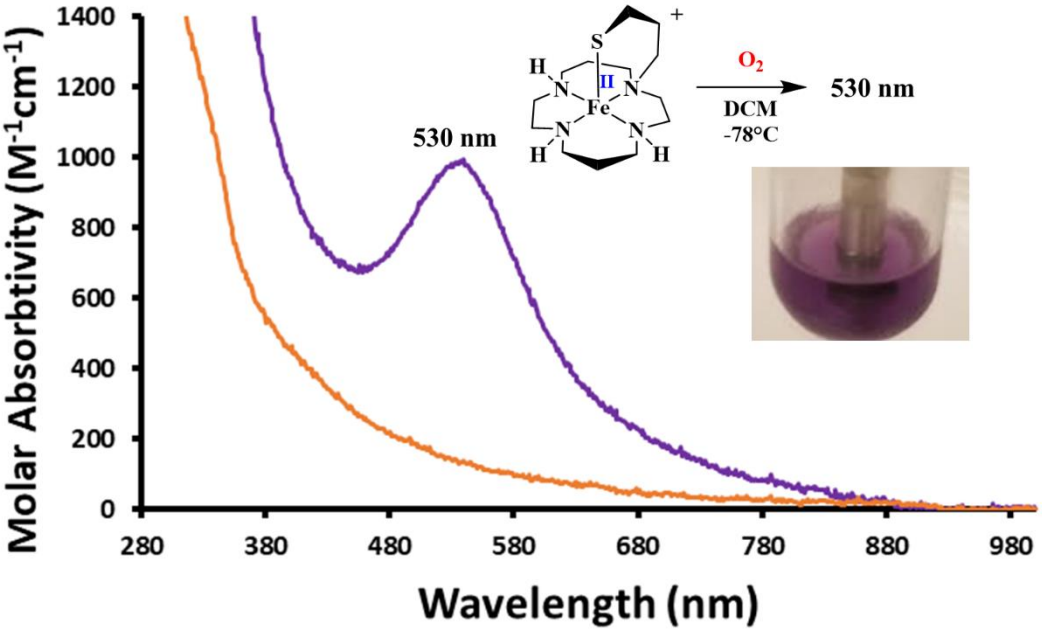

Figure 5. 5 EAS spectrum of **2** generated by **1** reacting with dioxygen in DCM at -73 °C forming a 530 nm species with similar extinction coefficient as the superoxide generated **2**.

5.2.2 Computational Experiments for Hydroperoxo Intermediate

Density function theory (DFT) geometry optimizations were performed with the PBE0 functional and the polarized triple zeta def2-TZVP starting from the crystal structure previously reported $[Fe^{II}CyclamPr,S]^+$ (**1**)[13] The structure of **1** was modified to fit the structure of **2** by adding the hydroperoxo ligand (OOH^-) *trans* to the thiolate. The Fe^{III} metal center was assumed to be S = 5/2, based on the spin-state of the experimental EPR for **2**. The same conditions were applied for the *cis* Fe^{III}-OOH. Frequency calculations were also performed and had no negative modes, confirming valid structures for both *trans* and *cis* hydroperoxos. The calculated structures for NO bound **3**, *trans* Fe^{III}-OOH, and *cis* Fe^{III}-OOH are summarized in **Table 5.1**. The Fe-S bond (Fe-S = 2.37597 Å) for the thiolate that is *trans* to the hydroperoxo (OOH^-) is relatively the same length as the *cis* Fe-S bond (Fe-S = 2.37696 Å). One would expect that binding of OOH^- would have a "push-pull effect" on the *trans* thiolate and elongate the Fe-S bond. However, this effect is seen on both configurations of **2** as the atom bound to the Fe center *trans* to the thiolate is elongated,

Table 5. 1 Bond distances for core atoms of *cis*-$[Fe^{III}CyclamPr,S(NO)]$ (**3**), obtained from X-ray crystallography, and calculated *trans* and *cis* $[Fe^{III}CyclamPr,S(OOH)]^+$ (**2**).

Bond (Å)	$[Fe^{III}CyclamPr,S(NO)]$ (3)	*Trans* $[Fe^{III}CyclamPr,S(OOH)]^+$	*Cis* $[Fe^{III}CyclamPr,S(OOH)]^+$
Fe-S	2.25802	2.37597	2.37696
Fe-N1	2.12506	2.20820	2.20078
Fe-N2	2.18096	2.18105	2.21617
Fe-N3	2.04180	2.16107	2.17464
Fe-N4	2.10002	2.13378	2.24377
Fe-O	1.73991	1.95933	1.91205
O-O	1.14590	1.41413	1.42087

the Fe-O (1.95933 Å) bond and Fe-N4 (2.24377 Å), for *trans* and *cis* configuration, respectively. The oxygen-oxygen (O-O) bond in both geometries agrees with agree with other metal-hydroperoxo O-O bonds (1.40-1.43 Å).[16]

Time dependent DFT (TD-DFT) calculations were performed on *trans* and *cis* **2** with the PBE0 functional, a polarized triple-zeta def2-TZVP basis set, the def2/J auxiliary basis set and RIJONX

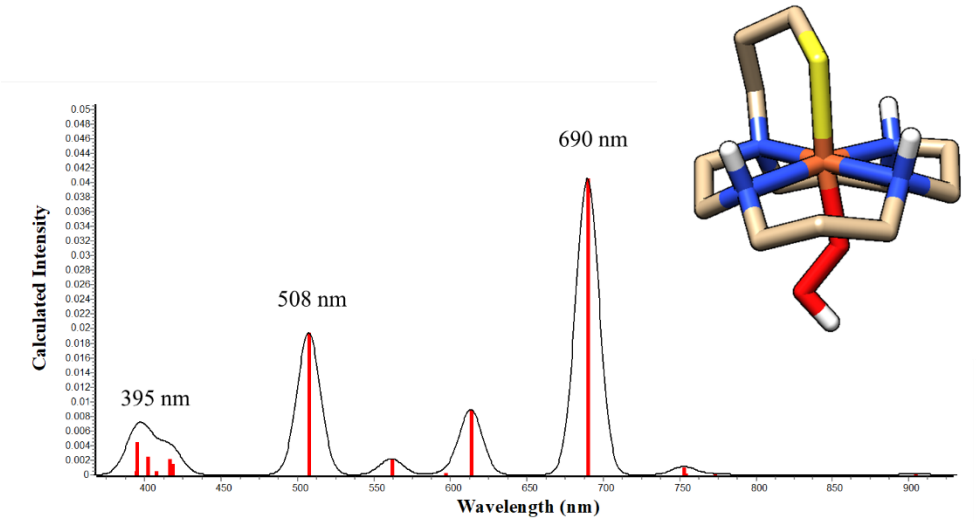

Figure 5. 6 TD-DFT simulated EAS of PBE0 geometry optimized *trans* **2**. The three prominent transitions have been labeled by wavelength (nm).

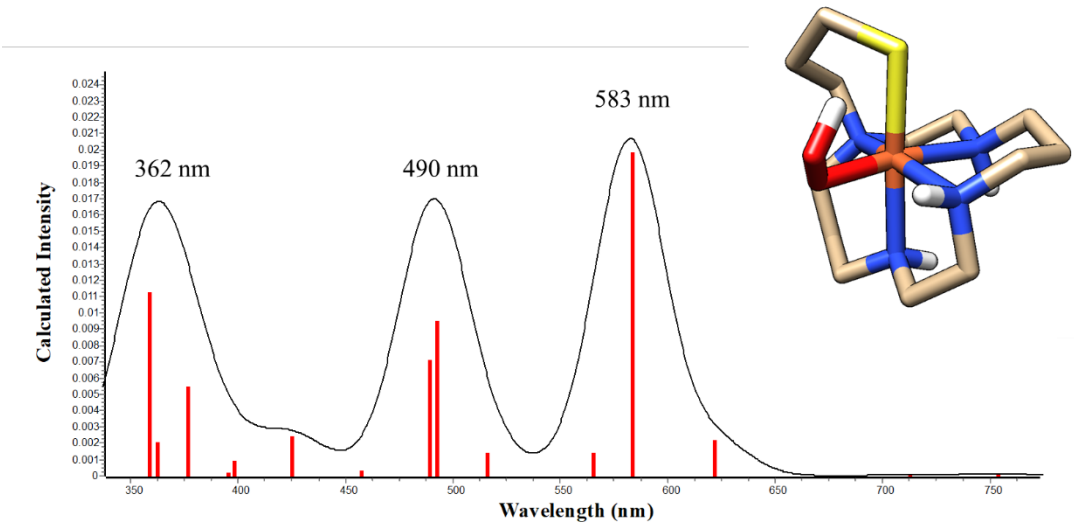

Figure 5. 7 TD-DFT simulated EAS of PBE0 geometry optimized *cis* **2**. The three prominent transitions have been labeled by wavelength (nm).

approximation for Coulomb fitting. The simulated EAS excited state for *trans* **2** (**Figure 5.6**) has three prominent natural transition orbitals (NTO) describing the charge transfer (CT) transitions at 395, 508, and 690 nm. The simulated spectrum does not agree with the experimentally observed **2** formed from dioxygen. The calculated EAS spectrum of *cis* **2** (**Figure 5.7**) also is comprised of three NTOs at 362, 490, and 583 nm. The simulated spectrum does not fully agree with the experimental spectrum of dioxygen generated **2**, however is a closer match than the *trans* configuration.

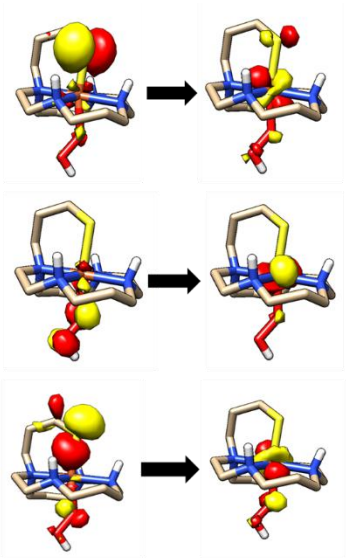

Transitions	S → Fe with O-Oπ*	O-Oπ* → Fe	S + ligand → Fe + O-Oπ*
395 nm	61 %	37 %	1 %
508 nm	66 %	21 %	9 %
690 nm	88 %	7 %	3 %

Figure 5. 8 Natural transition orbitals (NTO) describing the charge transfer (CT) transitions. Each transition is made up of a percentage of S to Fe and O-Oπ* CT character. The *trans* configuration also includes a mixture of S and ligand to Fe CT.

Analysis of the charge transfer transitions for *trans* (**Figure 5.8**) and *cis* (**Figure 5.9**) configurations were evaluated. The main component for *trans* Fe^{III}-OOH is a sulfur to Fe mixed with O-Oπ*, while the *cis* Fe^{III}-OOH is sulfur and O-Oπ* to Fe charge transfers, and is mostly

responsible for the lower energy transitions, while the higher energy transition bands are a mixture of sulfur to Fe or O-Oπ* to Fe CTs. The *trans* Fe^{III}-OOH also had a small component of sulfur and ligand to Fe and O-Oπ* CT that the *cis* configuration did not possess. Overall, the identity of the product formed via the activation of dioxygen by **1** not represented by the calculated structures of

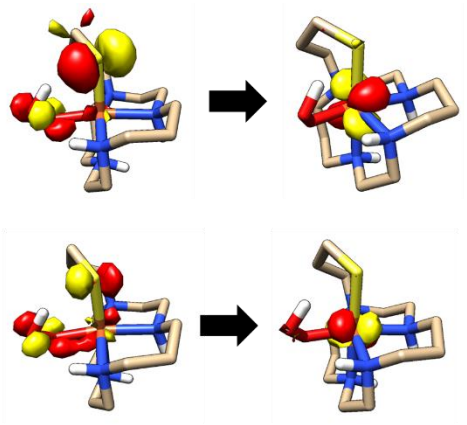

Transitions	S + O-Oπ* → Fe	S + O-Oπ* → Fe
362 nm	62 %	36 %
490 nm	75 %	20 %
583 nm	84 %	14 %

Figure 5. 9 Natural transition orbitals (NTO) describing the charge transfer (CT) transitions. Each transition is made up of a percentage of S to Fe and O-Oπ* CT character.

trans or *cis* Fe^{III}-OOH, or a better calculated model is needed. Calculated models for a Fe^{III}-superoxo are in progress and should be looked into further as to whether the dioxygen generated intermediate with a λ_{max} of 530 nm is such.

5.2.3 Shunt Pathway Hydroperoxo

Other pathways to generate non-heme Fe^{III}-OOH include reacting hydrogen peroxide with complex (**1**) in the presence of base (known as the shunt pathway).[11,12] The shunt pathway provides a more controlled generation of an Fe^{III}-OOH, given that superoxide is poorly soluble and can reversibly bind to metal centers. However, the reactivity of hydrogen peroxide and base can also lead to the formation of a μ-peroxo dimeric species if the peroxo reacts with another equivalent of

Fe^{II}. Hydrogen peroxide can also oxygenate the sulfur instead of binding to the metal center, causing decomposition of the complex. To avoid this, a two-electron oxidant, *meta*-chlorobenzoic acid(*m*CPBA) was employed in order to determine whether the shunt pathway is achievable and form a stable Fe^{III}-alkylperoxo (Fe^{III}-OOR) that is less likely to convert to a µ-peroxo dimeric species.

5.2.3.1 Addition of mCPBA

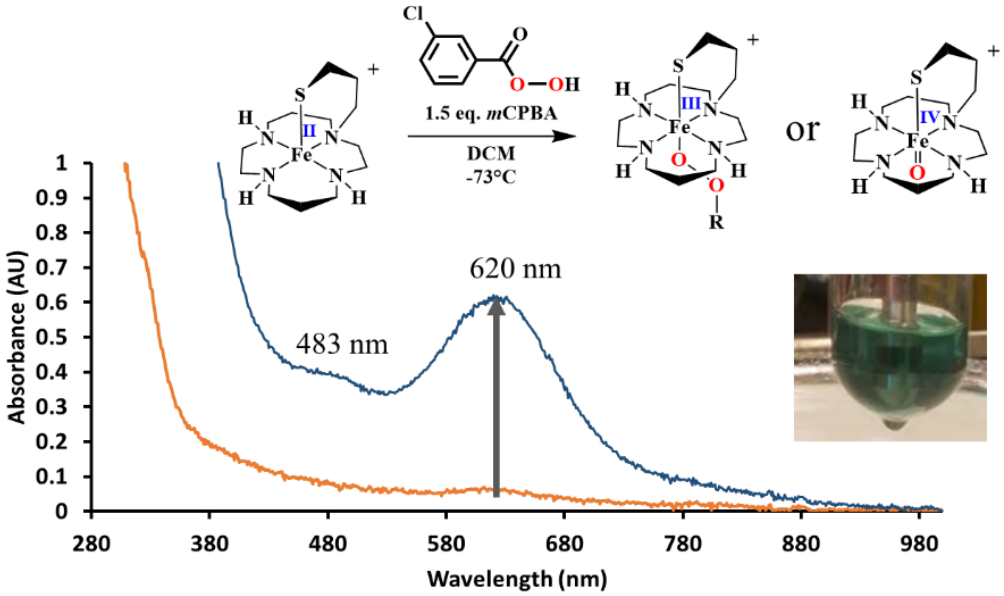

Figure 5. 10. EAS spectrum of 1.5 equivalents of *m*CPBA reacted with 0.77 mM of (**1**) in DCM at -73 °C. Proposed reactions products are either an Fe^{III}-OOR or Fe^{IV}-oxo. Scans are 30 seconds apart.

To investigate whether an alkylperoxo derivative of **2**, Fe^{III}-OOR, can be generated via a shunt pathway,[18-20] 1.5 equivalents of *m*CPBA was reacted with **1** in dichloromethane (DCM) at -73 °C (**Figure 5.10**). The use of 1.5 equivalents of the oxidant was used based on established Fenton chemistry,[21] in which 0.5 equivalents are used to oxidized Fe^{II} to Fe^{III}, while the hydroxide and benzoic acid would deprotonate the remaining equivalent of *m*CPBA to form the alkylperoxo which then binds to the open site of Fe^{III} and forms Fe^{III}-OOR. The expected EAS of an Fe^{III}-OOR

would be similar to the 530 nm of the reported Fe^{III}-OOH with a slight shift of the absorption band due to the alkyl group. However, upon addition of 1.5 equivalents of *m*CPBA to **1**, a metastable turquoise species with a λ_{max} = 620 nm and a shoulder at 483 nm formed (**Figure 5.10**). This is significantly different from Fe^{III}-OOH (**2**). Attempts at characterization of this intermediate with mass spectrometry, EPR, and XAS is ongoing. Proposed identities of this species, are (**a**) an Fe^{III}-OOR, or if the O-O bond of the *m*CPBA cleaved and acted as an oxo-atom donor (**b**) an Fe^{IV}-oxo. Both species can be distinguished from each other using electron paramagnetic resonance (EPR) and determining the spin states. Another technique to distinguish the proposed species is to perform X-ray absorption spectroscopy (XAS) to determine the oxidation state of the iron. Vibrational data will also help to determine the identity of the species, since the Fe^{III}-OOR has a strong O-O bond and weak Fe-O bond, while the FeIV-oxo would have a stronger Fe=O bond relative to the former. An ^{18}O labelled derivative of *m*CPBA will be introduced in order to verify the assignments.

5.2.3.2 Oxo Atom Donor Reactivity with [Fe^{III}CyclamPr,S]$^{+}$(1)

To pinpoint the identity of the metastable 620 nm species formed from *m*CPBA, another two-electron oxidant and oxo-atom donor iodosylbenzene (PhIO) was used.[22,23] Since PhIO acts as an oxo-atom donor, the formation of an Fe^{III}-OOR should not be observed. When 5 equivalents of PhIO in MeOH are added to **1** in a solution of DCM at -73 °C, a green metastable intermediate

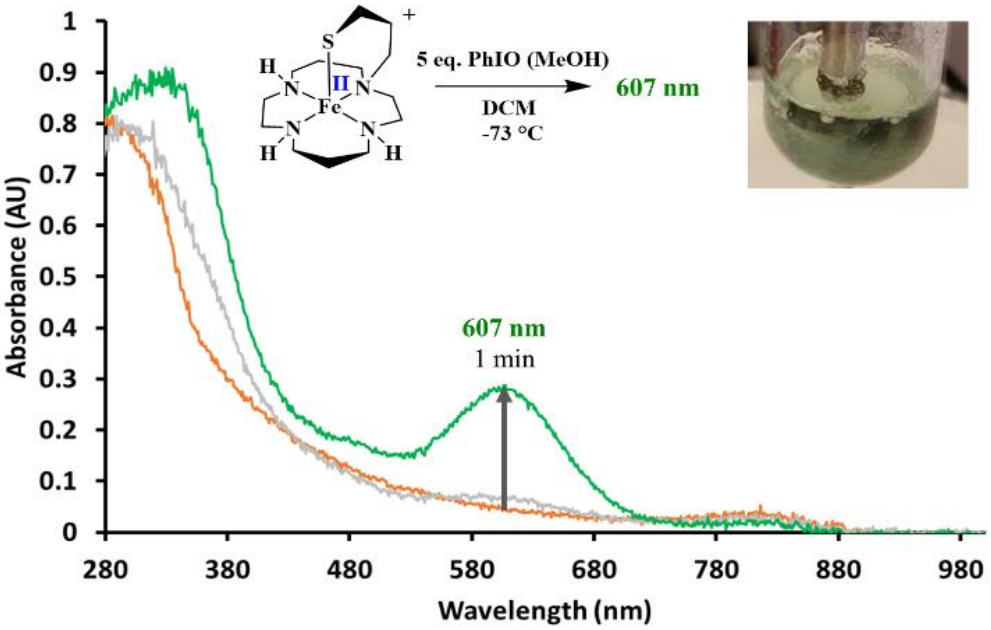

Figure 5. 11 EAS spectrum of 5 equivalents of PhIO in MeOH reacted with 0.77 mM of (**1**) in DCM at -73 °C. Scans are 30 seconds apart.

grows in over the course of one minute (**Figure 5.11**), which has an absorption band at 607 nm. Attempts to characterize this intermediate by mass spectrometry, EPR, and XAS is ongoing. A proposed structure for this green intermediate is an Fe^{IV}-oxo, however, the Kovacs group have observed that at low temperatures PhIO can bind to an Fe^{III} open site and form an adduct Fe^{III}-OIPh before cleaving the I-O bond.[24-26] To determine if the PhIO forms an adduct, reactivity of Fe^{II} (**1**) with pyridine N-oxide will be performed. The N-O bond of pyridine N-oxide is 72 kcal/mol[27] and stronger than the I-O bond (44 kcal/mol)[28] of PhIO making the adduct less likely

to less favorable to undergo N-O bond cleavage. By using different oxo-atom donors with a variety of I-O bond strengths the EAS would be expected to shift if the green species is an oxo atom donor ArIO-Fe^{III} adduct. EPR spectroscopy will be performed for the same reasons discussed previously in order to determine whether the green species has non-integer or integer spin, along with XAS. Another proposed intermediate for this 607 nm species is an Fe^{III}-OH, forms via hydrogen atom abstraction by the Fe^{IV}-oxo from MeOH. Adding another hydrogen atom source such as TEMPO-H (65.2 kcal/mol)[29] and observing the rate of formation of a putative Fe^{III}-OH along with a kinetic isotope effect will help to determine experimentally whether an Fe^{IV}-oxo is present and performing HAT.

To determine if the reactive species is an Fe^{III}-OH, a stepwise reaction will be performed and monitored by EAS, in order to generate an authentic Fe^{III}-OH *in situ* by using an outer-sphere oxidant, ferrocenium hexafluorophoshate ($FeCp_2PF_6$) to oxidize **1** to $[Fe^{III}CyclamPr\text{-}S]^+$ in the presence of tetrabutylammonium hydroxide. To investigate if the species generated by either the *m*CPBA and PhIO reactions are solvent bound (Fe^{III}-MeOH), 1 equivalent of PhIO was reacted with **4** in DCM at -73 °C to yield a λ_{max} of 545 nm (**Figure 5.12A**). The λ_{max} of this species is similar to the 540 nm species generated when 1 equivalent of $FeCp_2PF_6$ in MeOH was added to **1**

in DCM at room temperature (**Figure 5.12B**). Characterization is required in order to determine the identity of this species. The species at λ_{max} = 620 nm seen when **1** is reacted with 1.5 equivalents of *m*CPBA to generate a Fe^{III}-OOR was unanticipated. The use of PhIO to determine if the Fe^{IV}-

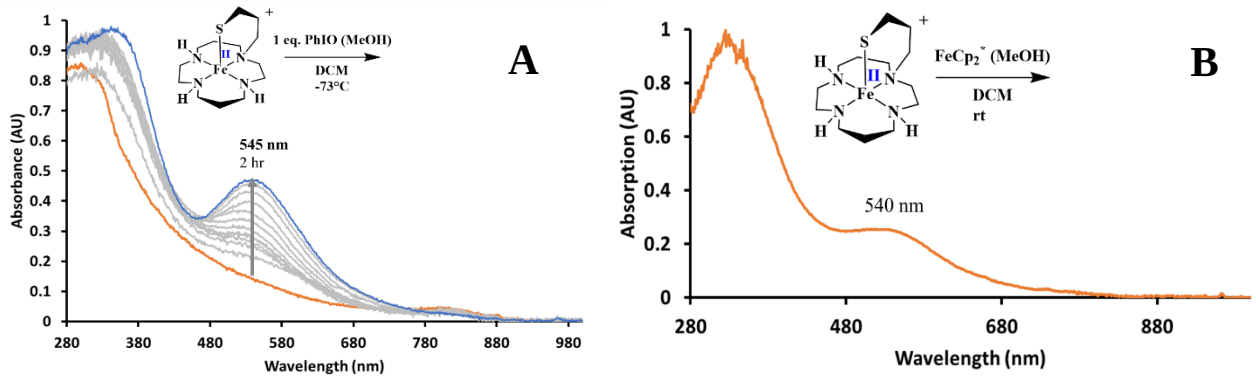

Figure 5. 12. (**A**) EAS spectrum of 1 equivalent of PhIO in MeOH reacted with 0.77 mM of **1** in DCM at -73 °C growing into maximum absorbance in 2 hours. (**B**) EAS spectrum of 1 equivalent of $FeCp_2PF_6$ in MeOH reacted with 0.77 mM of **1** in DCM at room temperature.

oxo is generated in either reaction is inconclusive without additional spectroscopic methods. Characterization methods such as EPR, XAS, and resonance Raman are needed in order to determine the nature of the species generated by the reaction of **1** with *m*CPBA and PhIO. The identity of the species will elucidate if the shunt pathway is possible in generating a thiolate ligated Fe^{III}-OOR.

5.3 Conclusions

Complex **1** has been shown to react with oxygen to afford a λ_{max} = 530 nm purple species with similar extinction coefficient to **2** formed with superoxide in the presence of protons. Investigations using calculated models and simulating EAS spectra give evidence that the purple species may not be a *trans* or *cis* Fe^{III}-OOH. Complex **1** was reacted with a two-electron oxidant to investigate if **2** can be generated via a shunt pathway using readily soluble oxidant, *m*CPBA.

When **1** was reacted with *m*CPBA, a turquoise intermediate at 620 nm formed instantly. To determine the identity of the 620 nm metastable intermediate, the use of a two-electron oxidant and oxo-atom donor, PhIO was used. When **1** was reacted with PhIO a green intermediate grew in at 607 nm within a minute. The proposed identity of the intermediates require further characterization, with an emphasis on the use of EPR, XAS, and resonance Raman in order to describe these species.

5.4 Experimental Details

5.4.1 General Methods

All reactions were performed under dinitrogen atmosphere in a glovebox, standard Schlenk techniques, or using a custom-made solution cell with a threaded glass connector to fit a dip probe. Reagents purchased from commercial vendors were of the highest purity and used without further purification. Acetonitrile (MeCN), toluene, diethyl ether (Et_2O), tetrahydrofuran (THF), dichloromethane (DCM) were rigorously degassed and purified using solvent purification columns housed in a custom stainless-steel cabinet, dispensed via a stainless steel Schlenk-line (GlassContour). Methanol (MeOH) was distilled from calcium methoxide and degassed prior to use. The synthesis of [Fe^{II}CyclamPr,S]PF_6 (**1**) was previously reported.[13]

^{1}H-NMR spectra were recorded on Bruker AV 300 or AV 301 FT-NMR spectrometers and are referenced to an internal standard of tetramethylsilane (TMS). Chemical shifts are reported in ppm and coupling constants (J) in Hz. Electrospray ionization mass spectrometry (ESI-MS) was performed on a Bruker Esquire LC-Ion Trap. Gas chromatography-mass spectrometry (GM-MS) was performed on an Agilent 5973 inert gas chromatograph/mass spectrometer (GC/MS). Infrared spectroscopy (IR) was performed on a Perkin Elmer FT-IR/FIR spectrometer with nujol mull on KBr.

Low-temperature electronic absorption spectra were recorded using a Varian Cary 50 or 60 spectrophotometers equipped with a fiber optic cable connected to a "dip" attenuated total reflection probe (C-technologies), with a custom-built two-neck solution sample holder with a threaded glass connector (sized to fit the dip probe) purged with argon gas. Modeling and molecular mechanics were performed on Avogadro (version 1.2.0).[30] Cyclic voltammograms were recorded in MeCN (0.1 M tetrabutylammonium(PF_6) solution) using a CH instruments (CHI600E) potentiostat with a glassy carbon working electrode, a $Ag/AgNO_3$ working electrode, and a platinum auxiliary electrode. Magnetic susceptibility data were acquired by Evan's method as modified for a superconducting solenoid.[31] Temperatures were obtained using Van Geet's method.[32]

Calculations were performed using the ORCA v. 4.1. quantum chemistry package developed by Neese and coworkers,[33] and employed a polarized triple-zeta def2-TZVP basis set, the def2/J auxiliary basis set for Coulomb fitting, and the atom-pairwise dispersion correction of Grimme (D3BJ).[34] Tight convergence criteria were required for self-consistent field (SCF) solutions. The Grid4 (GridX4) integration grid size, and the conductor-like polarizable continuum model with the dielectric constant e = 7.25 for tetrahydrofuran solvent (CPCM(THF)), were used for geometry optimizations.[35] Geometry optimizations and analytical frequency calculations were performed using the CAM-B3LYP functional, with the resolution of identity (RI) chain-of-spheres (RIJCOSX) approximation,[36,37] and initiated from the crystallographic coordinates when available. Analytical frequency calculations were performed on all optimized structures to determine whether the obtained stationary points corresponded to local minima. Chemcraft was used to visualize calculated EAS and IR spectra.[38] Excited states from TD-DFT calculations were analyzed using Natural Transition orbitals (NTOs) and by visualizing their difference densities between the

ground and excited states. Canonical molecular orbital isosurfaces and natural transition orbitals in the TD-DFT calculations were visualized at an isovalue of 0.05 a03 using UCSF Chimera.[39]

5.4.2 Generation of purple intermediate with O_2 to 1.

A solution of (**1**) (3.85 x 10^{-3} mmol) was dissolved in 5 mL DCM, placed in an argon purged dip probe cell and cooled to -73˚C. The solution was opened to air. The formation of a purple species characterized by EAS with λ_{max} = 530 nm.

5.4.3 Generation of turquoise intermediate with 1.5 equivalents mCPBA to 1.

A solution of (**1**) (3.85 x 10^{-3} mmol) was dissolved in 5 mL (solvent), placed in an argon purged dip probe cell and brought to -73 ˚C. 1.5 equivalents *m*CPBA (5.7 x 10^{-3} mmol) was added to the solution. Instantaneous formation of a turquoise blue species characterized by EAS with the λ_{max} = 620 nm and a shoulder at 483 nm.

5.4.4 Generation green intermediate with 5 equivalents PhIO to 1.

A solution of (**1**) (3.85 x 10^{-3} mmol) was dissolved in 5 mL DCM, placed in an argon purged dip probe cell and brought to -73 ˚C. Addition of 5 equivalents of PhIO in 250 µL MeOH (0.019 mmol) to the solution generated the formation of a green species grew in over 6 minutes characterized by EAS with λ_{max} = 607 nm.

5.4.5 Generation of proposed Fe^{III} solvent bound species with 1 equivalents PhIO to 1.

A solution of (**1**) (3.85 x 10^{-3} mmol) was dissolved in 5 mL DCM, placed in an argon purged dip probe cell and cooled to -73 ˚C. Addition of 1 equivalent of PhIO in 250 µL MeOH (3.85 x 10^{-3} mmol) and formation of a green species characterized by EAS with λ_{max} = 545 nm.

5.4.6 Generation of proposed Fe^{III} solvent bound species with 1 equivalents $FeCp_2PF_6$ to 1.

A solution of (**1**) (3.85×10^{-3} mmol) was dissolved in 5 mL DCM, placed in an argon purged dip probe cell and cooled to -73 ˚C. Addition of 1 equivalent of $FeCp_2PF_6$ in 250 µL MeOH (3.85×10^{-3} mmol) generated a species characterized by EAS with λ_{max} = 540 nm.

5.5 Chapter 5 References

(1) Bullock, R. M.; Chen, J. G.; Gagliadri, L.; Chirik, P. J.; Farha, O. K.; Hendon, C. H.; Jones, C. W.; Keith, J. A.; Klosin, J.; Minteer, S. D.; Morris, R. H.; Radosevich, A. T.; Rauchfuss, T. B.; Strotman, N. A.; Vojvodic, A.; Ward, T. R.; Yang, J. Y.; Surendranath, Y. Using nature's blueprint to expand catalysis with Earth-abundant metals. *Science* **2020**, 369, 786, 1-10 DOI: 10.1126/science.abc3183

(2) Feng, Y.; Long, S.; Tang, X.; Sun, Y.; Luque, R.; Zeng, X.; Lin, L. Earth-abundant 3d-tranistion-metal-catalysts for lignocellulosic biomass conversion. *Chem. Soc. Rev.* **2021**, 50, 6042-6093, DOI: 10.1039/D0CS01601B

(3) Albrecht, M.; Bedford, R.; Plietker, B. Catalytic and Organometallic Chemistry of Earth-Abundant Metals. *Organometallics* **2014**, 33, 20, 5619-5621, DOI: 10.1021/om5010379

(4) Shin, B.; Sutherlin, K. D.; Ohta, T.; Ogura, T.; Solomon, E. I.; Cho, J. Reactivity of a Cobalt(III)-Hydroperoxo Complex in Electrophilic Reactions. *Inorg. Chem* **2016**, 55, 23, 12391-12399, DOI: 10.1021/acs.inorgchem.6b02288

(5) Bae, S. H.; Li, X.; Seo, M. S.; Lee, Y.; Fukuzumi, S.; Nam, W. Tunneling Controls the Reaction Pathway in the Deformylation of Aldehydes by a Nonheme Iron(III)-Hydroperoxo Complex: Hydrogen Atom Abstraction versus Nucleophilic Addition. *J. Am. Chem. Soc.* **2019**, 141, 19, 7675-7679, DOIL 10.1021/jacs.9b02272

(6) Wang, B.; Li, C.; Cho, K.; Nam, W.; Shaik, S. The $Fe^{III}(H_2O_2)$ Complex as a Highly Efficient Oxidant in Sulfoxidation Reactions: Revival of an Underrated Oxidant in Cytochrome P450. *J. Chem. Theory and Computation.* **2013**, 9, 6, 2519-2525, DOI: 10.1021/ct400190f

(7) Kennepohl, P.; Neese, F.; Schweitzer, D.; Jackson, H. L.; Kovacs, J. A.; Solomon, E. I. Spectroscopy of Non-Heme Iron Thiolate Complexes: Insight into the Electronic Structure

of the Low-Spin Active Site of Nitrile Hydratase. Inorg. Chem. 2005, 44, 1826-1836, DOI: 10.1021/ic0487068

(8) Kovacs, J. A. and Brines L. M. Understanding How the Thiolate Sulfur Contributes to the Function of the Non-Heme Iron Enzyme Superoxide Reductase. *Acc. Chem. Res.* **2007**, *40* 501-509, DOI: 10.1021/ar600059h.

(9) Nam, E.; Alokolaro, P. E.; Swartz, R. D.; Gleaves, M. C.; Pikul, J.; Kovacs, J. A. Investigation of the Mechanism of Formation of a Thiolate-Ligated Fe(III)-OOH. *Inorg. Chem.* **2011**, 50, 5, 1592-1602, DOI: 10.1021/ic/101776m

(10) Hunt, A. P. and Lehnert, N. The Thiolate Trans Effect in Heme $\{FeNO\}^6$ Complexes and Beyond: Insight into the Nature of the Push Effect. *Inorg. Chem.* **2019**, 58,17, 11317-11332, DOI: 10.1021/acs.inorgchem.9b00091

(11) Matsumura, H.; Wakatabi, M.l Omi, S.l Ohtaki, A.; Nakamura, N.; Yohda, M.; Ohno, H. Modulation of Redo Potential and Alteration in Reactivity via the Peroxide Shunt Pathway by Mutation of Cytochrome P450 around the Proximal Heme Ligand. *Biochemistry* **2008**, 47, 16, 4834-4842, DOI: 10.1021/bi800142v

(12) Bailey, L. J. and Fox, B. G. Crystallographic and Catalytic Studies of the Peroxide-Shunt Reaction in a Diiron Hydroxylase. *Biochemistry* **2009**, 48, 38, 8932-8939, DOI: 10.1021/bi901150a

(13) Kitagawa, T.; Dey, A.; Lugo-Mas, P.; Benedict, J. B.; Kaminsky, W.; Solomon, E.; Kovacs, J. A. A Functional Model for the Cysteinate-Ligated Non-Heme Iron Enzyme Superoxide Reductase (SOR). *J. Am. Chem. Soc.* **2006**, 124, 45, 14448-14449 DOI: 10.1021/ja064870d

(14) Kitagawa, T. T. Biomimetic Modeling of Superoxide Reductase. Ph. D. Dissertation, University of Washington, Seattle, WA, **2007**

(15) Drago, R. S.; Epley, T. D. Enthalpies of Hydrogen Bonding and Changes in Δv Oh for a Series of Adducts with Substituted Phenols. J. Am. Chem. Soc. **1969**, 91 (11), 2883–2890. DOI: 10.1021/ja01039a010.

(16) Annaraj, J.; Cho, J.; Lee, Y.-M.; Kim, S. Y.; Latifi, R.; de Visser, S. P.; Nam, W. Structural Characterization and Remarkable Axial Ligand Effect on the Nucleophilic Reactivity of a Nonheme Manganese(III)-Peroxo Complex. *Angew. Chemie Int. Ed.* **2009**, 48 (23), 4150–4153. DOI: 10.1002/ange.200900118

(17) Cho, J.; Kang, H. Y.; Liu, L. V.; Sarangi, R.; Solomon, E. I.; Nam, W. Mononuclear Nickel(II)-Superoxo and Nickel(III)-Peroxo Complexes Bearing a Common Macrocyclic TMC Ligand. Chem. Sci. **2013**, 4, 4, 1502. DOI: 10.1039/c3sc22173c

(18) Coggins, M. K. and Kovas, J. A. Structural and Spectroscopic Characterization of Metastable Thiolate-Ligated Manganese(III)-Alkylperoxo Species. *J. Am. Chem. Soc.* **2011**, *133*, 12470-12473, DOI: 10.1021/ja205520u

(19) Opalade, A. A.; Parham, J. D.; Day, V. W.; Jackson, T. A. Characterization and chemical reactivity of room-temperature-stable Mn^{III}-alkylperoxo complexes. *Chem. Science.* **2021**, 38, 12, 12564-12575, DOI: 10.1039/D1SC01976G

(20) Jeoung, J.; Bommer, M.; Lin, T.; Dobbek, H. Visualizing the substrate-, superoxo-, alkylperoxo-, and product-bound states at the nonheme Fe(II) site of homogentisate dioxygenase. *PNAS* **2013**, 110, 31, 12625-12630, DOI: 10.1073/pnas.1302144110

(21) Winterbourn, C. C. Toxicity of iron and hydrogen peroxide: the Fenton reaction. *Toxicology Letters.* **1995**, *82*, 969-974, DOI: 10.1016/0378-4274(95)03532-x

(22) Nam. W.; Choi, S. K.; Lim, M. H.; Rohde, J.; Kim, I.; Kim, J.; Kim, C.; Que, L. Jr. Reversible Formation of Iodosylbenzene-Iron Porphyrin Intermediates in the Reaction of Oxoiron(IV) Porphyrin pi-Cation Radicals and Iodobenzene. *Ang. Chem. Int. Ed.* **2003**, 42, 1, 109-111 DOI: 10.1002/anie.200390036

(23) Yang, J.; Seo, M. S.; Kim, K. H.; Lee, Y. M.; Fukuzumi, S.; Shearer, J.; Nam, W. Structure and Unprecedented Reactivity of a Mononuclear Nonheme Cobalt(III) Iodosylbenzene Complex *Ang. Chem. Int. Ed.* **2020**, 59, 32, 13581-13585, DOI: 10.1002/anie.202005091

(24) Blakely, M. N.; Dedushko, M. A.; Poon, P. C. Y.; Villar-Acevedo, G.; Kovacs, J. A. Formation of a Teactive Alkyl Thiolate-Ligated Fe^{III}-Superoxo Intermediate Derived from Dioxygen. *J. Am. Chem. Soc.* **2019**, *141*, 1867-1870, DOI: 10.1021/jacs.8b12670

(25) Downing, A. N. Effects of Ligand-Constraints on the Reactivity of Biomimetic Thiolate-Ligated Transition Metal Complexes. Ph. D. Dissertation, University of Washington, Seattle, WA, **2021**

(26) Rogers, D. M. Structural Effects on the Kinetics and Thermodynamics of Making and Breaking O-O Bonds. Ph. D. Dissertation, University of Washington, Seattle, WA, **2023**

(27) Shaofeng, L.; Pilcher, G. Enthalpy of formation of pyridine-N-oxide: the dissociation enthalpy of the (N-O) bond. *J. Chem. Thermodyn.* **1988**, *20*, 463-465, DOI: 10.1016/0021-9614(88)90184-X

(28) Coleman, E. H.; Gaydon, A. G.; Vaidya, W. M.; Spectrum of Iodine Oxide (IO) in Flames. *Nature*, **1948**, *162*, 108-109, DOI: 10.1038/162108b0

(29) Porter, T. H. and Mayer, J. M. Radical Reactivity of the Fe (III)/(II) Tetramesitylporphyrin Couple: Hydrogen Atom Transfer, Oxyl Radical Dissociation, and Catalytic Disproportionation of a Hydroxylamine. *Chem. Sci.* **2014**, *5*, 372-380, DOI: 10.1039/C3SC52055B

(30) Hanwell, M. D.; Curtis, D. E.; Lonie, D. C.; Vandermeersch, T.' Zurek, E.; Hutchison, G. R. Avogadro: An advanced semantic chemical editor, visualization, and analysis platform *Journal of Cheminformatics* **2012**, 4:17 Version 1.2.0

(31) Evans, D. A., The Determination of the Paramagnetic Susceptibility of Substances in Solution by Nuclear Magnetic Resonance. *J. Chem. Soc.* **1959**, 2003-2005. DOI: 10.1039/JR9590002003

(32) Van Geet, A. L., Calibration of the Methanol and Glycol Nuclear Magnetic Resonance Thermometers with a Static Thermistor Probe. *Anal. Chem.* **1970**, *42*, 2227-2229. DOI: 10.1021/ac50158a064

(33) Neese, Frank. Software update: The ORCA program system – Version 5.0. *WIREs Computational Molecular Science.* **2022**, 12, 5 e1606, DOI: 10.1002/wcms.1606

(34) Grimme, Stefan; Ehrlich, Stephan; Goerigk, Lars. Effect of the damping function in dispersion corrected density functional theory. *J. Compt. Chem.* **2011**, 32, 7, 1456-1465, DOI: 10.1002/jcc.21759

(35) Barone, V.; Cossi, M., Quantum Calculation of Molecular Energies and Energy Gradients in Solution by a Conductor Solvent Model. *J. Phys. Chem.* **1998,** *102*, 1995 -2001. DOI: 10.1021/jp9716997

(36) Yanai, T.; Tew, D. P.; Handy, N. C. A new hybrid exchange-correltation functional using the Coulomb-attenuating method (CAM-B3LYP). **2004** *Chem. Phys. Lett.,* **2004**, 393, 51-57 DOI: 10.1016/j.cplett.2004.06.011

(37) Neese, Frank. Efficient, approximate, and parallel Hartree-Fock and hybrid DFT calculations. A 'chain-of-spheres' algorithm for the Hartree-Fock exchange. *Chemical. Physics.* **2009**, 356, 1-3, 98-109, DOI: 10.1016/j.chemphys.2008.10.036

(38) Zhurko, G. A. Chemcraft – graphical program for visualization of quantum chemistry computations. Ivanovo, Russia, **2005**. https://chemcraftprog.com

(39) Pettersen, Eric F.; Goddard, Thomas D.; Huang, Conrad C.; Couch, Gregory S.; Greenblatt, Daniel M.; Meng, Elaine C.; Ferrin, Thomas E. UCSF Chimera—a visualization system for exploratory research and analysis. *J. Compt. Chem.* **2004**, 25, 13, 1605-1612, DOI: 10.1002/jcc.20084